



HAL
open science

Unlocking the Potential of Photochromic Tungsten Oxide (WO_{3-x}) Materials: Synthesis, Characterization, and Shaping of Hybrid organic-inorganic WO₃-doped Systems (0D, 1D, 2D) for Optical Applications

Yazan Badour

► **To cite this version:**

Yazan Badour. Unlocking the Potential of Photochromic Tungsten Oxide (WO_{3-x}) Materials: Synthesis, Characterization, and Shaping of Hybrid organic-inorganic WO₃-doped Systems (0D, 1D, 2D) for Optical Applications. Material chemistry. Université de Bordeaux, 2023. English. NNT : 2023BORD0248 . tel-04280391

HAL Id: tel-04280391

<https://theses.hal.science/tel-04280391>

Submitted on 11 Nov 2023

HAL is a multi-disciplinary open access archive for the deposit and dissemination of scientific research documents, whether they are published or not. The documents may come from teaching and research institutions in France or abroad, or from public or private research centers.

L'archive ouverte pluridisciplinaire **HAL**, est destinée au dépôt et à la diffusion de documents scientifiques de niveau recherche, publiés ou non, émanant des établissements d'enseignement et de recherche français ou étrangers, des laboratoires publics ou privés.

THÈSE PRÉSENTÉE
POUR OBTENIR LE GRADE DE

DOCTEUR DE

L'UNIVERSITÉ DE BORDEAUX

ÉCOLE DOCTORALE DES SCIENCES CHIMIQUES

SPÉCIALITÉ : Physico-Chimie de la Matière Condensée

Par Yazan BADOUR

WO_{3-x}-based photochromic materials: Preparation and characterization of organic-inorganic hybrids (0D, 1D, 2D) for optical applications

**Etude des matériaux à base d'oxyde de tungstène photochromique (WO_{3-x}) :
Elaboration et caractérisation de systèmes organiques-inorganiques
hybrides (0D, 1D, 2D) pour des applications optiques**

Sous la direction de Manuel GAUDON et co-Encadrant : Sylvain DANTO

À Soutenir le 13 Octobre 2023

Membres du jury:

Mme. NAZABAL, Virginie	Directrice de recherche, ISCR, Rennes	Rapporteuse
M. DESSAPT, Rémi	Maître de Conférences, IMN, Nantes	Rapporteur
M. AYMONIER, Cyril	Directeur de recherche, ICMCB, Bordeaux	Examineur
M. GAUDON, Manuel	Professor, ICMCB, Bordeaux	Directeur de thèse
M. DANTO, Sylvain	Chercheur, ICMCB, Bordeaux	Invité
M. SONNEMANN, Guido	Professeur, ISM, Bordeaux	Invité

Contents

General introduction	14
Chapter I: State-of-the-art and objectives	18
1 Color: from basic concepts up to WO ₃ as NIR filter.....	19
1.1 Basics concepts of color.....	19
1.1.1 Visible light.....	19
1.1.2 Hue.....	20
1.1.3 Saturation.....	20
1.1.4 Chroma.....	20
1.1.5 Lightness.....	20
1.2 Colorimetry.....	21
1.3 Causes of color in inorganic materials.....	22
1.3.1 Color due to crystal field theory (Intra-atomic electronic transition)	22
1.3.2 Color due to charge transfer (Inter-atomic electronic transition through a bond).....	23
1.3.3 Color due to Valence Band (VB) to Conduction Band (CB) transitions.....	25
1.3.4 Color due to semi-local defects up to free electron gas	26
1.4 WO ₃ as a UV-NIR filter material.....	29
1.4.1 Selectivity of solar energy factor	30
1.4.2 Plasmonic semiconductors for near-infrared absorption.....	30
1.4.3 Sub-stoichiometric tungsten oxide for NIR filter applications	31
2 X-chromic (or chromogenic) effect in inorganic materials.....	34
2.1 Types of chromic effects	34
2.1.1 Photochromism	34
2.1.2 Electrochromism	34
2.1.3 Thermochromism.....	35
2.1.4 Solvatochromism	36
2.1.5 Gasochromism	36
2.2 X-chromic mechanisms: Crystal phase transitions or redox properties?	36
2.2.1 Crystal phase transition in chromic materials	36
2.2.2 Redox properties	37
2.3 Focus on photochromic materials	37
2.3.1 Different classes of photochromic compounds	38
2.3.2 Photochromic organic-inorganic hybrid materials	40
2.3.3 Applications of inorganic photochromic compounds	41
3 Tungsten oxide as the photochromic material of next future.....	44

3.1	The crystalline structures of WO_x	44
3.2	Synthesis of Tungsten Oxide Nanostructures	46
3.2.1	Sol-Gel	46
3.2.2	Hydrothermal	47
3.2.3	Electrodeposition	48
3.2.4	Polyol method	49
3.3	Photochromism in WO_x -based materials	52
3.3.1	Theoretical models explaining the WO_3 photochromism	52
3.3.2	Morphological modification	53
3.3.3	Doping.....	55
3.3.4	WO_3 - Schottky barriers at inorganic composite interfaces	56
3.4	WO_3 into hybrid devices and compounds	57
3.4.1	0D WO_3 colloidal suspensions (quantum dots and dispersed NPs)	58
3.4.2	2D Thin films (toward smart windows)	60
3.4.3	WO_3 in 1D fibers / 2D textiles	69
3.5	New perspectives: from 1D fibers towards 3D printing filaments: polymer/ WO_3 -based processing	73
3.5.1	3D printing-enabled polymer/particle materials	74
3.5.2	3D printing for polymer/particle processing.....	76
4	The positioning of our study besides state of the art.....	77
5	References.....	79
Chapter II: Characterization techniques		97
1	Characterizations Techniques :	98
1.1	Differential Scanning Calorimetry (DSC)	98
1.2	Melt flow index (MFI)	98
1.3	Mechanical Profilometer.....	99
1.4	Optical Profilometer.....	99
1.5	X-ray diffraction (XRD) analyses.....	100
1.5.1	Bragg's Law	100
1.5.2	FullProf Refinement.....	101
1.5.3	Limitations of Bragg's law on nanoparticles	101
1.5.4	Total scattering approach to nanoparticles structure description	101
1.5.5	Pair Distribution Function analysis.....	102
1.6	Scanning Electron Microscope (SEM)	103
1.7	Transmission electron microscopy (TEM).....	104
1.8	Electron Paramagnetic Resonance (EPR).....	104
1.9	X-ray Photoelectron Spectroscopy (XPS).....	105
1.10	Dynamic light scattering (DLS).....	106

1.11	UV-visible-NIR spectrophotometer	107
1.12	Optical fibers measurement	108
1.12.1	Definitions and light guiding principle	108
1.12.2	Types of optical fibers	109
1.12.3	Attenuation of the fibers	110
1.13	References:.....	111
Chapter III: Results and Discussion.....		113
1	Part 1: Powder modification for better photochromism: Oxidation.....	114
1.1	Elaboration and characterization of NPs and thin films.....	114
1.1.1	Polyol synthesis of WO ₃ powders	114
1.1.2	Pristine film elaboration.....	114
1.2	Structural, morphological, and chemical characterization of the as-prepared NPs.....	114
1.2.1	The four different WO ₃ nano-powders in a glimpse	114
1.2.2	Powder physicochemical characterizations.....	115
1.2.3	Powder optical properties.....	121
1.3	Electrical characterization of the prepared thin films	123
1.4	Conclusion of Part 1.....	127
2	Part 2: Powder modification for better photochromism: Doping.....	129
2.1	Elaboration and characterization of NPs and thin films.....	129
2.2	Structural, morphological, and chemical characterization of the as-prepared NPs.....	129
2.2.1	Powder physicochemical characterizations.....	129
2.2.2	Powder photochromic properties	135
2.2.3	Thin film photochromic properties	136
2.3	Conclusion for Part 2	140
3	Part 3: Thin and thick plastic thin film based on WO _{3-x} active NPs.....	142
3.1	Elaboration and characterization of NPs and plastic films	142
3.2	Suspension study: Results and discussions	142
3.3	From suspension to film: elaboration and optical properties	145
3.4	Photochromic properties of the films: kinetic aspects	148
3.5	Thermal insulation properties	150
3.6	Conclusion for Part 3	153
4	Part 4: Developing plastic photochromic fibers for sensing application: the combination of 0D WO _{3-x} structure in a 1D polymeric matrix.....	156
4.1	Functionalization of polysulfone plastic optical fibers by WO _{3-x} :	156
4.1.1	Core-fiber drawing (signal quality control of the non-modified PES POFs).....	156
4.1.2	The different routes used for the WO ₃ -PES composite fibers.....	157
4.1.3	SEM photographs of the different issued fibers.....	159
4.1.4	Photochromic properties of the prepared fibers	160

4.1.5	Revitalizing the post-coating method: Unleashing its potential as a powerful fiber modification technique.....	162
4.1.6	WO ₃ -PVP composite claddings	163
4.1.7	Interpretation of the “negative photochromism”	168
4.2	Conclusion of Part 4.....	171
5	Part 5: Hybrid organic-inorganic PMMA optical fibers functionalized with photochromic active WO ₃ nanoparticles: from materials design to photochromic fabrics.....	173
5.1	Elaboration of the lab-made PMMA doped with WO ₃	173
5.2	Main results and discussions.....	174
5.2.1	WO ₃ particle size distribution into monomer suspensions.....	174
5.2.2	Composites preform characterizations	174
5.2.3	Single fiber characterization	179
5.2.4	Photochromic properties of 2D textile	185
5.3	Conclusion for Part 5	186
5.4	References.....	187
1	Life cycle assessment: a powerful technique to evaluate the environmental impacts of products	194
2	Goal and scope of research	195
3	Function and functional unit	196
4	System boundaries	196
5	Life cycle inventory analysis (LCI)	197
6	Results and discussions:.....	201
7	Comparison of the final products.....	203
8	Conclusion:	205
9	References.....	205
	General conclusion	210

Acknowledgments:

I extend my heartfelt gratitude and appreciation to all those who have been a part of my remarkable journey throughout my Ph.D. It is with immense pleasure that I acknowledge their support, encouragement, and unwavering faith in my abilities.

First and foremost, I would like to express my deep gratitude to my family, especially my parents and brothers, for their unwavering love, support, and the sacrifices they made to provide me with the opportunity to pursue my dreams. Your resilience during times of adversity, surviving the war in Syria and the devastating earthquake that destroyed our home, has been a profound source of inspiration for me. You are the embodiment of strength, and your unwavering faith in my abilities has been the driving force behind my success.

I would like to express my heartfelt appreciation to my two thesis supervisors, Dr. Manuel Gaudon and Dr. Sylvain Danto, for their exceptional guidance and support throughout my Ph.D. journey. Their combined expertise and mentorship have been instrumental in my academic and personal growth.

Manuel Gaudon, in addition to being an outstanding supervisor, I am deeply grateful for the opportunity you provided me with by offering a scholarship to come to France. Your unwavering belief in my potential and your commitment to fostering my personal and professional development have played a pivotal role in shaping my academic journey. Your encouragement, insightful advice, and dedication to my research endeavors have been invaluable. Your ability to see beyond the challenges and provide solutions has been a source of inspiration for me. You were always the first support for me since the first beginning of my academic journey, I am so grateful for your help and for everything.

Sylvain, your dedication to my research and your tireless efforts to ensure that I had the resources and guidance necessary to excel in my work have not gone unnoticed. Your profound expertise in the field and your willingness to share your knowledge have been pivotal in my academic development. Your feedback and support have made the academic journey smoother and more fulfilling.

I am truly fortunate to have had the opportunity to work under the guidance of Manuel and Sylvain. Their support, encouragement, and mentorship have been the cornerstone of my success, and I am deeply grateful for the knowledge and insights I have gained from both of them.

To my dear friends from all around the world, I am blessed to have your unwavering friendship and support. Your presence in my life has added richness and diversity to my experiences. I am grateful for the late-night study sessions, the moments of laughter, and the encouragement you provided during the challenging phases of my research. Your belief in me, even when I had doubts, has been a constant source of motivation.

To my Ph.D. colleagues, thank you for the camaraderie and the shared experiences that made the research journey all the more enriching. Your presence in the academic world has been a constant reminder that we are part of a larger community, striving for knowledge and innovation.

In conclusion, I am immensely grateful to each and every one of you who has played a role, big or small, in my academic and personal growth. Your support and encouragement have been the cornerstone of my success, and I look forward to paying this gratitude forward by contributing to the advancement of knowledge and society in the years to come. Thank you for being a part of my journey.

Résumé de thèse

Ce résumé de thèse présente en détails les conclusions majeures de chaque chapitre de notre recherche sur les nanomatériaux photochromiques à base de WO_{3-x} et leurs applications potentielles dans le domaine de l'optique. Chaque chapitre a contribué à une avancée significative dans notre compréhension de ces matériaux et de leur utilité dans des dispositifs optiques intelligents. Dans ce résumé, nous allons fournir une vue d'ensemble plus complète de chaque chapitre d'étude et mettre en lumière les applications clés qui pourraient émerger de chaque étude.

Le domaine des matériaux X-chromiques, capables de modifier de manière réversible leurs propriétés optiques en réponse à des stimuli externes tels que la température, la lumière, la tension, la nature du gaz, etc., suscite un vif intérêt. Les matériaux inorganiques présentant des effets X-chromiques sont d'une grande importance pour diverses applications, notamment les fenêtres intelligentes, les écrans, les capteurs et les dispositifs électrochromiques. Ces phénomènes X-chromiques englobent généralement divers processus conduisant à des changements dans l'absorption et la réflexion de la lumière, à l'absorption d'énergie et à l'émission de lumière, au transfert d'énergie ou à une conversion de la lumière. Au sein des classes de composés inorganiques, les effets chromiques peuvent être optimisés en variant la composition, la structure cristalline et la morphologie des cristallites.

Les composés d'oxyde de tungstène (WO_{3-x}) se distinguent par leur versatilité en ce qui concerne le ratio W/O, ce qui permet de moduler leur potentiel rédox ainsi que leur coloration. Ils représentent donc une catégorie importante de matériaux X-chromiques. Aussi, au cours des dernières décennies, ces composés ont fait l'objet de recherches approfondies en raison de leur grande richesse structurale (pas moins de 7 formes allotropiques différentes). Par conséquent, les chercheurs ont reconnu le potentiel énorme de ces composés dans un large éventail d'applications. Cela inclut le développement de dispositifs optiques photochromiques, de capteurs de gaz, de photocatalyseurs, voire même de panneaux plats électrochromiques. Cependant, bien que largement étudiées, des limitations subsistent encore en ce qui concerne les propriétés photochromiques des dispositifs à base de WO_{3-x} freinant leur potentiel. Ces limites comprennent (i) la faible réversibilité (cinétique de décoloration lente) des matériaux à base de WO_{3-x} , (ii) le faible contraste de couleur avant et après irradiation, et (iii) la difficulté de fabriquer des dispositifs flexibles à base de WO_{3-x} . Ainsi, l'optimisation du photochromisme des nanoparticules de WO_{3-x} , suivie de leur incorporation dans une matrice polymère organique (films minces, films épais ou fibres), constitue le sujet central de la thèse. Cette recherche apporte une contribution significative aux travaux en cours sur les matériaux "X-chrome" à l'ICMCB.

Nos travaux peuvent être présentés comme se concentrant autour de deux axes principaux :

Axe 1 : Amélioration des propriétés photochromiques de l'oxyde de tungstène

Nous explorons ici l'utilisation de différentes méthodes chimiques pour améliorer l'activité photochromique des nanostructures de WO_{3-x} généralement sous forme pulvérulente. Cela implique le réglage de la sous-stœchiométrie en oxygène des nanoparticules préparées à partir des paramètres du

processus de germination-croissance en milieu polyol et/ou par le dopage structural par le cuivre (ions Cu^{2+}) des nanoparticules.

Axe 2 : Fabrication de matériaux photochromiques organiques-inorganiques

Les matériaux hybrides organiques-inorganiques combinent les meilleures caractéristiques des deux types de matériaux. Ils peuvent être légers, flexibles et polyvalents comme les matériaux organiques, tout en présentant une grande résistance thermique et mécanique propre aux matériaux inorganiques. En maintenant le photochromisme des nanoparticules intégrées dans la matrice polymérique, la haute transparence des films ou des fibres hybrides optimisées ouvre de nouvelles perspectives applicatives. Nous examinons le potentiel d'une telle stratégie pour développer des dispositifs photochromiques à base de WO_3 .

La thèse se compose de quatre chapitres, progressant de l'investigation des composés pulvérulents WO_{3-x} en se focalisant sur l'optimisation de leurs propriétés photochromiques, puis en allant vers leur incorporation dans des matrices polymères 1D, 2D et 3D. Le premier chapitre dresse un état de l'art sur les origines de la couleur dans les matériaux inorganiques, avec un aperçu détaillé des principaux mécanismes de transferts électroniques à l'œuvre. Ce chapitre examine également en profondeur les caractéristiques propres à l'oxyde de tungstène : sa structure cristallographique, les diverses méthodes de synthèse ainsi que ses propriétés X-chromiques, en mettant l'accent sur les dispositifs hybrides à base de WO_{3-x} documentés dans la littérature.

Chapitre 1 : Synthèse des nanopoudres de WO_{3-x} par précipitation polyolique

Dans ce premier chapitre, nous avons réalisé un progrès essentiel en contrôlant la sous-stœchiométrie des nanopoudres de WO_{3-x} par le biais d'une méthode de précipitation en milieu polyol réductrice, suivie d'une ré-oxydation partielle par peptisation dans des solutions aqueuses de chromate. Cette approche innovante nous a permis de produire des échantillons de WO_{3-x} présentant diverses stœchiométries. Les échantillons les plus ré-oxydés se sont révélés particulièrement prometteurs en tant que filtres solaires pour les fenêtres intelligentes, car ils combinent une transparence élevée dans le spectre visible avec une excellente absorption dans le proche infrarouge (NIR). Ce résultat est crucial pour améliorer l'efficacité énergétique des bâtiments en régulant la chaleur solaire. En outre, notre étude du mécanisme de coloration sous irradiation UV (photochromisme) de ces échantillons a révélé que la réduction rapide des cations de surface de W^{+6} à W^{+5} , associée à une absorption et à une désorption rapide de l'oxygène de surface, était le principal moteur de ce phénomène. Cette capacité des nanoparticules de WO_{3-x} à réagir rapidement aux rayons UV et à retrouver leur couleur initiale dans l'obscurité ouvre des opportunités pour des applications telles que la détection UV et le stockage d'énergie photo-induite (telle qu'une « batterie photochimique »).

De plus, une analyse structurale détaillée de ces nanocristallites a été menée en utilisant une combinaison d'outils, notamment l'analyse des motifs de diffraction des rayons X (DRX), l'analyse

des fonctions de distribution radiale (PDF) et la microscopie électronique à transmission (MET). Les résultats ont montré que malgré leur petite taille, les nanocristallites conservaient une structure monoclinique avec un groupe d'espace P21/n (c'est-à-dire la structure cristallographique stable observée pour des cristallites beaucoup plus gros). Cette information est cruciale pour comprendre les propriétés physiques de ces matériaux et leur utilisation potentielle dans divers dispositifs optiques. Par conséquent, nos conclusions de ce chapitre suggèrent que ces nanoparticules de WO_{3-x} peuvent être utilisées pour améliorer la performance de capteurs optiques, de filtres optiques et de dispositifs de stockage d'énergie photo-induite.

Chapitre 2 : Dopage du WO_{3-x} avec du Cuivre dans les films photochromiques intelligents

Le deuxième chapitre de notre thèse a abordé la question du dopage de nanoparticules de WO_{3-x} avec du cuivre (Cu) toujours préparées par la méthode de coprécipitation en milieu polyol et son impact sur les propriétés des films photochromiques intelligents. Cette approche a démontré son efficacité pour améliorer la cinétique de décoloration de ces films. Les films non dopés ont montré un mécanisme de coloration rapide, suivi d'un mécanisme légèrement plus lent en raison de la saturation de la surface en ions W^{+5} . En revanche, les films dopés aux ions Cu^{2+} ont présenté une cinétique de décoloration plus rapide grâce à une augmentation des lacunes d'oxygène dans le WO_{3-x} après le dopage et la création de niveaux électroniques accessibles au milieu de la bande interdite de ces semi-conducteurs (catalysant, en quelque sorte, le processus de décoloration). De plus, des études de cyclage sur les films dopés au Cu ont confirmé leur efficacité dans diverses applications optiques, notamment dans les textiles intelligents, les fenêtres et les filtres optiques. Par conséquent, les résultats de ce chapitre mettent en lumière le potentiel de ces films pour être utilisés dans des dispositifs qui requièrent à la fois une évolution rapide en coloration et une réversibilité totale sur moins d'une dizaine d'heures en décoloration : tels que les vitrages de bâtiments intelligents, les dispositifs de détection optique et les textiles photochromiques.

Chapitre 3 : Isolation thermique efficace grâce à des films composites pour fenêtres intelligentes

Le troisième chapitre de notre thèse a traité de la question cruciale de l'isolation thermique en utilisant des films composites fabriqués par les méthodes d'immersion– retrait d'un substrat au sein d'une suspension (« dip-coating ») ou de dépôt direct d'un volume de suspension contrôlé sur une surface contrôlée de substrat (« solvent casting »). Ces films ont été évalués avec soin pour leur capacité à réguler la transmission de la lumière solaire et à fournir une isolation thermique efficace. Les résultats ont montré que les films issus du procédé de solvent casting présentaient une meilleure absorption de la lumière et une moindre diffusion par rapport aux films élaborés par dip-coating, ce qui se traduisait par une efficacité photochromique accrue, c'est-à-dire un contraste plus élevé entre les états colorés et décolorés. De plus, la cinétique du comportement photochrome de ces films a été examinée en détail,

montrant que les films issus du dip-coating étaient avec des cinétiques de coloration/décoloration légèrement plus rapides en raison d'un effet de blocage des réactions photo-redox par la matrice de PVA moins important (ces films étant plus minces que ceux obtenus par solvant casting). Enfin, nous avons réalisé des mesures d'isolation thermique (en adossant ces films à des vitrages de modèles réduits de bâtiment que nous avons-nous-mêmes développés), qui ont montré que ces films intelligents offraient une performance thermique remarquable, en particulier lorsque les films étaient placés du côté avant des fenêtres, à proximité de la source de rayonnement. Ces résultats revêtent une grande importance pour les bâtiments à économie d'énergie (bâtiments dits intelligents avec auto-régulation thermique).

Chapitre 4 : Fibres optiques photochromiques à base de WO_{3-x}

Le quatrième chapitre de la thèse a exploré la fabrication de fibres optiques photochromiques en utilisant diverses techniques. Ces fibres se sont révélées capables de présenter un comportement photochromique similaire à celui des nanopoudres de WO_{3-x}, avec qui plus est des caractéristiques de coloration et de décoloration plus rapides. De plus, nous avons étudié l'impact de l'ajout d'un revêtement protecteur, montrant que l'ajout de couches de revêtement augmentait l'efficacité photochromique. Ces fibres pourraient avoir des applications potentielles dans les communications optiques, les capteurs et d'autres dispositifs photochromiques. L'étude des mécanismes sous-jacents a permis d'acquérir une meilleure compréhension du comportement photochromique de ces fibres, ouvrant la voie à des applications innovantes dans le domaine de l'optique.

Chapitre 5 : Fibres optiques hybrides inorganiques/organiques à base de WO_{3-x} -dopé PMMA/PES

Dans le cinquième chapitre, nous avons exploré la fabrication de fibres optiques hybrides inorganiques/organiques en dopant le PMMA avec du WO_{3-x}. Ces fibres ont montré des propriétés de photochromisme, avec un comportement de coloration et de décoloration contrôlable. De plus, nous avons fabriqué un tissu photochromique 2D à partir de ces fibres, démontrant ainsi le potentiel de ces matériaux dans la création de textiles photochromiques pour des applications telles que les vêtements intelligents et les textiles fonctionnels. La capacité de ces fibres à présenter un photochromisme négatif et positif ouvre de nouvelles perspectives pour des applications personnalisées dans les textiles, les dispositifs de signalisation optique et les technologies de l'information.

Enfin, dans une première tentative pour fabriquer des objets 3D à partir de filaments obtenus à partir de granulés commerciaux de PMMA avec différentes charges de nanopoudres de WO_{3-x}, nous avons prouvé avec succès la faisabilité de ce projet grâce à une collaboration avec la société RESCOLL à Pessac. Les premiers résultats, prometteurs, ouvrent la voie à de nouvelles possibilités de recherche et

de développement, offrant un aperçu de l'avenir prometteur de l'intégration de matériaux photochromiques dans l'impression 3D et d'autres domaines innovants de l'ingénierie.

Conclusion générale :

En conclusion, cette thèse jette les fondations d'une meilleure compréhension des nanomatériaux photochromiques à base de WO_{3-x} et de leurs applications potentielles dans une multitude de domaines de l'optique. Les résultats obtenus révèlent un fort potentiel dans les domaines de l'industrie des fenêtres intelligentes, des textiles intelligents, des dispositifs optiques et des fibres optiques photochromiques. Cependant, il est important de reconnaître que des recherches futures sont nécessaires pour pousser plus loin l'optimisation de ces matériaux et évaluer leur impact environnemental sur l'ensemble de leur cycle de vie. Les premiers résultats d'une étude en cours sur une évaluation de l'impact environnemental associé à l'addition d'« étiquettes » cousues ou imprimées sur des textiles sont reportés en tant que « chapitre additionnel » à la fin de ce manuscrit.

En outre, il est impératif de traduire ces découvertes en applications concrètes pour la société. Cela implique de relever le défi du transfert technologique pour converger vers des solutions pratiques et commerciales. Cette étape cruciale permettra de concrétiser ces avancées scientifiques en produits réels, contribuant ainsi de manière significative aux progrès technologiques et au développement de produits innovants.

En définitive, cette thèse représente un jalon significatif dans l'exploitation du potentiel des nanomatériaux photochromiques à base de WO_{3-x} pour résoudre des problèmes et créer de nouvelles opportunités dans le domaine de l'optique. Elle met en lumière l'importance continue de la recherche dans ce domaine en insistant sur la nécessité de concevoir des dispositifs pratiques basés sur ces découvertes, visant à améliorer notre qualité de vie, à promouvoir le développement durable et à favoriser des avancées significatives dans les domaines de l'énergie, des communications optiques et des matériaux intelligents. L'avenir promet des innovations passionnantes grâce à ces avancées, ouvrant la voie à une société plus avancée, plus durable et plus intelligente.

Mots-clés : Photochromisme, Oxyde de tungstène, Chrome, Fenêtres intelligentes, Isolation thermique.

General introduction

X-chromic materials change reversibly their optical properties under an external stimulus, such as temperature, light, voltage, gas, etc. Inorganic materials that exhibit chromic effects are of great interest for various applications, including smart windows, displays, sensors, and electrochromic devices. Generally, chromic phenomena include different processes resulting in changes in the absorption and reflection of light, absorption of energy and emission of light, absorption of light and energy transfer, or a conversion of light. In inorganic compound classes, the chromic effects can be optimized by varying the composition, the crystalline structure and the morphology of the crystallites. Thanks to the versatility of their W/O ratio, leading to redox potentialities, tungsten oxide compounds (WO_{3-x}) represent an important class of X-chromic materials. Over the past few decades, there has been a significant and thorough investigation into these compounds due to their large variety of structures. As a result, researchers have recognized the immense potential of these compounds in a wide range of applications. These include the development of photochromic optical devices, gas sensors, photocatalysts, and even electrochromic flat panel displays, among other exciting possibilities. Yet, although extensively investigated, limitations in the photochromic properties of WO_{3-x} devices remain, underpinning their potential. These limitations include (i) the poor reversibility (slow bleaching kinetic) of WO_3 -based materials, (ii) the low color contrast before and after irradiation, and (iii) the difficulty to fabricate WO_3 -based flexible devices. Herein, the optimization of the photochromism of WO_{3-x} nanoparticles, then, their incorporation of X-chromic tungsten oxides WO_{3-x} in an organic polymer matrix (thin film, thick films, or fibers) is the core subject of the thesis. It represents a significant contribution to the ongoing research on "X-chrome" materials at ICMCB.

Research focuses on two main axes:

- Axis 1: Improving the photochromic properties of tungsten oxide.

Here we investigate the implementation of different chemical methods to enhance the photochromism activity of nanostructured WO_{3-x} . It involves the tuning of the oxygen substoichiometry of as-prepared NPs from a polyol process and the structural doping by copper of the NPs.

- Axis 2: Fabricating organic-inorganic photochromic materials

Hybrid organic-inorganic materials combine the best features of both types of materials. For example, they can be lightweight, flexible, and versatile like organic materials, but also have high thermal and mechanical resistance like inorganic materials. Specifically, maintaining the photochromism of the nanoparticles embedded in the polymeric matrix, the high transparency of optimized hybrid films or fibers opens the applicative possibilities. Here we investigate the potential of such a strategy to develop photochromic WO_3 -based hybrid devices.

The thesis manuscript consists of four chapters spanning gradually from an investigation of the WO_3 compounds and optimization of their photochromic properties, to the incorporation of these compounds into 1D, 2D and 3D polymer matrix. The first chapter provides a general state-of-the-art on color origins in inorganic materials with a detailed overview of the main mechanisms. This chapter also discusses in deep the tungsten oxide, its structure, various synthesis methods, and its properties with a focus on the WO_{3-x} -based hybrid devices documented in the literature.

The second chapter describes in detail the instrumental characterization techniques employed in the study.

In the third chapter, we present the main results obtained. It is divided into five sections:

- (I) Addressing the optimization of the photochromic contrasts by oxidizing the clear blue WO_{3-x} crystallite to get yellow starting compounds, and the feasibility of fabrication of a microdose UV device using dip-coating technique.
- (II) Studying the doping route to improve the photochromic behavior of WO_3 by copper doping. The discussion focuses on the effect of the different concentrations of Cu (0.5, 1 and 2 mol%) introduced in the WO_{3-x} NPs prepared by the polyol method. Also, the photochromic (coloring and bleaching) behaviors of the doped and pristine films are compared and deeply analyzed.
- (III) Introducing a new type of photochromic smart windows consisting of a window glass coated with a thin film of tungsten trioxide/polyvinyl alcohol (WO_{3-x} /PVA) composites that can modify their transparency properties autonomously with incident light intensity.
- (IV) Exploring the detailed fabrication processes of plastic optical fibers using commercial polyether sulfone (PES) as the plastic fiber choice. The methods involve incorporating WO_{3-x} into the PES optical fibers. The specific methods employed in this process include three main routes to modify the PES- preform/fibers: (i) surface modification of the preform via dip-coating in different suspensions, (ii) bulk modification of the preform by embedding NPs, and (iii) post coating of PES-optical fibers. Following fabrication, an extensive characterization is performed on each model of the modified PES optical fiber to choose the best method for photochromic application.
- (V) Presenting a new class of transparent lab-made PMMA fibers doped with tungsten oxide compounds. The bulk PMMA preforms are prepared by free radical pre-polymerization in the presence of WO_3 nanoparticles with three different doping concentrations (0, 0.2 and 0.5%wt). We address the rheological properties of the produced polymeric and discuss the photochromic properties of the various proposed systems as preforms, optical fibers and fabrics.

In an additional chapter, we present the primary results of the environmental impact of the produced textiles on an industrial scale using the Life Cycle Assessment (LCA) method. The study answers the following questions: How can we employ our photochromic fibers in the field of textiles? How can we introduce an eco-design concept of the textile with the least materials consumption? How can we quantify their environmental impacts?

Finally, in conclusion, we propose a general outlook and perspectives to further extend the work.

Chapter I: State-of-the-art and objectives

- Y. Badour, V. Jubera, I. Andron, C. Frayret, and M. Gaudon, “Photochromism in inorganic crystallised compounds,” *Optc Mat:X*, vol. 12, p. 100110, Dec. 2021, doi: 10.1016/j.omx.2021.100110.

Chapter I: State-of-the-art and objectives

1 Color: from basic concepts up to WO₃ as NIR filter

Colors play a vital role in our lives, affecting our moods, stimulating emotions and adding beauty to the environment. Color is not only used literally; it also serves to express music, language and personality. Generally, we tend towards colors that appeal to us visually, which can have an indirect effect on our sense of well-being. Furthermore, colors can be used as warning signals or cues for certain actions. Colored substances are in high demand because they offer practical uses as well as aesthetic pleasure. Color vision is a complex process involving physical-chemical, physiological and psychological elements. Color comes from two primary sources: natural and synthetic. Nature offers an array of colors from the earth's skyline to plants and animals. But for color to exist, three conditions must be fulfilled: illumination source; material that interacts with emitted light; and human eye which analyses this interaction [1].

1.1 Basics concepts of color

1.1.1 Visible light

The term "visible light" refers to a band of the electromagnetic spectrum (360-780 nm) to which our eyes are sensitive. As this sensitivity is extremely low at each extreme, the commonly accepted range for visible light is 380-720 nm. Outside this region lie both ultraviolet (UV) and infrared (IR) regions: below 360 nm and above 780 nm respectively [1].

When all colors of the visible spectrum are present, normal white light is seen. Thus, if red, green and blue lasers were introduced together with adequate proportion into a scene, it would appear white to humans. Colors can only be distinguished when ordinary white light is split or filtered through refraction, reflection, or absorption of a specific wavelength by an object described as "colored". A material or object appears a certain hue due to the absorption of certain wavelengths of white light, leaving behind only the reflected hue. For instance, blue objects exhibit selective reflectance and act as filters; red and green wavelengths are absorbed, leaving only the blue part reflected to our eye [2]. Table 1 lists approximatively the subtracted wavelength ranges and the observed colors for these materials/objects:

Chpt.I-Table 1: Complementary colors relationships.

Wavelength range (nm)	Color	Complementary color
400-435	Violet	Greenish yellow
435-480	Blue	Yellow
480-490	Greenish blue	Orange
490-500	Bluish green	Red
500-560	Green	Purple
560-580	Yellowish Green	Violet
580-595	Yellow	Blue
595-605	Orange	Greenish blue
605-750	Red	Bluish Green

Chapter I: State-of-the-art and objectives

1.1.2 Hue

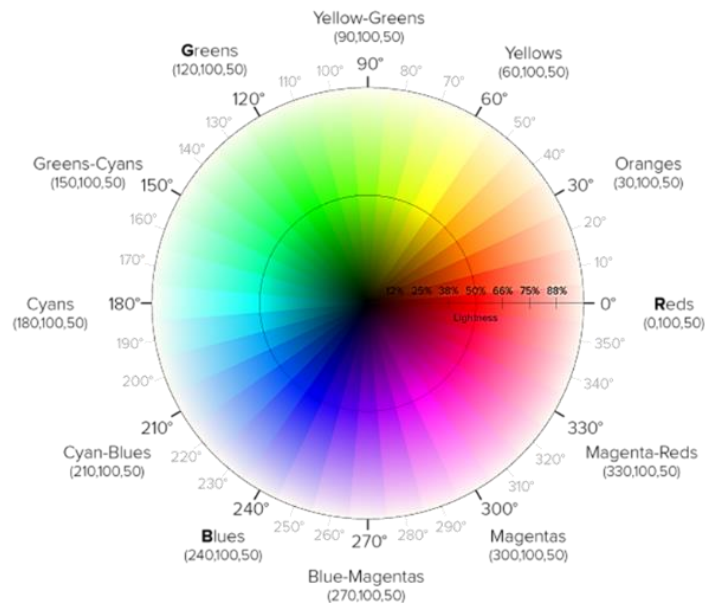
Hue is defined as the color of an object we see in illumination conditions, which exists in infinite numbers, for example, orange, yellow, green, blue and violet. It is possible to assign a value for each hue in degrees using the color wheel from 0 to 360 degrees known as the “color wheel” as shown in Figure1. In the color wheel, the hue values start at 0 degrees (red hue) then progress through the orange, yellow, green, blue and violet then return to red at 360 degrees. Using the hues values in degrees is important in the field of art and design to create balanced compositions [3].

1.1.3 Saturation

Saturation describes the intensity or purity of a given color, for example, a color is highly saturated meaning it looks rich and vivid. Whereas low saturated colors look dull. When a hue is fully pure (100% saturated), there is no addition of any other color to the original hue. On the other hand, a 0% saturation appears as a medium grey. The adjustment of the level of saturation gives the possibility to create different modes and purity.

1.1.4 Chroma

Chroma is a value to quantify the saturation of a color. The color wheel in Figure 1 shows the change of chroma for different degrees of color. The greater the saturation, the higher the chroma is. Chroma gradually varies from grey to fully pure colors from the center to the border of the color wheel [2].



Chpt.I-Figure 1: The colors wheel showing the 12 principal hues [2].

1.1.5 Lightness

The value of lightness gives the brightness or the darkness of a specific-colored object. This value varies from zero (black) to 100% (white light) in the case of white light for any given hue or chroma.

Chapter I: State-of-the-art and objectives

1.2 Colorimetry

Colorimetry is a scientific model used to measure color and it is applied to identify the color difference between two samples. It is generally used in different fields such as the commerce industry and labs to give a numeric value for a given color. This method is important for several applicable products including inks, plastics, textiles, pharmaceuticals and dyes. Colorimetry quantifies colors using three components, which states that the human eye possesses receptors for three primary colors (red, green and blue) and that all colors are seen as mixtures of these primaries. In colorimetry, these components are referred to as X-Y-Z coordinates. The X-Y-Z tri-stimulus values are useful for defining colors; they do not allow easy visualization of color. Therefore, under the Commission Internationale de l'Eclairage (CIE), various mathematical models and graphing methods have been established to facilitate color visualization. These conceptualizations are referred to as color spaces [3-4].

CIE L*a*b*- Color system

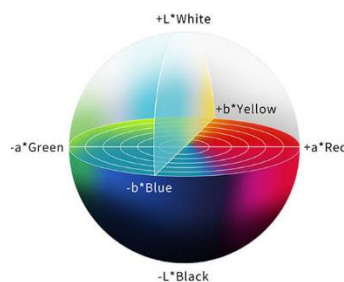
The CIE L*a*b* color space is a well-defined system established by the International Commission on Illumination to describe all colors that the human eye can see. The L*a*b* model is a three-dimensional model and can be presented in 3D space as shown in Figure 2. The main function of CIE is to provide a repeatable system of color communication standards for industrial users. The L*a*b* color space is based on the theory that color cannot be both green and red at the same time nor blue and yellow at the same time [5]. Therefore, single values can be used to describe the red/green and the yellow/blue attributes. In this color space, L* describes lightness; a* denotes the red/green value and b* is the yellow/blue color. The three coordinates are so denoted by a* (the red-green axis), b* (the yellow-blue axis), and L* (the lightness axis). The components of the color difference are obtained as differences between the test sample (T) and the reference one (R):

$$\Delta a^* = a_{T^*} - a_{R^*} \quad \text{Chpt.I-Equation 1}$$

$$\Delta b^* = b_{T^*} - b_{R^*} \quad \text{Chpt.I-Equation 2}$$

$$\Delta L^* = L_{T^*} - L_{R^*} \quad \text{Chpt.I-Equation 3}$$

The color ΔC difference (or color contrast) is determined by the geometrical distance between the two positions in the CIELAB color space. $\Delta C = \sqrt{(\Delta b^*)^2 + \Delta L^{*2} + \Delta a^{*2}}$.



Chpt.I-Figure 2: Representation of the CIELAB system [4].

Chapter I: State-of-the-art and objectives

1.3 Causes of color in inorganic materials

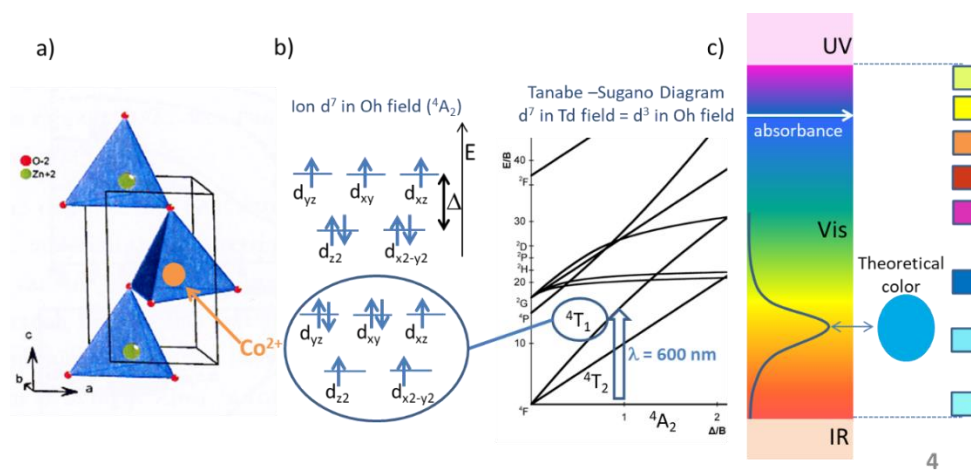
The world of minerals and inorganic materials is full of color. The majority of the compounds of an element of the d block (transition elements) exhibit color. This property indicates that certain structural characteristics might be responsible for the observed colors. It is commonly stated that there are multiple ways in which a material can selectively absorb light, and thus exhibit a defined color. Currently, light is understood as a behavior of particles with discrete packets of energy, known as photons. The photons can be absorbed at an atomic/molecular level by exciting the ground state electrons to a higher energy level. Hence in all «chemical coloration cases» (in opposition to “physical coloration sources” such as scattering, interferences, or even incandescence), under photon irradiation the color is the trace of electron travels into the matter. The chemical composition is the first key to apprehend the color origin of a material. Such transitions are governed by various selection rules [6]. The four main colorings (arbitrary classification) mechanisms that are relevant to this thesis and discussed are, taking a classification from short-length electron transfer to longer distance electron transfer: (i) the transfers governed by the crystal field theory (only the atomic orbitals of the chromophore has to be taken into account), (ii) the bond-transfers (the electrons typically move through a metal-ligand bond, or even “jump” some atoms as in semi-local defects), (iii) the charge-transfer between energy bands (on which the electrons move from one zone with a large degree of freedom in terms of space and energy to a second allowed zone with also a large degree of freedom), (iv) semi-local defects up to free electron gas effects (described basing on sometimes closely related F-centers, delocalized intervalence transfers, polaronic or plasmonic theory).

1.3.1 Color due to crystal field theory (Intra-atomic electronic transition)

Crystal field theory is a mathematical model developed to explain the optical properties of d-metal ions coordinated to an organic compound. A metal ion in a complex is surrounded by negatively charged ligands which generate an electric field and alter the energy levels of its orbitals [6]. The d-d transitions refer to electron transitions between ground and excited states of transition metals in the block d of the periodic table. These transitions are responsible for the vibrant colors found in various metal complexes. The energy required for such transitions varies depending on the metal ion and its ligands [7]. d-block elements in an ionic state usually possess one or more electrons in their d orbitals. Degenerate d-orbitals in an element's atomic state can be separated into higher and lower energy states when its ionized form has less than icosahedral symmetry (commonly octahedral or tetrahedral). For example, let us consider the case of zinc oxide ZnO doped with cobalt Co^{2+} which adopts a wurtzite crystal structure, which is the same as undoped ZnO. In this structure, ZnO consists of a repeating unit of close-packed oxygen atoms with zinc atoms occupying half of the available tetrahedral interstitial sites[8]. When Co is doped into ZnO, the Co atoms occupy substitutional sites in the crystal lattice, where they replace some of the Zn atoms. This arrangement produces an electric field around the Zn ion, which influences the energy level of any transition metal introduced into ZnO's lattice structure. When a cobalt ion replaces zinc in the crystal lattice, negatively charged oxygen ions surrounding it

Chapter I: State-of-the-art and objectives

create an electrostatic field that alters the energy levels of the cobalt ion's d orbitals. Figure 3 illustrates this splitting of 5d orbitals into two sets: an upper energy set consisting of three orbitals (d_{xy} , d_{xz} , d_{yz} orbitals) and a lower energy pair consisting of two orbits ($d_{x^2-y^2}$ and d_{z^2} orbitals), known as crystal field splitting. The splitting energy produces different d orbitals for cobalt ions, leading to their absorption of light in the visible range. Cobalt ions can exist in various oxidation states (Co^{2+} or Co^{3+}) depending on doping conditions. Let us consider the case of Co^{2+} ions in ZnO. In this scenario, the electronic energy levels associated with each Co^{2+} ion within this field can be represented using a Tanabe-Sugano diagram, in which the allowed transitions and their energy dependence versus the crystal field strength (Δ) for octahedral and tetrahedral coordination sites are presented [9], [10]. Figure 3 illustrates the energy differences between different electronic states of a Co^{2+} ion as a function of crystal field splitting parameter D and Racah parameters. The spectroscopic notation is used to label each electronic state, which contains its total angular momentum (spin) and electron occupation numbers for d-orbitals. For instance, the ground state of Co^{2+} in a tetrahedral field is labeled $4A_2$; this indicates it has total spin $S=3/2$ ($4 = 2S+1$) and seven electrons occupying its d-orbitals specifically in a single state configuration (A). For Co^{2+} in a tetrahedral field, the energy difference between its ground state and second excited state ($4T_1$) in an inorganic oxide (i.e., with oxygen anions as ligands) is around 600 nm (yellow-orange). The intensity/hue of cobalt blue pigments depends on several factors as cobalt ions concentration and crystal field strength [11]. A stronger field produces a $4A_2 \rightarrow 4T_1$ absorption band that shifts towards UV regions of the spectrum (through purple hues for the pigment); on the other hand, a weaker crystal field results in greenish-blue hues due to the absorption band shift towards red regions of the spectrum.



Chpt.I-Figure 3: a) The crystal structure of ZnO doped with Co^{2+} , b) Representation of d-splitting with fundamental and 2nd excited state associated with the corresponding d^7 Tanabe-Sugano diagram, c) The location of the visible-range absorption band of Co^{2+} -doped ZnO and its associated color.

1.3.2 Color due to charge transfer (Inter-atomic electronic transition through a bond)

Inorganic materials can display diverse colors as the result of charge transfer processes. Upon irradiation electrons can be excited from their ground state to higher energy levels and in some cases

Chapter I: State-of-the-art and objectives

this excitation results in the transfer of charge from one place to another (i.e., from one first ion interaction sphere through a second ion interaction sphere) [12]. This charge transfer creates a particular hue that corresponds to the complementary color of the absorbed wavelength. The mechanism of charge transfer depends on several factors, including the position and type of metal and its surrounding ligands, and the absorbed photon energy [13]. Charge transfer can occur through various possible pathways: metal-to-ligand, the ligand-to-metal, and metal-to-metal (from respectively cation-to-anion, anion-to-anion and cation-to-cation into ionic bond structures).

1.3.2.1 Ligand to metal charge transfer (LMCT)

In metal complexes, the ligand-to-metal charging transfer (LMCT) occurs when electrons are transferred between a molecular orbital that has a ligand-like and one with a metallic-like character [14]. This type of transition can occur when the energy difference between the metal-d orbitals and the ligand orbital is negligible. The LMCT transfer can be achieved if the following conditions have been met: (i) The ligands should have one pair of electrons with relatively high energy empty π^* orbitals like O^{2-} , Cl^- or S^{2-} . (ii) The metal should have a high oxidation state and low-lying metal d empty orbitals. A common example of LMCT is the diverse colors of a transition metal ion coordinated to a ligand. For example, the copper sulfate pentahydrate $CuSO_4 \cdot 5H_2O$ solution appears in blue. In this complex, the electronic configuration of Cu^{2+} is $[Ar] 3d^9$. Upon absorption of light, an electron in the H_2O ligand orbital is excited to an unoccupied d-orbital of the Cu^{2+} inducing a LMCT and can be simplified in the following reaction: $Cu^{2+} + H_2O \rightarrow Cu^{2+}(H_2O)$ [15]. This transition is responsible for the blue color observed in the excited complex (with additional electrons in the d-orbital).

1.3.2.2 Metal-to-ligand charge transfer (MLCT)

The metal-to-ligand charge transmission (MLCT) in metal compounds occurs when electrons transfer from a molecular orbital with a metallic character to one with a ligand-like nature. The MLCT transfer is preeminent if these conditions are met: (i) The ligands need to have high-energy empty, π^* orbitals such as CO , SCN^- or NO . (ii) The metal must be in a low state of oxidation, with highly-filled orbitals [12]. For example, the case of the Ferriox complex $[Fe(phen)_3]^{2+}$ which is strongly red colored. The coloration is attributed to a charge transfer between the d orbitals of the metal and the π^* system of the phenanthroline ligand. The absorption of light results in a change in the oxidation state of the iron atom from +2 to +3, and a change in the color of the complex from pale yellow to dark red [16]. The MLCT transition in $[Fe(phen)_3]^{2+}$ can be represented as follows: $[Fe(phen)_3]^{2+} + h\nu \rightarrow [Fe(phen)_3]^{3+} + e^-$.

1.3.2.3 Intervalence charge transfer (IVCT)

The IVCT is a type of electronic transition that happens in mixed-valence compounds containing two or more metal cations with different oxidation states: transfer of an electron from one of the cations with the lower oxidation state to a neighboring cation with the higher one, through a bridging ligand [17]. For example, one can cite the inter-valence charge transfer in "Prussian blue". This compound has the formula $KFe[Fe(CN)_6]$ and shows a very intense blue color owing to the transfer of an

Chapter I: State-of-the-art and objectives

electron from Fe^{2+} to Fe^{3+} . In the crystal structure of Prussian blue, the Fe^{2+} ions are bonded with the N atom while the Fe^{3+} ions are bonded with the C atom of the octahedral surrounding CN^- ligands. Therefore, the charge transfer takes place through the cyanide bridges [18].

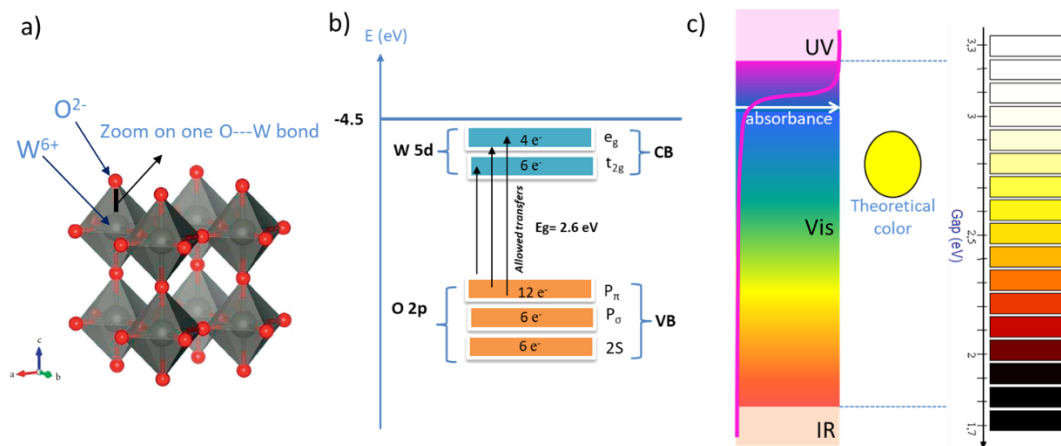
1.3.3 Color due to Valence Band (VB) to Conduction Band (CB) transitions

The phenomena of electronic transitions between the CB and VB explain the colors of various types of semiconductors (SC). In a SC, there are two distinct bands: the highest occupied energy level known as the valence band (VB) and the lowest unoccupied energy level known as the conduction band (CB) [19]. The energy difference between VB and CB is defined as the band gap corresponding to the wavelength of a photon that can absorb or emit a SC. When illuminating a semiconductor with light energetically exceeding the band gap, the light gets absorbed. The energy of the photon is used to lift an electron out of the valence band into the conduction band creating an electron-hole pair. This electron-hole pair is free to move within the material and can recombine from phonon (non-radiative deexcitation) or releasing light (as a form of radiative energy: luminescence phenomenon). Thus, the color of a semiconductor depends on the width of the band gap, and it is determined by the absorbed wavelength of the photons [20]. The range size of a typical bandgap is from 0.1-4 electron volts (eV) which indicates whether the materials are semiconductor or insulator (insulators are considered with more than 3 eV band gap and so associated with white coloration). The optical spectra of the SC are described by a unique absorption gap separating a range of wavelengths that is almost completely absorbed from the one that is nearly entirely transmitted. The position of the absorption frontier in the optical spectrum corresponds directly to the energy band gap and is therefore referred as the optical gap. The coloration of the semiconductor can be simulated by considering a theoretical spectrum that exhibits 100% absorption for energies greater than the gap and 0% absorption for energies less than the gap [21]. This theoretical spectrum can be used to generate a palette of colorations, as represented in Figure 4. The palette of colors is in a limited range of colors varies from white to black through grades of yellow and red and that is due to the precise amount of energy that a SC can absorb in visible light. In the case of a SC having an optical gap of less than 1.6 eV, electronic transitions within the visible light are allowed and appear in black. While, if it is larger than 3.1 eV, it will not absorb any of the visible wavelengths (no transitions are allowed), hence the SC (insulator) appears white [22]. Otherwise, the SC will absorb in the intermediate range and present different grades of yellow to red.

For example, in monoclinic yellow tungsten oxide WO_3 , the tungsten +6 ions are surrounded by six bonded oxygen ions. The tungsten atoms lay in a distorted octahedron with six oxygen atoms at the corners, the crystalline structure being constituted of corner-sharing octahedral sites in the 3 spatial axes. The VB in WO_3 consists mainly of oxygen 2p orbitals and the CB is made up of 5d orbitals separated by a band gap of 2.6 eV as shown in Figure 4. Upon UV irradiation (all radiations with higher energy than 2.6 eV), the electrons within the VB can be promoted to CB through the band gap

Chapter I: State-of-the-art and objectives

of WO_3 creating an electron-hole pair. These electrons recombine with the holes in the VB, in a non-radiative way, the color of tungsten oxide is so pale yellow.



Chpt.I-Figure 4: a) Monoclinic crystal structure of WO_3 , b) Simplified band diagram of WO_3 , c) The absorbance spectrum of WO_3 , and beyond, the palettes of coloration in SC as a function of band gap value.

1.3.4 Color due to semi-local defects up to free electron gas

1.3.4.1 F-like color centers

The presence of impurities or local defects in the crystal structure of inorganic materials can alter the different mechanisms of charge transfer resulting in a various range of colors of the same materials. The presence of such defects is translated to the creation of localized states within the band gap of the material leading to absorption at different wavelengths and then appearing of unusual broad of colors [19]. These states are spatially restricted and only weakly coupled to the surrounding crystal. There are two types of these states: shallow or deep depending on the required energy to create them. Shallow states are commonly linked to defects having low formation energy, while deep states are associated with defects that have higher formation energy (less common) [23]. This mechanism can be affected by different conditions: the crystal structure (certain crystal planes, complex structures), the synthesis method (low or high temperature), and the concentration of impurities or defects. One of the most known mechanisms is the semi-local defects, which involve the formation of these localized electronic states near the defects [24]. One well-known example is the blue color of sapphires. Sapphires are a form of the mineral corundum, which has a chemical formula of Al_2O_3 [25]. Normally, pure Al_2O_3 is colorless, but it gets a blue color from the presence of small amounts of titanium and iron impurities. When titanium and iron impurities replace some of the aluminum atoms in the corundum lattice structure, they create localized electronic states within the band gap of the material. These electronic states absorb light in the yellow and green regions of the visible spectrum [26].

In tungsten oxides, this mechanism is reported to may occur due to the presence of positively charged oxygen vacancies in the tungsten-based material (for example oxide film), which are created as a result of the preparation method and conditions (temperature, pressure, solvent...) and have the ability to trap photoexcited electrons [27], [28]. After that, F-like color centers are formed.

Chapter I: State-of-the-art and objectives

1.3.4.2. *Delocalized intervalence transfers (or closely related polarons)*

Polaron formation involves the localization of electronic charges associated with distortions in the surrounding crystal lattice [29].

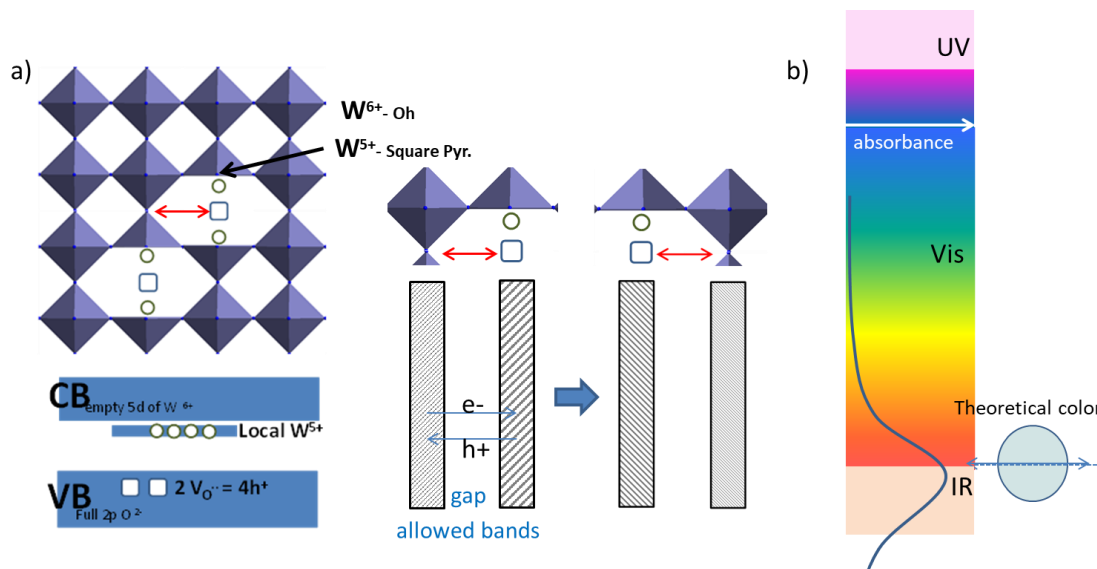
Polaronic absorption has been proposed to explain the absorption change of certain transition metal oxides as a result of redox reactions leading to the occurrence of a mixed-valence cation inside the structure. For instance, in electrochemical cells, at a reducing potential, the reduction of high oxidation number metal ions along with the intercalation of counter ions from the electrolyte (such as H^+ or Li^+) can be observed in the material for charge balance [30]. As a result, inserted electrons localize and create a displacement of surrounding ions from their equilibrium position, resulting in a potential well that stabilizes the electrons. The energetic stabilization can lead to the formation of an electron polaron band below the conduction band minimum, resulting in new absorption transitions, primarily in the visible region [31]. This mechanism is closely correlated to the intervalence charge transfer (IVTC) considering the electron polaron is trapped below the conduction band minimum on metal ions' highest empty orbitals, leading thus to consider the efficient reduction of some cations as starting point.

A related example, in close relation to our work, is the different colors in the sub-stoichiometric tungsten oxide WO_{3-x} exhibiting a range of colors (blue, yellow, up to black). The presence of oxygen vacancies in the crystal lattice in WO_{3-x} creates localized electronic states within the band gap [32]. These electronic states are described as semi-local defects and they are typically shallow states. So, tungsten can be considered a mixed-valence compound that can have oxidation states of +IV, +V, or +VI within WO_{3-x} to compensate for charges arising from oxygen vacancies. When an electron jumps to a W(+IV) site, tungsten is oxidized to W(+V), which distorts its octahedral environment. Following thermal or optical excitation, this distortion propagates through the crystal as the electron jumps from one site to another. Surrounded by oxygen atoms, the so-called electron polaron, accompanied by the lattice distortion, behaves like a negatively charged particle with reduced mobility compared to an isolated electron. The electron can be seen as a semi-localized particle around a W ion [33].

In Figure 5, a pseudo-cubic crystal structure of sub-stoichiometric WO_{3-x} is presented. It can be considered that all the oxygen vacancies are associated with local O^{2-} anions associated each one with two local W^{5+} cations, to form a “triple defect” forming two W^{5+} consecutive ions linked by an oxygen vacancy bridge where W^{5+} form a square pyramid and W^{6+} forms a fully octahedral. Upon excitation, some electrons can be trapped in the shallow electronic state near the conduction band (electron polarons). The transfer from one W center to a neighboring one to the electron polaron, (which can also be described as the intervalence charge transfer between W^{6+} and W^{5+}), requires a photonic excitation typically about 1 eV. Consequently, the red part of the spectrum is partially absorbed, and the WO_{3-x} appears in light blue color (absorption band of a large-width Gaussian shape at the frontier between visible and NIR: near-infrared ranges).

Chapter I: State-of-the-art and objectives

One can notice that the borders between intervalence charge transfers (IVTC) and delocalized intervalence transfers (polarons) are tricky. In a way, IVTC occurs in between two elements with different oxidation states as impurities into an insulating matrix, and the “doubles defects” constituted by these two doping ions are with a low occurrence probability and are isolated from each other. In delocalized intervalence transfers, the metal with two different oxidation states is in very large quantity, and the electron transfer cascade is extended in the whole periodic structure. In the following manuscript, this difference is not considered, IVTC and polaronic transfers are referring to the same mechanism.



Chpt.I-Figure 5: a) A schematic representation of the pseudo-cubic crystal structure for WO_{3-x} showing the creation of semi-local defects “trapping states”, and zoom on two sites (octahedral and square pyramid) showing the polaron hopping between them, b) The absorbance band and the resulting color as a result of the allowed transition.

1.3.4.2 Colors due to free electronic gas phenomena

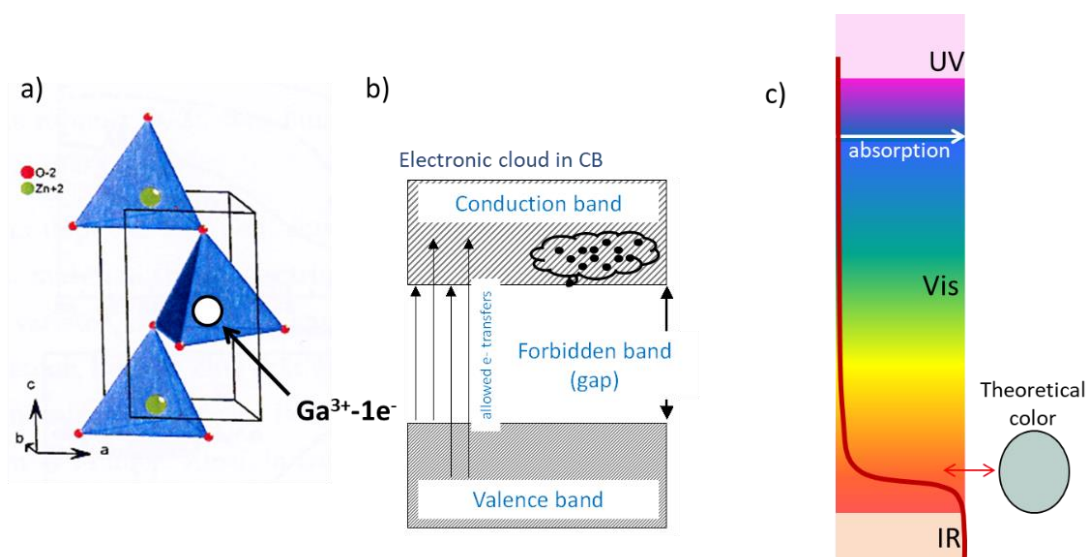
Plasmonic absorption involves the collective polarization of spatially delocalized charge carriers by interaction with light. The electronic charging that occurs can be balanced by ion intercalation or surface charge, including the formation of an electrochemical double-layer [34]. When charge carriers in a material interact with photons, it can increase the absorption and scattering of radiation at given wavelengths, depending on the carrier density. This plasmonic interaction results in metals having a characteristic luster when interacting with light [31]. Similarly, metal oxides that have a high density of delocalized electrons (still less than classical metals) are highly reflective of near-infrared light [35]. However, in nanomaterials of metals or doped metal oxides, free electrons undergo confined oscillations at resonant frequencies, producing strong absorption at a characteristic localized surface plasmon resonance (LSPR) frequency.

In conductive materials like metals, the electrons and holes behave like a gas of free carriers according to the Drude-Lorentz model [37]. In this model, the interactions between electrons are negligible as well as the interactions between electrons and ions. The Drude model can explain how

Chapter I: State-of-the-art and objectives

doping affects the behavior of free electrons in inorganic materials leading to a change in its absorption of light and thus in the optical properties of the material. For example, in the case of ZnO doped with Ga, the Ga^{3+} ions can substitute for Zn^{2+} ions in the ZnO crystal structure, resulting in a lattice distortion [37]. Also, the Ga^{3+} ions act as electron donors and introduce free electrons into the material increasing its electrical conductivity. The presence of this free electron gas in the conduction band increases the probability of the allowed transitions occurring, decreasing the energy required to excite an electron from the CB to VB as illustrated in Figure 6. But mainly, the irradiation light must get sufficient energy to not be absorbed by this electron gas. Hence, over this critical energy only (over the plasma frequency), the irradiation light is not absorbed and so reflected. The plasma frequency depends on the charge carrier concentrations and typically, in Ga-doped ZnO. This results in a change in the color of the material, as different wavelengths of light are absorbed (light blue color).

It will be seen in the next part (NIR filters), that some authors consider that for highly oxygen-deficient tungsten oxides, the high carrier concentration leads to the occurrence of plasmonic behavior for WO_{3-x} oxides.



Chpt.I-Figure 6: a) The crystal structure of ZnO doped with Ga^{3+} , b) Representation of the formation of electronic cloud in the CB, c) The location of the absorption band and its complementary color.

1.4 WO_3 as a UV-NIR filter material

UV-NIR filter materials can selectively absorb or reflect a specific wavelength of light within the UV-to-NIR region. These filters are used in various applications, such as optical coating, photography, and solar protection. As one preferred application, UV-NIR filter refers to materials that are transparent in the visible range and that are absorbing (or reflecting) the NIR range. These kinds of filters can be used in smart windows to ensure thermal insulation keeping a high transparency of solar selective absorbers for photothermal conversion.

Chapter I: State-of-the-art and objectives

Based on the various electron transfers previously described, the importance of this section is to highlight the different absorption mechanisms and how to develop a metal oxide chromic filter for solar control coatings. Furthermore, substoichiometric WO_{3-x} oxide constitutes an ideal illustration of the difficulty to interpret and so optimize NIR filtering properties.

1.4.1. Selectivity of solar energy factor

In solar energy absorption systems, materials with high absorption properties are typically used for efficient energy absorption. However, these materials, known as black body materials, also have high emissivity, which can reduce the efficiency of photothermal conversion, a key component of solar thermal conversion systems. To address this issue, solar selective absorbers (SSAs) with high absorption and low emission are often used, as they offer a better choice for photothermal conversion [38].

The effectiveness of SSAs is typically measured through the extinction values in the visible range (ranging from 380 nm to 780 nm) and near-infrared range (ranging from 780 nm to 2500 nm) by integrating over the entire spectral range in both cases. The A_{NIR} values, which represent the absorption of the solar spectrum in the infrared range for a fixed visible solar light transmission of 80%, and SSET, the selectivity of solar energy transmittance, can be calculated according to [39]:

$$A_{\text{NIR}} = \left(1 - \frac{\int_{780}^{2500} I_{\text{received}}(\lambda) d\lambda}{\int_{780}^{2500} I_{\text{sun}}(\lambda) d\lambda} \right) \cdot 100 \quad \text{Chpt.I-Equation 4}$$

$$\text{SSET} = 0.5 \left(1 + \frac{\int_{380}^{780} I_{\text{received}}(\lambda) d\lambda}{\int_{380}^{780} I_{\text{sun}}(\lambda) d\lambda} - \frac{\int_{780}^{2500} I_{\text{received}}(\lambda) d\lambda}{\int_{780}^{2500} I_{\text{sun}}(\lambda) d\lambda} \right) \quad \text{Chpt.I-Equation 5}$$

SSET is a value between 0 and 1: the larger the value, the more near-infrared light from the sun is blocked, and the more visible light is transmitted. A system with a SSET value of 0.5 blocks equally both the visible and near-infrared light, while a value lower than 0.5 means that it is more selective for the visible range. Therefore, the researchers want the SETS value to be as high as possible, as well as the value of A_{NIR} .

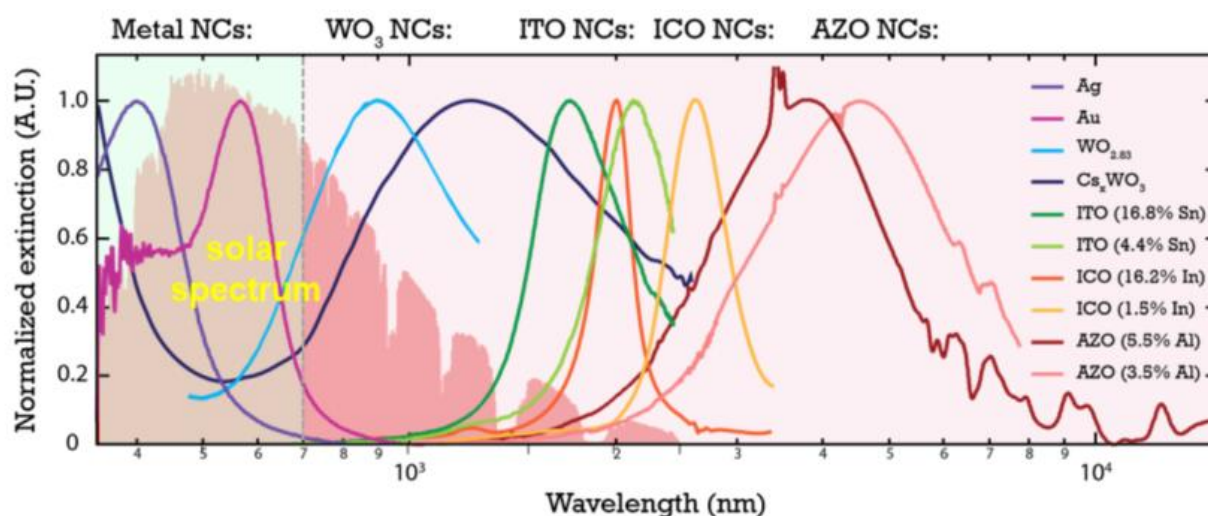
1.4.2. Plasmonic semiconductors for near-infrared absorption

Because of the selective absorption of upper wavelengths than the plasmon one (as shown previously in the part “colors due to free electronic gas phenomena”), the plasmonic materials are the best candidates for selective NIR filters.

To estimate which material composition is best suited for solar control coatings, their plasmonic absorption needs to be compared to the solar emission spectrum. The reference spectrum used is the Air Mass 1.5 (1.5AM) of the American Society for Testing and Materials, which corresponds to the solar spectrum when it passes through one and a half thicknesses of atmosphere, i.e., with an incidence angle of 41.8° relative to the horizontal. This emission is located at 9% in the UV range (up to 380 nm), 43% in the visible range (from 380 to 780 nm), and 78% in the near-infrared (NIR) range

Chapter I: State-of-the-art and objectives

(from 780 to 2500 nm). Figure 7 shows the solar emission spectrum superimposed on the normalized extinction spectra of different plasmonic nanoparticles. Thus, it can be observed that gold, like the other noble metals, is not a good candidate because it only absorbs in the visible range. ITO and AZO nanoparticles, used for the first electrochromic coatings in the literature, absorb too far into the infrared, leaving a significant portion of the NIR between 780 and 1500 nm to pass through [33], [40], [42]. Selenium nanoparticles absorb in the correct range of the NIR, but their bandgap absorption is localized in the visible range, which would compromise window transparency. Finally, the compositions whose plasmonic absorbance is ideally situated are rare earth hexaborides (RB, R=La, Ce, Pr, Nd, Gd) [41], tungsten oxides, and tungsten bronzes (MWOs, M = K, Na, Cs): their plasmonic absorption is in the near-infrared and their bandgap absorption is in the UV, leaving the visible window transparent.



Chpt.I-Figure 7: LSPR signals of several metals and semiconducting plasmonic materials, reported to the solar spectrum in the background of the figure [33], [40].

1.4.3 Sub-stoichiometric tungsten oxide for NIR filter applications

The use of tungsten oxides in the form of bulk material is already widespread for different chromic applications: they exhibit a significant color change from transparent to black depending on their synthesis history. This yellow-to-blue or even black coloration can arise from several mechanisms, depending on the stoichiometry of oxygen and the presence of ions such as Li^+ or H^+ as previously shown in the part delocalized intervalence transfers. We will see later that different phases with different oxygen stoichiometries can also be synthesized, and various polymorphs of WO_{3-x} are possible. In the first approximations, it has already been roughly estimated that:

- For $0 < x < 0.1$, the optical and electrical properties of the bulk material arise from polarons.
- For $x = 0.1$, bulk WO_{3-x} undergoes an insulator-metal transition. The density of polarons increases with σ until a compact structure is reached for $\sigma = 0.1$. Further increasing the number of added electrons would result in a distance between polarons that is smaller than

Chapter I: State-of-the-art and objectives

what is possible in the crystal structure, so the additional electrons are delocalized. The electrical and optical properties of bulk WO_{3-x} are then governed by delocalized electrons for $x > 0.1$ [31]. The color of tungsten oxides is so better described by plasmon theory.

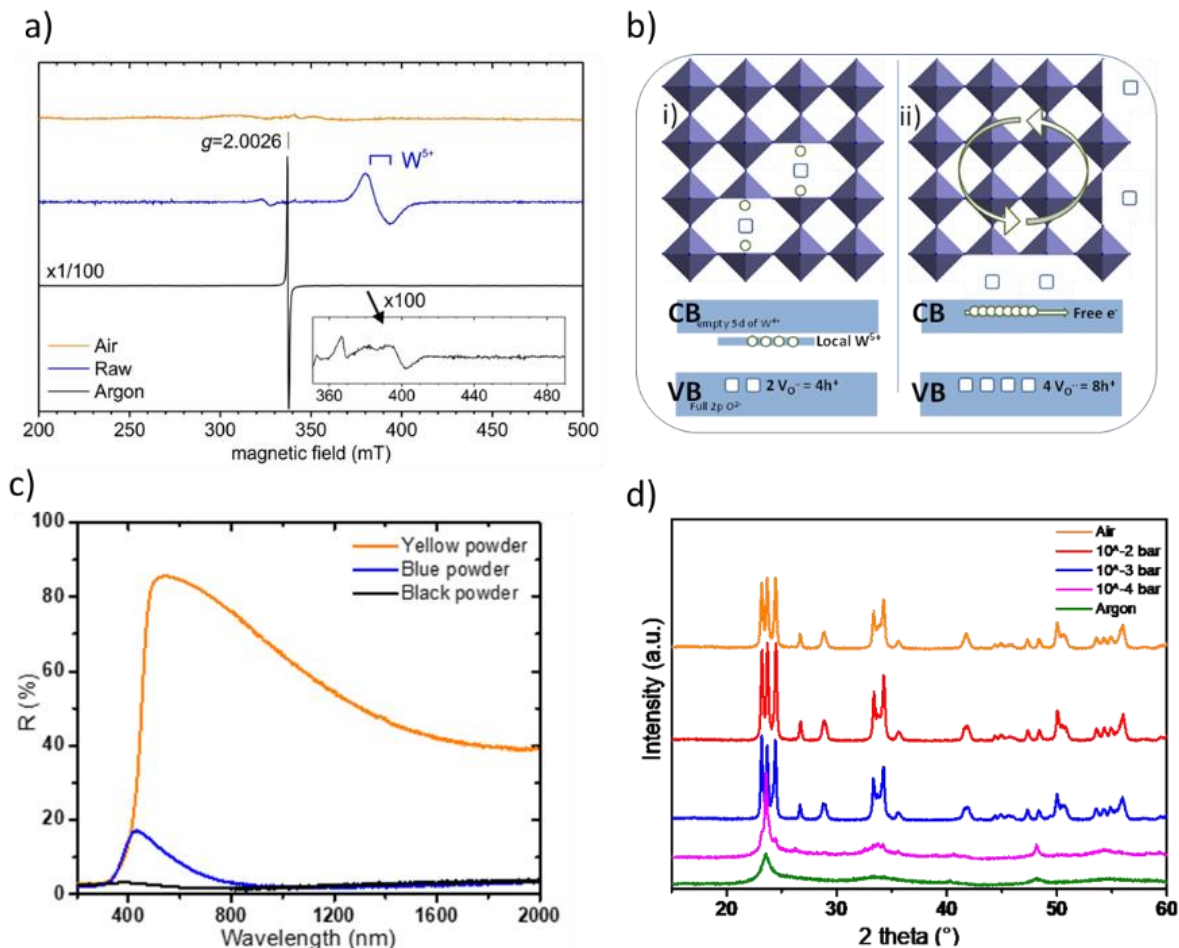
Marie Bourdin (ICMCB's Ph.D. student) has accomplished a detailed study of oxygen vacancies engineering in WO_{3-x} using different methods: controlling the oxygen pressure and thermal treatment. In the following section, we will review the main achievements of her work concerning this topic on the research of an optimized WO_{3-x} composition for NIR filter applications.

In this work, Bourdin *et al.* [43] have investigated the production of WO_{3-x} by the polyol method. After synthesis, a portion of the raw WO_{3-x} powder (blue powder), was annealed under argon (low oxygen partial pressure) at 600 °C for 2 hours, resulting in a black-colored compound (black powder). Another portion was annealed under air at 600 °C for 2 hours, resulting in a third product with a yellow color (yellow powder). EPR was chosen to demonstrate the difference in tungsten – oxygen stoichiometry between the yellow, the blue and the black samples (Figure 8.a). In the EPR signal of the yellow sample, no signal splitting is observed. This indicates a total absence of unpaired electrons, confirming a composition very close to $\text{WO}_{3.0}$ (the oxidation state of tungsten is perfectly equal to +6). The polyol synthesis, which takes place in a reducing medium, leads to the presence of W^{5+} ions in the raw powder. The growth steps in diethylene glycol, a reducing alcohol, result from the oxycondensation of both W^{6+} ions (mainly) and W^{5+} ions (to a lesser extent). As a result, the particles obtained are not stoichiometric $\text{WO}_{3.0}$ but instead exhibit an oxygen sub-stoichiometry, with a chemical formula of WO_{3-x} . Remarkably, the EPR signal does not indicate the presence of free electrons for the raw blue powder. However, post-annealing treatment under argon (at an oxygen partial pressure of about 10^{-5}) can produce two new effects: (i) oxygen exfoliation at the surface of the nanoparticles, leading to an additional reduction associated with segregation of tungsten W^{5+} at the material's surface, or (ii) migration of the oxygen deficiencies from the bulk to the material's surface. In the black sample, the oxygen surface exfoliation leads to supernumerary electrons relative to the oxygen vacancies in the crystallite core, resulting in the occurrence of free electrons well evidenced by EPR measurements. Figure 8.b depicts a schematic representation of the blue and black samples, with simplified crystallographic representation and associated energy band diagrams. This illustrates the complexity of a full description of the electron transfers, which can occur in tungsten oxides.

They measured the optical properties of each sample and analyzed the results (Figure 8.c). The yellow sample showed weak absorption in the near-infrared region and strong absorption in the ultraviolet region. This sample had a near-total reflection window in the visible region, with a diffuse reflection of about 90% around 500 nm. In contrast, the black WO_{3-x} absorbed almost all wavelengths of light in the UV-Visible-NIR range, due to the creation of free electrons gas (plasmonic) caused by oxygen sub-stoichiometry, causing the absorption of all photons in the energy range of the radiation. Knowing that a potential plasmonic effect related to free electrons should appear after accumulating a critical

Chapter I: State-of-the-art and objectives

(already high) number of free carriers, such an attribution appears justified. The blue raw sample showed interesting intermediate properties, with strong absorption in the UV and near-infrared regions and a small reflection window in the visible region, due to the absence of free electrons. Hence, blue raw powder obtained from polyol exhibits some interesting NIR filter properties.



Chpt.I-Figure 8: a) Low temperature (5 K) X-band EPR spectra of raw and annealed (under air or argon) WO₃ powders, b) Schematic representation of the blue and the black samples, with simplified crystallographic representation and associated energy band diagrams. c) Diffuse reflectance of the powders of the different WO₃ compounds. d) XRD patterns of WO₃ powders synthesized by polyol process and annealed at 600 °C under different oxygen partial pressures [43].

In conclusion, a slight change in the oxidizing-reducing character of the thermal treatment, particularly through the oxygen concentration in the synthesis atmosphere, has a significant impact on the physicochemical properties of the prepared tungsten oxide. Especially, the oxygen stoichiometry controls the localization of the electrons, and so the visible-NIR optical properties. The control of the oxygen stoichiometry and so, the localized/delocalized balance of the associated electron transfers, which can take place, can be used for the preparation of efficient NIR filters.

2 X-chromic (or chromogenic) effect in inorganic materials

As discussed in the previous section, the color of inorganic materials can be altered using different techniques but also can change as a response to various conditions and environments. In this section, we discuss in detail the chromic materials and their marvelous properties.

Chromic materials change reversibly their optical properties (color \leftrightarrow transparent) under the presence of external stimuli, such as temperature, light, voltage, gas, etc [44]. Inorganic materials that exhibit chromic effects are of great interest for various applications, including smart windows, displays, sensors, and electrochromic devices [45]. Generally, chromic phenomena include different processes resulting in changes in the absorption and reflection of light, absorption of energy and emission of light, absorption of light and energy transfer or conversion of light. In inorganic compound classes, the chromic effects can be optimized by varying the composition, the crystalline structure and the morphology of the crystallites. For example, the use of different metal ions, solvents, or functional groups can lead to different chromic behaviors. Depending on the external stimuli, chromism can be categorized in various ways.

2.1 Types of chromic effects

2.1.1 Photochromism

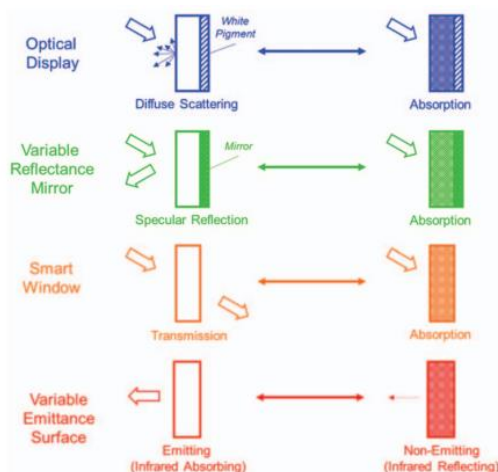
Briefly, photochromism refers to the reversible change in color upon a response to irradiation. The mechanism of these phenomena depends on the type of materials [46]. In some cases, it involves a reversible electron transfer reaction upon irradiation, leading to changes in oxidation states and electronic structure. In different cases, it undergoes a reversible isomerization of a molecule or a crystal as a response to light, leading to a change of color. There are two main categories of photochromic materials: reversible and irreversible photochromic materials. Reversible photochromic materials can color and bleach several times and return (fully or partially) to their initial state, while irreversible photochromic materials undergo a permanent change in color without the ability to return to their initial state [47]. Photochromic materials have been investigated and proven their feasibility in different areas of applications such as optical data storage, smart windows, and sensors [46]. For example, photochromic glasses are used in photochromic lenses for eyeglasses, which darken upon exposure to sunlight and become clear again when the light intensity decreases.

2.1.2 Electrochromism

Electrochromic (EC) materials change their colors between two colored states or between a colored state and a bleached state as a response to an electric field. Materials that reveal colored hues in their oxidized or reduced states are referred to as anodically coloring or cathodically coloring, respectively. Several EC materials that exist in multiple redox states reveal the unique ability to switch between several colored states [48]. Over the last few decades, EC materials and devices have found widespread application in various fields such as information displays, variable reflectance mirrors, smart windows, and variable emittance surfaces [49]. The four main principles behind these

Chapter I: State-of-the-art and objectives

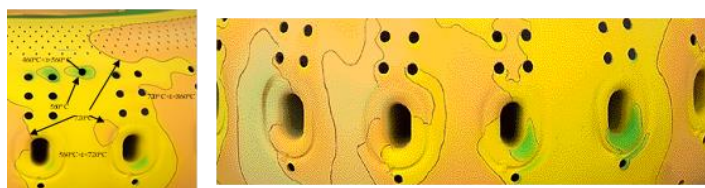
applications are illustrated in Figure 9. These materials and devices can be utilized on surfaces that are translucent, transparent, or reflective [50]. By controlling the electric current passing through the devices, the amount of light absorbed, reflected, or transmitted can be modulated. EC devices can generally be classified based on their operating mode, which is either transmission or reflection [51]. Recently, there has been a new revolution in the development of EC-based devices such as “electronic paper” with a focus on cheap printable EC “labels” with excellent viewing properties [49].



Chpt.I-Figure 9: The four principles of four different applications of EC devices [49].

2.1.3 Thermochromism

Thermochromism is the reversible change of color of a compound when it is heated or cooled. This change is noticeable and occurs over a specific temperature range [52]. Inorganic compounds show this phenomenon due to a change in crystalline phase, ligand geometry or the number of solvent molecules in the coordination sphere [53]. This change can be either reversible or irreversible, but when it is irreversible, it is often because the substance has undergone a change in its composition or removed a phase. A lesser number of examples are due to equilibria between complexes in solution or to equilibria between different molecular structures in the case of organometallic compounds [54]. Recently, the design of new thermochromic substances opens windows for new applications based on thermal indicators, such as in security inks, cosmetics, cooking tools, and smart textiles. For instance, irreversible thermochromic paints can be applied to turbine motors in airplanes, helicopters and other engines, allowing engineers to optimize the design of these motors based on their thermal history [53]. An illustration of such a turbine from Turbomeca SA coated by a Rolls-Royce thermochromic paint is in Figure 10.



Chpt.I-Figure 10: Example of a painting used as irreversible temperature indicators on a helicopter turbine motorization.

Chapter I: State-of-the-art and objectives

2.1.4 Solvatochromism

Solvatochromic materials change their color as a result of dissolving in different solvents. It is one of the oldest of chromisms, dated to 1878, but nowadays it includes the concept of gels, micelles, polymers and films, as well as various surfaces [55]. This phenomenon is attributed to the interaction between the solvent and the solute, which can alter the electronic properties of the solute, changing the absorption spectrum and its color. There are different ways to change the electronic structure of the solute by inducing a dipole moment in the solute or changing its molecular geometry [56]. Solvatochromism has practical applications in several fields, including analytical chemistry, materials science, and biochemistry. For example, solvatochromic dyes are used as indicators for pH, metal ions, and other analytes.

2.1.5 Gasochromism

Gasochromic materials change their color when exposed to gas or vapor as a result of the interaction between the gas and the vapor [57]. Gasochromic materials consist of transition metal oxides or other metal-based compounds. The gas interacts with the metal atoms or ions in the material, causing changes in their oxidation states or coordination geometry [58]. These interactions lead to a shift in the energy levels of the metal atoms or ions and therefore changes in their absorption spectrum and color. Gasochromic materials have practical applications in several fields, including gas sensing, smart windows, and chromogenic materials [59]. For example, gasochromic materials are used as sensors for the detection of toxic or flammable gases. The gas or vapor interacts with the gasochromic material, causing a color change that can be detected and quantified.

2.2 X-chromic mechanisms: Crystal phase transitions or redox properties?

Several types of chromic mechanisms can lead to a change in the color of a material. The most two known mechanisms are the phase transitions and redox properties of the material.

2.2.1 Crystal phase transition in chromic materials

A crystal is a highly ordered arrangement of atoms, ions, or molecules that repeat in a regular pattern throughout the solid [60]. In simple terms, a crystal phase transition is a change in a material's crystal structure in response to an external stimulus. For instance, a solid may change from one crystal structure to another when subjected to a certain amount of pressure, which causes the material's color to change since various crystal structures may absorb and reflect light in different ways [2]. This effect is common in minerals, where different crystal structures can give rise to different colors. For example, the mineral garnet can come in a variety of colors due to different crystal structures, including red, green, yellow, and brown. Crystal phase transitions can also be reversible or irreversible, meaning that the substance can switch back and forth to its original crystal structure if the external stimulus is removed or undergo a permanent new crystal structure [61]. This transition behavior is the essential cause behind most of the known chromatic materials. For example, the vanadium oxygen V-O system is a group of compounds including VO, V₂O₃, V₃O₅, V₄O₇, VO₂, V₂O₅, and others that have unique characteristics and properties [62]. Their structures exhibit a typical

Chapter I: State-of-the-art and objectives

metal-to-insulator phase transition (MIT) with obvious changes in optical, electrical, thermal, and magnetic properties [63]. Such a phase transition not only results in potential applications but also provides scientists with important and interesting materials to study the phase-transition mechanism. Among these compounds, vanadium dioxide (VO_2) is particularly interesting because its transition temperature is close to room temperature. Although its phase-transition mechanism is still controversial, the modification of the phase-transition has undergone considerable progress in recent years [64]. The first-order monoclinic (M) insulator phase to rutile (R) metallic phase transition in VO_2 is accompanied by a large and rapid change in the electrical and optical properties, with potential traditional applications in switching and sensing, as well as the modulation of infrared (IR) wavelengths [65], [66]. The phase transition mechanism has led to a variety of potential applications, including smart thermochromic windows (smart NIR filters).

2.2.2 Redox properties

Redox properties are the ability of a material to undergo redox reactions, which involve the transfer of electrons between chemical species. In the context of chromism, redox properties can lead to changes in the color of an inorganic material (oxides) as a response to a change in the oxidation state of the metal ions. Transition metal ions are elements that can have multiple stable oxidation states. The easy oxidation and reduction (redox property), and the existence of cations of different oxidation states in the intermediate oxides have been thought to be important factors for these oxides to possess desirable properties in selective oxidation and related reactions. Metal oxides are typically made up of metallic cations and oxygen anions, resulting in a lattice with less ionicity than that predicted by formal oxidation states. This leads to the presence of charged adsorbate species and the common dissociative adsorption of molecules. The exposed cations and anions on the surface of the oxides form acidic and basic sites as well as acid-base pair sites. The fact that cations can have different oxidation states allows the oxides to undergo oxidation and reduction, leading to the possibility of high densities of cationic and anionic vacancies. Redox chromism has been observed in a variety of oxide materials, including tungsten trioxide (WO_3), molybdenum trioxide (MoO_3), and nickel oxide (NiO) [61], [67].

Among these, WO_3 is the most well-known example of an oxide that exhibits redox chromism. The most common form of WO_3 is the hexagonal phase, which contains W^{6+} ions in a distorted octahedral coordination geometry. When WO_3 is reduced, either by chemical reduction, photonic irradiation or by exposure to reducing gases such as hydrogen, the W^{6+} ions are converted to W^{5+} , which results in a color change from yellow to blue up to black (as seen previously). This phenomenon is known as reduction-induced blue coloration. The contribution of redox properties of WO_3 will be discussed in detail in the next section.

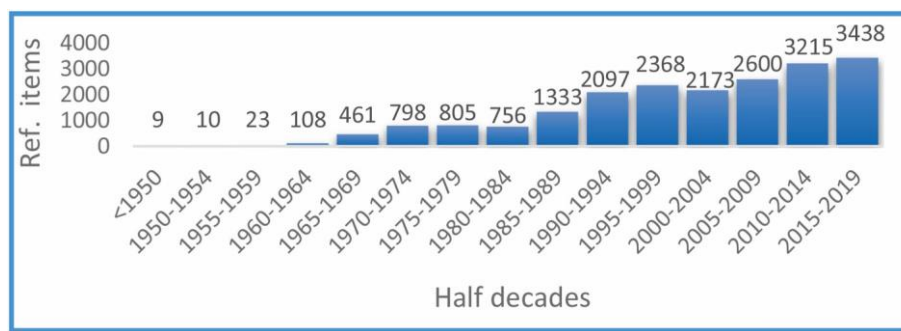
2.3 Focus on photochromic materials

The phenomenon of photochromism was first discovered in the late 1870s. The capacity to change coloration under UV light excitation, known as “phototropy”, was studied for the first time in 1899 by W. Marckwald, when he published his work concerning the reversible color change of a ketone of the

Chapter I: State-of-the-art and objectives

naphthalene family [68]. This term has been used by the scientific community for over 50 years. In 1950, the Israeli physical chemist Y. Hirshberg introduced the word “photochromy”, originating from the Greek roots phos (light) and chroma (color), which he used to describe the reversible coloration of colorless bianthrone ($C_{28}H_{16}O_2$)-derived compounds under ultraviolet irradiation [69], [70]. Thus, for twenty years, these two terms coexisted in the literature, while designating the same phenomenon. In 1970, after a symposium between more than 250 chemists, the use of only one of these two terms was decided, and “phototropism” was abandoned [46]. A third term emerged around 1920: “tenebrescence”, derived from the Latin Tenebrae (darkness, obscurity), which is exclusively used to describe photochromism in mineralogy.

The optoelectronic mechanisms underlying photochromism have been continuously inciting significant scientific interest ever since, as evidenced by the increasing number of publications since the 1970s (Figure 11).



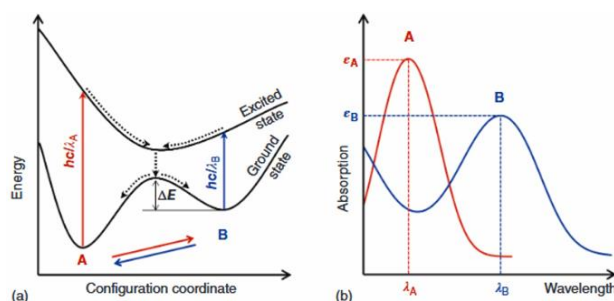
Chpt.I-Figure 11: Historic catalog of the number of items pertaining to “photochromism” extracted from the sci-Finder database.

2.3.1 Different classes of photochromic compounds

Photochromism generally designates any reversible change in the coloration of a material from a thermodynamically stable state A to a metastable state B, that is induced by electromagnetic radiation (Figure 12). The typical metastability of the B state is associated with a longer return to the stable state A, whether this return occurs naturally, or *via* an activation process (*e.g.*, thermally, by immersion in a particular atmosphere, by irradiation at a new wavelength, *etc.*). In most photochromic materials, ultraviolet (UV) radiation is absorbed by state A (at hc/l_A) in the absorbing wavelength range (ideally, at the maximal molar extinction coefficient e_A), thereby causing a change to state B. The return from state B to state A can be realized *via* irradiation-induced excitation at a new wavelength (l_B). The A and B states are energetically separated by a potential energy barrier (ΔE). The classification of photochromes is generally based on the type of stimulus that enables the reversion reaction ($B \rightarrow A$) to manifest. Knowing that the $A \rightarrow B$ transformation is always photoactivated, there are several ways to revert to the initial state. Under a low potential energy barrier (ΔE), the return reaction can be thermally activated and the photochrome is classified as type T [71]. The return to state A is spontaneous, owing to the metastability of state B, but often sluggish (between a few hours and a few days); however, it can be accelerated by temperature. On the contrary, under higher

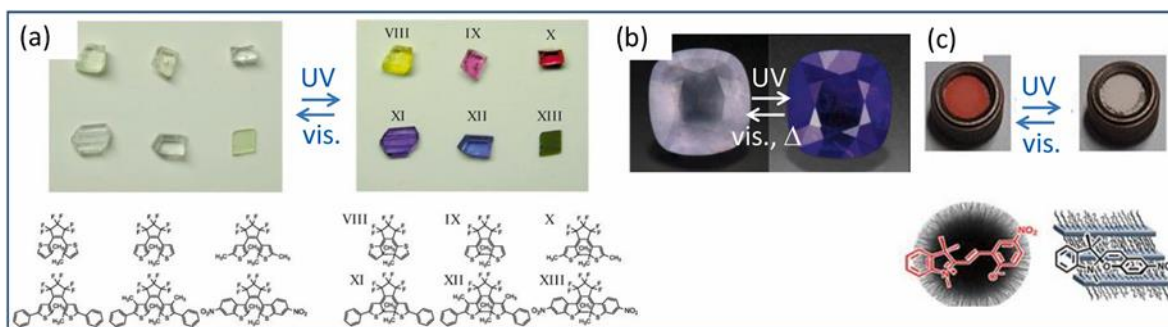
Chapter I: State-of-the-art and objectives

potential energy barriers, this reaction can only be photoactivated by a second specific irradiation, where the photochrome is classified as type P [72]. Under sufficient irradiation, switching between states A and B is usually very fast (picosecond duration times). A simple way to distinguish between the two photochromic compound types discussed above is that in type T thermal transformations are involved, whereas in type P purely photochemical mechanisms are involved.



Chpt.I-Figure 12: Bidirectional reaction induced by an electromagnetic excitation between two molecular/crystal states, A and B: (a) Diagram of potential energies and (b) associated absorption spectra [72].

In most photochromic compounds, the stable state A is initially colorless or pale, and becomes darkened once it transforms into state B under irradiation; this is positive photochromism. As an illustration, a wide variety of colorations were achieved for compounds derived from the diarylethene family after UV exposure as shown in Figure 13.a. Another illustration of positive photochromism is exhibited by the Hackmanite-type ore ($\text{Na}_8[\text{AlSiO}_4]_6\text{Cl}_{1.8}\text{S}_{0.1}$), where the amethyst coloration manifests after UV irradiation ($\lambda = 365 \text{ nm}$) (Figure 13.b). This material can revert to its initial coloration rapidly, *via* photo- or thermo-activation, or slowly, when left in the dark [73].



Chpt.I-Figure 13: (a) Crystals from a diarylethene derivative before (left) and after (right) UV radiation [74]. (b) Hackmanite stone from Burma before (left) and after exposure (right) to UV radiation (365 nm) [73]. (c) Reversible photochromism of a red merocyanine transforming into a colorless spiroopyrane upon exposure to visible radiation [75].

In the minority of cases, the already colored compound can sustain photo-bleaching under visible irradiation and becomes completely incapable of neither negative nor reverse photochromism. This phenomenon has been reported to date only for rare organic or hydride compounds. Barachevsky *et al.* has reported in a review that most studies on negative photochromism focus on spiro bicyclic organic compounds (in which the two cycles, spiroopyrane and spirooxazine, are connected by a single atom), that was initially colored owing to the presence of merocyanine [75], [76]. For example,

Chapter I: State-of-the-art and objectives

Yamaguchi *et al.* (Figure 13.c) demonstrated that a red-colored hybrid composed of merocyanine adsorbed on a mesoporous silica fiber lost its coloration upon exposure to visible radiation [75]. The obtained colorless compound, comprising a spiropyran combined with organophilic clay, exhibited better reversibility of the photochromism process, as evidenced by the compound recovering its red color after being kept for approximately 10 h in the dark. Furthermore, the restoration of the initial coloring could be accelerated by heat treatment. Accordingly, numerous studies on negative photochromism have focused on diarylethene-type compounds or thioindigo-type dyes ($C_{16}H_8O_2S_2$) [77], [78].

2.3.2 Photochromic organic-inorganic hybrid materials

Mixing organic and inorganic components at the molecular or nanometric level has huge implications for creating new and useful materials. These hybrid materials combine the best features of both types of materials - for example, they can be lightweight, flexible, and versatile like organic materials, but also have high thermal and mechanical resistance like inorganic materials [79]. This makes them useful in many fields, such as optics, solid electrolytes, catalysis, biomaterials, and biomedical applications [80]. Additionally, some photoactive molecules can be added to these hybrid materials to give them new properties like photochromism. The potential applications of using a hybrid approach to create photochromic materials with vastly improved properties are currently being extensively researched by many research groups [79], [81]. Photochromic active compounds have been successfully incorporated into a wide range of solid matrices, including both organic and inorganic materials such as polymers like PMMA and PET [80], [82], sol-gel derived silicates and aluminosilicates, as well as hybrid organic-inorganic composites like osmosis and surfactant-templated mesostructured materials [81]. The compounds can be integrated into the matrix in two ways: either through covalent bonding or doping.

In one study, Andersson *et al.* [83] synthesized photochromic pigments that can be added to various matrices using traditional coating or paint-based technology. They introduced photochromic spiropyran and spirooxazine dyes into surfactant-templated mesostructured particles using a simple one-pot spray synthesis technique. These dye-loaded materials are referred to as photochromic organic-inorganic hybrid pigments.

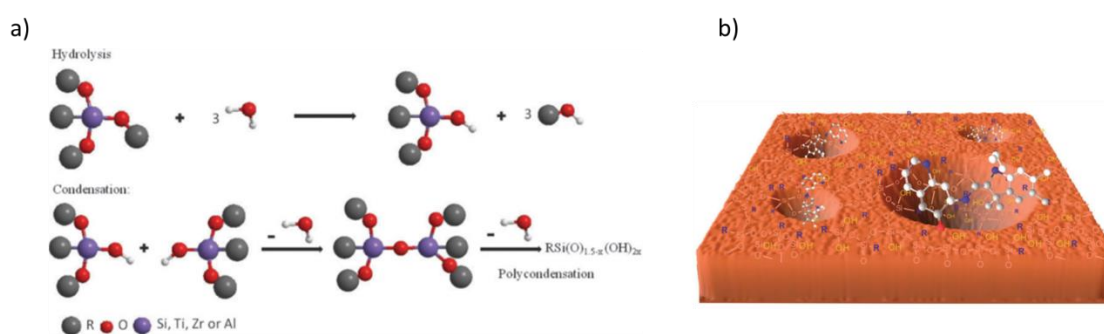
To develop practical photochromic devices, the materials used must be shaped into thin films, coatings, monoliths, or other suitable forms as required by engineering considerations.

However, it can be challenging to prepare photochromic hybrid materials by standard methods of vacuum evaporation or sputtering [84]. These methods typically require high temperatures, which can cause many photochromic compounds to decompose. As a result, these methods are limited to the preparation of hybrid materials containing inorganic photochromic compounds such as MoO_3 or WO_3 [80].

Chapter I: State-of-the-art and objectives

One potential solution to this challenge is the use of sol-gel processing. Sol-gel processing is a method of synthesizing hybrid materials that involve the hydrolysis and condensation of metal alkoxides in a liquid solution to form a gel, which is then dried and heated to form a solid material [85], [86]. This method can be used to prepare photochromic hybrid materials by incorporating photochromic compounds into the sol-gel matrix during the synthesis process.

The sol-gel method allows also the preparation of hybrid organic-inorganic matrices, by using organically modified alkoxide precursors $[RM(OR)_3]$, where R is an organic functional group and OR is the alkoxy group (Figure 14.a). The hybrid silica matrix in which the organic molecules are situated can be visualized in the scheme shown in Figure 14.b [87]. Precursors of these materials are used to regulate the size and polarity of the pores, depending on the nature and amount of the non-hydrolyzable organic groups utilized [88]. To prepare hybrid organic-inorganic matrices, difunctional alkoxides such as $RR'OM(OR)_2$ have also been employed, with methyl (-CH₃) and phenyl (-C₆H₅) being the most frequently used functional groups (R and R'). The preparation of hybrid photochromic WO₃-based compounds will be discussed in detail later in the following section.



Chpt.I-Figure 14: a) Sol-gel reactions of organically modified alkoxide precursors, b) Schematic representation of the pore structure in the hybrid silica matrix [89].

2.3.3 Applications of inorganic photochromic compounds

Ophthalmic lenses and glass building facades are among the most prominent practical applications of photochromism. Recently, a new cost-effective smart facade glazing has been developed which darkens reversibly under intense sunlight, thereby protecting the eyes from UV radiation, while allowing better control of solar illumination in buildings (Figure 15.a,b). Additionally, stemming from their thermal barrier and UV protection layer features, photochromic building panels and car windows present significant potential in reducing the overall energy consumption of modern buildings and cars, while improving safety [90]. The first inorganic photochromic lens model appeared in the 1970s and was marketed by Corning Inc. under the name “PhotoSun®”, and a few years later “PhotoGray®”. This model consisted of borosilicate glass doped with monovalent copper containing silver salts. The dark tint in these mineral glasses is derived from the precipitation of silver halide particles (chloride or bromide, about 100 Å) under UV irradiation, which are dispersed in the glass during its manufacture. Under the effect of UV rays, the following oxidation-reduction reaction takes place: Ag^+

Chapter I: State-of-the-art and objectives

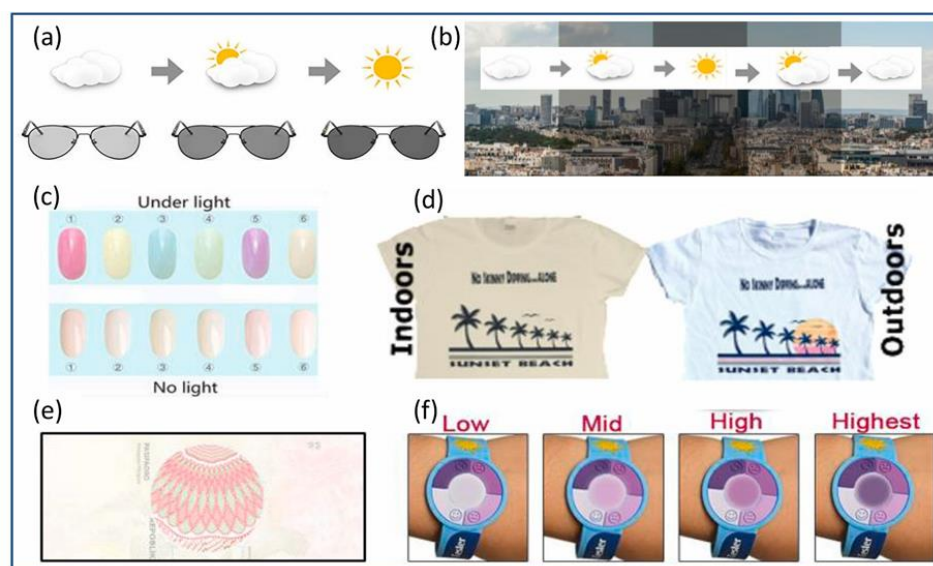
$+ Cu^+ \rightarrow Ag^0 + Cu^{2+}$ [91]. The metallic silver aggregates (~20 nm) that form on the surface of the silver halide particles absorb light and give a dark color to the material. In the dark, the returns to its original tint *via* a reverse reaction. Thermal agitation or irradiation in the visible region can accelerate the photobleaching process.

Inorganic transition optical lenses were dethroned in the 1990s by their organic counterparts for various reasons [92]: on one hand, the thicker parts of the mineral glass exhibited deeper darkening than the thinner parts, often resulting in a visually heterogeneous coloration. On the other hand, the more fragile and heavier inorganic glasses used for this technology (borosilicate glasses density = 3.21) could hardly compete with the comfort provided by organic lenses (density ~ 1.2). Organic lenses are made of transparent polymers (*e.g.*, poly di (ethylene glycol) bis (allyl carbonate)) or polycarbonates, where the photochromic molecules are dispersed inside the lens. These molecules, which comprise a carbon ring, are generally derived (according to Winder et al.) from the families of spironaphthoxazines or chromenes (naphthopyran and benzopyran) [93], and they all follow the same photochromism key mechanism, which is dependent on the latitude for opening and closing the carbon cycle.

Other practical applications taking advantage of the electromagnetic irradiation-triggered smart color change mechanism are aesthetic-related, such as photochromic dyes. For instance, the French company Euracli offers a range of products called EuraChrom®, consisting of three basic photochromic dyes (blue, red, yellow) which can be mixed with other non-photochromic dyes to produce a wide color palette. Additionally, Vivimed offers a range of organic dyes called Reversacol™, which are supplied in the form of polycrystalline powders. Similarly, photochromic inks and varnishes for application on a variety of substrates are commercially available, such as the photochromic nail polish offered by the Cattie Girl brand (Figure 15.c). Notably, a patent on water-based photochromic varnishes was filed in 2019 [94]. Morel et al. showed that many advances have been made in the design of photochromic materials for hair dyeing [95]. Indeed, photochromic coating dyes, such as Jarocol® and custom SolarActive® brand t-shirts, have recently become commercially available (Figure 15.d).

The unique feature of UV irradiation-induced color change has also been exploited for more “technological” functional applications. One such instance is security ink, which can realize optically variable patterns on paper that are difficult to forge, for document authentication purposes [96]. In particular, the Semlex company offers passports with patterns drawn using photochromic ink (Figure 15.e). Another example in this category is a smart cheap bracelet that can control the rate of UV irradiation (Figure 15.f).

Chapter I: State-of-the-art and objectives



Chpt.I-Figure 15: Diverse applications of photochromic compounds: (a) Photochromic lens (TJUTR Brand); (b) Photochromic smart windows; (c) Cattie Girl brand varnishes; (d) SolarActive® inks printed on a t-shirt; (e) A pattern designed with photochromic ink (Semlex); (f) A bracelet (Xiamen Guzhan Industry & Trade Co.) measuring the rate of UV radiation.

Other niche applications have been reported. Akiyama *et al.* proposed using europium (Eu)-doped BaMgSiO₄ photochromic materials with an apatite-like structure as photo-sensors [97]. Other researchers have reported photochromic materials that can be used as reversible holographic systems [98], [99]. A noteworthy common target application is the use of photochromic compounds for high-density optical data storage, an idea initially proposed in 1963 by [70] Fischer *et al.* This application exclusively concerns P-type photochromic compounds, since only a very brief irradiation (microseconds) allows information to be stored, and this information remains stable until a second irradiation. In addition, it is necessary for the initial state to be restored for a very short time duration. Thus, the cycle must be reversible and indefinitely repeatable and must be completed rapidly. Remarkably, as early as 1967, Smith *et al.* proposed a technique for bimodal data storage using silver halide-doped glasses [100]. An improvement of this storage medium has been suggested by Zhang *et al.*, who asserted that three different states can exist if two photochromes are linked, thereby enabling tri-modal storage [101]. This application can be further enriched by synergistically combining photochromism with the inherent properties of the active material, allowing for the realization of complex devices that are alternately triggered by two different external stimuli, such as light and electric current [102], [103].

However, few studies have discussed the influence of photochromism on a material's physical or chemical properties, such as the refractive index, dielectric constant, electrical conductivity, solubility, viscosity, and surface wettability. For example, Agranat and Yacoby demonstrated a correlation between the change in the dielectric constant (responsible for the photorefractive effect) and photochromism in KTa_{1-x}Nb_xO₃ perovskites [104].

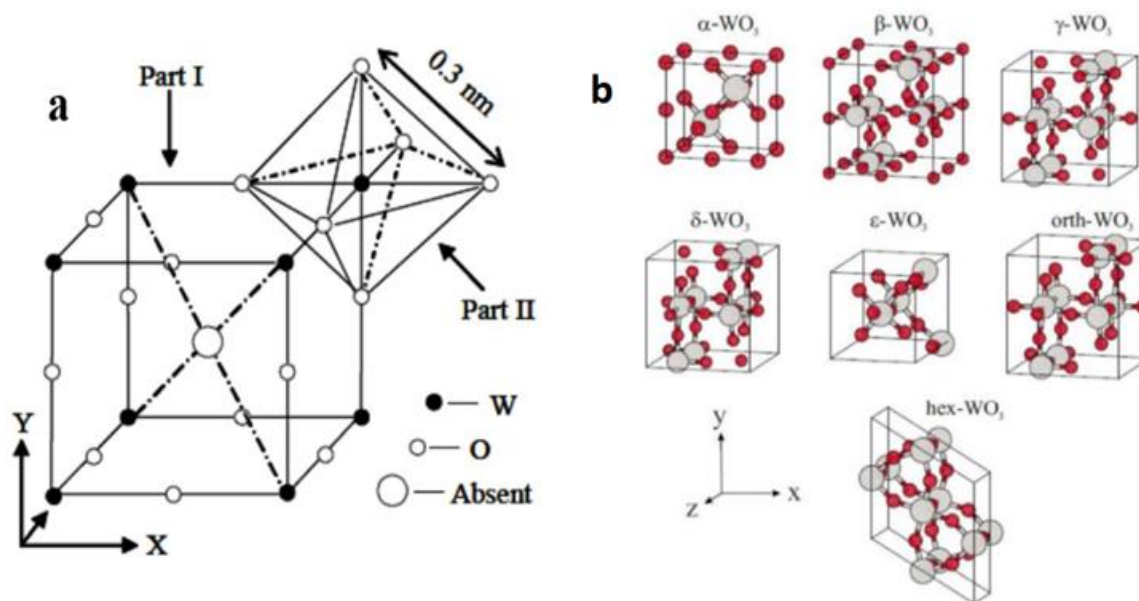
Finally, regarding negative photochromism, where the photobleaching process occurs under UV-light irradiation, whereas the darkening mechanism self-operates without illumination, Barachevsky et al. argued that new materials exploiting this feature could achieve improved performance in applications dedicated to data storage [76]. This advantageous optical property also makes it possible to develop smart camouflage clothing or coatings that lighten up or darken depending on the exterior brightness, for use in the military. These functionalities can also be integrated into consumer applications, such as photo-controlled paints for cars that can reflect more light under high sun exposure, thereby contributing to temperature regulation within the vehicle.

3 Tungsten oxide as the photochromic material of next future

Over the last several decades, tungsten oxide compounds (WO_x) have been intensively investigated owing to their interesting photochromic properties and structural versatility, which give rise to promising potential applications including optical devices, gas sensors, photocatalysts, flat panel displays, etc.

3.1 The crystalline structures of WO_x

Various distorted MO_3 -like structures exist, in which every off-center W atom is surrounded by a regular octahedron that is formed by the six nearest O atoms [105], [106]. The prototype crystal structure of WO_3 is the same as that of cubic ReO_3 , where a three-dimensional network is established via the corner-sharing of WO_6 -octahedra (Figure 16.a). Interestingly, WO_3 can be formed sequentially in six additional phases, which have been identified as follows: monoclinic II (ϵ - WO_3), triclinic (δ - WO_3), monoclinic I (γ - WO_3), orthorhombic (β - WO_3), tetragonal (α - WO_3), and hexagonal (h- WO_3) (Figure 16.b, Table 2).



Chpt.I-Figure 16: (a) Geometry of the ReO_3 -type unit-cell at the $[WO_6]$ octahedral site; (b) Unit cells of different (WO_x) phases [105].

Chapter I: State-of-the-art and objectives

Chpt.I-Table 2: Unit-cell parameters and densities of the different WO₃ phases [105-107].

Crystal	Space Group	a	b	c (Å)	α	β	γ (°)	ρ (g/cm ³)
ϵ -WO ₃	Pc	5.278	5.156	7.664	90	90.76	90	7.39
δ -WO ₃	P-1	7.313	7.525	7.689	88.85	90.91	90.94	7.28
γ -WO ₃	P2 ₁ /c	7.306	7.540	7.692	90	90.88	90	7.27
β -WO ₃	Pmnb	7.341	7.570	7.754	90	90	90	7.15
α -WO ₃	P4/nmm	5.272	5.272	3.920	90	90	90	7.07
Cubic WO ₃	Pm-3m	3.834	3.834	3.834	90	90	90	6.83
h-WO ₃	P6/mmm	7.298	7.298	3.899	90	90	120	6.42

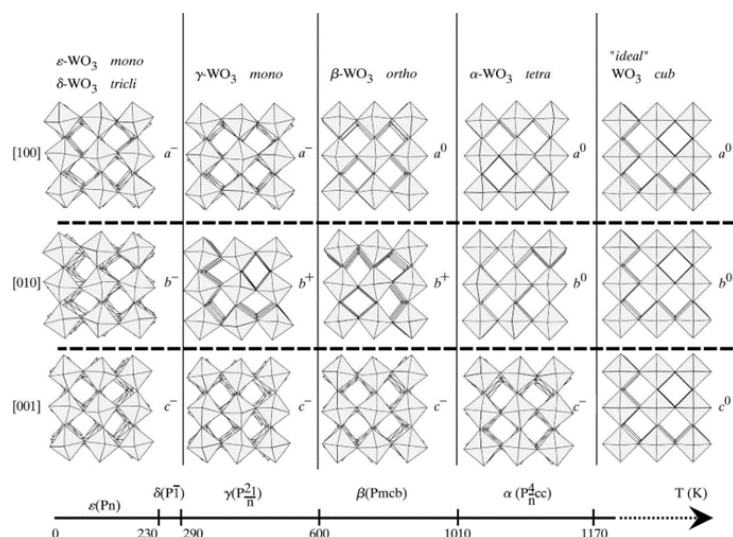
The seven phases of WO₃ can be differentiated by the tilting of their angles and the distortions of the WO₆ octahedra from the ideal cubic structure, thereby resulting in lower symmetries (Figure 17). The crystal phase transitions occur in the following sequence, where the stability domains of the various allotropic forms at different temperatures can be determined: monoclinic (ϵ -WO₃, < -43 °C), triclinic (δ -WO₃, -43 to 17 °C), monoclinic I (γ -WO₃, <17 to 330 °C), orthorhombic (β -WO₃, <330 to 740 °C), tetragonal (α -WO₃, >740 °C) [35–38]. The monoclinic γ -WO₃ phase with the P2₁/c (or P2₁/n) space group, which comprises a primitive monoclinic unit cell, a two-fold screw axis, and a c-glide plane perpendicular to the screw axis (Table 2) [107].

WO₃ can be also encountered in a non-stoichiometric structure, WO_{3-x} (where 0 < x ≤ 1). The wide variability of these nonstoichiometric structures stems from the WO_x lattice, which can withstand a considerable number of O deficiencies, resulting in the formation of different oxidation states for W. WO_x can vary from WO_{2.625} (W₃₂O₈₄) to WO_{2.96}, and can be identified by the local condensation associated with the edge-sharing octahedral site organization, which in turn arises from the pure corner-sharing networks of the WO₆ octahedra in stoichiometric WO₃.

The WO₃ allotropic forms also exhibit changes in terms of bandgap energy, as the occupied levels of the W 5d states slightly change with the phase transformations. Amorphous WO₃ typically possesses relatively large bandgap energy of approximately 3.25 eV, whereas the respective bandgap energy of monoclinic WO₃ in bulk form (large crystallite size) is ~2.6 eV [108].

Moreover, in nanostructured WO₃, the reduction in crystallite size results in a blue shift of the optical absorption band edge, corresponding to a widening of the bandgap energy, with reported values ranging from 2.60 to 3.52 eV. The largest blue shift can be theoretically attributed to the quantum confinement effect [109]. Since the color of WO₃ is mainly determined by the absorption edge energy of the material, its monoclinic form is usually yellowish, whereas its nanoparticles are white.

Chapter I: State-of-the-art and objectives



Chpt.I-Figure 17: Tilt patterns and stability temperature domains of the different WO_3 polymorphs [110].

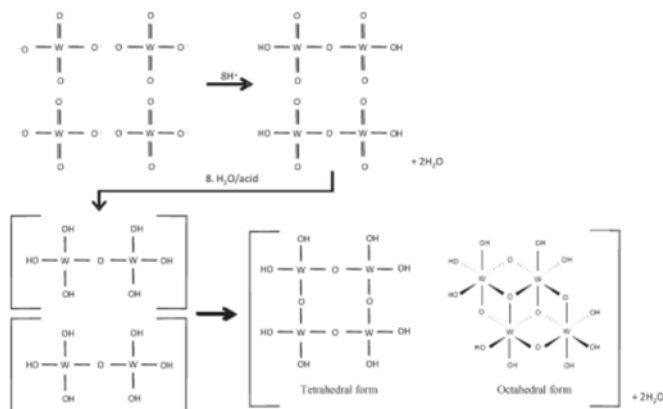
3.2 Synthesis of Tungsten Oxide Nanostructures

Fabricating WO_3 nanostructures has attracted increasing interest due to increased surface-to-volume ratio and quantum confinement effects, which reveals unique properties [106]. There are various approaches to synthesizing nanostructured WO_3 including vapor phase and liquid phase-based methods [106], [111]. Liquid-phase synthesis provides superior control of the material morphology and can be implemented at relatively low temperatures. Hydrolysis, condensation, etching and oxidation are the four most important chemical processes in liquid-phase synthesis. In this part, the most common liquid-phase synthetic methods (sol-gel, hydrothermal, electrodeposition and electrochemical anodization) of fabricating nanostructured WO_3 will be described in detail.

3.2.1 Sol-Gel

Sol-gel process begins with a precursor solution (sol). During the aging process, hydrolysis and polycondensation occur to form discrete particles (colloidal sol) or a network structure (gel) [81]. As shown in Figure 18 [112], H_2WO_4 is formed when the reagent WO_4^{2-} from Na_2WO_4 mixes with H^+ from nitric acid. Consequently, partial condensation polymerization occurs eliminating molecules of H_2O to form a shared oxygen bond between two tungsten atoms. As more acid is added, the tungsten oxo ligands can be hydrated to dihydroxy ligands ($W-(OH)_2$) which experience further condensation action to form a 3D network structure until six shared oxygen bonds form in a similar structure to a polyoxotungstate [112].

Chapter I: State-of-the-art and objectives

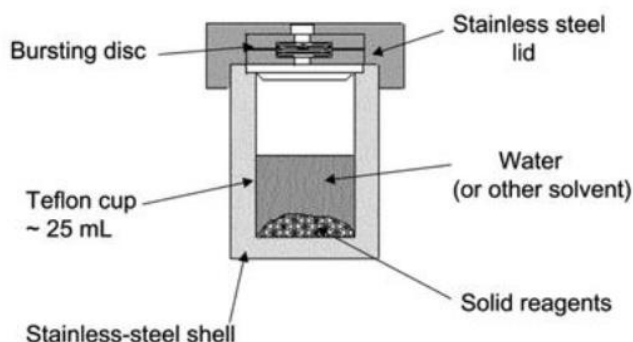


Chpt.I-Figure 18: Sol-gel condensation polymerization reaction of Tungsten oxide [112].

Hydrated WO_3 is typically produced in most sol-gel methods, and it requires a post-annealing treatment to obtain the anhydrous crystalline WO_3 . Sanato *et al.* [113] confirmed the presence of highly crystalline tungsten oxide hydrate as the result of post-annealing of WO_3 ; however, no specific crystal type of the hydrate could be determined in their study. The Raman peaks indicate that the hydrated WO_3 was still present after heat treatment at 300°C , while monoclinic WO_3 began to appear at 400°C calcination temperature.

3.2.2 Hydrothermal

Hydrothermal treatment is a simple and cost-effective and well-studied liquid-phase technique that offers remarkable advantages in controlling the product morphology and size at low processing temperatures with good homogeneity [114]. Hydrothermal synthesis is performed in autoclaves as shown in Figure 19 [115]. The hydrothermal synthesis of nanostructured WO_3 begins with a tungsten precursor, typically a tungstic acid solution (e.g. H_2WO_4 , WCl_6 and Na_2WO_4) which is dissolved into deionized water with additives such as HCl and surfactant as the cetyltrimethylammonium bromide (CTAB), and then aged at temperature ($180\text{--}200^\circ\text{C}$) for 12 to 24 hours to allow the nucleation and crystal growth to take place. The synthesized precipitates are finally washed with deionized water and then dried in air at $70\text{--}80^\circ\text{C}$ [115].



Chpt.I-Figure 19: A schematic of a Teflon-lined stainless steel autoclave [115].

Chapter I: State-of-the-art and objectives

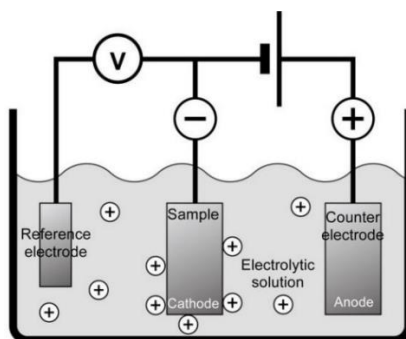
The control of nanostructured WO_3 shape can be achieved with the adding of the chelating ligands or capping reagents such as polyethylene glycol (PEG), polyvinyl alcohol (PVA), sulfates and oxalic acid [116], to the precursor solution which acts as structure directing and dispersing agents. The combination of these reagents modifies the free energies of the various crystallographic surfaces and accelerates their growth rates, resulting in the ability to control the final shape of the crystal [117]. Table 3 presents a summary of the nanostructured WO_x types that result from hydrothermal treatment with different additives.

Chpt.I-Table 3: A summary of the nanostructured WO_x types.

Morphology	Dimension[nm]	Precursor	Additives	T (°C)	Duration (h)	Phase
Nanocuboids [117]	120	Na_2WO_4	HBF_4	180	4	$\beta\text{-WO}_3$
Nanowire bundle [118]	D: 5-15 L: $> 5 \times 10^3$	H_2WO_4	Li_2SO_4 $\text{H}_2\text{C}_2\text{O}_4$	180	2-24	h-WO_3
Nanoplate [119]	W: 500	H_2WO_4	Citric acid	120	24	$\beta\text{-WO}_3$
Nanowire, hollow sphere, nanotube, solid ball [120]	Various	WCl_6	Urea	180	12	crystalline
Nanobelts [121]	W: 30-100 L: $> 1 \times 10^3$ T: ~ 15	H_2WO_4	Cetyltrimethylammonium bromide Na_2S	180	12	$\beta\text{-WO}_3$
Nanorods [116]	D: 5-25 L: 200-500	H_2WO_4	NaCl	180	24	h-WO_3

3.2.3 Electrodeposition

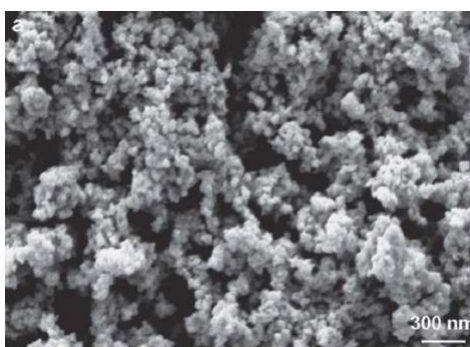
Electrodeposition is a process where an external potential is applied between a working electrode and counter electrode, with both immersed in an electrolyte solution as shown in Figure 20 [122]. The metal oxide film is formed by the accumulation of metal ions present in the electrolyte solution. The process usually requires only a low applied voltage, and the deposition duration ranges from 1 to 30 minutes. Excessive applied voltages and prolonged reaction time will result in the formation of compact films with low porosity [123].



Chpt.I-Figure 20: Schematic of an electrolytic cell used in the electrodeposition [122].

Chapter I: State-of-the-art and objectives

The morphological properties of the resulting WO_3 can be also tuned by the selection of the electrolyte solution and additives. The most popular choice of electrolyte employed is the peroxotungstic acid solution, while alcohol such as isopropanol or ethanol can be added to the solution to increase the stability [124]. The deposition mechanism can be summarized as (i) the formation of isolated nuclei and their growth to larger grains; (ii) the aggregation of grains; and (iii) the formation of crystallites [125]. Under optimal process conditions, electrodeposition can produce porous WO_x films with grains of 20–100-nm diameters as shown in Figure 21. As with most liquid phase synthesis methods, the as-electrodeposited WO_x is usually in a hydrated form. Post-annealing above 400°C is usually conducted to transform the $\text{WO}_3 \cdot n\text{H}_2\text{O}$ to monoclinic WO_3 [123].



Chpt.I-Figure 21: Surface morphology of an electrodeposited WO_3 film using peroxotungstic acid solution [59].

3.2.4 Polyol method

The Polyol method is a robust strategy for the preparation of well-defined metal and metal oxide nanoparticles in terms of size, shape, composition, and crystallinity [126]. Polyalcohol or polyols have emerged as a very useful class of reducing compounds for the preparation of metal nanoparticles, in what has become known as the “polyol process” [127]. This term was first used by Figlarz *et al.* [128] in 1988 while they developed the polyol method to synthesize metal powders, including Co, Ni, and Cu particles. They mixed the metal salts in ethylene glycol (EG) at different ratios followed by the addition of sulfuric acid (H_2SO_4) and heating until boiling.

In a typical polyol synthesis of metal particles, different steps in the course of the reaction have been identified: (i) the dissolution of the metal precursor that occurs either at room temperature or during the heating step, (ii) the possible formation of an intermediate phase acting as a cation reservoir, (iii) the nucleation step from monomer species and (iv) the growth step leading to the formation of the nano particles.

3.2.4.1 Physicochemical properties of the polyols

In the “polyol method”, polyol refers to a diol, mainly a 1,2-diol, such as ethylene glycol and its derivatives, di-, tri-, tetra- and so on up to poly (ethylene glycol), abbreviated as EG, DEG, TEG, TTEG and PEG, respectively, and also to different isomers of propanediol, butanediol, pentanediol, etc. Compounds having more than two hydroxyl groups, such as glycerol (GLY), pentaerythritol and carbohydrates, are also considered polyols.

Chapter I: State-of-the-art and objectives

The polyol medium offers several advantages [126], [127]: (i) the high boiling point allows syntheses at a relatively high temperature which produces well-crystallized materials, (ii) the reducing medium preserves the as-prepared metal particles from oxidation, as long as they remain in the medium, (iii) its ability to coordinate metal precursors and the particle surface, which minimizes coalescence and (iv) the high viscosity of the medium favors a diffusion-controlled regime for particle growth, resulting in controlled structures and morphologies. Table 4 shows the main properties of the main used polyols.

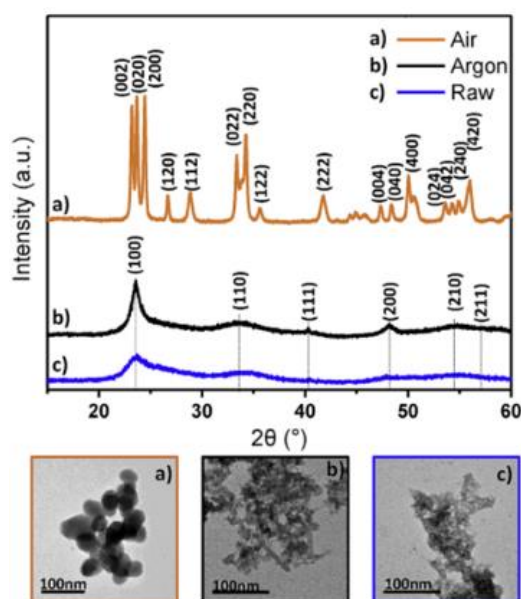
The high B.P. of polyols (Table 4) allows syntheses to be conducted at temperatures as high as 328°C without the use of autoclaves which usually leads to crystalline nanomaterials directly and suppressing the powder post-annealing step [127]. The presence of OH groups gives polyols coordinating properties and offers major benefits as: (i) to compensate for their lower polarity, expressed by the empirical solvent parameter E_T^N , in the 0.664–0.790 range, compared to water ($E_T^N = 1$), making them water-equivalent solvents in which both simple metal-salt precursors and polar compounds can be dissolved, (ii) to fine-tune the nucleation, growth and agglomeration of particles, since polyols can adsorb on the particle surface, especially on oxides, providing excellent colloidal stabilization.

Chpt.I-Table 4: Physical constants of selected polyols, water and ethanol [129], [130].

	MW (g mol ⁻¹)	B.P. (°C)	Viscosity (mP. s)	Dipole moment (D)	Dielectric constant	Empirical polarity
Water	18.01	100	0.89	1.85	80.1	1
Ethanol	46.06	79	1.07	1.69	25.3	0.654
Ethylene glycol (EG)	62.06	197	16.1	2.28	41.4	0.790
1,2-Propanediol	76.09	187	40.4	2.27	27.5	0.722
1,2-Butanediol	90.12	190	38 (20°C)	3.35	22.4	0.676
Glycerol (GLY)	92.09	290	934	2.56	46.5	0.812
Diethylene glycol	106.12	245	30.2	2.30	31.8	0.713
Tri ethylene glycol	150.17	285	49 (20°C)	5.58	23.7	0.682

Bourdin *et al.* [131] developed a polyol synthesis process to obtain WO_{3-x} NPs with tuneable chemical, morphological, structural, and optical properties where tungsten (VI) chloride was used as tungsten source and diethylene glycol (DEG) as solvent. The mixture was heated at 180 °C with continuous stirring and refluxed for 3 h. At the end of the reaction, a deep blue precipitate was obtained. The powder obtained was then separated into three batches. The as-prepared WO₃ powder constitutes the first batch (raw powder), the powders post-annealed at 600 °C under air (black) or under argon (yellow) being the second and third batches. The crystalline structure of the three batches of WO₃ oxide powders was analyzed by X-ray diffraction and the morphology by transmission electron microscopy. The XRD patterns indicate that the raw and argon-annealed powders have a similar crystalline structure with extremely small sizes around 5-10 nm (Figure 22).

Chapter I: State-of-the-art and objectives

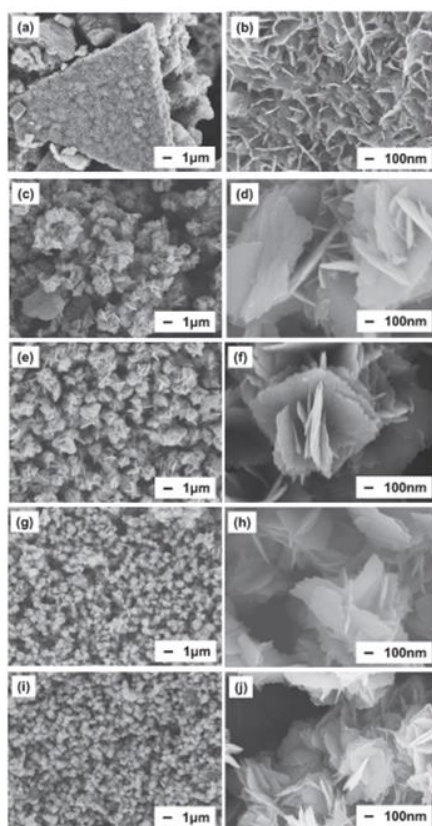


Chpt.I-Figure 22: XRD patterns and TEM images of the WO₃ powders synthesized by the polyol process: a) annealed under air; b) annealed under argon, c) raw powder [131].

The Polyol process allows fine control of the chemical composition of the oxide precipitates. Tungsten trioxide and titanium-doped tungsten trioxide has been reported by Perkodi *et al.* [132] using chlorides of tungsten and titanium in diethylene glycol as polyol medium and water as the reagent for hydrolysis at 190 °C. The particle sizes of the precursor materials were observed to be around 100 nm. Annealing of the samples was applied to obtain crystalline WO₃ and titanium-doped WO₃. The XRD data of the annealed samples revealed that the crystalline phase could be manipulated by varying the doping concentration of titanium doping in the tungsten trioxide matrix.

Furthermore, by using long-chain capping agents or polymers such as PVP, remarkable achievements have also been made towards controlling the shape of metal nanoparticles as reported by Akamatsu *et al.* [133], where microspheres consisting of WO₃ nanoplatelets were prepared by a simple polyol process using tungsten chloride, poly-(vinylpyrrolidone) (PVP), and ethylene glycol. The microsphere sizes were controlled by changing the molecular weight of the added PVP from 3500 to 1300000. Figure 23 shows the SEM images of the particles prepared by heating at 190 °C for 1 h with various molecular weights of PVP: 3500, 10000, 55000, 360000, and 1300000. For the lowest molecular weight PVP, bulky blockish particles that were several tens of micrometers in size and consisted of 30-nm-wide platelets were observed. In the other particles prepared using higher molecular weight PVPs (10000, 55000, 360000, and 1300000), no bulky blocks could be seen; instead, microspheres with uniform sizes consisting of nanoplatelets were observed.

Chapter I: State-of-the-art and objectives



Chpt.I-Figure 23: SEM images of particles prepared by heating at 190°C for 1 h with PVP of various molecular weights: (a and b) 3500; (c and d) 10000; (e and f) 55000; (g and h) 360000; and (i and j) 1300000 [133].

During the last decade, very significant progress in the understanding of the mechanisms of formation in polyols has been made. Nevertheless, further improvements are needed to establish this method on a less empirical basis.

3.3 Photochromism in WO_x -based materials

3.3.1 Theoretical models explaining the WO_3 photochromism

Hitherto, various theoretical models have been proposed to elucidate the photochromism mechanisms of WO_3 . In all cases, photoredox reactions creating some supplementary W^{5+} ions in the coloring state are admitted. Then, interpretation diverges depending on the localized or delocalized behavior of the electron transfers associated with the creation of the supplementary W^{5+} ions.

In the two earliest models, Deb *et al.* [109] proposed that photochromism is induced by F-centre-like absorptions between the ground and excited states of electrons trapped in oxygen vacancies, whereas Leiderer *et al.* [134] hypothesized that the light-induced decomposition of H_2O generates the formation of protons (H^+) and metastable oxygen radicals, leading to the stabilization of W^{5+} ions and thereby causing photochromism. Indeed, the protons and optically excited electrons lead to the formation of colored tungsten bronze HWO_3 species. Bechinger *et al.* [135] noted that the manifestation of blue coloration in WO_3 films stemmed from the systematically increasing H content when protons were used as injected ions. In addition, Sun *et al.* [136] suggested that structural defects,

Chapter I: State-of-the-art and objectives

such as localized impurities and dislocations, played important roles in the photochromic behavior of WO_3 . Even if most of the time, the photochromic model involves the creation of hydrogen tungsten bronze $H_x\text{WO}_3$ through bandgap irradiation due to the oxidation of the hydrogen of gaseous atmospheric water under UV excitation, it can be also proposed that the holes created in the valence band during the band transfer under UV irradiation are allowing surface oxygen “exfoliation”. Whatever, these mechanisms lead to the creation of supernumerary W^{5+} ions. The increase of the W^{5+} ion concentration is then associated with an increase of the F-centres and/or IVTC band (polaron band) intensity.

Considering that F-like color centers are predominant (quite local defects); these F-centre states are usually located below the conduction band by an amount greater than kT , which accounts for the inefficient photo-bleaching of the color centers at room temperature [137]. In an oxidizing atmosphere, the color centers are bleached due to the direct annihilation of trapped electrons in the ground state by the oxidants [137].

Considering delocalized defects (the model focuses on either an intervalence charge transfer (IVCT) or a closely related mechanism based on small polaron absorption) the reversibility of the mechanism is based on the relationship between optical modulation and the simultaneous insertion and extraction of ions and electrons under UV irradiation.

Despite the enormous number of studies discussing the mechanism of photochromism, this process is not fully understood yet. In addition, photochromism in nanocrystalline WO_3 films, or WO_3 -based organic or inorganic composites, has not been thoroughly studied. The recent developments regarding WO_3 -based inorganic compounds and their improved photochromism mechanism are discussed in detail below.

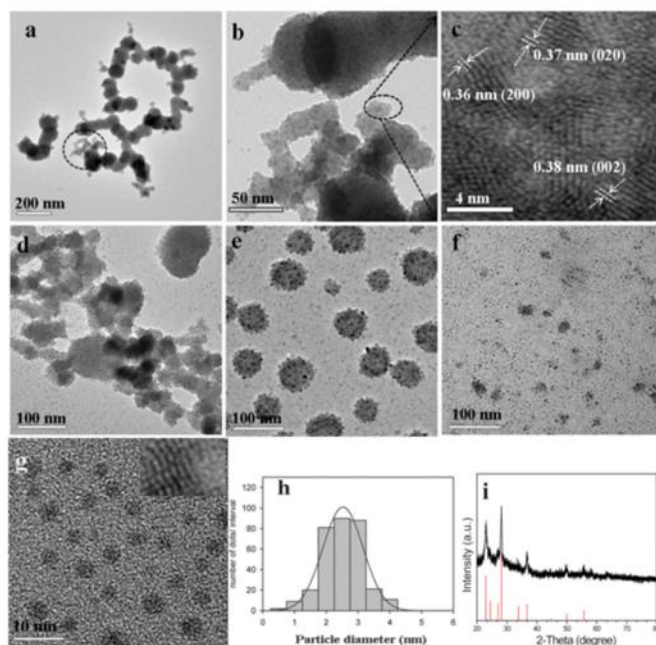
3.3.2 Morphological modification

Modifying the morphology of pure WO_3 such as quantum dots, nanosheets, nanoflakes, hollow spheres, and microflowers can improve their photochromic properties [32]. For instance, WO_3 quantum dots exhibit a blue shift of absorption peaks due to the quantum size effect, and ultrafine WO_3 quantum dots have extensive surface reactive sites, enhancing their photochromic activity [138], [140]. Nanosheets and nanoflakes have large surface areas that promote short ionic diffusion lengths for surface-attached species, leading to better photochromic properties [141], [142].

A typical example of the size effect is WO_3 quantum dots (QDs). In 2015, Wang *et al.* [143] created WO_3 QDs using a microwave-assisted method and observed their structural evolution over time. Initially, chain-shaped structures composed of WO_3 nanoparticles formed, which eventually transformed into spherical structures and then ultrafine nanoparticles as shown in Figure 24.a. When the reaction time extended to 20 min, sphere-shaped structures formed (Figure 24.e). Upon further extending the reaction time to 30 min, the spherical structures began to dissolve in the reaction system with the formation of ultrafine nanoparticles as shown in Figure 24.f. Well-crystallized ultrafine WO_3

Chapter I: State-of-the-art and objectives

nanoparticles were formed, after 40 min of microwave reaction (Figure 24.g). As shown in Figure 24.h, the as-obtained WO₃ QDs were ultrafine, with an average size of about 2.5 nm. Such ultrafine WO₃ QDs exhibited significant thermal/photonic stabilities, which is favorable for their photochromic properties. The resulting ultrafine WO₃ QDs were found to be highly stable and exhibited fast photochromic properties, turning blue after just 10 seconds of solar-light irradiation. Such enhanced photochromic properties were predominantly attributed to the sufficiently extensive surface reactive sites of the ultrafine WO₃ QDs, which were favorable for photochromic activity.



Chpt.I-Figure 24: TEM images of WO₃ samples during the formation process of as-prepared WO₃ QDs under microwave reaction at 160 °C for different periods: 10 min (a–c), 15 min (d), 20 min (e), 30 min (f), and 40 min (g), the particle size distribution (h) and XRD spectrum (i) of WO₃ QDs [143].

Sheet-like nanostructures are another type of structure that can affect the photochromic properties of WO₃. These nanosheets have a thin-layer morphology that provides a large surface area and a short distance for ions to travel on the surface. This makes them suitable for creating high-performance photochromic devices. In 2014, a team of researchers led by Miyauchi *et al.* [144] developed a special device that changes color in response to electric currents. They used a film of layered cesium tungstate (Cs₄W₁₁O₃₆²⁻) nanosheets, which were transparent in the visible-light range due to the quantum confinement effect. Cs₄W₁₁O₃₆²⁻ nanosheets coated on an Al substrate exhibited a rapid, reversible color change. When the nanosheets were exposed to an acidic solution, they quickly turned blue, and when exposed to air, they returned to their original color. The nanosheet structure allowed for the efficient transfer of electrons, resulting in a faster color change compared to traditional WO₃ particles.

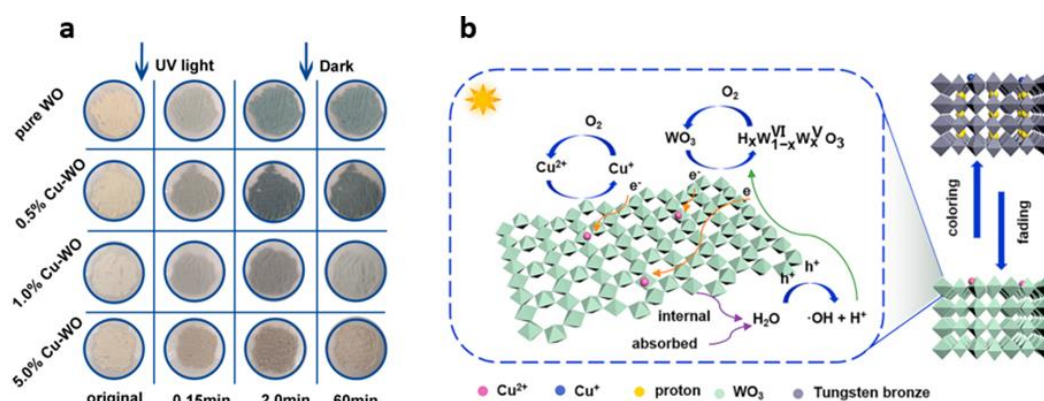
Chapter I: State-of-the-art and objectives

However, the improvement is limited by the intrinsic bandgap of around 3.0 eV. Therefore, researchers have explored other strategies, such as elemental doping and constructing WO₃-based composites to further enhance their photochromic properties.

3.3.3 Doping

Since WO₃ is an n-type wide-bandgap semiconductor, its photochromic transition from yellow to blue is achieved under UV irradiation below 370 nm. Doping with typical elements, such as Al, Cu, Mo, Zn, and Co, has been confirmed to be a feasible method for decreasing the bandgap of WO₃ via the introduction of a transition band between the CB and VB.

Recently (2021), Dong *et al.* [145] conducted a detailed study on the effect of Cu doping on the photochromic properties of WO₃. In their work, Cu@h-WO₃/WO₃·nH₂O hierarchical microsphere composites were fabricated using a hydrothermal method and modulated by modifying the doping amount of Cu. Figure 25 shows the color changes of the products during photochromism and self-bleaching. Pure WO changed from light yellow to light cyan after UV irradiation for 2.0 min, maintaining this color for at least 60 min. The self-bleaching process was greatly accelerated upon increasing the Cu doping concentration, and a return to the original color could be achieved within 60 min by simply keeping the materials in the dark, without the need for additional treatment. As shown in Figure 25.b, the photogenerated electrons excited from the h-WO₃ VB after UV irradiation were partly trapped by Cu²⁺ cations during their migration to the WO₃ surface, caused by interfacial charge transfer (IFCT), resulting in the efficient separation of photo-induced electron-hole pairs. W⁶⁺ and Cu²⁺ were reduced to W⁵⁺, Cu⁺, and Cu⁰, respectively. The generated protons were subsequently inserted into the lattice along the open channels and then interacted with the elongated W–O chains to form hydrogen tungsten bronze (H_xW^{VI}_{1-x}W^V_xO₃).



Chpt.I-Figure 25: (a) Photos of samples after photochromism and self-bleaching; (b) Schematic diagram of the photochromic mechanism in Cu@h-WO₃/WO₃·nH₂O hierarchical microspheres [145].

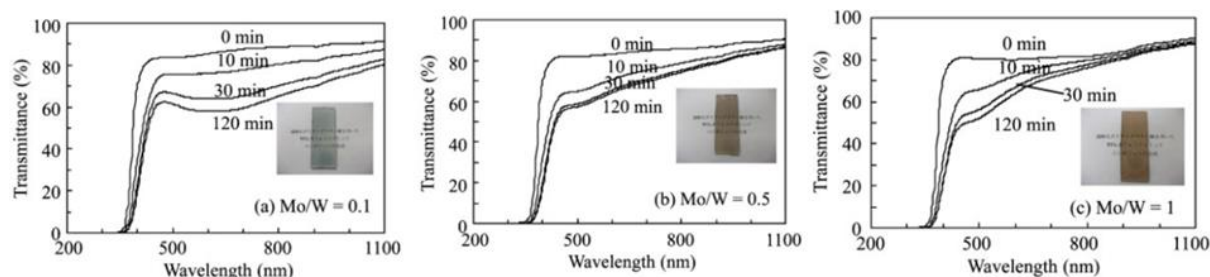
The effect of Mo doping on the photochromic behavior of WO₃-based composite films was studied by Miyazaki *et al.*, who fabricated composite films using a transparent urethane resin matrix [146]. Figure 26 shows the transmittance spectra of the composite films obtained before and after ultraviolet–visible (UV–Vis) light irradiation, where the absorption peak positions can be observed to

Chapter I: State-of-the-art and objectives

shift to lower wavelengths (blue shift) with an increase in the Mo/W ratio. In addition, the reaction rate constants of the Mo-doped films were larger than those of the non-doped films, confirming the enhanced photochromic reversibility of the former.

Avellaneda *et al.* investigated the influence of Nb, Ta, Ti, and Zr doping on the photochromic properties of doped-WO₃ films prepared *via* dip coating on a glass substrate [147]. The differences between the colored and photo-bleached state responses for the doped and undoped WO₃ films were measured in the wavelength range of 300–2100 nm at various temperatures: 25, 100, 120, and 150 °C. The best photochromic response was reported for the WO₃: Zr films, for which $\Delta T = 59.35\%$ (435 nm, at 100 °C).

The photochromic behavior was highly improved by Al³⁺ doping, as reported by Shen *et al.* [148]. Al-doped WO₃ powder with significantly enhanced structural, morphological, and photochromic properties was successfully synthesized using a hydrothermal route at low temperatures. Moreover, the color contrast (ΔC) of all WO₃ samples was calculated before and after UV irradiation (365 nm, 5 min), where the photochromic activity of the Al-doped WO₃ samples was revealed to increase along with the increasing Al³⁺ doping concentration, reaching a maximum at a molar concentration of 0.25%, beyond which photo-activity began to decrease. This behavior was attributed to the escalating recombination of electron/hole pairs as the concentration of local defects became too high.



Chpt.I-Figure 26: Transmittance spectra of composite films with various Mo/W ratios before and after UV-vis light irradiation. Inset photographs in respective graphs show the films after 120 min of UV-vis irradiation [146].

3.3.4 WO₃- Schottky barriers at inorganic composite interfaces

Another way to enhance the photochromic properties of WO₃ is through semiconductor coupling, particularly with transition metal oxides (TMOs). This is a useful approach as it can facilitate the separation of the photo-generated electron and hole pairs by having different positions for their valence and conductor bands. This helps to prevent the recombination of electrons and holes, thereby improving the overall efficiency of the photochromic process. The preceding part clearly established that most inorganic photochromic compounds are based on the photoreduction of the metallic element in wide-bandgap semiconductors, such as MoO₃, WO₃, TiO₂, V₂O₅, or Nb₂O₅. Despite the unique properties and contribution of WO₃ (in terms of its synthetic methods history, crystallite size, oxygen/tungsten stoichiometry, *etc.*) having been extensively discussed, the mechanisms governing the photochromic effect in such transition metal oxides are not yet fully understood and remain subject of

Chapter I: State-of-the-art and objectives

interest. However, it is widely accepted that photochromism is induced by irradiation at specific wavelengths, which allow electron transfer across the semiconductor forbidden bandgap, where electrons from the VB have enough energy to be excited to the CB, thus creating exciton pairs. In pristine transition metal oxides, charge depletion can then occur when atmospheric water is “oxidized” by the VB holes [149]. Protons can thus be integrated into the crystal structure (bronze creation) and trap the remaining unpaired electrons, leading to the reduced metallic species W^{5+} in WO_3 , Mo^{5+} in MoO_3 , V^{4+} in V_2O_5 , *etc.* In general, the blue color results from the intervalence charge transfer (IVCT) typically occurring between the $TMO^{(n-1)+}$ defects and TMO^{n+} species, which produces absorption on the border between the visible and near-infrared parts of the spectrum.

Two recent reviews by Wang *et al.* and He *et al.* have demonstrated the benefits of establishing a Schottky interface with a second compound in WO_3 -based photochromic materials [150], [151]. Their works again highlighted the strongest limitation of WO_3 photochromic materials, namely, their negligible reversibility, or ability to recover the photobleached state only *via* oxidative treatments. Thus, these reviews have verified that the photochromic efficiency of inorganic oxides can be effectively enhanced when combining them with other organic or inorganic materials. This discovery has led to the creation of solid-solid interfaces, which can be described as Schottky barriers. A substantial improvement in the charge depletion rate can be realized in such interfaces (*i.e.*, spatial separation of the holes and electrons created by irradiation), thus promoting the photo redox reactions occurring at the start of photochromism. The most interesting aspect is that charge depletion is not associated with chemical TMO transformation and the introduction of protons, therefore allowing for the reversibility of the photochromic phenomenon (*i.e.*, self-reversibility without the use of heat treatment or an oxidative atmosphere). In view of these discoveries, numerous novel composite or mixed oxide materials with improved multicolor and reversible photochromism performance, visible-light coloration properties, and fast photo response have been prepared during the last two decades.

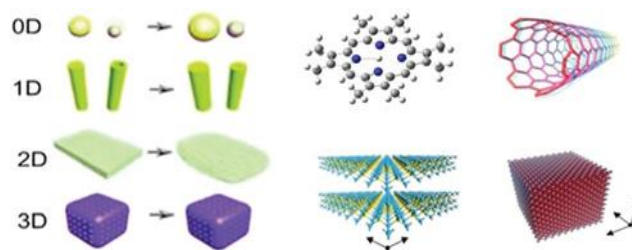
Numerous studies have confirmed that using a photochromic TMO (such as MoO_3) alone does not yield satisfying photochromic contrast, whereas its combination with gold or platinum nanoparticles, and the subsequent formation of Schottky barriers, leads to a drastic improvement in the overall photochromic performance [152], [154]. This effect can be evidenced in the solar transmittance contrast between thin composite films in their photobleached and colored states, as well as the extension of their light response from UV radiation to visible sunlight. The enhancement in the visible-light photochromism of MoO_3/Au or MoO_3/Pt thin-films can be explained by the electrons captured by Au and Pt, which results in a longer electron-hole pair separation time, analogous to the photocatalytic enhancement effect when Pt or Au metals are deposited on inorganic semiconductor surfaces [155], [156].

3.4 WO_3 into hybrid devices and compounds

Tungsten oxide (WO_3) can exist in different dimensions when combined with other materials. The possibility to combine WO_3 within crystallographic structures in various scales gives rise to new and

Chapter I: State-of-the-art and objectives

innovative applications. In this section, we will discuss the recent advances in the topic of tungsten oxide hybrid materials and devices at different scales including: 0D, 1D, 2D, and 3D for X-chromic applications, as shown in Figure 32.



Chpt.I-Figure 32: Schematic illustration of the design of WO_{3-x}/WO_3 nanostructures with different shapes/dimensions. 0D nanoparticles, 1D nanowires and nanotubes, 2D thin layers and 3D porous nanostructure.

3.4.1 0D WO_3 colloidal suspensions (quantum dots and dispersed NPs)

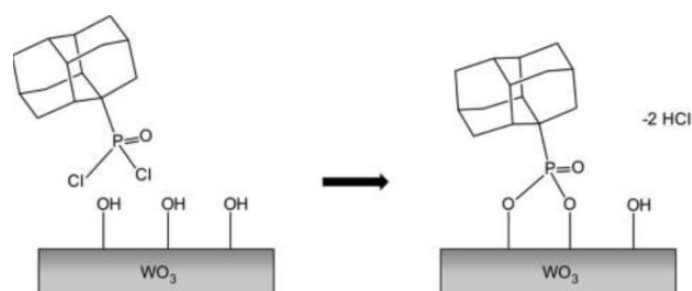
Zero-dimensional (0D) materials define as a material with three dimensions in the nanometric scale (0–100 nm). The 0D materials have a significant proportion of surface atoms which increase their surface density of states. For these types of NPs, certain quantum effects (e.g., quantum size effect, quantum limitation effect, quantum tunneling effect, quantum interference effect, etc.) can be generated as a result of the size effect. Nano-structured WO_3 can exhibit improved properties and new features that the bulk WO_3 can not have, owing to the increased surface-to-volume ratio which alters the quantum phenomenon [138]. Recently, many researchers have investigated the synthesis of nanostructured WO_3 in various shapes, such as quantum dots, nanoflakes, nanofibers, nanotubes, nanorods and nanosheets [49], [52].

A nano-colloidal dispersion is a uniformly mixed solution of two phases, maintained stable by the continuous random motion of particles, known as Brownian motion. The dispersed phase of the solution typically ranges in size from 1 nm to 1 μ m. In certain cases, stabilizing agents such as surfactants may be used to ensure the stability of a colloidal dispersion. Generally, in liquid phase preparation methods, the degree of dispersion of the nanostructured WO_3 in the colloidal suspension is an important factor to obtain the desired shape and size of the final NPs. To achieve this goal, many types of dispersants have been used to reach a well-defined homogeneity of the mother solution or by surface modification of the NPs.

Surface modification of metal oxides: Modifying inorganic surfaces of metal oxides with grafted organic molecules enables precise control over the properties of the surface/interface in various applications such as adhesion, corrosion, sensing, and optics [157]. Indeed, surface modification of nanoparticles can be employed to promote their solubility or compatibility with solvents or polymeric matrices facilitating their homogeneity in composite materials. This technique can also be utilized to prevent aggregation or promote self-assembly of nanoparticles [158]. Various types of molecules can be employed to modify oxide nanoparticles, which depend on the type of oxide being used.

Chapter I: State-of-the-art and objectives

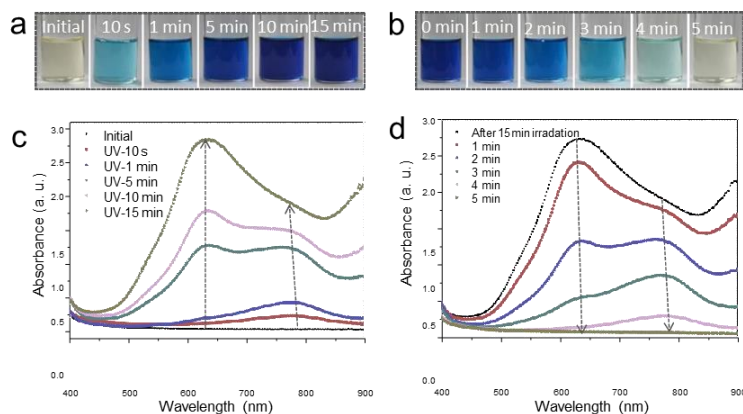
To modify oxide NPs, organ silanes and phosphonic acids are the most used coupling molecules. The surface and interface properties of metal oxide surfaces can be controlled and modified using organophosphorus acids, such as phosphonic acids and their derivatives. Li *et al.* [159] demonstrated the creation of a covalent attachment of phosphonic dichloride derivatized diamondoids to tungsten through a reaction between the phosphonic dichloride functional group on the diamondoids and the tungsten surface oxide. Tungsten surfaces were oxidized in oxygen plasma, yielding several nanometre-thick tungsten oxide layers terminated by hydroxyl groups. Then, they immersed the WO_3 in a toluene solution of the prepared solution for 2 days to ensure complete coating. Condensation between phosphonic dichloride and the metal oxide surface hydroxyl eliminates HCl and forms covalent bonds between the phosphonate and the substrate as shown in Figure 33



Chpt.I-Figure 33: Proposed Reaction for the surface modification [159].

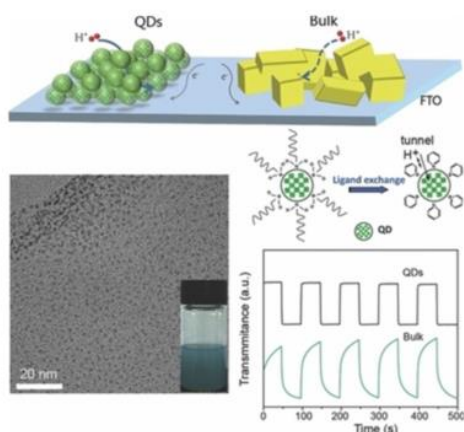
Also, several studies have examined various types of dispersant including organic (polymeric) and inorganic ones. Liu *et al.* [160] fabricated (WO_{3-x} QDs) by the hydrothermal treatment of ammonium tungstate hydrate in the presence of polyvinyl pyrrolidone (PVP) as a dispersant agent. The use of PVP made the obtained WO_{3-x} QDs well dispersed in water, which confirmed that the addition of PVP could improve the stability of the products. As shown in Figure 34.a,b the dispersion of WO_{3-x} QDs is transparent, pale yellow and exhibits excellent stability and solubility in water and the aggregates have not been found after standing for several weeks. They also investigated the photochromic behavior as shown in Figure 34.c,d, which proved the rapid coloration process from the original color to deep blue under the irradiation of a UV lamp with a power of 25 W, and the corresponding UV/Vis absorption. Apparently, the initial sample showed no absorption peak in the Vis-NIR region. Subsequently, the intensity of these absorption bands gradually increased and underwent a slight blue shift during the different irradiation times.

Chapter I: State-of-the-art and objectives



Chpt.I-Figure 34: Photograph (a) and UV/Vis-NIR absorbance spectra (c) of the WO_{3-x} QDs suspensions at different duration of UV lamp (25 W) irradiation. Photograph (b) and UV/Vis-NIR absorbance spectra (d) of the WO_{3-x} QDs suspensions storage in the dark for different times [160].

In the study of Cong *et al.* [161], they investigated the synthesis of 3 nm tungsten oxide quantum dots for electrochromic supercapacitors by hydrothermal method (as shown in Figure 35). The researchers found that compared to bulk tungsten oxide, the quantum dot tungsten oxides exhibited a wider forbidden band and accelerated Faraday electrochemical process, thereby displaying excellent electrochemical and electrochromic behavior. One of the key challenges addressed in the paper was to ensure the dispersion stability of the quantum dots, which was achieved by wrapping them in an octane diamine ligand and modifying their surface with a conductive pyridine ligand. The final supercapacitor device exhibited a fading time of 1 s and a coloring efficiency of $154 \text{ cm}^2/\text{C}$. Notably, hydrothermal synthesis of tungsten oxide quantum dots is known to be challenging due to the tendency of the material to agglomerate into clusters or lumps during the process.



Chpt.I-Figure 35: Comparison of bulk (green) and quantum dot (black) tungsten materials [161].

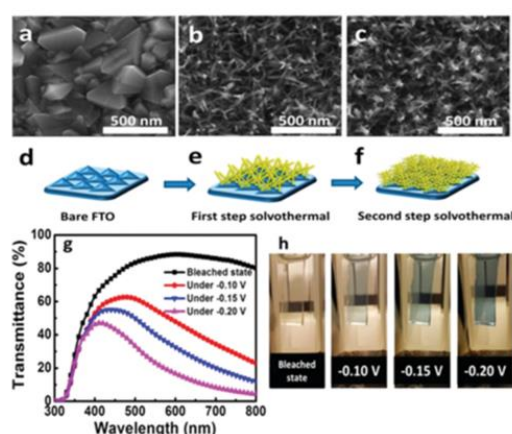
3.4.2 2D Thin films (toward smart windows)

The 2D morphology has many advantages including the large specific surface area, increased number of active sites and confined thickness, making these structures a promising candidate for gas sensing,

Chapter I: State-of-the-art and objectives

catalytic applications and electronic or photonic devices. Various techniques for film preparation can result in differences in band gaps, compositions, and microstructures, leading to variations in photochromic performance [162], [163]. Solution-based methods, such as sol-gel, hydrothermal, and lower-temperature solution methods, have been more widely utilized compared to vapor-based methods (such as CVD) [106]. Solution-based methods are preferred due to their feasibility, which offers mild reaction conditions, adjustable morphologies, and lower costs. One way to fabricate a thin film of WO_3 is to deposit it directly on a glass substrate.

Chu *et al.* [164] synthesized nanoplates on FTO glass using a seed layer and a surfactant-free hydrothermal method. The resulting 2D nanostructure showed promise for practical applications in smart windows due to its fast-switching speeds of 12 s and 3 s for coloration and bleaching, respectively. Mathuri *et al.* [165] also utilized an FTO glass substrate and synthesized WO_3 nanoplates with varying hydrothermal reaction times (8-16 hours) and temperatures (120-180 °C), resulting in hexagonal and monoclinic WO_3 nanoplates. The deposited WO_3 films possessed diverse surface morphologies, such as buds-like, bricks-like, sheets, and platelets-like structures, depending on the reaction temperature and time. The optical bandgap of the deposited WO_3 films ranged from 2.5-2.9 eV and 2.6-2.75 eV, respectively. Li *et al.* [166] developed hierarchical nano tree-like WO_3 architectures on FTO via seed-mediated growth, as depicted in Figure 36.a-f. H_2WO_4 , $\text{SC}(\text{NH}_2)_2$, $\text{C}_4\text{H}_4\text{O}_4$, aqueous HCl, and FTO glass were used to form a WO_3 seed layer, which was then placed in an autoclave with the same precursors to grow the WO_3 nano trees architecture. The optical modulation of the nanotrees was found to be 74.7% at 630 nm at a potential of 0.2 V, as shown in Figure 36.g. The coloration efficiency was measured to be $75.35 \text{ cm}^2 \text{ C}^{-1}$ with fast switching responses of 2.64/7.28 s, as depicted in Figure 36.h. The large surface area of the WO_3 nano trees led to their excellent electrochemical and EC properties, indicating their potential application in EC smart windows.

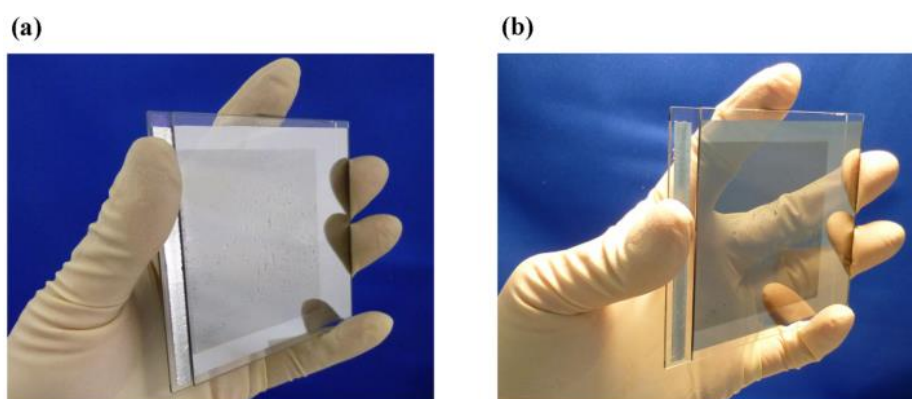


Chpt.I-Figure 36: (a–c) SEM images of WO_3 nanowires and nanotree grown on FTO and (d–f) corresponding schematic illustrations, respectively. (g) UV-vis spectra of WO_3 nanotrees at various potential and photographs of its color change [166].

Chapter I: State-of-the-art and objectives

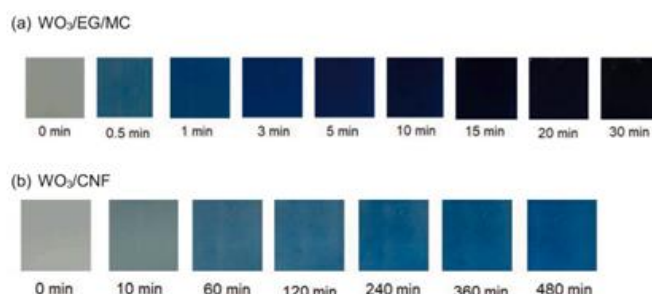
Recently, a group led by K. Tajima in Japan has developed a smart window system in which an electrochromic material is able to transform from transparent to reflective for controlling radiative heating [167].

Their solid-state device consisted of a layered structure of glass/ITO/Mg₄Ni/Pt/PEI/WO₃/ITO/glass, where ITO serves as a transparent conducting electrode; Mg₄Ni/Pt absorbs and desorbs hydrogen to transition from transparent to reflecting; PEI serves as a hydrogen electrolyte; and WO₃ takes in hydrogen to be stored when it is not infiltrating the Mg₄Ni. Figure 37 shows photographs of the switchable mirror which contained the adhesive electrolyte layer. The device could be switched between the reflective Figure 37.a and the transparent state (Figure 37.b) by applying a voltage.



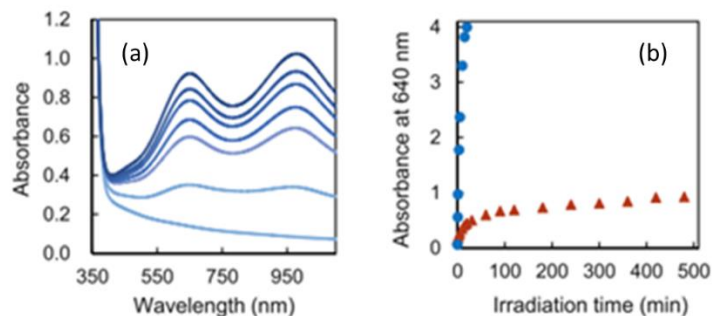
Chpt.I-Figure 37: Photograph of the adhesive electrolyte mirror in the (a) reflective state and (b) transparent state [167].

Recently in 2020, the Yamazaki group also studied the impact on photochromism of WO₃/cellulose-based materials with different derivatives: methyl cellulose (MC), hydroxyethyl cellulose, carboxymethyl cellulose (CMC) and cellulose nanofiber (CNF) [168]. Their latest results indicated that Gly is the best dispersant to prepare excellent photochromic films with a high coloring rate, however, the WO₃/Gly/MC film being unstable on a high humid day, they used EG as a second-best agent. The coloration rate of the WO₃/EG/MC film was much faster than that of the WO₃/CNF film as shown in Figure 38-39. This fact is attributable to the fast H⁺ diffusion through hydrogen bonding in the WO₃/EG/MC film.



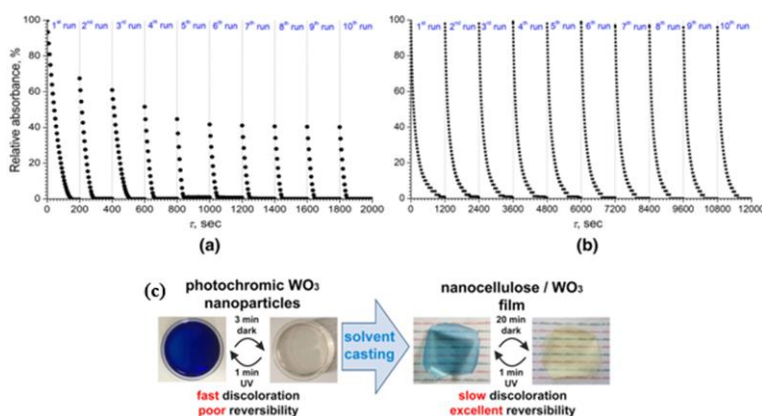
Chpt.I-Figure 38: Color change of the (a) WO₃/EG/MC and (b) WO₃/CNF films under UV irradiation [168].

Chapter I: State-of-the-art and objectives



Chpt.I-Figure 39: (a) the absorption spectra of each film and (b) time course of the absorbance at 640 nm of $WO_3/EG/MC$ films in red dots and WO_3/CNF films in blue dots [168].

Flexible WO_3 -containing composite films cellulose made from nanocellulose remain completely unexplored and this triggered the interest to be investigated by Evdokimova *et al.* [169] where they produced reversible photochromic hybrid films of nanocrystalline cellulose (CNC) as a matrix and tungsten oxide as a photochromic component (CNC/WO_3) via a simple and quick solvent casting method. The photochromic proprieties were tested by UV-irradiation (6 W UV lamp) and the bleaching of the film occurred upon its storage in the dark. Pure WO_3 sol demonstrated very poor reversibility in the coloration/bleaching process. As can be seen from Figure 40, the reversibility of the WO_3 sol coloration significantly collapsed after 5 cycles. In opposite, CNC/WO_3 film performed good reversibility of color switching without any notable loss of efficiency after 10 cycles. Thus, introducing WO_3 nanoparticles into the biopolymer matrix allowed stabilization and extension of the photochromic coloration reversibility.



Chpt.I-Figure 40: The changes in the relative intensity of the absorption peak (624 nm) of UV-irradiated: (a) WO_3 sol; (b) CNC/WO_3 film. (c) Comparison of the photochromic proprieties of pure WO_3 and CNC/WO_3 film [169].

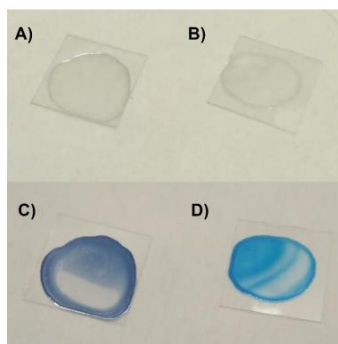
3.4.2.1 WO_3 – Vinyl derivatives

Many vinyl polymer matrixes such as (polyvinyl alcohol) (PVA) and polyvinyl pyrrolidone (PVP) play an important role in the enhancement of the photochromism of WO_3 where they act as good proton donors and achieve fast diffusion of the liberated proton via hydrogen bonding [170].

Chapter I: State-of-the-art and objectives

WO₃-vinyl polymers-based composites have been studied by several groups. In 2012, Songara *et al.* [171] reported the preparation of hydrated tungsten oxide nanoparticles using a simple wet chemical method while varying the concentration of HCl. The gradual change in the crystal structure of hydrated WO₃ from hexagonal (WO₃·0.33H₂O) to pure orthorhombic (WO₃·H₂O) had been demonstrated by XRD studies as a result of variation in HCl concentration from 1 M to 6 M in the reaction conditions. The effect of the crystal phase variations on the photochromic behavior of these materials had been studied by making films of these materials in a PVA matrix and then exposing them to UV light of 315 lx intensity for 5 min. Interestingly, it was observed that as the phase vary from pure hexagonal (WO₃·0.33H₂O) to mixed phase of hexagonal and orthorhombic the photochromic color change of the films varied from blue to green, whereas no color change was observed for film purely orthorhombic (WO₃·H₂O).

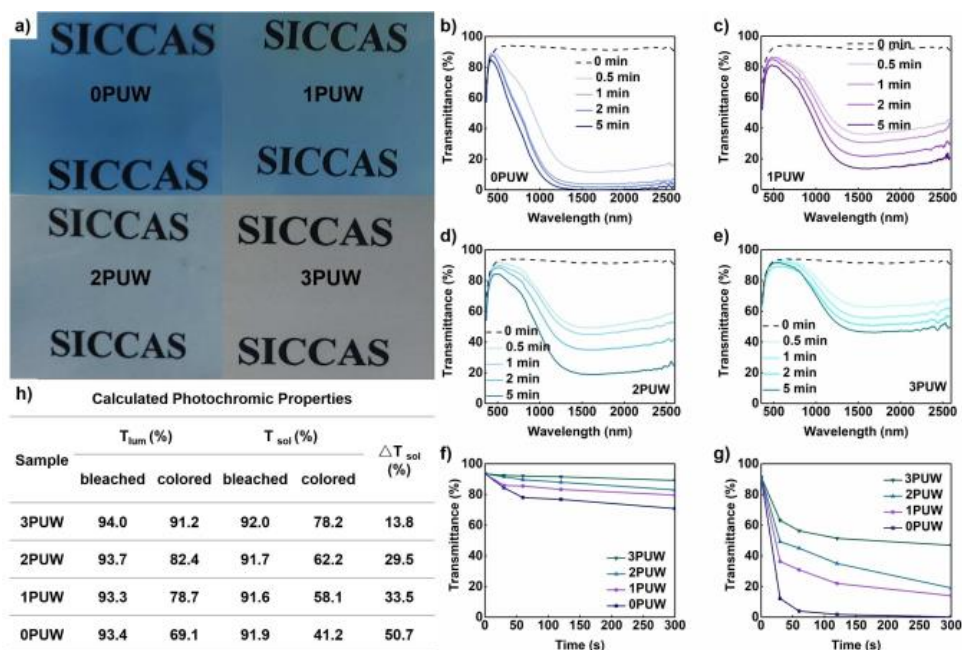
The cation effect on the structure and photochromic properties of the WO₃@PVP aqueous sols were investigated by Kozlov *et al.* [172], where they found that WO₃@PVP (polyvinylpyrrolidone) photochromic aqueous sols could only be prepared by slightly acidifying sodium tungstate solutions while acidifying of ammonium metatungstate solutions resulted in nonphotochromic sols. Also, they noticed that the existence of sodium cations in WO₃@PVP materials favored the formation of reduced tungsten species (W⁺⁵) upon UV irradiation which enhanced the photochromic and photocatalytic properties as shown in Figure 41. This effect was attributed to the formation of stable Na-tungsten bronzes.



Chpt.I-Figure 41: Appearance of dried (A,C) NH₂ and (B,D) Na₂ sols (A,B) before and (B,D) after UV irradiation [172].

Li *et al.* [173] investigated the photochromic behavior of WO₃ nanoparticles dispersed in different films of mixed PU and PVP with different proportions. Figure 42. shows the different kinds of foils with different degrees of blue color after the application of UV light. Figure 42 (b-e) shows the coloration-changing spectra of WO₃-based photochromic foils. Figure 42 (f-g) shows the changes at $\lambda = 550$ and 1500 nm, respectively, which illustrate that the composite foils had an obvious absorption in the infrared region compared to the visible region. Its coloration time was less than 5 min, and the discoloration time was about 3 hours at room temperature or 1 hour at 60 °C, as shown in Table 28 (h).

Chapter I: State-of-the-art and objectives



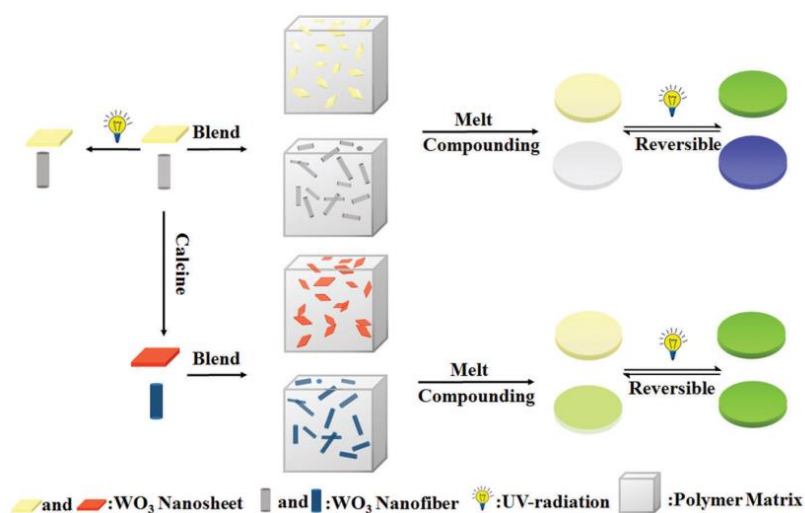
Chpt.I-Figure 42: a) Photos of the as-prepared WO_3 -based composite foils after irradiating for 5 min under UV light. b-e) Variation in transmittance spectra of the WO_3 -based composite foils with different irradiation times. f-g) Changes of transmittance at $\lambda = 550$ and 1500 nm, respectively. c-d) Changes of transmittance at $\lambda = 1500$ nm at $60^\circ C$ and room temperature in oven atmosphere, respectively. k-l) Cycling property of 2PUW sample which irradiation of 5 min and bleach of 60 min ($\lambda = 1500$ nm). h) Calculated solar transmittance, calculated modulation efficiency and calculated luminous transmittance [173].

3.4.2.2 WO_3 - Thermoplastic polymer

WO_3 has poor mechanical performances and is complicated to process which limits its utilization in the bulk state under harsh conditions. The solution to minimize these issues is fabricating WO_3 -polymeric hybrid composites. Even though many previous studies in the literature have discussed this topic, the combination of WO_3 and engineering plastics is far less reported, and the structure/property relationship in these inorganic/polymeric systems remains unclear [174].

Zhang *et al.* [175] have successfully prepared a series of photochromic hybrid thermoplastics by blending different weight percentages and types of WO_3 compounds with an acrylic random copolymer P (MMA-co-BA) as shown in Figure 43. The nanorod morphology was found to effectively reinforce the WO_3 /P (MMA-co-BA) composites, while the WO_3 nanosheets tended to deteriorate the mechanical performance. The photochromic behavior of the products could be tuned by the morphology and loading level of WO_3 in the composites, but the surface polarity did not play a critical role here. Faster bleaching was observed for the composites with WO_3 nanosheets which were attributed to the larger unit volume of single nanosheets or clusters concentrating at the localized regions in the composites. In contrast, the nanorods with a smaller unit volume and better dispersion in the entire composite would lower the “effective” WO_3 concentrations.

Chapter I: State-of-the-art and objectives

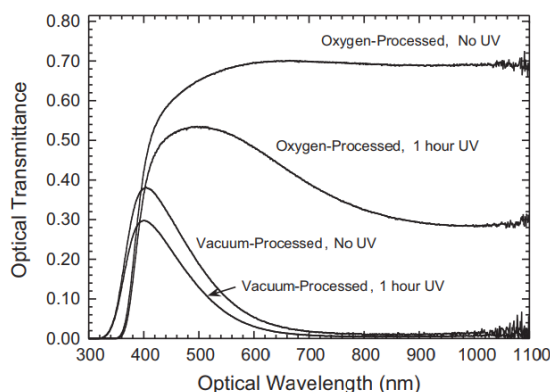


Chpt.I-Figure 43: Schematic illustration of the fabrication of hybrid photochromic thermoplastics. WO₃ crystals and polymers [87].

The use of nanocrystal WO₃ as a pigment for polycarbonate (PC) reinforcement is investigated by Sangpraserdsuk *et al.* [176]. The authors prepared the WO₃ powder and mixed it with polymer resin, using a solution-based process. Another modified tungsten trioxide particles by silane treatment were also explored and mixed with PC. The PC/WO₃ films behaved as both the NIR absorptive and NIR reflective materials, depending on the illumination conditions. Before exposure to sunlight, the films were capable of reflecting NIR waves. In turn, after exposure to sunlight, the NIR absorbance of the materials obviously increased. By using the silane-modified WO₃ as a pigment, the photochromic properties of the PC composite films were enhanced, i.e., the color contrast was increased whereas the bleaching time was decreased. The percentage of NIR absorbance of the PC composites, after exposure to sunlight, was also increased. The improvement has attributed to the presence of the silane coupling agent on the surface of WO₃ which promoted more oxidation of the intercalated metal oxide and led to an accelerated bleaching process.

Oxygen engineering of fluorinated ethylene propylene (FEP), and tungsten-oxide nanocomposite films was reported by DeJournett *et al.* [177]. They investigated the effect of oxygen on photochromic properties. The synthesis process was based on chemical vapor by introducing the tungsten carbonyl precursor species for deposition into the polymer via vapor phase diffusion which allowed for particles formation throughout the bulk of the polymer. Adding oxygen to the synthesis process resulted in increased optical transmission, as confirmed in Figure 44, where the related transmission spectra for the WO₃/FEP composite processed with oxygen indicates that the transparency of the material was greatly increased in the visible while retaining its photochromic response.

Chapter I: State-of-the-art and objectives



Chpt.I-Figure 44: Optical transmission spectra for an oxygen-processed, tungsten-oxide, polymer matrix nanocomposite before and after 1 h exposure to ultraviolet light. Also shown are the absorption spectra before and after exposure to ultraviolet light for material processed in a vacuum without an oxygen background [177].

WO₃ is a promising filler for the improvement of radiation protective properties of polymers. It has recently been investigated by Cherkishina *et al.* [178], by adding WO₃ to the polyimide matrix. The samples were tested to show the effect of high-energy electrons with energies ranging from 0.5 to 5 MeV on a polyimide composite with tungsten-oxide filler using electron-beam irradiation. The polymer composite exhibited high resistance to a flux of high-energy electrons incident at angles of $\phi = 0^\circ$ (normal incidence) and 45° meaning that the composite can be used for protection against electron irradiation.

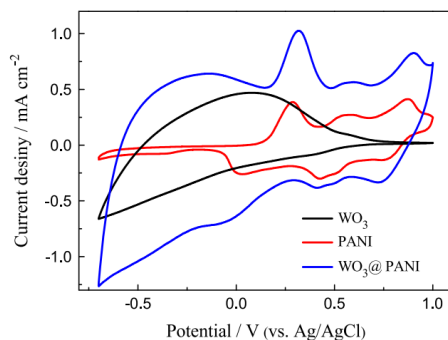
3.4.2.3 WO₃-Conducting Polymer Hybrids

WO₃ is one of the most promising inorganic electrochromic materials. However, WO₃ suffers from some limitations: single color change and slow switching speed. As a comparison, organic electrochromic materials (conducting polymers) possess many advantages such as multicolor, fast switching speed, flexibility, and easy-to-tune electrochromic properties through molecular tailoring [48], [124], [125]. Recently, extensive research has been conducted into the development of organic/inorganic hybrid films since they can benefit from both the advantages of conducting conjugated polymers and transition metal oxides. The electrochromism in conjugated polymers occurs through changes in the π -electronic character accompanied by reversible insertion and extraction of ions through the polymer films upon electrochemical oxidation and reduction.

Cai *et al.* [179] employed solvothermal and electropolymerization methods to fabricate WO₃/PANI (poly aniline) core/shell nanowire array. To compare the EC properties of the hybrid films with WO₃ and PANI, cyclic voltammetry (CV) and chronoamperometry were conducted in a three-compartment system containing 0.5 M H₂SO₄ as an electrolyte, Ag/AgCl as the reference electrode and Pt foil as the counter electrode. Figure 45 compared the CV curves of WO₃, PANI and WO₃/PANI films in the potential region from -0.7 to 1.0 V (vs. Ag/AgCl) at a scan rate of 20 mV s⁻¹. The CV curve of the WO₃/PANI nanowire array exhibited both characteristic peaks of WO₃ nanowire and PANI film and showed significantly high exchange current densities compared to the WO₃ and PANI film, which

Chapter I: State-of-the-art and objectives

confirmed the fact that proton insertion/extraction was facilitated. This improved electrochromic behavior was mainly attributed to the donor–acceptor interaction, and the porous space among the core/shell nanowires, which provided a large surface area for charge-transfer reactions. As the potential was rising from -0.7 V to 1.0 V, the WO₃/PANI core/shell nanowire array film showed multicolor electrochromism: from deep blue (-0.7 V) to light yellow (-0.2 V), and green (0.2 V), finally purple (1.0 V) as shown in the photographs of the WO₃/PANI sample in Figure 46.

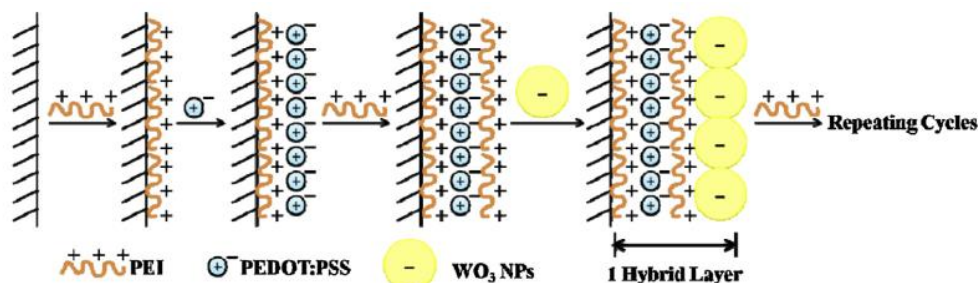


Chtp.I-Figure 45: The 10th CV curves of WO₃, PANI and WO₃/PANI films [179].



Chtp.I-Figure 46: Photographs of a WO₃/PANI core/shell nanowire array sample (2 * 4 cm² in size) under different applied potentials [179].

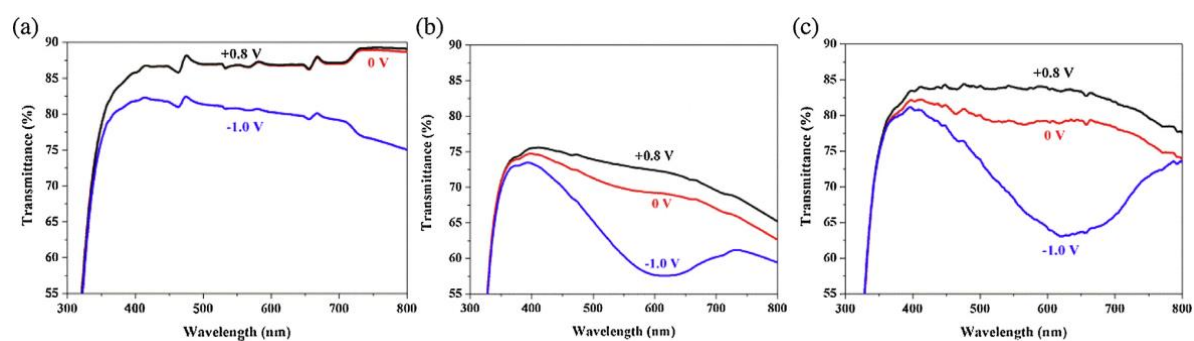
Ling *et al.* [180] used a layer-by-layer assembly method to design multilayer hybrid films based on (PEDOT: PSS) and tungsten oxide nanoparticles (WO₃ NPs). Polyethylenimine (PEI) is deposited in between to introduce electrostatic force between the components (as intermediate layers to attract the anionic species), as illustrated in Figure 47.



Chtp.I-Figure 47: Scheme for the formation of electrochromic multilayer hybrid film [PEI/PEDOT: PSS/WO₃-NPs] [180].

Chapter I: State-of-the-art and objectives

The EC properties of the hybrid films were compared with respect to PEDOT: PSS and WO₃-NP, and spectro-electrochemical characterization was conducted on 10-layer PEDOT: PSS, WO₃-NP films, and 5-layer hybrid films. The transmittance of WO₃-NPs, PEDOT: PSS and hybrid thin films were recorded at constant potentials of +0.8, 0, and -1.0 V, respectively. The optical transmittances against the wavelength of all three films are shown in Figure 48(a-c). With comparable thickness of each film, the optical contrast of the hybrid film (DT = 20%) is significantly higher than that of WO₃-NP (DT = 7.3%) and PEDOT: PSS (DT = 9.6%) films. Owing to the efficient charge transfer between the two active components and complementary electrical conductivity of the two components in the redox switching process, the coloration efficiency of the hybrid film is significantly improved to 117.7 cm²/C at a wavelength of 633 nm.



Chpt.I-Figure 48: UV-Vis's spectrum of 10 layers of (a) WO₃-NP, (b) PEDOT: PSS, and 5 layers of (c) Hybrid thin films under different potentials of +0.8, 0, and -1.0 V [180].

3.4.3 WO₃ in 1D fibers / 2D textiles

One of the most popular tungsten oxide nanostructures for usage in a variety of applications is one-dimensional (1D). Nanowires, nanorods, and nanotubes are examples of 1D nanostructures [181], [182]. The most common and easiest method of synthesis for these 1D tungsten oxide nanostructures is hydrothermal, followed by electrochemical, vapor deposition, and electrostatic spinning. When tungsten oxide is formed during the hydrothermal process, a guiding agent is used to surround the material, which directs the substance's growth in that direction [183]. Nanostructures with different aspect ratios can be produced by adjusting the temperature, time, and material ratio. 1D tungsten oxide nanostructures are desirable for a variety of applications, including catalysis, energy storage, and sensing [181]. 1D nanostructures' high surface-to-volume ratio boosts their reactivity while their 1D morphology allows for effective charge and mass transport. The nanostructures' aspect ratio can be precisely altered to modify their characteristics for certain purposes [182].

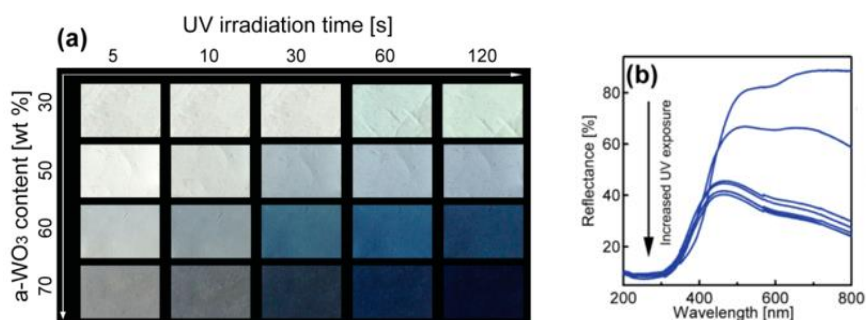
Reddy *et al.* [184] utilized a hydrothermal method to produce WO₃ fibers with lengths of 50–200 nm and widths of 20–60 nm, which were then electrophoretically deposited onto a conductive substrate. Au nanoparticles and PEDOP were coated on the surface of WO₃ to obtain PEDOP-Au@WO₃ composite electrodes. These hybrid electrodes were found to be effective replacements for expensive Pt-based counter-electrode solar cells. Additionally, the one-dimensional tungsten oxide material can

Chapter I: State-of-the-art and objectives

form a functional framework on a flexible substrate at low temperatures or even room temperature, making it an ideal material for flexible electrochromic device supercapacitors.

Recently, some hybrid WO_3 /polymer nanofibers have been prepared via electrospinning, while these electrospun nanofibers are all applied in the form of nonwoven fabric rather than continuous monofilament because of low mechanical strength.

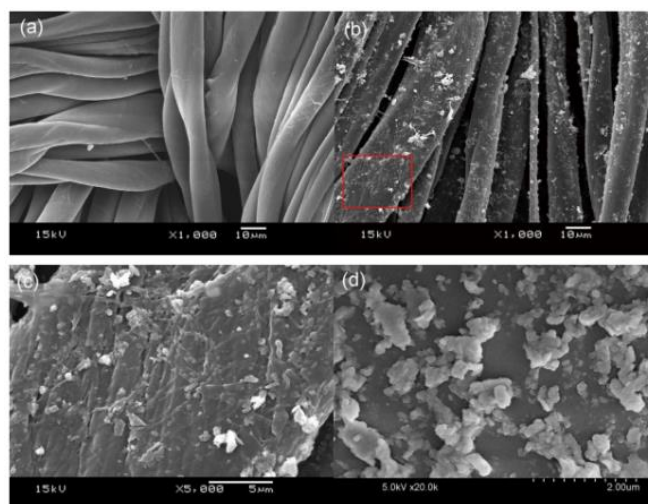
The feasibility to fabricate organic/inorganic fibrous membranes of amorphous WO_3 (a- WO_3) and polyvinylpyrrolidone (PVP) has been achieved by Wei *et al.* [185] via in situ solution phase reaction and nanofiber-electrospinning. The photochromic responses of the hybrid membranes were investigated using UV irradiation with a 5 W UV lamp over irradiation times. The photographs in Figure 49.a are showing the different states of the membranes as a function of UV irradiation time. The diffuse reflectance spectra of the hybrid membrane 70% WO_3 @PVP showed a notably decreased reflectance value with continuous UV irradiation and reached saturation within 2 min (Figure 49.b).



Chpt.I-Figure 49: (a) Photographs showing the photochromic behaviors of W1–W4 as a function of the UV illumination time. (b) Reflectance spectra showing the coloration of the membrane W4 upon UV illumination under ambient conditions, recorded at 15s intervals. (The relative ratios of the inorganic and organic components in the membranes were varied by changing the a- WO_3 contents from 30 wt% (W1), 50 wt% (W2), 60 wt% (W3) to 70 wt%(W4)) [185].

The integration of WO_3 into the polymer matrix was achieved also by the sol-gel method as proved in the work of Zhang *et al.* [186] where they treated the tungsten hexachloride and tri-block non-ionic polymer at 100 °C to prepare cellulose-based WO_3 nanocomposites and fibers. The surface morphologies of the samples are shown in Figure 50. The surface of the pristine fibers was smooth (Figure 50-a). Whereas according to Figure 50.b-d, it can be found that the sample surface can be well covered by the WO_3 nanoparticles. However, the WO_3 nanoparticles distribution on the fiber surface was not quite uniform at a microscopic level.

Chapter I: State-of-the-art and objectives



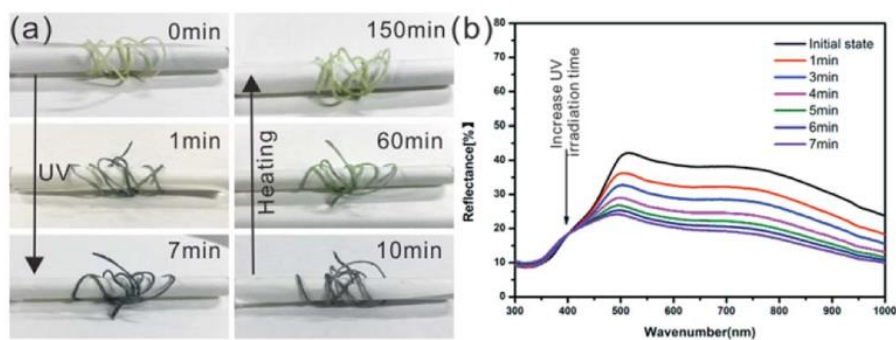
Chpt.I-Figure 50: SEM images of (a) pristine cellulose fibers, (b) low and (c) high magnification views of cellulose-based WO_3 nanocomposites; (d) FE-SEM image of cellulose-based WO_3 nanocomposites [80].

Although these nanocomposite fibers based on WO_3 have been thoroughly investigated and have been used as photochromic film devices, these researches are mainly focused on photochromic composite films, while the photochromic fibers based on WO_3 are rarely reported. The integration of tungsten oxide (WO_3) into microfibers is a relatively new area of research and development. While there has been a significant amount of research done on the synthesis and applications of WO_3 nanoparticles, the integration of WO_3 into microfibers is still a relatively unexplored field. One possible reason could be the difficulty in achieving uniform dispersion of WO_3 nanoparticles within the fibers [49]. Although it can be difficult to distribute nanoparticles uniformly throughout a fiber matrix, doing so is necessary to produce a final product with the desired characteristics. But as work on nanofibers and nanocomposites advances, it's possible that additional research will be done on the incorporation of WO_3 into microfibers and its potential uses. Its weak stability in basic and acidic conditions is another problem. Since WO_3 is known to be vulnerable to acid and base attack, losing its photochromic characteristics may happen. By integrating WO_3 into a protective matrix to increase their chemical stability, this issue can be solved. The photochromic qualities of WO_3 , which are influenced by environmental conditions including humidity and temperature, provide another difficulty when using WO_3 as a cladding or soaking dye on microfibers.

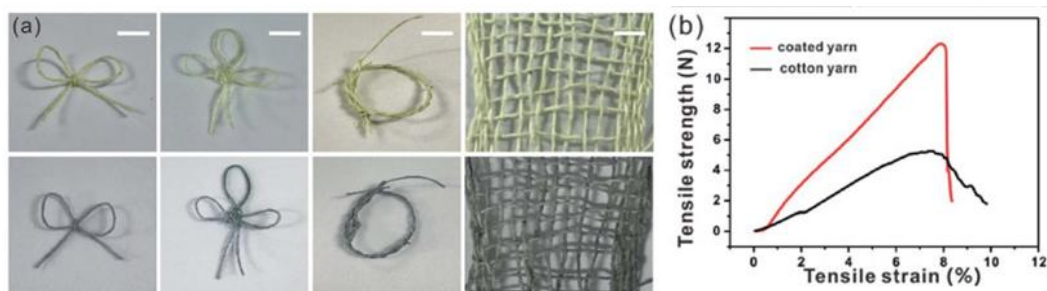
One of the latest reported articles concerning the continuous fabrication of photochromic fibers with an active cladding of WO_3 /PVA was reported by Ling *et al.* [187]. They prepared WO_3 nanorods by a simple one-step hydrothermal method, and then uniformly dispersed in PVA solution to form homogeneous composite coating solution. The photochromic fiber was fabricated by coating the as-obtained composite solution onto the surface of cotton fiber. The reversible photochromic response of the prepared composite fibers was investigated upon continuous UV irradiation and infrared heating process as shown in Figure 51.a. The color of composite fibers changed from initial light yellow to dark blue under UV exposure within 7 min, and gradually turns back to its initial status by using

Chapter I: State-of-the-art and objectives

infrared lamp heating within about 2 h. It is obvious from Figure 51.b that the reflective intensity remarkably decreases with continuous UV exposure, and reached saturation within 7 min. The prepared photochromic fiber can be woven into some interesting shapes as shown in Figure 52-b shows the tensile strength elongation curves of prepared photochromic fiber and pure cotton fiber, the photochromic fiber had a higher breaking strength of 12.2 N, which is almost three times than that of cotton fiber. The WO_3 -based photochromic solution coating method may provide a step toward the development of photochromic fiber for functional textiles.



Chpt.I-Figure 51: (a) Optical pictures of the prepared photochromic fiber show gradual color change under UV irradiation and infrared heating; (b) UV-Vis diffuse reflectance spectra of one single photochromic fiber with different UV irradiation time [187].

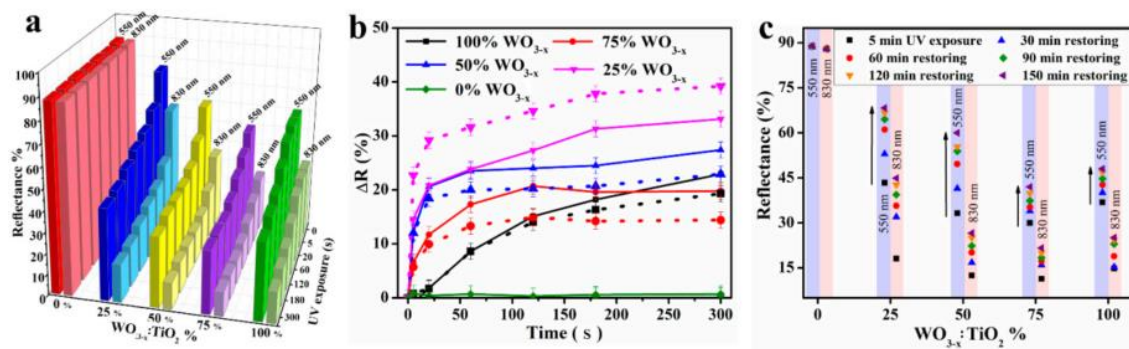


Chpt.I-Figure 52: (a) Pictures of the various shapes woven by prepared photochromic fiber before (upper) and after (below) UV irradiation, the scale bar is 1 cm; (b) tensile strength–elongation curves for cotton and photochromic fiber [187].

The same concept was used by Giannuzzi *et al* [188], where they developed a smart photochromic textile using a commercial textile as a substrate and several blends of WO_{3-x} : TiO_2 NCs as a soaking solution. They investigated the performance of the as-prepared photochromic textiles with varying WO_{3-x} : TiO_2 compositions and compared them with two bare oxides by recording the reflectance spectra. Figure 53.a depicts the reflectance changing values of photochromic fabrics with discrete compositions based on NC as a function of UV irradiation time with two characteristic wavelengths of 550 nm and 830 nm. The reflectance values decreased within the initial 30 seconds, after which the changing rate gradually decreased with increasing exposure time. Figure 53.b shows the comparison of reflectance differences (ΔR) between the no-exposure state and different UV exposure times for all NC compositions (solid line for $\lambda = 550$ nm and dashed line for $\lambda = 830$ nm). It is evident that the presence of TiO_2 increases the coloring kinetics for all mixture compositions compared to pure WO_{3-x} .

Chapter I: State-of-the-art and objectives

The greatest ΔR values were achieved with a $\text{WO}_{3-x}:\text{TiO}_2$ ratio of 1:3 for both wavelengths. The bleaching study shows the reflectance decay immediately after 5 minutes of UV exposure. Figure 53.c displays the representative reflectance values during the bleaching process of $\text{WO}_{3-x}:\text{TiO}_2$ functionalized textiles. All samples exhibited good reversible photochromic properties, and TiO_2 blending was found to be beneficial for photochromic recovery.



Chpt.I-Figure 53: (a) Representative reflectance values at $\lambda = 550$ nm and $\lambda = 830$ nm of nanocrystalline coated textile with different $\text{WO}_{3-x}:\text{TiO}_2$ compositions exposed to different UV irradiation times. (b) ΔR (difference between reflectance value after 5 min of UV exposure and no-exposed samples) variation at different UV exposure; solid lines are related to $\lambda = 550$ nm and dashed lines are related to $\lambda = 830$ nm. (c) Reflectance values during the bleaching process were carried out after 5 min of UV irradiation and recorded at different time intervals [188].

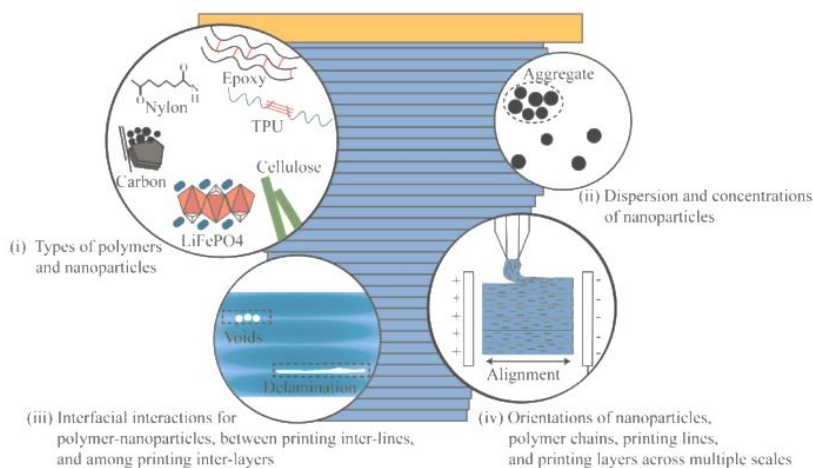
3.5 New perspectives: from 1D fibers towards 3D printing filaments: polymer/ WO_3 -based processing

3D printing, also known as additive manufacturing (AM), refers to the process of creating objects by joining materials layer by layer from 3D model data [189]. Other terms used to describe 3D printing include additive fabrication (AF), additive processes (AP), additive techniques (AT), layered manufacturing (LM), and solid freeform fabrication (SFF) [190]. AM methods offer many advantages beyond material and cost savings. The main advantage is the ability to overcome many of the problems associated with traditional machining techniques such as the creation of intricate details, undercuts, voids, and complex internal geometries where material variations can be precisely controlled using additive manufacturing [190], [191]. Also, 3D printing is designed for producing customized items, such as dental crowns and bridges, with a high degree of precision and accuracy. In contrast, traditional subtractive manufacturing can only produce rigid designs for one patient during a specific period [192]. 3D printing can create complicated designs for example patterned dots, thin-diameter lines, regular lattices, low-thickness films, porous membranes, and depth-changing motifs with varied continuity or heterogeneity in functionally graded structures [192], [193]. Different 3D printing platforms offer varying degrees of control over material variations. Some platforms enable point-by-point material variations, such as material jetting and binder jetting, while others provide discrete control within a layer, such as material extrusion and ink writing, or between layers, such as powder bed fusion and vat polymerization [190].

Chapter I: State-of-the-art and objectives

3.5.1 3D printing-enabled polymer/particle materials

Various materials can be processed by 3D printing such as polymers, nanoparticles, and their composites including soft and rigid hybrid systems, metals and alloys, ceramics, glasses and so on. This combination offers different functions in a wide range of applications: structural supports, thermal exchange, electrical micromachines, optical devices, surface modifications, and biomedical [192], [194], [195]. Nevertheless, processing composite materials has its challenges. For an instant, while particles can improve composite properties, their addition may lead to discontinuity, inefficient interactions with polymers, or brittleness at high concentrations [190], [196]. Hence, the successful incorporation of particles into polymer composites requires the manipulation of defined parameters such as the types of polymers and nanoparticles used, their dispersion and concentration, interfacial interactions, and orders of nanoparticles or polymer chains during printing [191], [192]. Understanding and manipulating these parameters can enhance composite performance, improving mechanical or functional properties as shown in Figure 54.



Chpt.I-Figure 54: Critical parameters for 3D printing [197].

3.5.1.1 Types of polymers and nanoparticles

3D printing can process liquid monomers, particle colloids, polymer solutions, gels, plastic powders, and continuous thin sheets. In composite mechanics, the intrinsic properties of the constituent phases are crucial to achieving enhanced mechanical properties through synergistic effects [197], [198]. Therefore, the type of polymer and nanoparticle used is critical to determine the appropriate processing parameters, material structures, and resulting system properties. While subtractive manufacturing methods can handle thousands of polymer materials, 3D printing is only capable of handling tens of small and macromolecule types. For example, most resins used on 3D printing platforms are acrylate-, urea-, urethane-, or epoxy-based monomers, and filament-based 3D printing can only process a limited range of polymers, with most being engineering polymers such as PVA, HDPE, PP, and ABS [199]. For the NPs addition, the size and aspect ratio of particles determines their efficiency in interaction and transferring stress to the surrounding polymer molecules. When particles

Chapter I: State-of-the-art and objectives

are smaller, they have a higher specific surface area to interact with the polymer chains, which increases their ability to transfer stress and to be fully incorporated [197].

3.5.1.2 Dispersion and concentrations of nanoparticles

The final composites' reinforcing effectiveness is determined by the dispersion and concentration of the NPs. Aggregations of NPs might damage the composite by acting as flaws. Due to the attractive forces between nanoparticles that create Van der Waals-induced aggregations, it is extremely difficult to achieve a balance between high nanoparticle loading and uniform dispersion.[199]. To ensure isotropic properties, composites must have a uniform dispersion of nanoparticles that can bear loads from different directions [200]. There are several processing techniques that can produce solid polymer powders or liquid solutions containing nanoparticles with an acceptable level of homogeneity. The use of compatibilizers, surface coatings for the particles, ultrasonication, vacuum drying to eliminate any moisture, and ball milling are some examples of these techniques [200], [202]. Before being combined with polymer matrices, pre-processing frequently leads to lower nanoparticle sizes and more uniform dispersion. Utilizing an in-situ polymerization process to create isotropic composite characteristics by pre-distributing the nanoparticles in the monomers is another crucial strategy [203]. For example, Weng *et al.* [200] synthesized core-shell particles comprising epoxide functional groups to bond well with SLA-printed epoxy resins. The particles had a polybutadiene-copolystyrene core and a polymethyl methacrylate-polystyrene-poly glycidyl methacrylate copolymer shell, which was prepared using an emulsion polymerization method. The resulting printed solid and cellular materials demonstrated significantly improved mechanical properties, including Young's modulus, strength, and impact resistance. Also, the concentration and inclusion of nanoparticles in the polymer matrix play a significant role in determining the resolution of 3D printing. Most 3D printing methods have processing resolution limits in the range of tens of microns [192], [197]. For instance, the filamentary materials used deposition modeling (FDM) and liquid deposition modeling (LDM) methods typically result in printing line widths of tens of microns due to a die-swell phenomenon [192].

3.5.1.3 Interfacial interactions

Increasing the adhesion between hydrophilic polymers and hydrophobic particles, introducing oxygen functional groups through particle oxidation, and using molecular coatings or coupling agents to modify surface tension and improve affinity are all examples of material chemistry techniques that are used to improve polymer-particle interfacial interact. For example, there is a need to enhance the adhesion between hydrophilic polymers (e.g., PVA, PEG) and most hydrophobic particles (e.g., carbons or ceramics) [206]. The oxidation of these particles may introduce oxygen functional groups (e.g., C–O, C=O, O–C=O, –NHCOO–, –NHCO–) and form strong bonding (e.g., N–H, O–H, and F–H) with the polymer chains [205-210]. An example is using a coupling agent with polypropylene (PP) grafting on maleic anhydride to increase the attachment between PP and glass fibers [207].

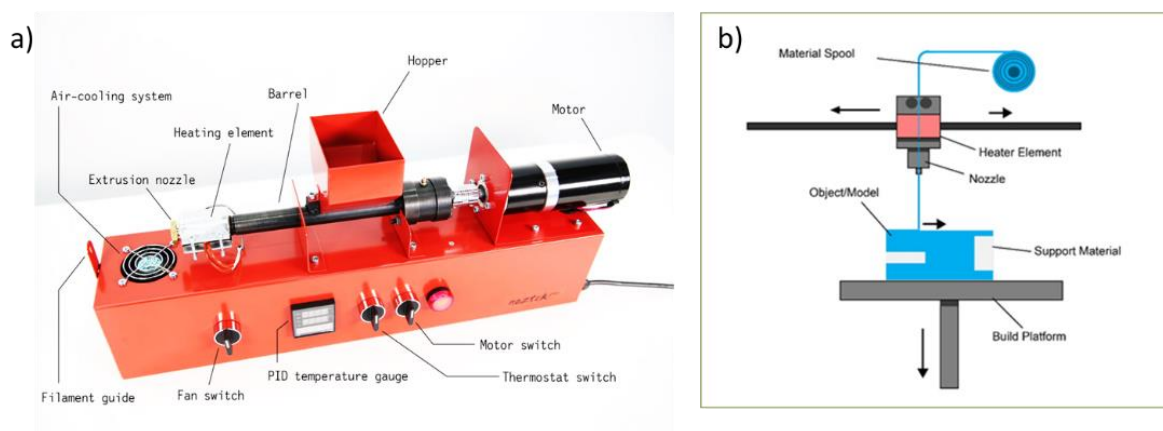
Chapter I: State-of-the-art and objectives

3.5.2 3D printing for polymer/particle processing

Based on energy sources, material types, and processing techniques (such as viscosity), three-dimensional printing is divided into four categories: ink jetting, EHD, binder jetting, photocuring-based (including stereolithography (SLA), 2/MPP, and digital light processing (DLP), extrusion-based (including FDM, LDM), and power fusion-based processes [192], [197], [205]. Since we will use extrusion-based 3D printing to print filaments in our work, we will focus on this method to get more insights and details. To our knowledge, it is important to highlight that there are no references about integrating WO_3 inside plastic filaments for 3D printing applications.

3.5.2.1 Extrusion-based processes: FDM-based printing

To create well-dispersed polymeric/NPs composite filaments for 3D printing, the extrusion approach is frequently utilized. Hot-melt extrusion involves an extruder, which comprises a feeding hopper, barrels, single or twin screws, and a die as shown in Figure 55.a. An extruder's main job is to combine polymeric materials in a homogenous mixture. For a successful result, the proper balancing of variables, including temperature, pressure, and velocity, is essential [208]. The screw is the fundamental component of an extruder, while the rest of the components (motor, gearbox, hopper, barrel, and die) are necessary to support the proper performance of the screw [209]. Extruders also come equipped with auxiliary equipment, including heating or cooling devices for the barrels, a conveyor belt to cool down the product, and a water pump.



Chpt.I-Figure 55: a) Extrusion machine to produce composite filament, b) Typical FDM extrusion printer using extruded filaments [208-210].

However, to print this type of extruded filaments, FDM is a well-established method that can accommodate a wide range of materials. The plastics suitable for FDM can be classified into three categories: commodity, engineering, and high-performance. Commodity plastics, which are affordable and easy to use, include amorphous polymers such as ABS, PS, PVC, and PMMA, as well as semicrystalline polymers like PP, PE, and PEVA [210]. Engineering polymer filaments offer moderate temperature resistance and mechanical strength and fall into the amorphous (e.g., PC, PVA) and semicrystalline (e.g., PLA, PBT, PET, POM, PA, PCL, PLGA) categories. When printing particle-

Chapter I: State-of-the-art and objectives

included polymer composites using pre-impregnate fibers, the first step is to add the fillers (e.g., glass, metal oxide) with polymers, such as nylon or urethane elastomers [211]. The wrapped fibers are then directly extruded from a nozzle (Figure 55.b). It is worth noting that most commercially available filaments for this type of printing contain chopped carbon or glass fibers rather than nanofillers [209].

4 The positioning of our study besides state of the art

The incorporation of X-chromic tungsten oxides WO_{3-x} in polymer matrix is the core subject of the thesis. It represents a significant contribution to the ongoing research on "X-chrome" materials at ICMCB. In the second chapter of this thesis, we investigate the implementation of different techniques to develop the photochromism of nanostructured tungsten oxide WO_{3-x} . The first method is the tuning of the oxygen sub-stoichiometry of as-prepared NPs from a polyol process via peptization of the NPs in an aqueous solution of different $Cr_2O_7^{2-}$ concentrations. The W/O stoichiometric ratio has been analyzed by multiple technics. The most re-oxidized samples exhibit the best selectivity (high visible transparency but with high NIR absorptivity) for the use of these compounds as solar filters, i.e., with the best contrast between the visible and near-infrared transmission. The prepared thin films by dip coating prove to be efficient for UV photo-detection even at a very low power density (9.2 W/m^2) for the UV illumination. The second method is structural doping by copper (Cu). The bleaching kinetic is enhanced due to shallow states created in the band gap of the WO_3 semiconductor associated with copper cation doping, which could in turn extend the light-harvesting ability of this compound to the visible and near-infrared region.

In the third part, we present the fabrication of WO_{3-x} /PVA composite films as smart photochromic coatings on glass substrate by two methods: solvent casting (SC) and dip-coating (DC). After carefully analyzing the relationship between the SC and DC film characterizations and their optical performance, we conclude that the SC method leads to films that are better candidates for post-optical application in terms of scattering reduction, improved visible/infrared contrast, and better photochromic efficiency. The photochromic SC smart windows proposed here are equally efficient while being more affordable than electrochromic panels or VO_2 thermochromic thin films to reduce the inner house temperature (almost 20°C) upon solar irradiation, demonstrating their great potential as smart cost-effective energy-saving materials.

In the last part, we investigate for the first time, the integration of the nanostructured WO_{3-x} inside microfibers. We discuss the direct incorporation of NPs in a matrix of plastic optical fibers (POFs) of polymethyl methacrylate by bulk radical polymerization. The fabricated doped preforms show irreversible photochromic behavior. But surprisingly, the single fiber proves to be an efficient photochromism through a large degradation of transmission signal upon UV irradiation and nearly full reversibility (regain of the transmission under dark conditions through WO_3 bleaching). Furthermore, the coloring study of the single-doped fiber reveals a fast response to the UV dose upon irradiation time. The WO_3 -polymer composite fibers demonstrate their great potential as novel inorganic/organic

Chapter I: State-of-the-art and objectives

materials in the domain of photochromic sensors and textiles. Additionally, we propose the design of polymer core / composite cladding fibers. Here the cladding consists of the nanostructured WO_{3-x} dispersed in a PVP matrix coated on a commercial core of polyether sulfone (PES). The photochromic plastic fibers show a phenomenon of “negative” photochromism where the transmitted signal is amplified under UV-irradiation.

Finally, in a supplementary chapter, we investigate the environmental impact of our lab-scale products on an industrial scale using the life cycle assessment method.

5 References

- [1] R. L. M. Allen, "Colour and constitution," in *Colour chemistry*, R. L. M. Allen, Ed., Boston, MA: Springer US, 1971, pp. 14–20. doi: 10.1007/978-1-4615-6663-2_2.
- [2] K. Nassau and C. F. Bohren, "The physics and chemistry of color," *Am J Phys*, vol. 53, no. 10, pp. 1018–1019, Oct. 1985, doi: 10.1119/1.13997.
- [3] G. R. NOAKES, "Physics, physiology and psychology of colour," *Nature*, vol. 167, no. 4259, p. 961, 1951, doi: 10.1038/167961a0.
- [4] S. Westland, "The CIE System," in *Handbook of visual display technology*, W. and F. M. Chen Janglin and Cranton, Ed., Cham: Springer, 2016, pp. 161–169. doi: 10.1007/978-3-319-14346-0_11.
- [5] F. J. J. Clarke, R. McDonald, and B. Rigg, "Modification to the JPC79 colour–difference formula," *J Soc Dyers*, vol. 100, no. 4, pp. 128–132, Apr. 1984, doi: 10.1111/J.1478-4408.1984.TB00969. X.
- [6] H. Langhals, "Color chemistry: synthesis, properties and applications of organic dyes and pigments," *Ang Chem Intern Ed*, vol. 43, no. 40, pp. 5291–5292, Oct. 2004, doi: 10.1002/anie385122.
- [7] M. G. Brik, N. M. Avram, and C. N. Avram, "Exchange charge model of crystal field for 3d-ions," in *Optical properties of 3d-ions in crystals: spectroscopy and crystal field analysis*, Heidelberg: Springer Berlin, 2013, pp. 29–94. doi: 10.1007/978-3-642-30838-3_2.
- [8] A. Kołodziejczak-Radzimska and T. Jesionowski, "Zinc oxide from synthesis to application: a review," *Materials*, vol. 7, no. 4, pp. 2833–2881, Apr. 2014, doi: 10.3390/ma7042833.
- [9] V. V Butova et al., "Synthesis of ZnO nanoparticles doped with cobalt using bimetallic ZIFs as sacrificial agents," *Nanomater*, vol. 10, no. 7, Jun. 2020, doi: 10.3390/nano10071275.
- [10] R. L. Carlin, "Inorganic electronic spectroscopy (Lever, A. B. P.)," *J Chem Educ*, vol. 46, no. 9, p. A628, Sep. 1969, doi: 10.1021/ed046pA628.1.
- [11] R. O. Kuzian, A. M. Daré, P. Sati, and R. Hayn, "Crystal-field theory of Co^{2+} in doped ZnO," *Phys Rev B*, vol. 74, no. 15, p. 155201, Oct. 2006, doi: 10.1103/PhysRevB.745201.
- [12] A. B. P. Lever, "Charge transfer spectra of transition metal complexes," *J Chem Educ*, vol. 51, no. 9, p. 612, Sep. 1974, doi: 10.1021/ed051p612.
- [13] R. Otero, A. L. Vázquez de Parga, and J. M. Gallego, "Electronic, structural and chemical effects of charge-transfer at organic/inorganic interfaces," *Surf Sci Rep*, vol. 72, no. 3, pp. 105–145, Jul. 2017, doi: 10.1016/j.surfrep.2017.03.001.

Chapter I: State-of-the-art and objectives

- [14] H. C. London et al., “Ligand-to-metal charge-transfer photophysics and photochemistry of emissive d_0 titanocenes: a spectroscopic and computational investigation,” *Inorg Chem*, vol. 60, no. 18, pp. 14399–14409, Sep. 2021, doi: 10.1021/acs.inorgchem.1c02182.
- [15] K. Nagase, H. Yokobayashi, and K. Sone, “Spectrophotometric and thermal analytical studies on the dehydration of copper (II) sulfate and its double salts,” *Thermochim Acta*, vol. 23, no. 2, pp. 283–291, Apr. 1978, doi: 10.1016/0040-6031(78)85070-9.
- [16] Z. Yang, Y. Yan, A. Yu, B. Pan, and J. J. Pignatello, “Revisiting the phenanthroline and ferrozine colorimetric methods for quantification of Fe (II) in Fenton reactions,” *J Chem Eng*, vol. 391, p. 123592, Jul. 2020, doi: 10.1016/j.cej.2019.123592.
- [17] Z. Zhou, Y. Guo, X. Kong, Y. Wang, and T. Liu, “Control of electron coupling and electron transfer through non-covalent interactions in mixed-valence systems,” *Wiley*, pp. 349–363, 2023, doi: 10.1002/9783527835287.ch11.
- [18] J. Launay, “Mixed-valent compounds and their properties: recent developments,” *Eur J Inorg Chem*, vol. 2020, no. 4, pp. 329–341, Jan. 2020, doi: 10.1002/ejic.201901180.
- [19] L. H. Galvão Tizei and M. Amato, “Electronic structure and optical properties of semiconductor nanowires polytypes,” *Eur Phys J B*, vol. 93, no. 1, p. 16, Jan. 2020, doi: 10.1140/epjb/e2019-100375.
- [20] A. J. Dekker, “The crystalline state,” in *Solid state physics*, A. J. Dekker, Ed., London: Macmillan Edu UK, 1981, pp. 1–31. doi: 10.1007/978-1-349-00784-4_1.
- [21] S. Adachi, “Properties of group-IV, II-V and II-VI semiconductors,” *Wiley*, 2005. doi: 10.1002/0470090340.
- [22] M. Kumar Mohanta, T. Kanta Sahu, S. Alam, and M. Qureshi, “Tuning the electronic structure of monoclinic tungsten oxide nanoblocks by indium doping for boosted photoelectrochemical performance,” *Chem Asian J*, vol. 15, no. 22, pp. 3886–3896, Nov. 2020, doi: 10.1002/asia.202000787.
- [23] A. Jangizehi, F. Schmid, P. Besenius, K. Kremer, and S. Seiffert, “Defects and defect engineering in soft matter,” *Soft Matter*, vol. 16, no. 48, pp. 10809–10859, 2020, doi: 10.1039/D0SM01371D.
- [24] J. B. Ketterson, “Defects and diffusion in crystalline solids,” *Phys. Solids*, Oxford Univ. Press, 2016, pp. 797–810. doi: 10.1093/acprof:oso/9780198742906.003.0040.
- [25] S. Chen, H. Tan, C. Zhang, Y. Teng, and E. Zu, “Study on gemological characteristics of blue sapphires from baw-mar mine, Mogok, Myanmar,” *Crystals (Basel)*, vol. 11, no. 11, p. 1275, Oct. 2021, doi: 10.3390/cryst11111275.

Chapter I: State-of-the-art and objectives

- [26] J. K. Bristow, D. Tiana, S. C. Parker, and A. Walsh, “Defect chemistry of Ti and Fe impurities and aggregates in Al₂O₃,” *J Mater Chem. A* vol. 2, no. 17, pp. 6198–6208, 2014, doi: 10.1039/C3TA15322C.
- [27] P. Gerard, A. Deneuve, G. Hollinger, and T. M. Duc, “Color in ‘tungsten trioxide’ thin films,” *J Appl Phys*, vol. 48, no. 10, pp. 4252–4255, Oct. 1977, doi: 10.1063/1.323411.
- [28] N. Mott, “On metal-insulator transitions,” *J Solid State Chem*, vol. 88, no. 1, pp. 5–7, Sep. 1990, doi: 10.1016/0022-4596(90)90201-8.
- [29] C. J. Dahlman, Y. Tan, M. A. Marcus, and D. J. Milliron, “Spectroelectrochemical signatures of capacitive charging and ion insertion in doped anatase titania nanocrystals,” *J Am Chem Soc*, vol. 137, no. 28, pp. 9160–9166, Jul. 2015, doi: 10.1021/jacs.5b04933.
- [30] H.-C. Lu, B. Z. Zydlewski, B. Tandon, S. A. Shubert-Zuleta, and D. J. Milliron, “Understanding the role of charge storage mechanisms in the electrochromic switching kinetics of metal oxide nanocrystals,” *J Chem Mat*, vol. 34, no. 12, pp. 5621–5633, Jun. 2022, doi: 10.1021/acs.chemmater.2c00930.
- [31] A. Agrawal, R. W. Johns, and D. J. Milliron, “Control of localized surface plasmon resonances in metal oxide nanocrystals,” *Annu Rev Mater Res*, vol. 47, no. 1, pp. 1–31, Jul. 2017, doi: 10.1146/annurev-matsci-070616-124259.
- [32] S. Zeb, G. Sun, Y. Nie, H. Xu, Y. Cui, and X. Jiang, “Advanced developments in nonstoichiometric tungsten oxides for electrochromic applications,” *Adv Mater*, vol. 2, no. 21, pp. 6839–6884, 2021, doi: 10.1039/D1MA00418B.
- [33] G. Garcia, R. Buonsanti, A. Llordes, E. L. Runnerstrom, A. Bergerud, and D. J. Milliron, “Near-infrared spectrally selective plasmonic electrochromic thin films,” *Adv Opt Mater*, vol. 1, no. 3, pp. 215–220, Mar. 2013, doi: 10.1002/adom.201200051.
- [34] P. R. Somani and S. Radhakrishnan, “Electrochromic materials and devices: present and future,” *Mater Chem Phys*, vol. 77, no. 1, pp. 117–133, Jan. 2003, doi: 10.1016/S02540584(01)00575.
- [35] G. A. Niklasson and C. G. Granqvist, “Electrochromics for smart windows: thin films of tungsten oxide and nickel oxide, and devices based on these,” *J Mater Chem*, vol. 17, no. 2, pp. 127–156, 2007, doi: 10.1039/B612174H.
- [36] J. J. Smee, “Review of descriptive inorganic, coordination, and solid-state chemistry, 3rd edition,” *J Chem Educ*, vol. 90, no. 1, pp. 19–20, Jan. 2013, doi: 10.1021/ed300777d.
- [37] J. Kim et al., “Optical properties of gallium-doped zinc oxid: a low-loss plasmonic material: first-principles theory and experiment,” *Phys Rev X*, vol. 3, no. 4, p. 041037, Dec. 2013, doi: 10.1103/PhysRevX.3.041037.

Chapter I: State-of-the-art and objectives

- [38] Y. Chen et al., “Core-shell structured $Cs_xWO_3@ZnO$ with excellent stability and high performance on near-infrared shielding,” *Ceram Int*, vol. 44, no. 3, pp. 2738–2744, Feb. 2018, doi: 10.1016/j.ceramint.2017.11.004.
- [39] C. M. Staller, S. L. Gibbs, C. A. Saez Cabezas, and D. J. Milliron, “Quantitative analysis of extinction coefficients of tin-doped indium oxide nanocrystal ensembles,” *Nano Lett*, vol. 19, no. 11, pp. 8149–8154, Nov. 2019, doi: 10.1021/acs.nanolett.9b03424.
- [40] A. Llordés, G. Garcia, J. Gazquez, and D. J. Milliron, “Tunable near-infrared and visible-light transmittance in nanocrystal-in-glass composites,” *Nature*, vol. 500, no. 7462, pp. 323–326, Aug. 2013, doi: 10.1038/nature12398.
- [41] G. Garcia et al., “Dynamically modulating the surface plasmon resonance of doped semiconductor nanocrystals,” *Nano Lett*, vol. 11, no. 10, pp. 4415–4420, Oct. 2011, doi: 10.1021/nl202597n.
- [42] T. M. Mattox, A. Agrawal, and D. J. Milliron, “Low temperature synthesis and surface plasmon resonance of colloidal lanthanum hexaboride (LaB_6) nanocrystals,” *J Chem Mat*, vol. 27, no. 19, pp. 6620–6624, Oct. 2015, doi: 10.1021/acs.chemmater.5b02297.
- [43] M. Bourdin et al., “Investigation on the coloring and bleaching processes of WO_{3-x} photochromic thin films,” *J Mater Chem C Mater*, vol. 8, no. 27, pp. 9410–9421, 2020, doi: 10.1039/D0TC02170A.
- [44] P. Talvenmaa, “Introduction to chromic materials,” in *Intelligent textiles and clothing*, Elsevier, 2006, pp. 193–205. doi: 10.1533/9781845691622.3.193.
- [45] Y. Badour, V. Jubera, I. Andron, C. Frayret, and M. Gaudon, “Photochromism in inorganic crystallised compounds,” *Optical Materials: X*, vol. 12, p. 100110, Dec. 2021, doi: 10.1016/j.omx.2021.100110.
- [46] S. D. Cohen and G. A. Newman, “Inorganic photochromism,” *J Photographic Sc*, vol. 15, no. 6, pp. 290–298, Nov. 1967, doi: 10.1080/00223638.1967.11737423.
- [47] Y. Ru et al., “Recent progress of photochromic materials towards photocontrollable devices,” *Mater Chem Front*, vol. 5, no. 21, pp. 7737–7758, 2021, doi: 10.1039/D1QM00790D.
- [48] J. Liu et al., “Metal–organic framework-based flexible devices with simultaneous electrochromic and electrofluorochromic functions,” *ACS Appl Electron Mater*, vol. 3, no. 3, pp. 1489–1495, Mar. 2021, doi: 10.1021/acsaelm.1c00097.
- [49] B. Li, J. Dang, Q. Zhuang, and Z. Lv, “Recent advances in inorganic electrochromic materials from synthesis to applications: critical review on functional chemistry and structure engineering,” *Chem Asian J*, vol. 17, no. 7, Apr. 2022, doi: 10.1002/asia.202200022.

Chapter I: State-of-the-art and objectives

- [50] K. Wang et al., “Advances in energy-efficient plasmonic electrochromic smart windows based on metal oxide nanocrystals,” *Adv Eng Sus*, vol. 2, no. 12, p. 2100117, Dec. 2021, doi: 10.1002/aesr.202100117.
- [51] W. Zhang, H. Li, and A. Y. Elezzabi, “Electrochromic displays having two-dimensional CIE color space tunability,” *Adv Funct Mater*, vol. 32, no. 7, p. 2108341, Feb. 2022, doi: 10.1002/adfm.202108341.
- [52] J. H. Day, “Thermochromism of inorganic compounds,” *Chem Rev*, vol. 68, no. 6, pp. 649–657, Dec. 1968, doi: 10.1021/cr60256a001.
- [53] H. Huang, L. Huang, G. Li, and D. Wang, “Study on thermoelectric performance of thermochromic coating PV/T system,” *Energy Reports*, vol. 8, pp. 311–318, Aug. 2022, doi: 10.1016/j.egy.2022.02.146.
- [54] A. Seeboth, D. Löttsch, R. Ruhmann, and O. Muehling, “Thermochromic polymers function by design,” *Chem Rev*, vol. 114, no. 5, pp. 3037–3068, Mar. 2014, doi: 10.1021/cr400462e.
- [55] J. He and J. S. Chen, “The solvatochromic materials: a progress review,” *Mat Forum*, vol. 914, pp. 182–192, Feb. 2018, doi: 10.4028/www.scientific.net/MSF.914.182.
- [56] C. Reichardt, “Solvatochromic dyes as solvent polarity indicators,” *Chem Rev*, vol. 94, no. 8, pp. 2319–2358, Dec. 1994, doi: 10.1021/cr00032a005.
- [57] A. Mirzaei, J.-H. Kim, H. W. Kim, and S. S. Kim, “Gasochromic WO₃ nanostructures for the detection of hydrogen gas: an overview,” *App Sci*, vol. 9, no. 9, p. 1775, Apr. 2019, doi: 10.3390/app9091775.
- [58] S. Xue et al., “Nanoporous WO₃ gasochromic films for gas sensing,” *ACS Appl Nano Mater*, vol. 4, no. 8, pp. 8368–8375, Aug. 2021, doi: 10.1021/acsanm.1c01557.
- [59] S. Yamamoto, T. Hakoda, A. Miyashita, and M. Yoshikawa, “Structural and gasochromic properties of WO₃ films prepared by reactive sputtering deposition,” *Mater Res Express*, vol. 2, no. 2, p. 026401, Jan. 2015, doi: 10.1088/2053-1591/2/2/026401.
- [60] P. Coppens, D. V. Fomitchev, M. D. Carducci, and K. Culp, “Crystallography of molecular excited states: transition-metal nitrosyl complexes and the study of transient species,” *J Chem Soc*, no. 6, pp. 865–872, 1998, doi: 10.1039/a708604k.
- [61] J. Goodenough, “Metallic oxides,” *Progress Solid State Chem*, vol. 5, pp. 145–399, 1971, doi: 10.1016/0079-6786(71)90018-5.
- [62] U. Schwingenschlögl and V. Eyert, “The vanadium Magnéli phases V_nO_{2n-1},” *Ann Phys*, vol. 13, no. 9, pp. 475–510, Sep. 2004, doi: 10.1002/andp.200410099.

Chapter I: State-of-the-art and objectives

- [63] T. S. Kasirga et al., “Photoresponse of a strongly correlated material determined by scanning photocurrent microscopy,” *Nat Nanotechnol*, vol. 7, no. 11, pp. 723–727, Nov. 2012, doi: 10.1038/nnano.2012.176.
- [64] K. Liu, C. Cheng, Z. Cheng, K. Wang, R. Ramesh, and J. Wu, “Giant-amplitude, high-work density microactuators with phase transition activated nanolayer bimorphs,” *Nano Lett*, vol. 12, no. 12, pp. 6302–6308, Dec. 2012, doi: 10.1021/nl303405g.
- [65] B. Hu et al., “External-strain induced insulating phase transition in VO₂ nanobeam and its application as flexible strain sensor,” *Adv Mater*, vol. 22, no. 45, pp. 5134–5139, Dec. 2010, doi: 10.1002/adma.201002868.
- [66] S.-H. Bae et al., “The memristive properties of a single VO₂ nanowire with switching controlled by self-heating,” *Adv Mater*, vol. 25, no. 36, pp. 5098–5103, Sep. 2013, doi: 10.1002/adma.201302511.
- [67] T. He and J.-N. Yao, “Photochromism in transition-metal oxides,” *Res Chem Interms*, vol. 30, no. 4, pp. 459–488, Jun. 2004, doi: 10.1163/1568567041280890.
- [68] W. Marckwald, “Ueber Phototropie,” *Zeits physik chemie*, vol. 30U, no. 1, pp. 140–145, Oct. 1899, doi: 10.1515/zpch-1899-3007.
- [69] Y. Hirshberg, “Reversible formation and eradication of colors by irradiation at low temperatures. a photochemical memory model,” *J Am Chem Soc*, vol. 78, no. 10, pp. 2304–2312, May 1956, doi: 10.1021/ja01591a075.
- [70] E. Fischer and Y. Hirshberg, “Low-temperature photochromism and its relation to thermochromism,” *J Chem Educ*, vol. 40, no. 3, p. 112, Mar. 1963, doi: 10.1021/ed040p112
- [71] I. A. Rostovtseva, N. A. Voloshin, E. V. Solov’eva, A. V. Chernyshev, I. A. Metelitsa, and A. V. Metelitsa, “Spiropyrans and spirooxazines: synthesis and photochromic properties of benzoxazolyl-substituted spirobenzopyrans,” *Russ Chem Bull*, vol. 67, no. 8, pp. 1476–1481, Aug. 2018, doi: 10.1007/s11172-018-2242-0.
- [72] H. Tian and J. Zhang, Eds., “Photochromic materials: preparation, properties and applications.” Wiley, 2016. doi: 10.1002/9783527683734.
- [73] D. Kondo and D. Beaton, “Hackmanite/Sodalite from Myanmar and Afghanistan,” *Gems & Gemology*, vol. 45, no. 1, pp. 38–43, Apr. 2009, doi: 10.5741/GEMS.45.1.38.
- [74] M. Irie, T. Fukaminato, K. Matsuda, and S. Kobatake, “Photochromism of Diarylethene molecules and crystals: memories, Switches, and Actuators,” *Chem Rev*, vol. 114, no. 24, pp. 12174–12277, Dec. 2014, doi: 10.1021/cr500249p.

Chapter I: State-of-the-art and objectives

- [75] T. Yamaguchi, A. Maity, V. Polshettiwar, and M. Ogawa, "Negative photochromism based on molecular diffusion between hydrophilic and hydrophobic particles in the solid state," *Inorg Chem*, vol. 57, no. 7, pp. 3671–3674, Apr. 2018, doi: 10.1021/acs.inorgchem.7b03132.
- [76] V. A. Barachevsky, "Negative photochromism in organic systems," *Rev J Chem*, vol. 7, no. 3, pp. 334–371, Jul. 2017, doi: 10.1134/S2079978017030013.
- [77] D. Fanghänel, G. Timpe, and V. Orthman, "Photochromic compounds with N=N and C=N chromophores," *J Org Photoch*, 1990, pp. 105–175. doi: 10.1007/978-1-4615-8585-5_3.
- [78] C. Bohne and R. H. Mitchell, "Characterization of the photochromism of dihydropyrenes with photophysical techniques," *J Photochem Photobio C*, vol. 12, no. 2, pp. 126–137, Sep. 2011, doi: 10.1016/j.jphotochemrev.2011.08.001.
- [79] C. Sanchez, B. Julián, P. Belleville, and M. Popall, "Applications of hybrid organic–inorganic nanocomposites," *J Mater Chem*, vol. 15, no. 35–36, p. 3559, 2005, doi: 10.1039/b509097k.
- [80] C. Sanchez, B. Lebeau, F. Chaput, and J.-P. Boilot, "Optical properties of functional hybrid organic–inorganic nanocomposites," *Adv Mater*, vol. 15, no. 23, pp. 1969–1994, Dec. 2003, doi: 10.1002/adma.200300389.
- [81] M. Zayat, D. Almendro, V. Vadhillo, and D. Levy, "Sol-gel materials for optics and electrooptic," *Handbook Sol-Gel Sci*, 2017, pp. 1–28. doi: 10.1007/978-3-319-19454-7_145-1.
- [82] Q. Mu et al., "Chemical basis of interactions between engineered nanoparticles and biological systems," *Chem Rev*, vol. 114, no. 15, pp. 7740–7781, Aug. 2014, doi: 10.1021/cr400295a.
- [83] N. Andersson, P. Alberius, J. Örtengren, M. Lindgren, and L. Bergström, "Photochromic mesostructured silica pigments dispersed in latex films," *J Mater Chem*, vol. 15, no. 34, p. 3507, 2005, doi: 10.1039/b505319f.
- [84] T. HE and J. YAO, "Photochromism in composite and hybrid materials based on transition-metal oxides and polyoxometalates," *Prog Mater Sci*, vol. 51, no. 6, pp. 810–879, Aug. 2006, doi: 10.1016/j.pmatsci.2005.12.001.
- [85] B. C. Dave, B. Dunn, and J. I. Zink, "Chemical and electrochemical reactions in porous sol-gel materials," *Nanopor Mat*, pp. 141–159. doi: 10.1007/0-306-47066-7_10.
- [86] G. Suyal, M. Mennig, and H. Schmidt, "Sol-gel synthesis of cuprous halide nanoparticles in a glassy matrix and their characterization," *J Mater Chem*, vol. 13, no. 7, pp. 1783–1788, 2003, doi: 10.1039/B303330A.
- [87] P. Judeinstein and C. Sanchez, "Hybrid organic–inorganic materials: a land of multidisciplinary," *J Mater Chem.*, vol. 6, no. 4, pp. 511–525, 1996, doi: 10.1039/JM9960600511.

Chapter I: State-of-the-art and objectives

- [88] C. Rottman, G. S. Grader, Y. De Hazan, and D. Avnir, "Sol-gel entrapment of ET (30) in ormosils: interfacial polarity-fractality correlation," *Langmuir*, vol. 12, no. 23, pp. 5505–5508, Jan. 1996, doi: 10.1021/la960517h.
- [89] R. Pardo, M. Zayat, and D. Levy, "Photochromic organic-inorganic hybrid materials," *Chem Soc Rev*, vol. 40, no. 2, p. 672, 2011, doi: 10.1039/c0cs00065e.
- [90] R. Tällberg, B. P. Jelle, R. Loonen, T. Gao, and M. Hamdy, "Comparison of the energy saving potential of adaptive and controllable smart windows," *J Sol Eng Mat*, vol. 200, p. 109828, Sep. 2019, doi: 10.1016/j.solmat.2019.02.041.
- [91] H. J. Hoffmann, "The use of silver salts for photochromic glasses," in *Photochromism*, Elsevier, 2003, pp. 822–854. doi: 10.1016/B978-044451322-9/50026-9.
- [92] B. Van Gemert, "The commercialization of plastic photochromic lenses: a tribute to John Crano," *Molec Crys and Liq Cry Sci*, vol. 344, no. 1, pp. 57–62, Jun. 2000, doi: 10.1080/10587250008023814.
- [93] R. Winder, "Photochromes, 1st ed.," vol. 344. LONDON: Sunlight Express, Chem Ind, 2006.
- [94] J. Jiyue and D. Yongqiu, "Photochromic water-based nail polish and preparation method Thereof," CN 110200835
- [95] O. J. X. Morel and R. M. Christie, "Current trends in the chemistry of permanent hair dyeing," *Chem Rev*, vol. 111, no. 4, pp. 2537–2561, Apr. 2011, doi: 10.1021/cr1000145.
- [96] H. Rosset, "Security element having a variable optical effect and security sheet or document or article comprising it," FR 2933428, 2010
- [97] M. Akiyama, "Blue-green light photochromism in europium doped BaMgSiO₄," *Appl Phys Lett*, vol. 97, no. 18, p. 181905, Nov. 2010, doi: 10.1063/1.3509417.
- [98] N. I. Fernandes, G. Poirier, and M. Nalin, "Thermo and photochromic properties of Na₂O–WO₃–SbPO₄ glasses," *Solid State Ion*, vol. 181, no. 23–24, pp. 1125–1130, Aug. 2010, doi: 10.1016/j.ssi.2010.06.011.
- [99] N. Crespo-Monteiro, N. Destouches, L. Nadar, S. Reynaud, F. Vocanson, and J. Y. Michalon, "Irradiance influence on the multicolor photochromism of mesoporous TiO₂ films loaded with silver nanoparticles," *Appl Phys Lett*, vol. 99, no. 17, p. 173106, Oct. 2011, doi: 10.1063/1.3653282.
- [100] G. P. Smith, "Photochromic glasses: properties and applications," *J Mater Sci*, vol. 2, no. 2, pp. 139–152, Mar. 1967, doi: 10.1007/BF00549573.
- [101] R. Zhang, "The syntheses, NMR and photochromic properties of modified dimethyl dihydro pyrenes," 2007, doi: <http://hdl.handle.net/1828/247>.

Chapter I: State-of-the-art and objectives

- [102] T. He and J. Yao, "Photochromism of molybdenum oxide," *J Photochem Photobiol C Photochem Rev*, vol. 4, no. 2, pp. 125–143, Oct. 2003, doi: 10.1016/S1389-5567(03)00025-X.
- [103] D. F. Eaton, "International union of pure and applied chemistry organic chemistry division commission on photochemistry," *J Photochem Photobiol B*, vol. 2, no. 4, pp. 523–531, Dec. 1988, doi: 10.1016/1011-1344(88)85081-4.
- [104] A. Agranat and Y. Yacoby, "A correlation between a dielectric induced photorefractive effect and the photochromic effect," *Solid State Commun*, vol. 52, no. 5, pp. 531–534, Nov. 1984, doi: 10.1016/0038-1098(84)90870-6.
- [105] P. M. Woodward, A. W. Sleight, and T. Vogt, "Ferroelectric tungsten trioxide," *J Solid State Chem*, vol. 131, no. 1, pp. 9–17, Jun. 1997, doi: 10.1006/jssc.1997.7268.
- [106] H. Zheng, J. Z. Ou, M. S. Strano, R. B. Kaner, A. Mitchell, and K. Kalantar-zadeh, "Nanostructured tungsten oxide - properties, synthesis, and applications," *Adv Funct Mater*, vol. 21, no. 12, pp. 2175–2196, Jun. 2011, doi: 10.1002/adfm.201002477.
- [107] B. O. Loopstra and H. M. Rietveld, "Further refinement of the structure of WO_3 ," *Acta Crystallogr B*, vol. 25, no. 7, pp. 1420–1421, Jul. 1969, doi: 10.1107/S0567740869004146.
- [108] F. Wang, C. Di Valentin, and G. Pacchioni, "Electronic and structural properties of wo_3 : a systematic hybrid DFT study," *J Phys Chem C*, vol. 115, no. 16, pp. 8345–8353, Apr. 2011, doi: 10.1021/jp201057m.
- [109] S. K. Deb, "Opportunities and challenges in science and technology of WO_3 for electrochromic and related applications," *Solar Energy Mater Solar Cells*, vol. 92, no. 2, pp. 245–258, Feb. 2008, doi: 10.1016/j.solmat.2007.01.026.
- [110] P. Roussel, P. Labbé, and D. Groult, "Symmetry and twins in the monophosphate tungsten bronze series $(\text{PO}_2)_4(\text{WO}_3)_{2m}$ ($2 \leq m \leq 14$)," *Acta Crystallogr B*, vol. 56, no. 3, pp. 377–391, Jun. 2000, doi: 10.1107/S0108768199016195.
- [111] A. Baserga et al., "Nanostructured tungsten oxide with controlled properties: Synthesis and Raman characterization," *Thin Solid Films*, vol. 515, no. 16, pp. 6465–6469, Jun. 2007, doi: 10.1016/j.tsf.2006.11.067.
- [112] M. Breedon et al., "Synthesis of nanostructured tungsten oxide thin films: a simple, controllable, inexpensive, aqueous sol-gel method," *Cryst Growth Des*, vol. 10, no. 1, pp. 430–439, Jan. 2010, doi: 10.1021/cg9010295.
- [113] C. Santato, M. Odziemkowski, M. Ulmann, and J. Augustynski, "Crystallographically Oriented Mesoporous WO_3 Films: Synthesis, characterization, and applications," *J Am Chem Soc*, vol. 123, no. 43, pp. 10639–10649, Oct. 2001, doi: 10.1021/ja011315x.

Chapter I: State-of-the-art and objectives

- [114] M.-A. Einarsrud and T. Grande, "1D oxide nanostructures from chemical solutions," *Chem. Soc. Rev.*, vol. 43, no. 7, pp. 2187–2199, 2014, doi: 10.1039/C3CS60219B.
- [115] O. Yayapao, T. Thongtem, A. Phuruangrat, and S. Thongtem, "CTAB-assisted hydrothermal synthesis of tungsten oxide microflowers," *J Alloys Compd*, vol. 509, no. 5, pp. 2294–2299, Feb. 2011, doi: 10.1016/j.jallcom.2010.10.204.
- [116] X. Song, Y. Zhao, and Y. Zheng, "Hydrothermal synthesis of tungsten oxide nanobelts," *Mater Lett*, vol. 60, no. 28, pp. 3405–3408, Dec. 2006, doi: 10.1016/j.matlet.2006.03.022.
- [117] Z. Gu, Y. Ma, W. Yang, G. Zhang, and J. Yao, "Self-assembly of highly oriented one-dimensional h-WO₃ nanostructures," *Chemical Communications*, no. 28, p. 3597, 2005, doi: 10.1039/b505429j.
- [118] X. Han, L. Li, and C. Wang, "Controlling the morphologies of WO₃ particles and tuning the gas sensing properties," *New J Chem*, vol. 36, no. 11, p. 2205, 2012, doi: 10.1039/c2nj40600d.
- [119] Z. Liu, Z.-G. Zhao, and M. Miyauchi, "Efficient visible light active CaFe₂O₄/WO₃ based composite photocatalysts: effect of interfacial modification," *J Phys Chem C*, vol. 113, no. 39, pp. 17132–17137, Oct. 2009, doi: 10.1021/jp906195f.
- [120] H. Long, W. Zeng, S. Xu, Y. Li, and W. Chen, "Hydrothermal fabrication of WO₃·H₂O with varied morphologies and their gas sensing performances," *J Mater Sci Mater Electron*, vol. 25, no. 11, pp. 5158–5164, Nov. 2014, doi: 10.1007/s10854-014-2286-3.
- [121] Y. Shen, H. Zhu, R. Huang, L. Zhao, and S. Yan, "Synthesis and photochromic properties of WO₃ powder induced by oxalic acid," *Sci China B Chem*, vol. 52, no. 5, pp. 609–614, May 2009, doi: 10.1007/s11426-009-0095-y.
- [122] N. Lupu, "Electrodeposited nanowires and their applications," *InTech*, 2010. doi: 10.5772/39476.
- [123] B. Yang, H. Li, M. Blackford, and V. Luca, "Novel low density mesoporous WO₃ films prepared by electrodeposition," *Curr Appl Phys*, vol. 6, no. 3, pp. 436–439, Jun. 2006, doi: 10.1016/j.cap.2005.11.035.
- [124] T. Pauporté, "A simplified method for WO₃ electrodeposition," *J Electrochem Soc*, vol. 149, no. 11, p. C539, 2002, doi: 10.1149/1.1509070.
- [125] M. Deepa, M. Kar, and S. A. Agnihotry, "Electrodeposited tungsten oxide films: annealing effects on structure and electrochromic performance," *Thin Solid Films*, vol. 468, no. 1–2, pp. 32–42, Dec. 2004, doi: 10.1016/j.tsf.2004.04.056.

Chapter I: State-of-the-art and objectives

- [126] H. Dong, Y.-C. Chen, and C. Feldmann, "Polyol synthesis of nanoparticles: status and options regarding metals, oxides, chalcogenides, and non-metal elements," *Green Chem*, vol. 17, no. 8, pp. 4107–4132, 2015, doi: 10.1039/C5GC00943J.
- [127] J. Park, J. Joo, S. G. Kwon, Y. Jang, and T. Hyeon, "Synthesis of monodisperse spherical nanocrystals," *Angew Chem Int Ed*, vol. 46, no. 25, pp. 4630–4660, Jun. 2007, doi: 10.1002/anie.200603148.
- [128] F. Fievet, J. Lagier, B. Blin, B. Beaudon, and M. Figlazer, "Homogeneous and heterogeneous nucleations in the polyol process for the preparation of micron and submicron size metal particles," *Solid State Ion*, vol. 32–33, pp. 198–205, Feb. 1989, doi: 10.1016/0167-2738(89)90222-1.
- [129] C. G. Granqvist, "Handbook of inorganic electrochromic materials.," Elsevier, 1995. doi: 10.1016/B978-0-444-89930-9.X5000-4.
- [130] J. G. Speight, "Lange's handbook of chemistry", 17th Edition. New York: McGraw-Hill Education, 2017.
- [131] M. Bourdin et al., "Nanoparticles (NPs) of WO₃-type compounds by polyol route with enhanced electrochromic properties," *J Alloys Compd*, vol. 823, p. 153690, 2020, doi: <https://doi.org/10.1016/j.jallcom.2020.153690>.
- [132] P. Porkodi, V. Yegnaraman, and D. Jeyakumar, "Polyol mediated synthesis of tungsten trioxide and Ti doped tungsten trioxide," *Mater Res Bull*, vol. 41, no. 8, pp. 1476–1486, Aug. 2006, doi: 10.1016/j.materresbull.2006.01.030.
- [133] T. Akamatsu, T. Itoh, N. Izu, and W. Shin, "Preparation of WO₃ nanoplatelet-based microspheres and their NO₂ gas-sensing properties," *J Ceramic Soc Jpn*, vol. 122, no. 1428, pp. 674–678, 2014, doi: 10.2109/jcersj2.122.674.
- [134] C. Bechinger, G. Oefinger, S. Herminghaus, and P. Leiderer, "On the fundamental role of oxygen for the photochromic effect of WO₃," *J Appl Phys*, vol. 74, no. 7, pp. 4527–4533, Oct. 1993, doi: 10.1063/1.354370.
- [135] C. Bechinger, E. Wirth, and P. Leiderer, "Photochromic coloration of WO₃ with visible light," *Appl Phys Lett*, vol. 68, no. 20, pp. 2834–2836, May 1996, doi: 10.1063/1.116340.
- [136] M. Sun, N. Xu, Y. W. Cao, J. N. Yao, and E. G. Wang, "Nanocrystalline tungsten oxide thin film: preparation, microstructure, and photochromic behavior," *J Mater Res*, vol. 15, no. 4, pp. 927–933, Apr. 2000, doi: 10.1557/JMR.2000.0132.
- [137] B. W. Faughnan, R. S. Crandall, and M. A. Lampert, "Model for the bleaching of WO₃ electrochromic films by an electric field," *Appl Phys Lett*, vol. 27, no. 5, pp. 275–277, Sep. 1975, doi: 10.1063/1.88464.

Chapter I: State-of-the-art and objectives

- [138] Y. Yao et al., “WO₃ quantum-dots electrochromism,” *Nano Energy*, vol. 68, p. 104350, Feb. 2020, doi: 10.1016/j.nanoen.2019.104350.
- [139] A. Hasani et al., “Tungsten trioxide doped with CdSe quantum dots for smart windows,” *ACS Appl Mater Interfaces*, vol. 10, no. 50, pp. 43785–43791, Dec. 2018, doi: 10.1021/acsami.8b15183.
- [140] C. Liu et al., “Enhancing photoelectrochemical activity of CdS quantum dots sensitized WO₃ photoelectrodes by Mn doping,” *RSC Adv*, vol. 5, no. 45, pp. 35506–35512, 2015, doi: 10.1039/C5RA01787D.
- [141] A. Azam et al., “Two-dimensional WO₃ nanosheets chemically converted from layered WS₂ for high-performance electrochromic devices,” *Nano Lett*, vol. 18, no. 9, pp. 5646–5651, Sep. 2018, doi: 10.1021/acs.nanolett.8b02150.
- [142] T. G. Novak, J. Kim, P. A. DeSario, and S. Jeon, “Synthesis and applications of WO₃ nanosheets: the importance of phase, stoichiometry, and aspect ratio,” *Nanoscale Adv*, vol. 3, no. 18, pp. 5166–5182, 2021, doi: 10.1039/D1NA00384D.
- [143] S. Wang, S. V. Kershaw, G. Li, and M. K. H. Leung, “The self-assembly synthesis of tungsten oxide quantum dots with enhanced optical properties,” *J Mater Chem C Mater*, vol. 3, no. 14, pp. 3280–3285, 2015, doi: 10.1039/C5TC00278H.
- [144] K. Fukuda et al., “Exfoliated nanosheet crystallite of cesium tungstate with 2D pyrochlore structure: synthesis, characterization, and photochromic properties,” *ACS Nano*, vol. 2, no. 8, pp. 1689–1695, Aug. 2008, doi: 10.1021/nm800184w.
- [145] X. Dong et al., “Rational modification in the photochromic and self-bleaching performance of hierarchical microsphere Cu@h-WO₃/WO₃·nH₂O composites,” *Solar Energy Mater Solar Cells*, vol. 219, p. 110784, Jan. 2021, doi: 10.1016/j.solmat.2020.110784.
- [146] H. Miyazaki, M. Inada, H. Susiki, and T. Ota, “Molybdenum doping effects on photochromic properties of WO₃ based composite films,” *J Ceram Soc Jpn*, vol. 121, no. 1409, pp. 106–108, 2013, doi: 10.2109/jcersj2.121.106.
- [147] C. Avellaneda, “Photochromic properties of WO₃ and WO_{3-x} (X=Ti, Nb, Ta and Zr) thin films,” *Solid State Ion*, vol. 165, no. 1–4, pp. 117–121, Dec. 2003, doi: 10.1016/j.ssi.2003.08.023.
- [148] Y. Shen et al., “Hydrothermal synthesis and studies on photochromic properties of Al doped WO₃ powder,” *J Alloys Compd*, vol. 629, pp. 27–31, Apr. 2015, doi: 10.1016/j.jallcom.2014.11.218.
- [149] S. K. Deb, “Optical and photoelectric properties and colour centres in thin films of tungsten oxide,” *Philosophical Magazine*, vol. 27, no. 4, pp. 801–822, Apr. 1973, doi: 10.1080/14786437308227562.

Chapter I: State-of-the-art and objectives

- [150] T. He and J. Yao, "Photochromic materials based on tungsten oxide," *J Mater Chem*, vol. 17, no. 43, p. 4547, 2007, doi: 10.1039/b709380b.
- [151] S. Wang, W. Fan, Z. Liu, A. Yu, and X. Jiang, "Advances on tungsten oxide based photochromic materials: strategies to improve their photochromic properties," *J Mater Chem C Mater*, vol. 6, no. 2, pp. 191–212, 2018, doi: 10.1039/C7TC04189F.
- [152] T. He, Y. Ma, Y. Cao, W. Yang, and J. Yao, "Improved photochromism of WO₃ thin films by addition of Au nanoparticles," *Phys Chem Phys*, vol. 4, no. 9, pp. 1637–1639, Apr. 2002, doi: 10.1039/b108531j.
- [153] J. N. Yao, Y. A. Yang, and B. H. Loo, "Enhancement of photochromism and electrochromism in MoO₃/Au and MoO₃/Pt thin films," *J Phys Chem B*, vol. 102, no. 11, pp. 1856–1860, Mar. 1998, doi: 10.1021/jp972217u.
- [154] T. He et al., "Enhancement effect of gold nanoparticles on the UV-light photochromism of molybdenum trioxide thin films," *Langmuir*, vol. 17, no. 26, pp. 8024–8027, Dec. 2001, doi: 10.1021/la010671q.
- [155] A. L. Linsebigler, G. Lu, and J. T. Yates, "Photocatalysis on TiO₂ Surfaces: Principles, Mechanisms, and Selected Results," *Chem Rev*, vol. 95, no. 3, pp. 735–758, May 1995, doi: 10.1021/cr00035a013.
- [156] M. A. Fox and M. Dulay, "Heterogeneous photocatalysis," *Chem Rev*, vol. 93, no. 1, pp. 341–357, Jan. 1993, doi: 10.1021/cr00017a016.
- [157] G. Kickelbick and U. Schubert, "Organic functionalization of metal oxide nanoparticles," *Chem Inform*, vol. 35, no. 1, Jan. 2004, doi: 10.1002/chin.200401218.
- [158] M.-A. Neouze and U. Schubert, "Surface modification and functionalization of metal and metal oxide nanoparticles by organic ligands," *Monatsh Chem*, vol. 139, no. 3, pp. 183–195, Mar. 2008, doi: 10.1007/s00706-007-0775-2.
- [159] F. H. Li et al., "Covalent attachment of diamondoid phosphonic acid dichlorides to tungsten oxide surfaces," *Langmuir*, vol. 29, no. 31, pp. 9790–9797, Aug. 2013, doi: 10.1021/la401781e.
- [160] Q. Liu, C. Hu, and X. Wang, "Hydrothermal synthesis of oxygen-deficiency tungsten oxide quantum dots with excellent photochromic reversibility," *Appl Surf Sci*, 2019.
- [161] S. Cong, Y. Tian, Q. Li, Z. Zhao, and F. Geng, "Single-crystalline tungsten oxide quantum dots for fast pseudocapacitor and electrochromic applications," *Adv Mater*, vol. 26, no. 25, pp. 4260–4267, Jul. 2014, doi: 10.1002/adma.201400447.

Chapter I: State-of-the-art and objectives

- [162] J. L. Wang, J. W. Liu, S. Z. Sheng, Z. He, J. Gao, and S. H. Yu, "Manipulating nanowire assemblies toward multicolor transparent electrochromic device," *Nano Lett*, vol. 21, no. 21, pp. 9203–9209, Nov. 2021, doi: 10.1021/acs.nanolett.1c03061.
- [163] M.-H. Jo, K.-H. Kim, and H.-J. Ahn, "P-doped carbon quantum dot graft-functionalized amorphous WO₃ for stable and flexible electrochromic energy-storage devices," *Chem Eng J*, vol. 445, p. 136826, Oct. 2022, doi: 10.1016/j.cej.2022.136826.
- [164] J. Chu et al., "Facile fabrication of WO₃ crystalline nanoplate on FTO glass and their application in electrochromism," *Micro Nano Lett*, vol. 11, no. 11, pp. 749–752, Nov. 2016, doi: 10.1049/mnl.2016.0199.
- [165] Z. Jiao, J. Wang, L. Ke, X. W. Sun, and H. V. Demir, "Morphology-tailored synthesis of tungsten trioxide (hydrate) thin films and their photocatalytic properties," *ACS Appl Mater Interfaces*, vol. 3, no. 2, pp. 229–236, Feb. 2011, doi: 10.1021/am100875z.
- [166] Y. Li, W. A. McMaster, H. Wei, D. Chen, and R. A. Caruso, "Enhanced electrochromic properties of WO₃ nanotree-like structures synthesized via a two-step solvothermal process showing promise for electrochromic window application," *ACS Appl Nano Mater*, vol. 1, no. 6, pp. 2552–2558, Jun. 2018, doi: 10.1021/acsanm.8b00190.
- [167] K. Tajima, H. Hotta, Y. Yamada, M. Okada, and K. Yoshimura, "Electrochromic switchable mirror glass fabricated using adhesive electrolyte layer," *Appl Phys Lett*, vol. 101, no. 25, p. 251907, Dec. 2012, doi: 10.1063/1.4772938.
- [168] S. Yamazaki, K. Isoyama, and D. Shimizu, "Visualization of ultraviolet irradiation using WO₃-cellulose derivatives composite film," *Opt Mater (Amst)*, vol. 106, p. 109929, Aug. 2020, doi: 10.1016/j.optmat.2020.109929.
- [169] O. L. Evdokimova et al., "Highly reversible photochromism in composite WO₃/nanocellulose films," *Cellulose*, vol. 26, no. 17, pp. 9095–9105, Nov. 2019, doi: 10.1007/s10570-019-02716-2.
- [170] L.-M. Ai, W. Feng, J. Chen, Y. Liu, and W. Cai, "Evaluation of microstructure and photochromic behavior of polyvinyl alcohol nanocomposite films containing polyoxometalates," *Mater Chem Phys*, vol. 109, no. 1, pp. 131–136, May 2008, doi: 10.1016/j.matchemphys.2007.11.002.
- [171] S. Songara et al., "Tuning of crystal phase structure in hydrated WO₃ nanoparticles under wet chemical conditions and studies on their photochromic properties," *J Phys Chem Solids*, vol. 73, no. 7, pp. 851–857, Jul. 2012, doi: 10.1016/j.jpcs.2012.02.020.
- [172] A. L. Popov et al., "PVP-stabilized tungsten oxide nanoparticles: pH sensitive anti-cancer platform with high cytotoxicity," *Mater Sci Eng: C*, vol. 108, p. 110494, Mar. 2020, doi: 10.1016/j.msec.2019.110494.

Chapter I: State-of-the-art and objectives

- [173] R. Li et al., “Enhanced coloration/bleaching photochromic performance of WO₃ based on PVP/PU composite matrix,” *Chem Select*, vol. 4, no. 33, pp. 9817–9821, Sep. 2019, doi: 10.1002/slct.201902068.
- [174] M. Faustini, L. Nicole, E. Ruiz-Hitzky, and C. Sanchez, “History of organic-inorganic hybrid materials: prehistory, art, science, and advanced applications,” *Adv Funct Mater*, vol. 28, no. 27, p. 1704158, Jul. 2018, doi: 10.1002/adfm.201704158.
- [175] N. Li, M. Huo, M. Li, T. Li, J. Zhou, and J. Zhang, “Photochromic thermoplastics doped with nanostructured tungsten trioxide,” *New J Chem*, vol. 42, no. 13, pp. 10885–10890, 2018, doi: 10.1039/C8NJ01531G.
- [176] T. Sangpraserdsuk, M. Phiriyawirut, P. Ngaotrakanwivat, and J. Wootthikanokkhan, “Mechanical, optical, and photochromic properties of polycarbonate composites reinforced with nano-tungsten trioxide particles,” *J Reinforced Plast Compos*, vol. 36, no. 16, pp. 1168–1182, Aug. 2017, doi: 10.1177/0731684417710107.
- [177] T. J. DeJournett and J. B. Spicer, “The influence of oxygen on the microstructural, optical and photochromic properties of polymer-matrix, tungsten-oxide nanocomposite films,” *Solar Energy Mater Solar Cells*, vol. 120, pp. 102–108, Jan. 2014, doi: 10.1016/j.solmat.2013.08.023.
- [178] N. I. Cherkashina, “Stability of polymer composites with tungsten oxide against electron irradiation,” *Tech Phys*, vol. 65, no. 1, pp. 107–113, Jan. 2020, doi: 10.1134/S1063784220010028.
- [179] G. F. Cai, J. P. Tu, D. Zhou, J. H. Zhang, X. L. Wang, and C. D. Gu, “Dual electrochromic film based on WO₃/polyaniline core/shell nanowire array,” *Solar Energy Mater Solar Cells*, vol. 122, pp. 51–58, Mar. 2014, doi: 10.1016/j.solmat.2013.11.015.
- [180] H. Ling, L. Liu, P. S. Lee, D. Mandler, and X. Lu, “Layer-by-layer assembly of PEDOT: PSS and WO₃ nanoparticles: enhanced electrochromic coloration efficiency and mechanism studies by scanning electrochemical microscopy,” *Electrochim Acta*, vol. 174, pp. 57–65, Aug. 2015, doi: 10.1016/j.electacta.2015.05.147.
- [181] S. Zhang, S. Cao, T. Zhang, Q. Yao, A. Fisher, and J. Y. Lee, “Monoclinic oxygen-deficient tungsten oxide nanowires for dynamic and independent control of near-infrared and visible light transmittance,” *Mater Horiz*, vol. 5, no. 2, pp. 291–297, 2018, doi: 10.1039/C7MH01128H.
- [182] B. Moshofsky and T. Mokari, “Length and diameter control of ultrathin nanowires of substoichiometric tungsten oxide with insights into the growth mechanism,” *Chem Mater*, vol. 25, no. 8, pp. 1384–1391, Apr. 2013, doi: 10.1021/cm302015z.
- [183] H. Gu et al., “Highly efficient, near-infrared and visible light modulated electrochromic devices based on polyoxometalates and W₁₈O₄₉ nanowires,” *ACS Nano*, vol. 12, no. 1, pp. 559–567, Jan. 2018, doi: 10.1021/acsnano.7b07360.

Chapter I: State-of-the-art and objectives

- [184] B. N. Reddy, P. N. Kumar, and M. Deepa, "A Poly(3,4-ethylenedioxyppyrrrole)-Au@WO₃ - based electrochromic pseudo capacitor," *Chem Phys Chem*, vol. 16, no. 2, pp. 377–389, Feb. 2015, doi: 10.1002/cphc.201402625.
- [185] J. Wei, X. Jiao, T. Wang, and D. Chen, "Electrospun photochromic hybrid membranes for flexible rewritable media," *ACS Appl Mater Interfaces*, vol. 8, no. 43, pp. 29713–29720, Nov. 2016, doi: 10.1021/acsami.6b10620.
- [186] B. Zhang, R. Liu, Y. Pan, Q. Wang, and B. Liu, "Cellulose-based WO₃ nanocomposites prepared by a sol–gel method at low temperature," *IOP Conf Ser Mater Sci Eng*, vol. 301, p. 012075, Jan. 2018, doi: 10.1088/1757-899X/301/1/012075.
- [187] Z. Ling et al., "Continuous and rapid fabrication of photochromic fibers by facilely coating tungsten oxide/polyvinyl alcohol composites," *RSC Adv*, vol. 8, no. 50, pp. 28581–28587, 2018, doi: 10.1039/C8RA05170D.
- [188] R. Giannuzzi et al., "Photochromic textiles based upon aqueous blends of oxygen-deficient WO_{3-x} and TiO₂ nanocrystals," *Textiles*, vol. 2, no. 3, pp. 382–394, 2022, doi: 10.3390/textiles2030021.
- [189] D. G. Bekas, Y. Hou, Y. Liu, and A. Panesar, "3D printing to enable multifunctionality in polymer-based composites: A review," *Compos B Eng*, vol. 179, p. 107540, Dec. 2019, doi: 10.1016/j.compositesb.2019.107540.
- [190] M. Fera, F. Fruggiero, A. Lambiase, and R. Macchiaroni, "State of the art of additive manufacturing: Review for tolerances, mechanical resistance and production costs," *Cogent Eng*, vol. 3, no. 1, p. 1261503, Dec. 2016, doi: 10.1080/23311916.2016.1261503.
- [191] H. Zhu, H. Ou, and A. Popov, "Incremental sheet forming of thermoplastics: a review," *The International Journal of Advanced Manufacturing Technology*, vol. 111, no. 1–2, pp. 565–587, Nov. 2020, doi: 10.1007/s00170-020-06056-5.
- [192] T. D. Ngo, A. Kashani, G. Imbalzano, K. T. Q. Nguyen, and D. Hui, "Additive manufacturing (3D printing): A review of materials, methods, applications and challenges," *Compos B Eng*, vol. 143, pp. 172–196, Jun. 2018, doi: 10.1016/j.compositesb.2018.02.012.
- [193] B. I. Oladapo, S. A. Zahedi, and A. O. M. Adeoye, "3D printing of bone scaffolds with hybrid biomaterials," *Compos B Eng*, vol. 158, pp. 428–436, Feb. 2019, doi: 10.1016/j.compositesb.2018.09.065.
- [194] H. Wang, H. Wang, W. Zhang, and J. K. W. Yang, "Toward near-perfect diffractive optical elements via nanoscale 3d printing," *ACS Nano*, vol. 14, no. 8, pp. 10452–10461, Aug. 2020, doi: 10.1021/acsnano.0c04313.

Chapter I: State-of-the-art and objectives

- [195] K. T. Q. Nguyen, S. Navaratnam, P. Mendis, K. Zhang, J. Barnett, and H. Wang, “Fire safety of composites in prefabricated buildings: From fibre reinforced polymer to textile reinforced concrete,” *Compos B Eng*, vol. 187, p. 107815, Apr. 2020, doi: 10.1016/j.compositesb.2020.107815.
- [196] K. Song, Y. Zhang, and M. L. Minus, “Polymer interphase self-reinforcement and strengthening mechanisms in low-loaded nanocomposite fibers,” *Macromol Chem Phys*, vol. 216, no. 12, pp. 1313–1320, Jun. 2015, doi: 10.1002/macp.201500011.
- [197] W. Xu et al., “3D printing for polymer/particle-based processing: A review,” *Compos B Eng*, vol. 223, p. 109102, Oct. 2021, doi: 10.1016/j.compositesb.2021.109102.
- [198] K. Song et al., “Structural polymer-based carbon nanotube composite fibers: understanding the processing–structure–performance relationship,” *Materials*, vol. 6, no. 6, pp. 2543–2577, Jun. 2013, doi: 10.3390/ma6062543.
- [199] S. Mubarak, D. Dhamodharan, and H.-S. Byun, “Recent advances in 3D printed electrode materials for electrochemical energy storage devices,” *J Energy Chem*, vol. 81, pp. 272–312, Jun. 2023, doi: 10.1016/j.jechem.2023.01.037.
- [200] Y. Li et al., “Isotropic stereolithography resin toughened by core-shell particles,” *Chem Engineering J*, vol. 394, p. 124873, Aug. 2020, doi: 10.1016/j.cej.2020.124873.
- [201] O. Guillaume et al., “Surface-enrichment with hydroxyapatite nanoparticles in stereolithography-fabricated composite polymer scaffolds promotes bone repair,” *Acta Biomater*, vol. 54, pp. 386–398, May 2017, doi: 10.1016/j.actbio.2017.03.006.
- [202] J. Hector Sandoval and R. B. Wicker, “Functionalizing stereolithography resins: effects of dispersed multi-walled carbon nanotubes on physical properties,” *Rapid Prototyp J*, vol. 12, no. 5, pp. 292–303, Oct. 2006, doi: 10.1108/13552540610707059.
- [203] V. V. Shinde, A.-D. Celestine, L. E. Beckingham, and B. S. Beckingham, “Stereolithography 3D printing of microcapsule catalyst-based self-healing composites,” *ACS Appl Polym Mater*, vol. 2, no. 11, pp. 5048–5057, Nov. 2020, doi: 10.1021/acsapm.0c00872.
- [204] M. Korey et al., “Recycling polymer composite granulate/regrind using big area additive manufacturing,” *Compos B Eng*, vol. 256, p. 110652, May 2023, doi: 10.1016/j.compositesb.2023.110652.
- [205] T. N. A. T. Rahim, A. M. Abdullah, and H. Md Akil, “Recent developments in fused deposition modeling-based 3d printing of polymers and their composites,” *Polymer Rev*, vol. 59, no. 4, pp. 589–624, Oct. 2019, doi: 10.1080/15583724.2019.1597883.

Chapter I: State-of-the-art and objectives

- [206] S. Jambhulkar, W. Xu, R. Franklin, D. Ravichandran, Y. Zhu, and K. Song, “Integrating 3D printing and self-assembly for layered polymer/nanoparticle microstructures as high-performance sensors,” *J Mater Chem C Mater*, vol. 8, no. 28, pp. 9495–9501, 2020, doi: 10.1039/D0TC02660C.
- [207] H. Uematsu, Y. Suzuki, Y. Iemoto, and S. Tanoue, “Effect of maleic anhydride-grafted polypropylene on the flow orientation of short glass fiber in molten polypropylene and on tensile properties of composites,” *Adv Polym Technol*, vol. 37, no. 6, pp. 1755–1763, Oct. 2018, doi: 10.1002/adv.21834.
- [208] M. H. Wankhade and S. G. Bahaley, “Design and development of plastic filament extruder for 3D Printing,” *IRA Int J Technol Eng*, vol. 10, no. 3, p. 23, May 2018, doi: 10.21013/jte. v10.n3.p1.
- [209] T. Hachimi, N. Naboulsi, F. Majid, R. Rhanim, I. Mrani, and H. Rhanim, “Design and Manufacturing of a 3D printer filaments extruder,” *Proc Struct Integrity*, vol. 33, pp. 907–916, 2021, doi: 10.1016/j.prostr.2021.10.101.
- [210] X. Wang, M. Jiang, Z. Zhou, J. Gou, and D. Hui, “3D printing of polymer matrix composites: A review and prospective,” *Compos B Eng*, vol. 110, pp. 442–458, Feb. 2017, doi: 10.1016/j.compositesb.2016.11.034.
- [211] W. Liu, J. Zhou, Y. Ma, J. Wang, and J. Xu, “Fabrication of PLA filaments and its printable performance,” *IOP Conf Ser Mater Sci Eng*, vol. 275, p. 012033, Dec. 2017, doi: 10.1088/1757

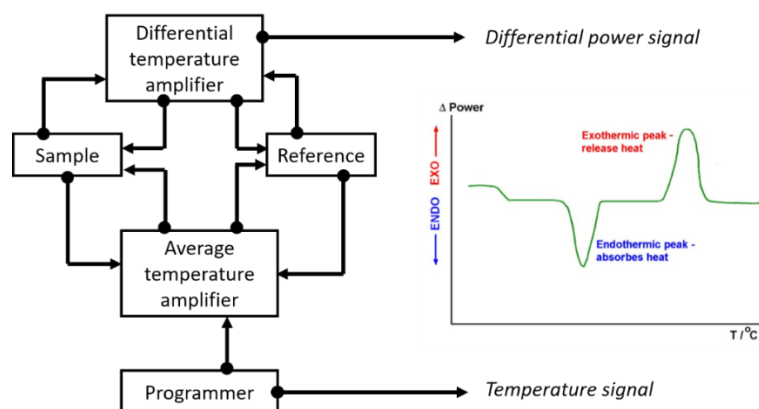
Chapter II: Characterization techniques

Chapter II: Characterization techniques

1 Characterizations Techniques :

1.1 Differential Scanning Calorimetry (DSC)

Differential scanning calorimetry (DSC) is a technique for calculating the amount of energy necessary to reduce the temperature difference between a substance and an inert reference material. This is accomplished by submitting both specimens to the same controlled temperature settings in a temperature-controlled facility (Figure 1). DSC determines the temperature at which these transitions take place and measures the quantity of heat involved. This technique yields useful quantitative data on physical and chemical changes involving endothermic or exothermic processes, as well as changes in heat capacity. DSC is commonly used to analyze polymers, organic compounds, and inorganic materials. The DSC concept incorporates a thermo-analytical approach in which the difference in heat required to raise the temperature of a sample relative to a reference material is assessed as a function of temperature. This difference in heat flow presents itself in two ways: (i) the sample's baseline heat capacity, which increases with temperature, and (ii) transitions within the sample, which are depicted as events overlaid on the baseline heat capacity.



Chpt.II-Figure 1: Differential scanning calorimetry (DSC).

In this work, differential scanning calorimetry (DSC) experiment was performed using Perkin-Elmer DSC 8000.

1.2 Melt flow index (MFI)

The melt flow index (MFI) measures the flowability of a thermoplastic polymer melt. It is calculated by measuring the amount of polymer that flows through a given capillary in ten minutes at a constant temperature and pressure. Polymer processors frequently utilize the MFI value to identify the proper polymer grade for various processes. The MFI result is typically stated in grams per ten minutes (g/10min), whereas the test load conditions are specified in kilograms.

In this work:

MFI was measured according to the ASTM D1238 standard using the Dynisco Polymer Test Model. We used the ASTM D1238 standard for Melt Flow Index MFI testing. Prior to measurement, the prepared cylindrical preforms were cut into small pieces to facilitate their loading into the melt

Chapter II: Characterization techniques

indexer machine (MIM) entrance. The MIM was preheated at 130 °C for around 30 min and then 5 g of the sample was loaded in the MIM. A weight load of 2.2 kg was set up on the piston, and a stopwatch was used to monitor the weight of the extruded filament for 10 mins.

1.3 Mechanical Profilometer

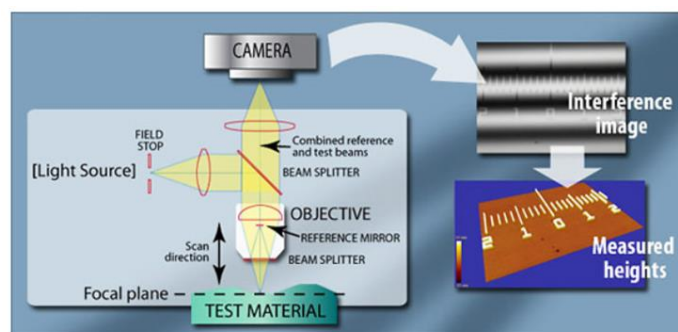
A mechanical profilometer is used to detect surface profiles by measuring the relative height variation of a stylus in contact with the surface of a sample while moving the sample along an axis. The sample and stylus are visualized via a camera. The measurement analysis allows for the determination of several parameters, such as the height of a "step" (such as the etch depth or thickness of a lithographically formed layer), surface roughness, and the radius of curvature of a sample.

In this work:

The Dektat 6M by Veeco is the profilometer used for measuring the thickness of the solvent-casted films.

1.4 Optical Profilometer

A Mirau interferometer is used in this apparatus, which comprises a semi-reflective plate placed in front of a long-distance objective lens. The incident wave is divided into two beams, each with its geometric path. One beam targets the surface of the object under observation, while the other serves as a reference beam. The reflected wave has a phase change due to the sample's height. The resulting interference between the two beams is then processed by digital software as shown in Figure 2. There are two measurement modes: Vertical Shift Interference (VSI) mode for heights greater than 150 nm, and Phase Shift Interference (PSI) mode for heights less than 150 nm. In VSI mode, the objective lens moves in the z-direction to observe the interferences on each plane of the sample, thereby determining the interplanar height. In PSI mode, the objective lens remains stationary, and the phase variations caused by small height variations are studied. The theoretical resolution of the instrument is 2 nm. The software associated with the measurement device allows for the determination of various topographical parameters, such as the surface roughness coefficient (R_a).



Chpt.II-Figure 2: Optical profilometer measurement principle.

In this work:

Thickness measurements were carried out with a three-dimensional optical interferometric profilometer, the Veeco WYCO NT1100 model.

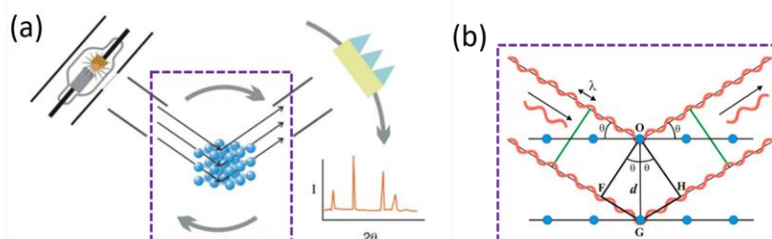
Chapter II: Characterization techniques

1.5 X-ray diffraction (XRD) analyses

A common analysis utilized in material science is X-ray diffraction (XRD), an effective characterization technique used to investigate the crystalline structure of materials that demonstrate long-range order. It also gives insight into purity and offers a quantitative analysis of the phases.

1.5.1 Bragg's Law

The concept proposes that X-rays reflect on the surface of hypothetical "mirrors" produced by atomic planes within the crystal lattice, causing Bragg's diffraction. These atomic planes are represented by horizontal lines with scattering centers (represented in Figure 3a as blue circles). As a result of the repeating nature of the crystal, these planes are consistently spaced at a distance designated as d , as seen in Figure 3.b. A wave front is formed when two X-ray beams with wavelengths (λ) arrive in phase at their respective atomic planes with an angle of incidence. To obtain a cooperative effect, after reflection, both X-ray beams should still be in phase, a situation that will only happen if the difference of path traveled by the wave fronts corresponds with an integer number of wavelengths. This condition is $2d_{hkl}\sin(\theta) = n\lambda$. Here, d_{hkl} represents the distance between two crystallographic planes, θ is the Bragg angle, n denotes the order of reflection and λ is the wavelength of the X-ray beam.



Chpt.II-Figure 3: Bragg's law: scattering and diffraction.

In this work:

Routine diffractograms are obtained at the ICMCB using a PANalytical X'pert MDP-PRO diffractometer with a Bragg-Brentano θ - θ geometry. The instrument is equipped with a graphite back-reflection monochromator, spinner, and sample changer with a capacity of 3x15 positions. X-ray radiation is generated from a copper source (average $K\alpha = 1.5418 \text{ \AA}$). The operating voltage is set at 45 kV, and the intensity at 40 mA. Data collection is performed over a range of diffraction angles (2θ) from 8° to 80° , with an acquisition time of 30 minutes. Sample preparation involves depositing the powdered material onto an aluminum sample holder and compacting the powder using a glass slide to ensure mechanical stability and reproducibility of the results.

For structural characterizations, data is collected using a similar setup to the routine analyses. However, a front-end germanium monochromator is added to obtain monochromatic radiation ($K\alpha = 1.5406$). In this case, sample preparation is more complicated. The powder distribution is achieved using a razor blade instead of compacting with a glass slide to avoid preferential grain orientation on the surface. Acquiring diffractograms over long counting durations allows for profile refining using the Le Bail method and atomic location determination using the Rietveld method.

Chapter II: Characterization techniques

1.5.2 FullProf Refinement

The Le Bail technique computes the average profile function of diffraction peaks and lattice parameters. This approach requires prior knowledge of the space group and the determination of the lattice parameters of the researched material. The Rietveld refinement of the XRD pattern is one of the crystallographic techniques used to derive information such as crystal structure (precise quantification of unit-cell characteristics), local defects such as vacancies, interstitial site occupancies from doping ions, and so on. FullProf is a Rietveld analysis (structure profile refinement) software that analyses X-ray powder diffraction data as a function of the scattering variable T (2-theta or TOF). The program can also be used as a Profile Matching tool without knowing the structure (i.e., peak intensities can be freely changed for the best fit between predicted and observed patterns: La Bail fitting step).

By refining the scale factor (K) and peak intensities according to Friedel's law ($I_{hkl} \propto K \cdot |F_{hkl}|^2$, where $|F_{hkl}|^2$ represents the squared modulus of the structure factor), the Rietveld refinement method is used to calculate atomic locations (and their occupancy) and isotropic displacement parameters (denoted as B_{iso}). This analysis can provide crystallographic information about the phase(s), such as the space group, lattice parameters (a , b , c), and angles (α , β , γ), as well as the atomic or Wyckoff positions. Furthermore, for qualitative analysis, the Rietveld refinement process is used to quantify the weight % of different phases. The refinement method can be used to determine the weight fraction of each phase. Si, LaB_6 , and Al_2O_3 phases are frequently employed as weight references.

1.5.3 Limitations of Bragg's law on nanoparticles

Powder diffraction measurements are now frequent and have become routine, rapid, and automated. However, the analysis of nanoparticle powders faces difficulties due to their divergence from crystalline order. For example, the assumption of infinite crystal domains no longer applies below 50 nm. This deviation is caused by the change of the great broadening of Bragg peaks due to crystalline defects. Peak broadening theoretical models have limits, particularly when dealing with extremely disordered nanoparticle powders. The loss of information content makes phase identification and discrimination of broadening effects, such as strain, structural flaws, and size non-uniformity, difficult.

1.5.4 Total scattering approach to nanoparticles structure description

Researchers have conducted extensive research to determine the atomic structure of these nanostructured materials to understand why they behave differently than bulk crystals. The influence of their finite size, which modifies their electrical structure, is one critical aspect leading to their distinctive behavior [1]. Furthermore, the huge number of atoms on the surface induces strain effects and gives rise to a variety of unique crystal defects, causing them to display structural features that differ from their bulk counterparts [2]. The intensity of dispersed radiation becomes diffuse as a result of these defects and aperiodic effects. This diffuse scattering, like the constructive interferences seen in Bragg scattering, includes useful information. Total Scattering methods are approaches that treat both diffuse and Bragg scattering data equally, providing a comprehensive knowledge of the scatterer.

Chapter II: Characterization techniques

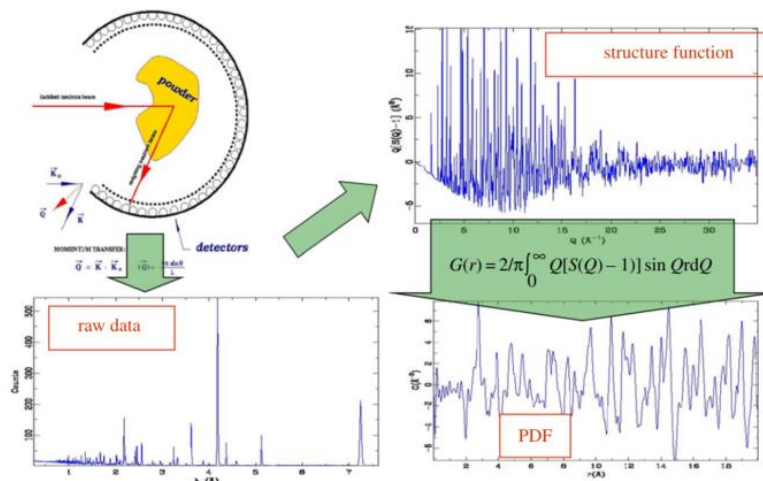
1.5.5 Pair Distribution Function analysis

Pair Distribution Function (PDF) analysis is one of the fundamental branches of total scattering analysis. Developed in the 1930s by Warren *et al.*, the technique was initially used to analyze liquids and amorphous materials [3]. The PDF is calculated by averaging the entire scattering pattern of a powder sample across all directions. It indicates the probability of finding pairs of atoms at specified distances in actual space. Mathematically, the PDF is defined as follows:

$$G(r) = \frac{2}{\pi} \int_{Q_{min}}^{Q_{max}} Q[S(Q) - 1] \sin(Qr) dQ \quad \text{Chpt.II-Equation 1}$$

$G(r)$ is one of the correlation functions that exist in the literature and contains the same information about the short- and long-range structure [4]. The scattering vector's magnitude, Q , is described as $Q = 4\pi \sin(\theta)/\lambda$, where θ represents half of the scattering angle, 2θ , and λ represents the wavelength of the X-rays. It is preferable to measure Q at the greatest attainable values in complete scattering experiments, potentially reaching $Q = 30 \text{ (\AA}^{-1}\text{)}$ or much higher. The PDF equation is essentially a sine Fourier transform of a whole coherent scattering function $S(Q)$ from Q_{min} to Q_{max} which can be obtained by normalizing the experimental data to the total scattering cross-section, i.e., the square of the average atomic scattering factor.

Multiple adjustments are used to total scattering data to obtain the Pair Distribution Function (PDF), as detailed in reference [1], [2]. The final step in obtaining the PDF, however, is to conduct a Fourier transform. Figure 4 shows a schematic representation of this procedure. In the bottom right panel, the PDF function represents the chance of detecting a pair of atoms separated by a distance, r . The PDF function is simple to understand since the peaks correspond to actual interatomic distances within the material.



Chpt.II-Figure 4: Top left: A powder or nanoparticulate sample is exposed to a powerful X-ray or neutron beam at the upper left, and the intensity is recorded as a function of angle. This produces a raw diffraction pattern (bottom left) that includes a variety of measurement effects. The signal is then normalized and corrected for instrumental aberrations, yielding the reduced structure-function, $F(Q) = Q[S(Q)-1]$ (top right), where Q represents the momentum transferred during scattering. The PDF (bottom right), $G(r)$, is obtained from $F(Q)$ using a Fourier transform relationship indicated in the diagram. [2]

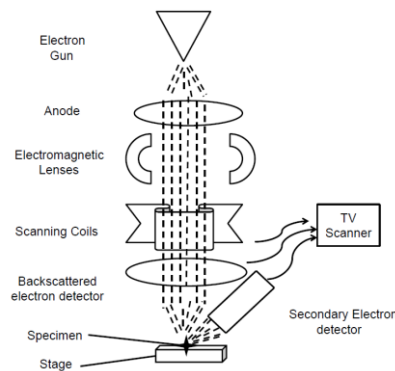
Chapter II: Characterization techniques

In this work:

For our samples: The total scattering data, necessary for the pair distribution function (PDF) analyses, were collected at the high energy (76.7 keV - Q_{\max} up to 40 \AA^{-1}) XPDF i15-1 beamline of Diamond Synchrotron (United Kingdom) using the rapid access program. The samples were packed into 1.0 mm diameter glass capillaries and mounted on the beamline goniometer to perform the measurements at room temperature. Data sets were collected using a Perkin Elmer 2D detector and processed with the DAWN and GudrunX software packages to obtain the differential correlation function ($D(r)$). These data were latter fitted in the real-space $D(r)$ with the TOPAS v6 software package using a dQ_{damping} macro term of 0.075 [5]. Unit cell lattice parameters, beta angle, tungsten atomic site positions, and spherical crystallite domain diameter sizes were refined.

1.6 Scanning Electron Microscope (SEM)

SEM is a laboratory tool that provides detailed images (at the scale of tens of nanometres) of a sample with a large depth of field. The principle of the apparatus relies on scanning the surface of the sample with an electron beam. Due to the electron bombardment, the material emits particles that can be X-ray photons or secondary electrons, backscattered electrons, or Auger electrons, depending on the nature of the electron-matter interaction. Detecting these particles provides access to multiple pieces of information. The most common consists in obtaining an image of the sample through the collection of secondary electrons. X-ray photons and backscattered or Auger electrons provide information about the chemical nature of the studied sample. The electron source can be a tungsten filament, a LaB6 crystal, or a field emission gun. Focusing and scanning of the electron beam are achieved by electron lenses, which play a similar role to optical lenses in an optical microscope. Specifically, the lenses consist of coils through which current passes. Schematically, an SEM typically consists of an electron gun and an electron column that produces a fine electron beam traversing the sample Figure 5. The equipment includes a specimen stage for moving the sample in three spatial directions and detectors for capturing and analyzing the radiations emitted by the sample after scanning. To ensure the lifespan of the electron gun and the quality of the beam, the entire column must be maintained under a high vacuum.



Chpt.II-Figure 5: Schematic of SEM device main parts [6].

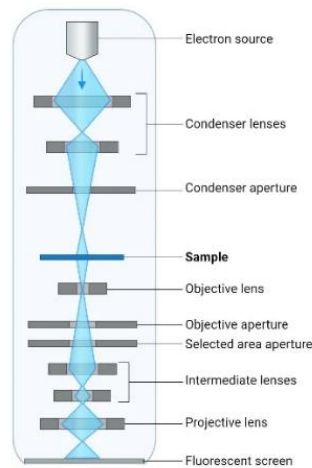
In this work:

Chapter II: Characterization techniques

The equipment used for SEM observations is a TESCAN Vega II SBH microscope and JEOL JSM-6700F.

1.7 Transmission electron microscopy (TEM)

TEM is used to reveal sub-micrometer, internal fine structure in solids. The interaction of the electron beam with the atoms in the sample produces a variety of radiation. While the transmitted beam is often the focus of observations, studying the emitted X-rays provides additional information on the sample's composition. The electron microscope is composed of a column with key components including the electron gun, electromagnetic lenses, and various detectors. Electrons are emitted from a source (LaB₆, tungsten) or a field emission gun, then accelerated in a vacuum-column to energies ranging from 10 keV to 3 MeV. They then pass through a condenser system and are focused by magnetic lenses. The electrons then traverse the sample, which should not exceed a thickness of 100 nm to ensure that the electrons do not lose all their energy. The object is then focused by the objective system. The microscope is also equipped with a projection lens system to transfer the image to the screen and perform magnification operations (Figure 6).



Chpt.II-Figure 6: Schematic of TEM device main parts.

In this work with the collaboration of Placamatt lab in ICMCB, High-Resolution Transmission Electron Microscopy (HRTEM, JEOL 2200FS, operating at 200 kV) is used.

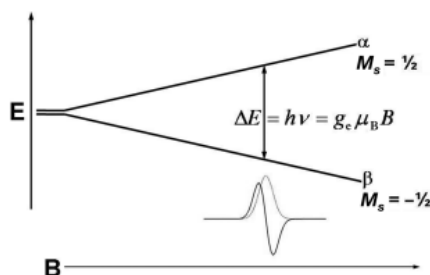
1.8 Electron Paramagnetic Resonance (EPR)

The EPR technique, created in 1944 by Soviet physicist Yevgeny Zavoisky, is used to characterize species containing unpaired electrons, such as radicals, transition elements, and structural flaws. The approach is based on the Zeeman effect, which asserts that in the presence of an external magnetic field, the energy levels of spin states become non-degenerated, giving rise to $2S+1$ unique levels. The existence of two Zeeman levels and the ability to induce transitions from the lower to higher energy levels is the foundation of EPR spectroscopy.

For a species with a single unpaired electron ($S = 1/2$), the presence of external magnetic field results in the emergence of two states ($M_s = +1/2$ and $M_s = -1/2$) (Figure 7). If the resonance requirement is met,

Chapter II: Characterization techniques

the absorption energy of the electromagnetic wave is equal to the energy difference between these two levels, as shown by the equation: $E = h\nu = g \cdot \mu \cdot B$ Chpt.II-Equation 2,



Chpt.II-Figure 7: Energy levels for an electron spin ($S = \pm 1/2$) in an applied magnetic field B .

where g denotes the Landé factor, μ is the Bohr magneton, and B is the external magnetic field. As a result, the principal signal received is connected to the interaction of the electron spin and the external magnetic field. It is worth mentioning that numerous external factors can influence the Landé factor's value. Interactions between the electron spin and a (non-zero) nuclear spin, distortion of the environment around the paramagnetic electron, and ferromagnetic interaction are the three key variables.

In this work:

The EPR analyses were performed using a Bruker ESP300E spectrometer equipped with a rectangular TE104 cavity and an Oxford ESR-900 liquid helium cryostat, allowing experiments to be conducted at very low temperatures (down to 4 K). The modulation frequency in the magnetic field was set to 100 kHz, and its amplitude was optimized based on the width (peak-to-peak) of the detected signals. The microwave frequency used was 9.54 GHz (X-band) with a power of a few mW (between 1 and 10 mW). The spectrometer was calibrated using a reference sample of DPPH ($g = 2.0036$). The powder spectra presented were normalized with respect to the sample mass (between 50 and 150 mg per tube) and other spectroscopic parameters that could influence the intensity of the observed signals (number of scans, detector gain, etc.). Finally, the WinEPR and WinSimfonia software programs were used to analyze the EPR spectra and simulate the detected signals.

1.9 X-ray Photoelectron Spectroscopy (XPS)

XPS is a useful chemical analysis technique for material surface characterization. The kinetic energy of excited electrons emitted when a material is subjected to an X-ray beam is determined by XPS spectroscopy. There are two kinds of electrons: core electrons and valence electrons. The energy distribution of the bonding electrons can be determined using the equation: $E_c = h\nu - E_L - W$, where E_L is the binding energy of the ionized level and W is the extraction work function. By comparing the obtained peaks with the XPS spectra of elements from the periodic table, the chemical composition and oxidation states of elements in the first few atomic layers of the material (thickness less than 100 Å) can be identified.

In this work:

Chapter II: Characterization techniques

To explore the surface electronic structure of the products a ThermoFisher Scientific K-ALPHA spectrometer was used for XPS surface analysis with an Al K_{α} monochromatic source ($h\nu = 1486.6$ eV) and a 200 mm X-Ray spot diameter. A pressure of 10^7 Pa was reached in the chamber when transferring the powders pressed onto copper tape. The full spectra (0-1100 eV) were obtained with a constant pass energy of 200 eV and high-resolution spectra at constant pass energy of 40 eV. Charge neutralization was applied during the analysis. High-resolution spectra (such as C1s, O1s, W4f) were quantified and/or fitted using the AVANTAGE software provided by ThermoFisher Scientific (Scofield sensitivity factors used for quantification).

1.10 Dynamic light scattering (DLS)

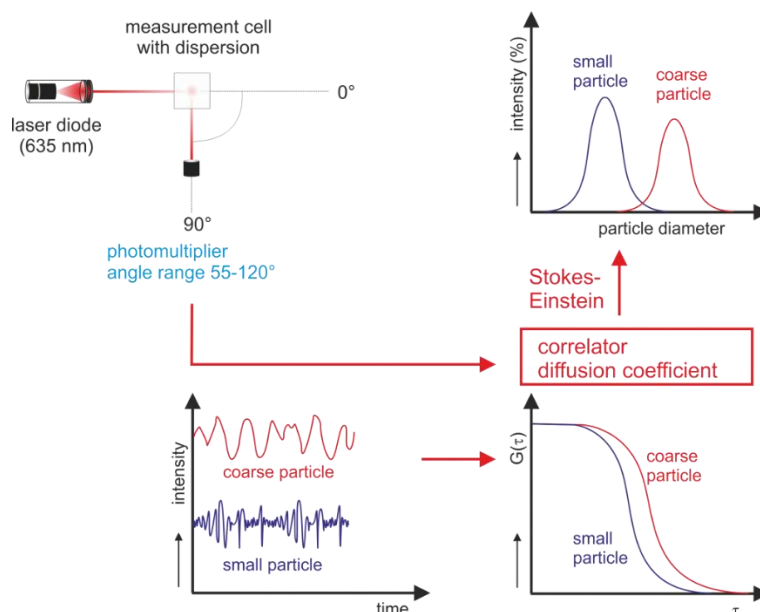
DLS also known as Quasi Elastic Light Scattering (QELS) or Photon Correlation Spectroscopy (PCS), is a non-invasive, well-established technique for measuring the size and size distribution of molecules and particles in the submicron and lower than 10 nm range. DLS operates on the idea of measuring the Brownian motion of particles and correlating motion with particle size. Brownian motion is the random movement of particles caused by successive collisions with the solvent molecules that surround them. DLS is commonly utilized in the measuring of particles suspended in a liquid. When an incident light beam illuminates a dispersion, a portion of the beam is scattered, another portion is absorbed, and in the case of a dilute dispersion, a fraction may be transmitted. When the incident beam has a wavelength smaller than the size of the particles, scattering occurs in all directions (Rayleigh scattering). For a laser with a coherent monochromatic wavelength, the scattered intensity varies over time. This temporal variation in scattered intensity is linked to local concentration fluctuations induced by the Brownian motion of particles in solution.

Depending on the angle of analysis of the scattered light, variations in scattered intensity (constructive or destructive interference) enable the determination of the particle's diffusion coefficient through the analysis of the temporal correlation of the scattered light. The diffusion coefficient of the particles provides information about their hydrodynamic diameter (assuming they are spherical). In dynamic light scattering measurements, the intensity fluctuations of scattered light, which are dependent on diffusion, are measured and analyzed. The Stokes-Einstein equation connects the diffusion coefficient and particle diameter.

$$x = kT / (3\pi\eta D) \times 10^{12} \quad \text{Chpt.II- Equation 3}$$

Where: x : hydrodynamic diameter of an equivalent spherical particle (nm) k : Boltzmann constant (1.38×10^{-23} J·K⁻¹) T : absolute temperature (K), η : viscosity of the dispersing medium (mPa·s), and D : translational diffusion coefficient (m²·s⁻¹). The hydrodynamic diameter considers both the particle diameter and its solvation layer. This diameter is highly influenced by the physicochemical properties of the solvent, such as viscosity and ionic strength. When the ionic strength is high, variations in the thickness of the diffuse layer can be observed. The autocorrelation function (G) exhibits a decaying exponential behavior over time in the case of a monomodal particle size distribution. However, it becomes more complex when dealing with a distribution of particles of different sizes.

Chapter II: Characterization techniques



Chpt.II-Figure 8: Measurement principle of the DLS.

In this work:

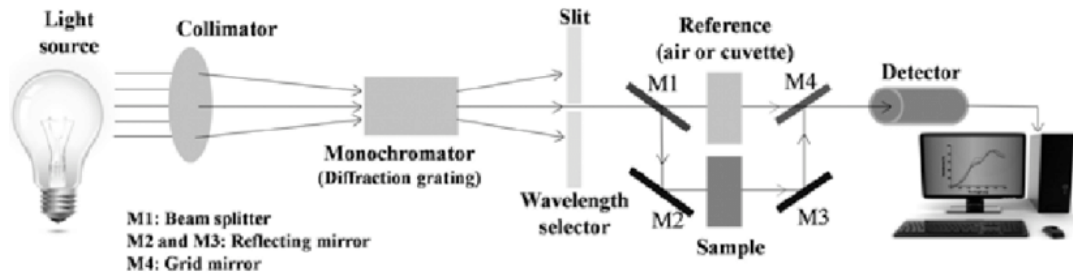
In our case, we adopted the monomodal analysis mode, which assumes that the decay of the autocorrelation function can be described as if there was only one type of spherical particle present. This method, known as the cumulant method, provides an approximation of the particle size distribution in terms of intensity. The cumulant method yields accurate results for a narrow monomodal distribution, characterized by the average particle diameter and polydispersity. The number distribution is calculated using Mie theory based on the intensity distribution. To represent the volume distribution, knowledge of the refractive indices (n) of both the medium and the particles is required. VASCO™ nanoparticle size analyzer was used to determine the size distribution profile of the pristine and doped NPs in the suspensions used for this study. A real-time signal was measured; acquisitions were implemented every 30 s if the noise of the signal did not exceed 1.06%, and 8 acquisitions were accomplished during 16 min. Size distributions of the nanoparticles in different solvents were analyzed by the Cumulant algorithm (assuming monodisperse dispersion), provided by NanoQ software.

1.11 UV-visible-NIR spectrophotometer

Absorption spectrophotometry involves measuring the attenuation of a monochromatic light beam as it passes through an absorbing material. In the context of this thesis, measurements were conducted using a double-beam Cary 5000 spectrophotometer manufactured by Agilent Technologies. This instrument enables measurements to be performed in transmission or reflection mode. In experimental terms, the spectrophotometer provides the measurement of I/I_0 , where I_0 represents the intensity of light measured at the reference output, and I represent the intensity of light measured at the sample output. The transmission value, T , is derived from this intensity ratio, where $T = I/I_0$ (Figure 9). The reflectance spectra in this study were measured with a Varian Cary UV-Vis-NIR spectrophotometer in

Chapter II: Characterization techniques

the wavelength range of 200 to 2500 nm, with a step of 1 nm and a band length of 2 nm. This spectrophotometer is a single-beam spectrometer that is well-suited for measuring the diffuse reflectance of a powder sample since it has an integration sphere as a detector (*i.e.*, the detector records the reflection in all the directions, thus the reduced diffuse reflectance is the complementary of the absorbance: $R = 1 - A$). Halon polymer was used as a white reference for the blank.

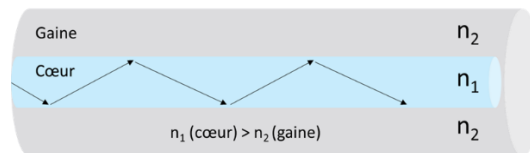


Chpt.II-Figure 9: Double beam UV-Vis's spectrometer working principle.

1.12 Optical fibers measurement

1.12.1 Definitions and light guiding principle

An optical fiber is a dielectric waveguide with the ability to direct light over vast distances. As schematically represented in Figure 10, it typically consists of at least two materials (glass, polymeric or a mix of both glass/polymeric) with differing refractive indices: a high-refractive-index core (refractive index n_1) and a low-refractive-index cladding (refractive index n_2). The notion of total internal reflection is used to guide light along the entire fiber [7].



Chpt.II-Figure 10: Schematic representation of the propagation of a light beam in an optical fiber with a step-index profile.

As previously stated, the principle of total internal reflection is used to guide light in the fiber. Two key conditions must be met for this phenomenon to occur. The first requirement is that the refractive index of the core exceeds that of the cladding ($n_1 > n_2$). The second requirement is that the angle produced by the incident beam with the normal to the core/cladding contact be more than a critical angle c , as defined by Snell's law [8]:

$$\sin(\Phi_c) = \frac{n_2}{n_1} \quad \text{Chpt.II- Equation 4}$$

When $\Phi > \Phi_c$, total reflection occurs. As a result, light is steered through the fiber by entire internal reflections at the core/cladding interface (Figure 11).

The requirements for light signal propagation within the fiber are defined in the preceding paragraph. The numerical aperture (NA), a fiber property, defines the conditions for injecting the light signal at the fiber's end. $ON = n_0 \cdot \sin(\Theta_{\max})$, where n_0 denotes the refractive index of the medium surrounding

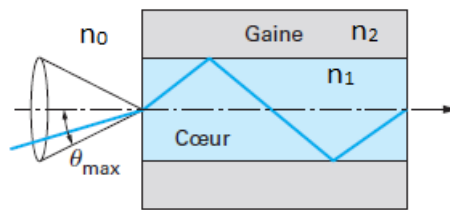
Chapter II: Characterization techniques

the fiber and Θ_{\max} denotes the maximum angle of incidence at the fiber's entrance. This angle is known as the half-angle of acceptance, and $2\Theta_{\max}$ is known as the acceptance cone (Figure 11). This angle is expressed in terms of the following equation:

$$\sin(\Theta_{\max}) = \frac{\sqrt{(n_1)^2 - (n_2)^2}}{n_0} \quad \text{Chpt. II – Equation 5}$$

If the surrounding medium is air ($n_0 = 1$), the relationship becomes:

$$ON = \sin(\Theta_{\max}) = \sqrt{(n_1)^2 - (n_2)^2} \quad \text{Chpt. II – Equation 6}$$



Chpt.II-Figure 11: The numerical aperture (cone of acceptance) of an optical fiber.

All light rays within the cone of angle $2\Theta_{\max}$ are restricted and steered within the fiber. The greater a fiber's numerical aperture, the lighter rays that can be successfully steered within the optical fiber.

1.12.2 Types of optical fibers

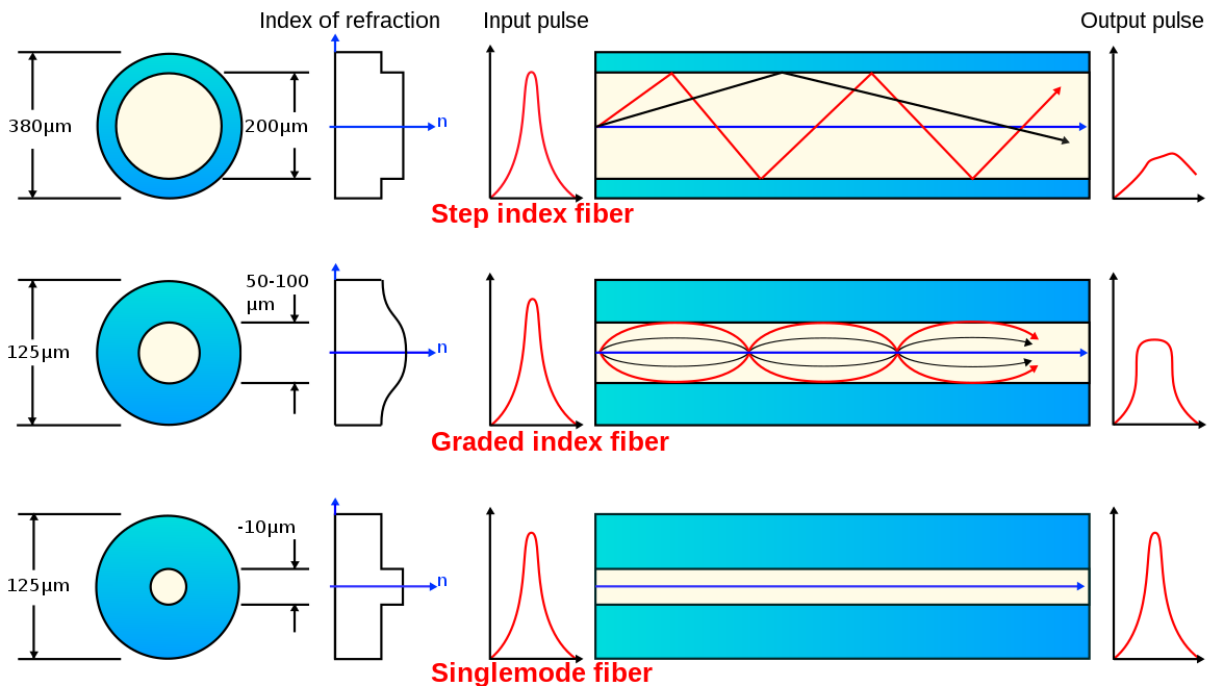
Step-index multimode fibers, graded-index multimode fibers, and single-mode fibers are the three types of optical fibers based on their refractive index transverse profile. These three fiber varieties are defined primarily by the size of the core and cladding, as well as by their index profile, which shows the variation in refractive index between the fiber's core and cladding [9]. Figure 12 illustrates the variation of these properties.

-Step-index multimode fibers (Figure 12.a) have a large core. However, the presence of multiple propagation modes leads to the temporal spreading of pulses (intermodal dispersion), resulting in significant attenuation in the fiber.

-When compared to step-index fibers, graded-index multimode fibers (Figure 12.b) have a smaller core. They are intended to reduce the influence of intermodal dispersion while maintaining a high numerical aperture. The core material's refractive index is not constant, but gradually falls as it approaches the cladding. This fluctuation in the index affects the direction of the light rays, which have a sinusoidal shape. Longer pathways pass through zones with lower refractive indices and hence propagate at faster rates, decreasing the effects of intermodal dispersion [10]. The attenuation in this type of fiber is lower than in step-index fibers.

-Single-mode fibers (Figure 12.c), as the name implies, allow only the propagation of a single mode. The attenuation in this type of fiber is low.

Chapter II: Characterization techniques



Chpt.II-Figure 12: Diagram illustrating the dimensions, index profile, and optical signals at the input and output of a fiber for (a) step-index multimode, (b) graded-index multimode, and (c) single-mode configurations [9].

1.12.3 Attenuation of the fibers

Attenuation measurement in optical fibers was recorded using the well-established cut-back method. The attenuation coefficient is defined as the logarithm relationship between the transmitted input power $P(0)$ and the output power $P(x)$ observed after propagation of a distance x in an optical fiber system as presented in the following equation [9]:

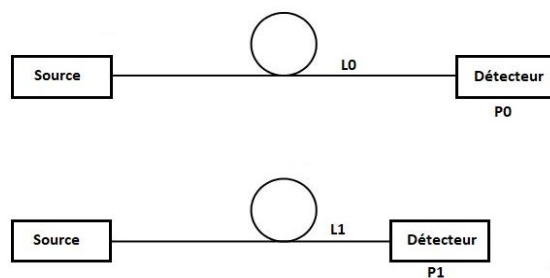
$$\alpha_{\text{total}} \text{ (dB/km)} = (10/x) \cdot \text{Log}[P(0)/P(x)] \quad \text{Chpt.II-Equation 7}$$

This equation is known as Beer's Law and clearly shows that the power of the transmitted signal decreases exponentially with the propagated distance. The same experimental set up used for axial transmission was adapted for the attenuation one.

In this work:

Prior to the measurement, the end facets of each measured fiber were carefully polished prior to measurements to ensure proper light coupling efficiency. The fibers were tied to keep straight during this measurement to avoid any bending losses. A 100 W halogen broadband source and an optical spectrum analyzer (Avantes starline AvaSpec-ULS4096CL-EVO) were used to collect the data.

Chapter II: Characterization techniques



Chpt.II-Figure 13: Attenuation measurement by the cut-back method.

1.13 References:

- [1] C. L. Farrow and S. J. L. Billinge, “Relationship between the atomic pair distribution function and small-angle scattering: implications for modeling of nanoparticles,” *Acta Crystallogr A*, vol. 65, no. 3, pp. 232–239, May 2009, doi: 10.1107/S0108767309009714.
- [2] S. J. L. Billinge, “The atomic pair distribution function: past and present,” *Z Kristallogr Cryst Mater*, vol. 219, no. 3, pp. 117–121, Mar. 2004, doi: 10.1524/zkri.219.3.117.29094.
- [3] S. Banerjee et al., “Improved models for metallic nanoparticle cores from atomic pair distribution function (PDF) analysis,” *J Phys Chem C*, vol. 122, no. 51, pp. 29498–29506, Dec. 2018, doi: 10.1021/acs.jpcc.8b05897.
- [4] C. R. Mullis et al., “Spatial correlation function of X-Ray–selected active galactic nuclei,” *Astrophys J*, vol. 617, no. 1, pp. 192–208, Dec. 2004, doi: 10.1086/425248.
- [5] A. A. Coelho, P. A. Chater, and A. Kern, “Fast synthesis and refinement of the atomic pair distribution function,” *J Appl Crystallogr*, vol. 48, no. 3, pp. 869–875, Jun. 2015, doi: 10.1107/S1600576715007487.
- [6] L. Reimer, “Electron optics of a scanning electron microscope,” Springer: Berlin, vol.45, pp. 13–56, 1998, doi: 10.1007/978-3-540-38967-5_2.
- [7] G. Barton, “Fabrication of microstructured polymer optical fibres,” MA: Springer US, 2008, pp. 83–110. doi: 10.1007/978-0-387-68617-2_5.
- [8] E. A. J. Marcatili, “Extrapolation of Snell’s law to optical fibers,” *J Opt Soc Am*, vol. 63, no. 11, p. 1372, Nov. 1973, doi: 10.1364/JOSA.63.001372.
- [9] S. Addanki, I. S. Amiri, and P. Yupapin, “Review of optical fibers-introduction and applications in fiber lasers,” *Results Phys*, vol. 10, pp. 743–750, Sep. 2018, doi: 10.1016/j.rinp.2018.07.028.
- [10] K. Schuster et al., “Material and technology trends in fiber optics,” *Advanced optical technologies*, vol. 3, no. 4, pp. 447–468, Aug. 2014, doi: 10.1515/aot-2014-0010.

Chapter III: Results and Discussion

- Y. Badour, S. Danto, C. Labrugère, M. Duttine, and M. Gaudon, “Cu-doped and un-doped WO₃ photochromic thin films,” *J Electron Mater*, vol. 51, no. 4, pp. 1555–1567, Apr. 2022, doi: 10.1007/s11664-021-09389-3.
- Y. Badour, S. Danto, S. Albakour, S. Mornet, N. Penin, L. Hirsch, and M. Gaudon “Low-cost WO₃ nanoparticles / PVA smart photochromic glass windows for sustainable building energy savings,” *Solar Energy Mater and Solar Cells*, vol. 255, p. 112291, Jun. 2023, doi: 10.1016/j.solmat.2023.112291.
- Y. Badour, S. Danto, M. Gonidec, C. Labrugère, M. Suchomel, G. Philippot, and M. Gaudon, “Fine-tuned photochromic WO_{3-x} thin films for UV photo-sensing: a details study from structural analysis to UV photo-sensing application” *Opt Mater* (submitted).
- Y. Badour, M. Gaudon, M. Pedros, and S. Danto, “Hybrid organic-inorganic PMMA optical fiber functionalized with photochromic active WO₃ nanoparticles: from materials design to photochromic fabric” *Adv Func Mater* (submitted).
- Y. Badour, M. Gaudon, E. Rusconi, Y. Petit, and S. Danto, “Developing plastic photochromic fibers for sensing application: the combination of 0D WO_{3-x} structure in a 1D polymeric matrix.” (to be submitted in august).
- K. Kamali, Y. Badour, M. Gaudon, S. Danto, and G. Sonnemann, “Prospective life cycle assessment of photochromic textiles made in labs for commercial application” (to be submitted in august).

Chapter III: Results and Discussion

1 Part 1: Powder modification for better photochromism: Oxidation

As discussed in chapter 1, the modification of the oxygen substoichiometry (x) of the WO_{3-x} can alter its photochromism and may improve its optical properties. In this first part, we address the optimization of the photochromic contrasts by oxidizing the clear blue WO_{3-x} raw crystallites obtained from the polyol route. Hence, it is possible to prepare from yellow to blue starting compounds with a rapid intense blueish photochromism under UV irradiation. Also, the structural, optical, and electrical characterization properties of thin films issued from dip-coating powder suspensions are deeply investigated.

1.1 Elaboration and characterization of NPs and thin films

1.1.1 Polyol synthesis of WO_3 powders

Chemical reagents were purchased from Sigma Aldrich and used as received. Tungsten (VI) chloride was used as a tungsten source, diethylene glycol (DEG) as a solvent, and potassium dichromate, $\text{K}_2\text{Cr}_2\text{O}_7$ as an oxidizer agent. WCl_6 (7.2 g) was added to 100 mL of DEG and 20 mL of distilled water. The mixture was heated at 180 °C under continuous stirring and refluxed for 3 h. At the end of the reaction, a deep blue precipitate was obtained. The precipitate was washed and centrifuged several times with ethanol to remove any traces of solvent and dried in an oven at 80°C. The as-obtained raw powders were oxidized by introduction into an aqueous solution where the strong oxidizer was previously solubilized. The raw powder and a series of oxidized powders with different oxidizer dosages (0, 0.005, 0.01, 0.02 M in 100 mL for 1 g of WO_3 powder) were prepared and named: WOR, WOX1, WOX2, and WOX3, respectively. For comparison, one submicronic particle-sized powder (WOT sample) was prepared by calcination under air at 600 °C of the WOR sample.

1.1.2 Pristine film elaboration

The raw and oxidized nanoparticles (NPs) were separately dispersed in ethanol to prepare the suspensions (the weight content in NPs is 90 $\text{g}\cdot\text{L}^{-1}$). Then the suspensions were dip-coated on a standard glass substrate to obtain pristine and doped thin films. The dip-coating parameters are (i) the dip-coating speed: 133 $\text{mm}\cdot\text{min}^{-1}$ and (ii) for multilayers, the number of successive dip-coating steps which were separated by 30 min drying in an oven (90 °C) in between two steps.

1.2 Structural, morphological, and chemical characterization of the as-prepared NPs

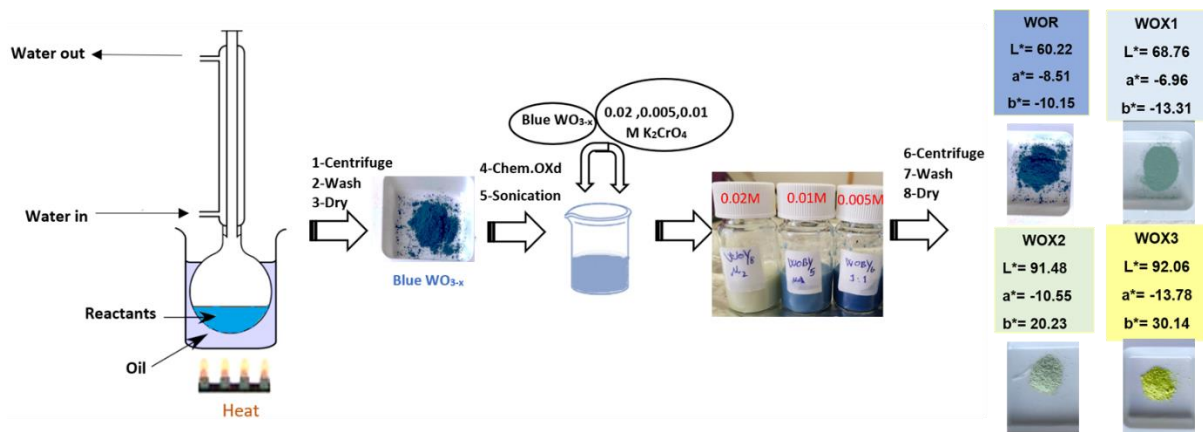
1.2.1 The four different WO_3 nano-powders in a glimpse

To tune the oxygen sub-stoichiometry of the as-prepared WO_3 nano-powders from the polyol process (WOR sample), this sample was dipped into an oxidizing aqueous solution, with $\text{Cr}_2\text{O}_7^{2-}$ polyanion used as the oxidizer. The effect of different concentrations of the oxidizer agent (0.005, 0.01, 0.02 M) leading to WOX1, WOX2 and WOX3 samples, respectively on the blue WO_3 powder was examined. As depicted in Figure 1, a gradual transition of color is evident, shifting from a light blue hue in the initial state to a lighter yellow shade in the oxidized state. Notably, the color becomes increasingly distinct as the concentration of the oxidizer rises. It was noticed that a higher dosage of the oxidizer

Chapter III: Results and Discussion

causes a dissolution of the powder, so the maximum limit, which can be used is about 0.02 M. Based on the abundant literature on tungsten oxide powder, higher oxidizer dosages result in lower surface oxygen sub-stoichiometry of the nanoparticles, which lowers the intensity of the inter-valence band (W^{5+} to W^{6+} electron inter-atomic transfer) responsible for the red part of the visible range and near-infrared absorption. In $L^*a^*b^*$ color-space, the b^* color parameter, relative to the blue – yellow color axis, so especially sensible to the powder color variation versus the oxidation, can be used to quantify the phenomenon (one can also use the luminosity L^* directly linked to the maximum of reflectance, also an adequate parameter to quantify the oxidation phenomenon). The b^* significantly evolves from -10.15 (more blue than yellow) for the WOR raw powder to +30.14 (more yellow than blue) for the WOX3 most oxidized sample. On another side, the L^* value increases for the as-prepared oxidized samples from 68.76, to 91.48 and then 92.06, as the oxidizer dosage increases.

These four samples were compared with one submicronic particle-sized WO_3 powder (WOT sample) obtained from the calcination under air at $600^\circ C$ of the WOR sample. This powder, thanks to a full oxidation under the high-temperature heat treatment under air, exhibits a yellow color with $L^*a^*b^*$ parameters very close to the WOX3 sample.

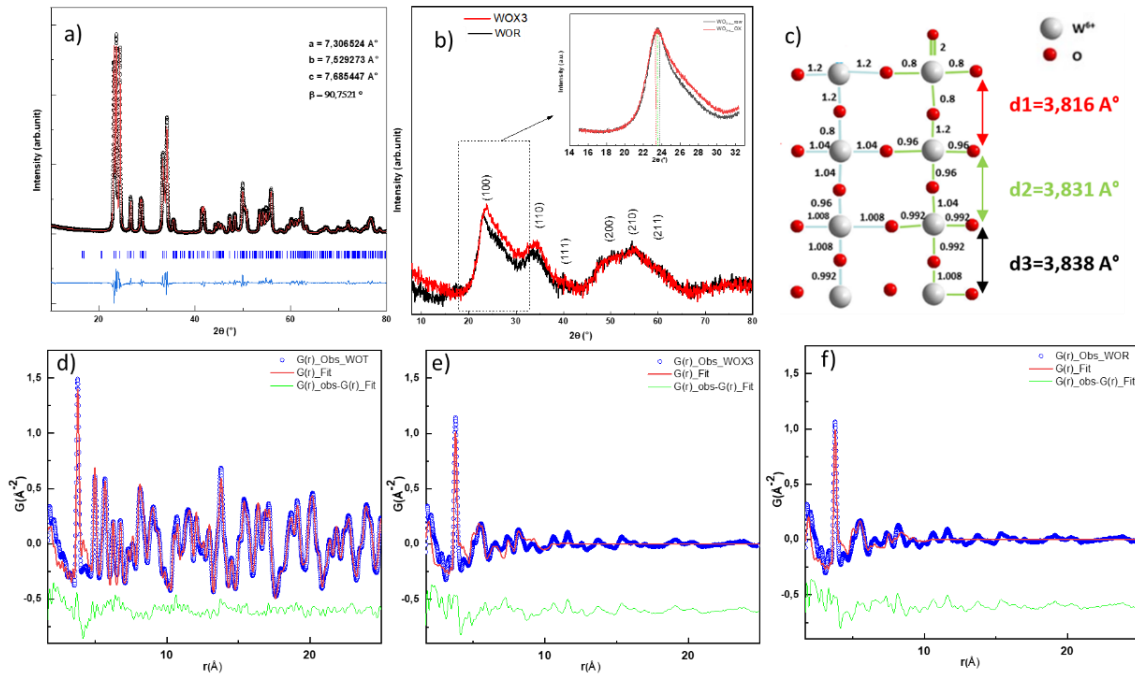


Chpt.III-Figure 1: Experimental flow starting from polyol precipitation and the oxidizing step parameters leading to the 4 studied samples from raw powder (WOR) to the most oxidized powder (WOX3).

1.2.2 Powder physicochemical characterizations

Firstly, the WOT obtained after a post-annealing under air exhibits from X-ray diffraction a $P2_1/n$ monoclinic structure, as the standard tungsten oxide structure (Figure 2.a). The profile matching of this air-annealed sample is achieved in the $P2_1/n$ space group using unit-cell parameters in good agreement with the numerous data reported in the literature [1]. The matching quality is good, and the reliability factors are below 10%: $R_{exp} = 5.16\%$; $R_p = 9.47\%$. The WOT sample can be said to be a “standard” or “reference” $WO_{3.00}$ powder sample.

Chapter III: Results and Discussion



Chpt.III-Figure 2: a) XRD with profile pattern matching refinement for WOT, b) XRD pattern of WOR and WOX3 powders with a specific zoom on (100) peak. Representation of experimental, calculated and difference PDF $G(r)$ curves for: d) WOT, e) WOX3, f) WOR.

From the diffraction pattern peak profiles, it is possible to roughly determine the average crystal size of the particles with the help of Debye-Scherrer formula [2]: $t = K \cdot \lambda / (\beta \cdot \cos \Theta)$, with t the mean size of the ordered (crystalline) domains, which may be slightly smaller or equal to the particle size, K the proportionality factor (also called the Scherrer's constant), which value is assumed to be $K = 0.9$, β corresponds to the full width at half maximum (FWHM), λ the X-ray wavelength and θ the Bragg angle of the peak. It should be noted that the observed peak width is affected by the instrumental broadening as well as the broadening caused by the size effect (size broadening), so the instrumental broadening is subtracted from the total peak width to calculate the crystallite size. The calculated crystallite sizes were obtained equal to (i) 5.5 ± 1.6 nm for WOR, and 3.2 ± 0.3 nm for WOX3 whereas for the WOT sample of the monoclinic crystalline network, a size of 26.5 ± 3.5 nm is calculated. For WOR and WOX3 especially, this calculation on the crystallite size is a rough approximation since the XRD patterns show broad peaks, high background contribution besides peak intensity and furthermore a non-standard peak profile (with back asymmetry).

The broad diffraction peaks of the WOR and WOX3 samples are characteristic of very small coherent domain-sized crystallites, but some of the low 2θ peaks also exhibit a peak asymmetry (back asymmetry) which is more difficult to interpret. The peak asymmetry can be issued from the monoclinic distortion of the unit-cell edge or lattice parameter gradient considering a cubic average symmetry. Indeed, X-ray diffraction peak back asymmetry was already observed in nanoparticles of inorganic oxides prepared from polyol synthesis and exhibiting a gradient of lattice parameters from core to surface of the particles [1] [3]. Thus, the raw and oxidized nanopowders may have a lattice parameter gradient. This can be explained by considering two different hypotheses: (i) each

Chapter III: Results and Discussion

nanometric particle constituting the blue and yellow samples exhibit a gradient of unit-cell parameters. It could be reasonably considered that this unit-cell parameter gradient is created from surface proximity (O/W ratio diverging from the surface to core of the crystallites); (ii) the different crystallites do not exhibit the same unit-cell parameters (for instance, due to a variation of oxygen sub-stoichiometry between each crystallite). Whatever the hypothesis, the difference in unit-cell parameters from one sample to another could be explained by slight differences in terms of global chemical composition: for instance, different oxygen sub-stoichiometry, or slight differences of surface strain contribution on unit-cell parameters depending on crystallite size. By varying the oxygen sub-stoichiometry of raw powder either by chemical oxidation, a broadening of the main peak (100) with a back shoulder is observed as displayed using zoom into representative angular range (inset of Figure 2.b). The peaks become broader with the increase of oxidation conditions as shown for the oxidized sample. A solid-state chemistry model based on the bond-valence model of Brown *et al.* [4], can help to interpret the drastic modifications of the interatomic distances between the planes near the crystallite surface in comparison with the bulk material. A surface can be described as an area of missing bonds (with the subsequent excess of energy). The missing bonds around the surface atoms should cause a shortening of the bonds between these surface atoms and the atoms of the first underlayer. Indeed, the bond valence law expresses that the cation-anion distance and the coordination number of an ion are linked by Equation 1:

$$V = \sum_{i=0}^n bv_i = \sum_{i=0}^n \exp((r_0 - L_i)/0.37) \quad \text{Chpt.III- Equation 1}$$

where V is the valence of the ion (equal to the oxidation degree modulus: here = 6 for W^{+6}), bv_i is the bond valence of each bond implying the central ion, r_0 is an empirically determined parameter characteristic of the A–X bond (r_0 is tabulated equal to 1.917 Å for W^{+6} – O^{-2} bond), and L_i is the length of each i bond of the first coordination sphere. The valence is then a function of the number of bond lengths; when the coordination number I decreases (as on surface planes), each bond length should also decrease to maintain the V value of 6 for each ion of the WO_3 cubic structure. Thus, crystallite surfaces affect the lattice parameters. A Pauling–Brown bond relaxation approach was then adopted to predict surface effects. In the first step, it was identified “natural” surface planes considering the easiest and only acceptable way (from a thermodynamic point of view) to produce a stable tungsten oxide surface. First, it is straightforward to identify the (100) planes as natural cutting planes of these ReO_3 -type structures since they are clearly the densest planes. Also, to maintain a $WO_{3.0}$ stoichiometric oxide (with only W^{6+} ions) one must cut only half of the double bond between W^{+6} and O^{-2} forming the adequate chemical pattern for the stoichiometric oxide surface. The second step consists of the attribution of the bond valence of the successive (100) bond layers from the surface to the bulk, layer by layer, to respect the ions’ V valence value ($V = 6$ for W^{+6} ions). As shown in Figure 2.c, the calculation for the first, second and third layers are reported. These simple calculations of d spacing confirm our implication that, for our 5 nm WOR sample, the interatomic distance between surface atoms will be smaller than the equilibrium spacing between atoms in bulk material and could so be associated with a back asymmetry (short distance corresponding to large

Chapter III: Results and Discussion

diffraction angles). The atoms at the surface of a particle (indeed at any free surface) perceive an environment that is distinctly different from that perceived by atoms within the bulk of the crystal (since there are no atoms to interact with on the outside of the free surface). For instance, a 3 nm crystallite (close to WOX3 and WOR) gets approximately 55% of surface atoms (1st layer, only), whereas a 25 nm (close to WOT) crystallite exhibits a surface/core ratio of only 4.7%. Hence, the result is an effective surface tension on the surface of these particles, which implies that the atoms within the particles are under an effective force. Nonetheless, the variation of the d spacing between surface neighboring planes in regard to the bulk configuration is very low and such a hypothesis cannot explain such a huge back asymmetry of our oxide nanoparticles (in Figure 2.b inset are reported the angle positions associated with the three first calculated d spacing from surface). Obviously, considering now possible oxygen substoichiometry, cutting some W-O double bonds on the oxide surfaces will disrupt more drastically the d spacing configuration. Also, the WOX3 sample, which is without any doubt with a very low oxygen sub-stoichiometry from its yellow color, exhibits the largest and most asymmetric X-ray diffraction peak. Hence, explaining the observed peak profiles as originating from a surface perturbation combined with their nanometric size seems inconclusive, PDF analysis of selected samples (WOT as reference, WOR and WOX3) provides additional details on the atomic organization and coherent domain size, which is related to the maximum distance where peaks are observed. Differential correlation functions $D(r)$ obtained, refined models, and difference curves displayed from PDF measurements performed on the three powders are presented (Figure 2.d, e, f) in the 1.5–25 Å range. As expected, the WOT sample exhibits a monoclinic framework with the $P2_1/n$ space group and the coherent domain is largely exceeding the range of 1.5-25 Å, which is in good agreement with a crystallite size of 26.5 nm calculated with the Debye-Scherrer equation on XRD data. Regarding the WOR and WOX3 samples, the maximum distance where peaks are observed is close to the limit of the 25 Å range. This value is a bit smaller than the crystallite diameters obtained from the Debye-Scherrer equation: 5.5 nm for WOR and 3.2 nm for WOX3 but remains consistent with regards to XRD data quality. However, we were able to fit the PDF data with the $P2_1/n$ space group and only up to 10 Å, while adding a cubic space group did not improve the quality of the fit. This indicates that the building blocks of the WOR and WOX3 samples are closer to a monoclinic structure than to a cubic one in the first coordination shells, but the network distortion becomes so important after 10 Å that conventional crystal structure refinement fails. X-ray peaks' asymmetry seems well to be caused by the monoclinic lattice symmetry. Thus, XRD peak back-asymmetry, previously observed on both the later samples, probably originates from the (iso- or anisotropic) large distribution of lattice parameters in between crystallites. The “average” monoclinic distortion of the three studied samples can be quantified from different points of view. For illustration, we based the discussion on the monoclinic unit-cell distortion (UCD) quantified in regard to the pseudo-cubic equivalent unit cell [5]: $UCD = [(a_m - a_0)^2 + (b_m - a_0)^2 + (c_m - a_0)^2]^{1/2}$, with a_m , b_m and c_m : the monoclinic parameters extracted from pdf, and a_0 : the pseudo-cubic cell parameters calculated as the cubic root of the monoclinic volume extracted from the PDF; *i.e.* UCD corresponds to the standard deviation in between the monoclinic and pseudo-cubic unit-cells. Also, it can be proposed for

Chapter III: Results and Discussion

discussion the tungsten ion average out of centering (W_{oc}) (localization of the tungsten center out of the octahedral site geometrical center), considering the two Wyckoff positions, again in regard to the pseudo-cubic symmetry; *i.e.* the W_{oc} corresponds to the standard deviation of the two tungsten positions regarding the (0.25, 0, 0.25) and (0.25, 0, 0.75) reference in-cubic positions. Table 1 lists a summary of the refined parameters against the $D(r)$ functions, including a , b , c and β unit-cell parameters as well as the W cation positions. Also, UCD and W_{oc} calculated distortion factors are depicted in the last column. For both distortion calculation assessments, monoclinic distortion amplitude is growing from WOR to WOT with WOX3 having intermediate values in between the raw blue powder and the post-annealed under-air yellow sample. In other words, it means that if the monoclinic distortion is significantly decreased from the obtaining of a very small crystallite size (comparison of WOR and WOX3 in regard to WOT), the effect of the surface re-oxidation clearly decreases these surface effects (WOX3 in regard of WOR).

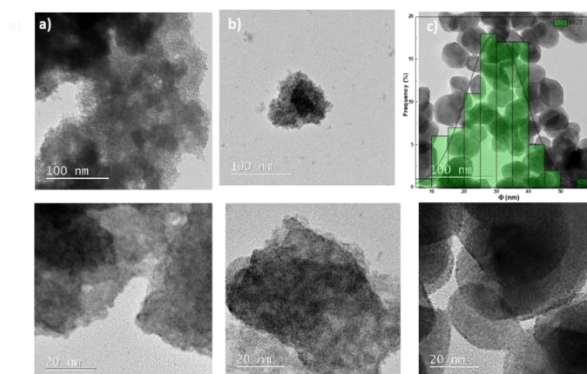
Chpt.III-Table 1: Structural parameters for the WOT, WOR and WOX3 samples, extracted from PDF analyses.

Sample	$a_m(\text{Å})$	$b_m(\text{Å})$	$c_m(\text{Å})$	beta angle (°)
	x (W_1)	y (W_1)	z (W_1)	UCD (Å)
	x (W_2)	y (W_2)	z (W_2)	W_{oc}
WOT	7.3075	7.534	7.688	90.8
	0.2552	0.0399	0.2843	0.271
	0.2452	0.0253	0.7813	0.0704
WOR	7.4013	7.5532	7.5822	92.74
	0.2611	0.0435	0.2666	0.137
	0.2415	0.0090	0.7622	0.0504
WOX3	7.4006	7.4592	7.6588	92.25
	0.2627	0.0344	0.2714	0.191
	0.2412	0.0096	0.7702	0.0536

TEM micrographs of the different samples are reported in Figure 3. The WOT size distribution shows significantly larger isotropic particles of about 28 nm average diameter (Figure 3.c). This measurement is in good agreement with XRD and PDF analyses for which it was shown an average size of 25 nm. The WOR and WOX3 samples present very small particles (Figure 3a,4b) with a size of around 3 nm, difficult to distinguish from each other. The particle size distribution width is quite narrow (between 2 and 4 nm), but the agglomeration of the particles and their superimposition tend to limit the accuracy of the particle size distribution calculation. This very small size is in good

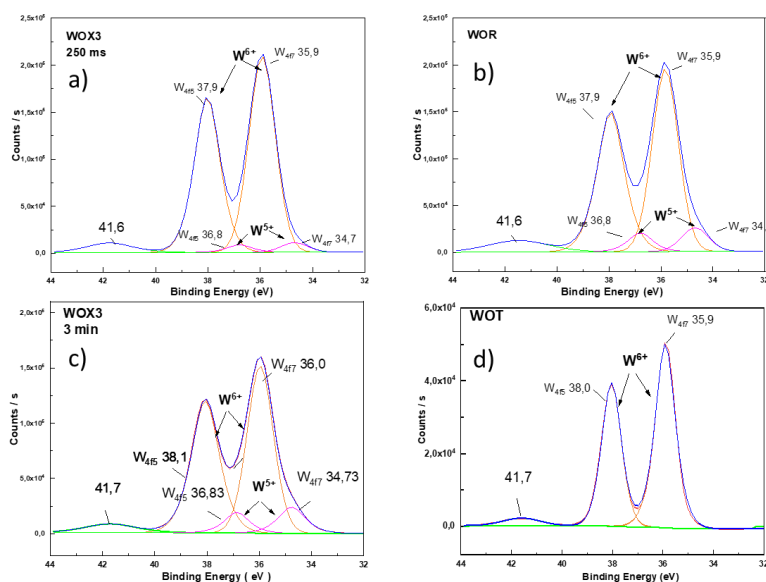
Chapter III: Results and Discussion

agreement with the previous discussion extracted from the X-ray diffraction patterns as well as from PDF analyses.



Cht.III-Figure 3: Transmission Electronic Microscopy (TEM) micrographs of WO_3 powders: a) WOR, b) WOx_3 , c) WOT.

XPS was used to analyze the surface composition. The XPS spectra of the WOR, WOT, and WOx_3 powders are compared (Figure 4).



Cht.III-Figure 4: High-resolution XPS spectra of W_{4f} and O_{1s} : a) WOx_3 with 250 ms analysis time, b) WOR, c) WOx_3 with 3 min analysis time, d) WOT.

Firstly, the samples with a regular 3 min analysis time (Figures 4a, b, d) are compared. Figure 4.d shows that the air annealing post-treatment produces the full oxidation of the tungsten ions up to the +VI oxidation state. Indeed, the WOT spectrum is constituted only by two peaks, which were assigned without any doubt to the W^{6+} state ($4f^{7/2}$ peak at 36.02 eV and $4f^{5/2}$ at 38.35 eV) [6], [7]. The absence of W^{5+} ions in the air-annealed sample is in good agreement with its pale-yellow color. The sample (WOT) can thus be considered a reference demonstrating that no further reduction of W^{6+} to W^{5+} is occurring during the XPS spectrum acquisition, at least for this sample. However, the W_{4f} fitting of the WOx_3 sample (Figure 4a) shows a significant residual signal of W^{5+} . The W^{5+} signal corresponds to the two relatively peaks located at 33.95 and 36.10 eV. The occurrence of W^{5+} inside

Chapter III: Results and Discussion

this compound is not in coherence with the yellow color of the oxidized powder compared to the spectrum of WOT. Clearly, the W^{5+} concentrations in between WOX3 and WOR samples are not as much different than expected where the estimation of the W^{5+} content is 0.16 and 0.13 in the WOR and WOX3, respectively. XPS characterization gives an estimation of the W^{5+} proportion on the powder surfaces (a few Å in depth). So, it can be assumed that the W^{5+} content occurs with an increasing gradient from the bulk to the surface. This effect can lead to an overestimation of the W^{5+} content from XPS investigations.

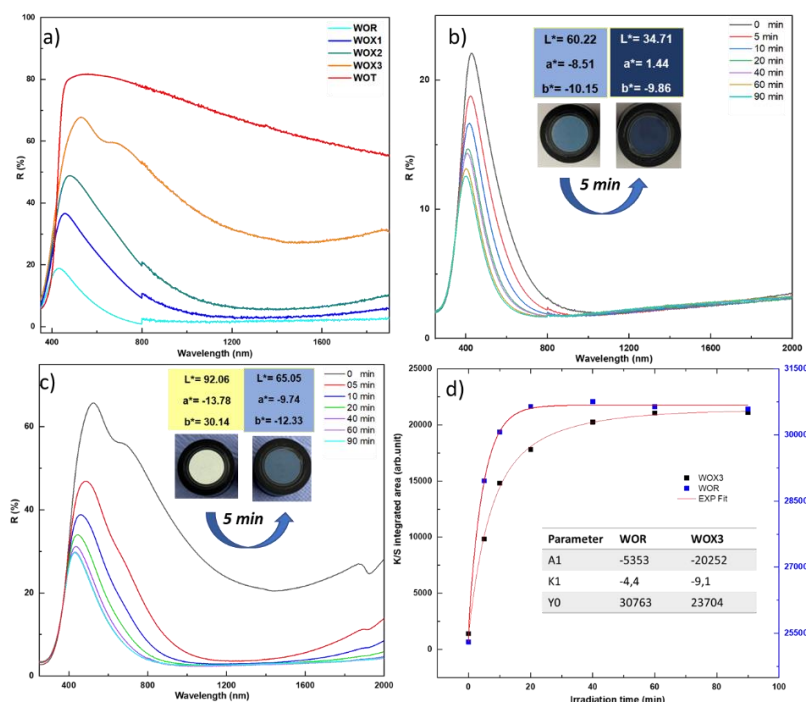
For the WOX3 sample, the chemical composition is shown to quickly vary during the first seconds of the XPS analysis. Considering this situation, we adapted a different condition to analyze the WOX3 by decreasing the analysis time to 250 ms instead of the regular analysis time of 3 min. As shown in Figure 4.c, the W^{5+} signal tends to be less significant for the 250 ms signal than for the 3 min signal. This result gives a rough estimation for the real content of W^{5+} equal to 0.04. Also, it is worthy mentioning that the WOR signal did not change versus analysis time. XPS experiments show that the additional surface oxygen anions on WOX samples created from oxidative peptization are especially prompt to be removed as shown in ultra-vacuum conditions.

1.2.3 Powder optical properties

Before UV illumination, the optical spectra of the powders from diffuse reflection measurements are reported in Figure 5.a. Firstly, the WOT reference powder shows a strong UV-vis absorption as well as a quasi-total reflection window in the visible spectrum, up to nearly 90% reflection at 500 nm. The pale-yellow color is explained by the occurrence of the tungsten oxide gap located on the frontier between the UV range and the visible range, inducing a slight absorption of the purple hues. Secondly, in the studied oxidized series, the comparison between the samples shows a progressive divergence in their reflectance spectra: the higher the oxidizer dosage, the lower the intensity of the $W^{5+} \rightarrow W^{6+}$ inter-valence charge transfer responsible for the visible-near infrared absorption (large absorption band centered at about 1-micron wavelength). Consequently, the maximum reflectivity percentage located at 480 nm increases from 18% for the WOR, to 36% for WOX1, to 48% for WOX2, and up to 70% for the WOX3. The luminosity L^* , directly linked to this maximum of reflectance, can be used to quantify the phenomenon. As already reported in Figure 1, the L^* value increases for the three as-prepared samples from 88.76, to 91.48 and then 92.06, as the oxidizer dosage increases. But obviously, the evolution of color in between the samples is better characterized from the b^* chromatic hue axis from yellow to blue: the b^* parameter rises from -10.15 for the light blue WOR sample up to +30.14 for the WOX3, most oxidized sample. At 2000 nm, the comparison of the reflectivity percentage between the three samples exhibits the same behavior: with values varying from 10%, 19%, and 37% for WOX1, WOX2, and WOX3, respectively. The reflectance contrast (ΔR taken as equal to the reflectance difference in visible and IR range) between 500 and 2000 nm is 55% for WOX3, whereas it reaches less than 30% for the other two samples. Hence, the most oxidized samples, exhibit the best selectivity (high visible transparency but with the maintaining of a quite high

Chapter III: Results and Discussion

NIR absorptivity) for the use of these compounds as solar filters, *i.e.*, with the best contrast between the visible and near-infrared transmission.



Chpt.III-Figure 5: a) Diffuse reflectance spectra of the studied powders. Photochromic study based on the reflectance evolution vs irradiation time for WOR sample (b), and WOX3 (c) samples. d) Evolution of the average K/S absorbance (400–2500 nm) vs irradiation time of both the WOR and WOX3 samples.

Ex-situ diffuse reflectance on WOT, WOR, and WOX3 samples after 5, 10, 20, 40, 60 and 90 min of irradiation are performed, and the results are presented in Figure 5.b. The reflectance (R%) of the powders vs. UV-light irradiation time on 350-2000 nm wavelength range is recorded and can be transformed in Kubelka-Munk ($K/S = (1-R)^2/(2 \times R)$) absorbance spectra. K/S transforms exhibit an intensity of the absorption phenomena proportional to the chromophore concentration (herein, the W^{5+} ions concentration) and are so used for kinetic analysis.

While WOT does not exhibit any significant photochromic property, both the two WOR and WOX3 samples exhibit a photochromic effect mainly concentrated in the near-infrared part of the spectrum. As no photochromism is offered by the WOT sample, the reflectance evolution which is not visible is not displayed. The associated chromatic coordinates in L^* , a^* , b^* space presented in Figure 5.b allow the comparison of the photochromic efficiency of the WOR and WOX3 samples from the optical contrast calculated between the non-irradiated and 90 min irradiated samples. Indeed, even if our samples exhibit a photochromic effect mainly concentrated in the near-infrared part of the spectrum, the impact of the inter-valence transfer in the visible range allows the observation of visible ΔC contrast:

$$\Delta C = \sqrt{(\Delta b^{*2} + \Delta L^{*2} + \Delta a^{*2})} \quad \text{Chpt.III-Equation 2}$$

Chapter III: Results and Discussion

Photochromic contrasts are about 55.3 and 27.1 for WOX3 and WOR, respectively. The $\text{Cr}_2\text{O}_7^{2-}$ used for the sample oxidation greatly improves the photochromic efficiencies in terms of color contrasts.

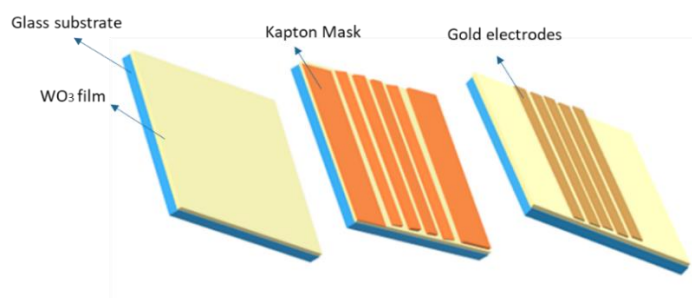
To express the kinetic differences of the coloring against UV-irradiation between both the WOR and WOX3 samples, an exponential growth function was used to fit the experimental data, according to the equation:

$$Y = A1.\exp(t/K1) + Y0 \quad \text{Chpt.III-Equation 3}$$

with t in min, $K1$ is the characteristic time in min., $A1$ is the characteristic amplitude and $Y0$ is the y -offset (Figure 5.d). The values of the three parameters are shown in the inset, Figure 5.d. The WOR recorded a faster kinetic compared to WOX3 (4.4 to 9.1 min). For both powders, the asymptotic growth shape of the coloring kinetics can be interpreted considering that the photochromic effect consists of photo-reduction of the surface cations from W^{+6} to W^{+5} for short times and then, while the surface becomes saturated with W^{+5} ions, this fast mechanism stops afterward, coloration mechanism being prolonged only thanks to surface to bulk W^{5+} ion diffusion. However, the larger photochromic contrast as previously shown from the color parameters for the WOX3 sample in regard to the WOR sample, is well demonstrated from the $A1$ characteristic amplitudes, which is about 4 times larger for the WOX3 sample than for the WOR sample.

1.3 Electrical characterization of the prepared thin films

Before the electrical characterization, the device was prepared in this way: 1- The coated film was masked using our Kapton® designed mask (2*2 cm with a spacing of 1.5 mm between the electrodes), 2- Then, the film was sputtered by gold to form the electrode by using a conventional sputtering instrument (BIO-RAD SEM Coating Unit PS3, BIO-RAD Laboratories Ltd. Hercules, CA, USA), 3- At the end, the mask was eliminated and kept for multiple usages. The process is summed up in Figure 6. The four-point probe method was employed to measure the device's resistivity. The method requires the measurement of sheet resistance (R_s) and thickness (t) to calculate the bulk resistivity as $\rho = R_s \times t$ [8]. In the four-point probe method, the sheet resistance is measured as $R_s = \pi/\ln(2) \times (V/I) \times k$, where I is the current, V is the voltage, and k is a geometric correction factor that depends on the ratio of the dimensions of the sample to the spacing of the probes. The correction factors for these rectangular samples were determined via a formula and correction graphs [9].



Chpt.III-Figure 6: Preparation of the photoconductor device.

Chapter III: Results and Discussion

Figure 7.a represents a prior comparative study of the resistivity change for WOR films prepared from the coating of 4 or 10 layers (equivalent measured thickness 422 and 985 nm) as a function of irradiation time. The results indicate a lower resistivity value within the 10-layer film, which makes it the preferred number of layers for post-photoconduction measurement (UV sensing): increasing the number of successive coatings beyond 10 layers has shown no supplementary gain of conductivity. Characterization of the photoconductor structures showed that the resistivity asymptotically decreases with irradiation time when the incident illumination power density is kept constant (5.6 W/m²) for both 10-layer WOR and WOX3 films (Figure 7.b). In regard to previous coloring kinetic studies (showing asymptotic growth), the asymptotic decrease of the electrical conductivity is without any doubt correlated to the W⁵⁺ ion concentration. For 10-layer films, the resistivity drastically decreased from 1.72×10⁵ Ω.cm to 8.62×10² Ω.cm and from 4.71×10⁴ Ω.cm to 1.83×10² Ω.cm for WOX3 and WOR films respectively as UV irradiation time increased with a change of color from light blue (WOR) or light yellow (WOX3) to dark blue for both films. As the photochromic phenomenon is based on the photoreduction of W⁶⁺ ions in W⁵⁺ defects at the particle surfaces, it appears obvious that the W⁵⁺-W⁶⁺ intervalence charge transfer can be correlated with the resistivity mechanism as the increased number of charge carriers upon irradiation until the saturation, stabilizing the resistivity after 35 min [10].

Due to the better resistivity contrast (difference between the two states: non-irradiated and irradiated states), the WOX3 film was chosen to perform photoconduction measurements. Herein, photoconduction means assessment of the change of resistivity versus UV irradiation; the collected current while 5V is applied with the 4 probes system varying with the UV irradiation is called photocurrent. The photocurrent characteristics are measured at 365 nm UV-light illumination under three different light intensities: 5.6, 7.3, and 9.2 W/m² (surface powers were modified through the source – sample distance) and while switching off the irradiation between two states: ON (25 seconds of irradiation) and OFF (dark condition). It is important to insist on the very low surface power of the UV source we use in comparison to the literature. Since the as-prepared WO₃ films are hugely light sensible, they are able to detect UV micro-dose. Whatever the irradiation power, the WOX3 possesses a higher photocurrent (I_P) compared to the negligible dark current (I_{dark}) values. This confirms the generation of an increased number of photo-induced charge carriers during irradiation compared to dark conditions. Furthermore, the photo-sensing properties of the photodetectors such as photo-responsivity (R), external quantum efficiency (EQE-indicated that the ratio of the number of charge carriers circulating in the circuit to the number of photons absorbed to generate them [11] and photoreactivity (D^* , the ability of a photodetector to measure weak optical signals) are calculated

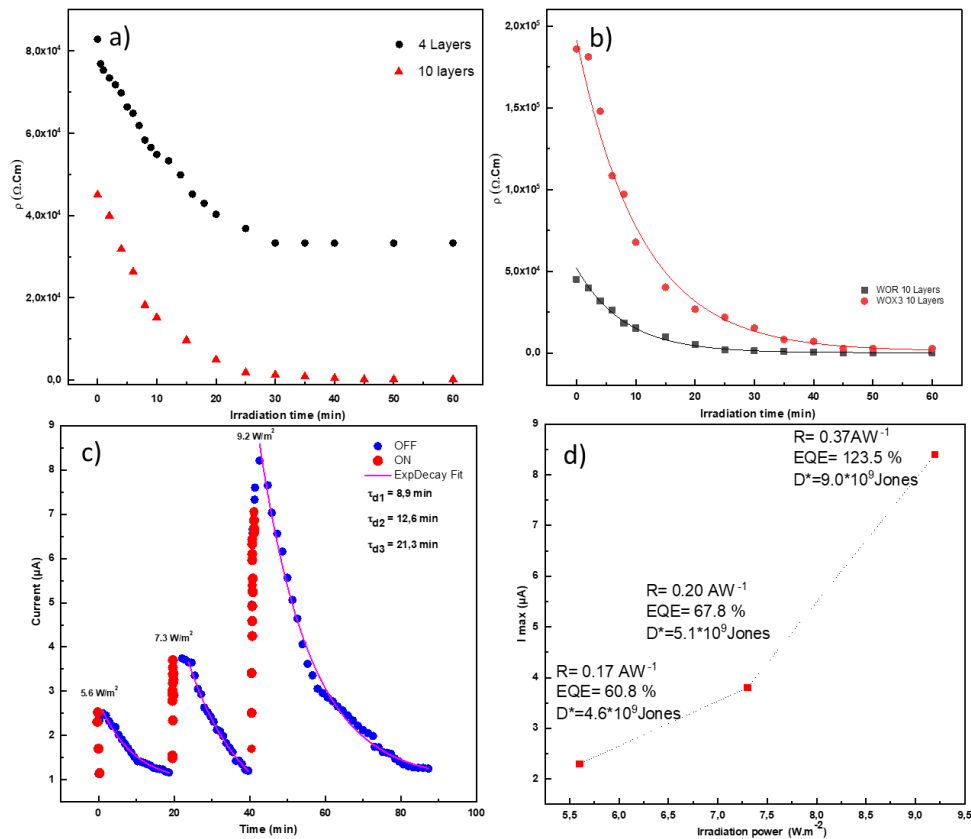
using the equations and reported in Figure 7.d: $R = \frac{I_P}{P_{in} \times A}$, $EQE = \frac{R \cdot h \cdot c}{e \cdot \lambda}$, $D^* = \sqrt{\frac{A}{2 \cdot e \cdot I_{dark}}}$

where I_P donates the photocurrent value of the film (interpreted directly from Figure 7.c where I_P is the maximum current during the ON state), c represents the velocity of light, e gives the charge of an electron, h mentions Planck's constant, and A is the effective exposed area of the film to UV

Chapter III: Results and Discussion

irradiation (where A is reduced to 2.5 mm² due to the excess coverage by the parallel metal electrodes on the semiconductor surface), which limits the exposure area of photoactive material for the incoming photons.

The responsivity and EQE behaviors as a function of irradiation power density are shown in Figure 7.d. The maximum responsivity of 0.37 A/W, EQE of 123.5%, and $D^*=9.0*10^9$ Jones was obtained at the highest optical power density of 9.2 W/m². Surprisingly, the R and EQE were found to be increased as the optical power increased which can be explained by the improved photodetectivity D^* in a such low dose of UV. The same behavior was observed by Kumar *et al.* [12], who fabricated a high-quality AlGaIn/GaN Schottky barrier photodetector. They studied the evolution of responsivity as a function of power density and found that the obtained responsivity first increases with the increase of optical power density and reaches a peak at an optical power density of 9 μ W cm⁻² and with increasing the optical power density; the responsivity was observed to exhibit a decrease. We believe that we did not reach the peak of evolution and the observations are still in the low domain of optical power density. Nevertheless, our goal is to study the sensitivity of the photodetector in low UV irradiance, and we expect to observe this behavior in this range of study. The obtained WO_{3-x} film for UV photo-detection exhibits comparable performance when compared to many of the previous reports on such properties on metal oxide semiconductors as presented in Table 2.



Chpt.III-Figure 7: a) Resistivity of the 4 and 10 layers WOR film as a function of irradiation time, b) Resistivity of the 10 layers WOX3 film as a function of irradiation time c) Time-dependent photo-response (current versus time) of the 10 layers WOX3 film as a function of irradiation power density

Chapter III: Results and Discussion

WO₃ film measured under different irradiation. d) Maximum current as a function of the UV dose with calculated R and EQE parameters for each point.

Chpt.III-Table 2: Photosensitivity parameters of the as-prepared films compared with literature.

Sample	Photocurrent (μA)	R (A/W)	EQE (%)	REF
WO _{3-x}	8.3	0.37	123.5	Presented work
WO ₃	17.05	0.947	304.2	[13]
WO ₃	0.18	0.000245	-	[14]
CuO/Si	0.96	0.000389	0.024	[15]
MgO/ZnO	7.1	40	146	[16]

The time-dependent photoresponse current increases along with the increment in UV light intensity with a slower decay behavior as the intensity of UV light is more intense. The as-prepared photodetector can so be used as an efficient micro-dose UV-sensor. In each coloring segment, the photocurrent did not saturate after irradiation but persisted to increase in the first times of the OFF state then decreased slowly during the dark conditions (decay phase). To better quantify the photoresponse of the film, the photocurrent-time curve was modeled using a decay-exponential model, the fitting model was limited to the decay phase due to the persisting current in the OFF state, which makes it impossible to fit the rising segment for the third part.

$$K(t) = K0 + Nd \cdot e^{-(t-tc)/\tau_d} \quad t > tc \quad \text{Chpt.III-Equation 4}$$

$K(t)$ is the current at a given time, $K0$ is the y-asymptote, Nd is the decay amplitude of the exponential, tc is the time offset between exponential growth and decay, and τ_d is the time constant of the exponential decay term. From exponential curve fits, we obtain time constants listed in Table 3.

Chpt.III-Table 3: Exponential decay fitting results for each UV irradiation power.

	5.6 mW/m ²	7.3 mW/m ²	9.2 mW/m ²
τd (S)	534	756	1278
K0	0.2	0.3	1.1
Nd	1.5	4.7	7.2

The slow decay behavior as revealed from kinetic fitting results in Table 3 (where the τ_d increases with the UV power intake) can be linked to the slow bleaching behavior of the film, which will be deeply investigated in the next part (Part 2: doping effect) [17]. Anyway, the photochromism bleaching associated with photocurrent decay is due to the reoxidation of W^{5+} to W^{6+} by the oxygen in the air consuming a long time to return to the initial state. Also, we propose that the slow switching behavior originates from the persistent photoconductivity (PPC) effect intrinsic to WO_3 [18]. PPC phenomenon is related to metastable bulk defects located between shallow and deep energy levels considering that the oxygen vacancies can be excited to a metastable charged state after a structural

Chapter III: Results and Discussion

relaxation [19]. In another approach, electron–hole separation near the surface can contribute to the PPC effect where the surface built-in potential separates the photo-generated electron–hole pairs and accumulates holes at the surface [20], [21]. As shown in Figure 7.d the photo-responsivity increases with the UV power. Indeed, after illumination, the charge separation makes the electron–hole recombination difficult and originates PPC. The PPC effect causes the conductivity of WO_3 to increase under illumination and the increased conductivity to persist even when the illumination is stopped. The PPC effect in WO_3 can also be discharged by heating the material to 155°C and above, however, such an approach is impractical for photo-detection [14].

1.4 Conclusion of Part 1

In conclusion, tuning the sub-stoichiometry of the as-prepared WO_{3-x} nano-powders has been accomplished successfully via reductive polyol precipitation followed by a partial chemical re-oxidation thanks to peptization into chromate aqueous solutions. W/O stoichiometric ratio has been analyzed by multiple technics. The most re-oxidized samples exhibited the best solar selectivity (high visible transparency but with high NIR absorptivity) for the use of these compounds as solar filters on smart window panels. The coloring mechanism of the studied samples was governed mainly by fast photo-reduction of the surface cations from W^{+6} to W^{+5} associated with facile surface oxygen absorption-desorption. In other words, the efficient photochromic properties of the as-prepared NPs are due to the capacity of the NPs to easily release surface oxygen anions under UV radiation and to re-absorb surface oxygen anions under dark conditions. The detailed structural analysis of the WO_{3-x} nanocrystallites was performed by coupling XRD pattern analysis, PDF analysis and TEM graphs. The crystal structure of all studied samples can be described in terms of exhibiting a monoclinic framework with P21/n space-group, with monoclinic distortion maintained despite the obtaining of the very low crystallite size. From an applicative point of view, the UV photo-detection measurements yielded a good responsivity of 0.37 A/W and external quantum efficiency of 123.5 % even at a very low power density (9.2 W/m^2) of the UV illumination. The possibility to extract photo-induced current below the open circuit voltage, with tuneable intensity versus the light irradiation time, opens new possibilities as the next generation of photo batteries providing future optimization of the device design can sufficiently amplify the extracted currents. These experimental results support that WO_{3-x} films could exhibit promising usability in different optical applications such as smart windows, optical filters and UV detectors, with a special ability for quantification of UV micro-doses.

Chapter III: Results and Discussion

Chapter III: Results and Discussion

2 Part 2: Powder modification for better photochromism: Doping

As discussed in this chapter, doping the WO_3 crystalline structure with typical elements like Al, Cu, Mo, Zn, Co, etc can improve its photochromism. It has been proved to decrease the oxide bandgap and especially, by introducing narrow electronic bands between the CB and the VB, is able to tune the photochromic UV-irradiation response. In this part, we study the photochromic behavior of Cu-doped WO_3 thin film obtained by dip-coating Cu-doped WO_{3-x} NPs dispersed in ethanol suspensions. Also, the photochromic (coloring and bleaching amplitudes and kinetics) behaviors of the doped and pristine films are compared and deeply analyzed.

2.1 Elaboration and characterization of NPs and thin films

Elaboration of Cu-doped WO_{3-x} NPs and thin films.

The WO_{3-x} NPs were prepared as reported in section 1.1.1 of this chapter. In the same way, using the polyol method and copper (II) chloride as the doping source, a series of Cu-doped- WO_3 samples were prepared while varying Cu concentration from 0%, 0.5%, 1%, 2% and have been labeled as WO, WCu05, WCu1, and WCu2, for raw powders, respectively. In another batch, the as-synthesized powders (0%, 0.5%, 1%, 2% Cu) were annealed at 600°C under air atmosphere for 2 hours and have been labeled as WOT, WCuT05, WCuT1, and WCuT2, respectively.

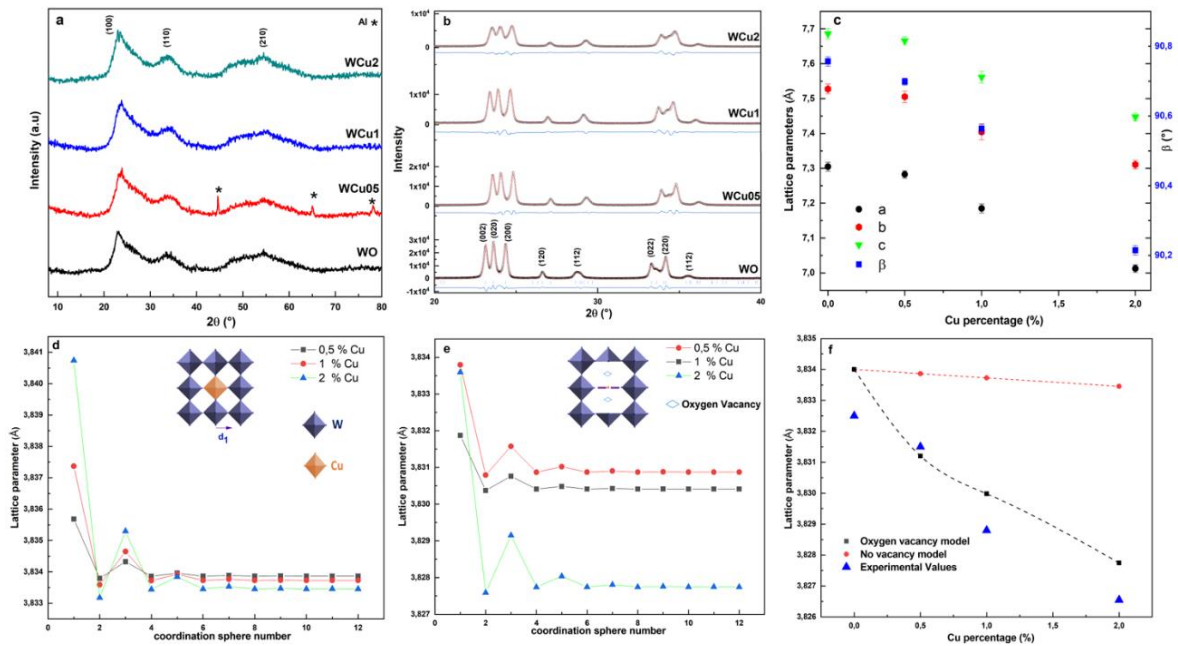
The Pristine WO and WCu1 raw NPs were separately dispersed in ethanol to prepare the suspensions (weight content in NPs is 90 $\text{g}\cdot\text{L}^{-1}$); then the suspensions are dip-coated on a standard glass substrate to obtain pristine and doped thin films using the same parameters as the ones reported in section 1.1.2.

2.2 Structural, morphological, and chemical characterization of the as-prepared NPs

2.2.1 Powder physicochemical characterizations

The structure of the as-prepared powders was characterized by X-ray diffraction. No second phase corresponding to impurities such as Cu, Cu_2O or CuO was detected in the X-ray patterns associated with all the samples. The XRD diagrams show that all raw powders: WO, WCu05, WCu1 and WCu2, get the same XRD signature, with characteristic asymmetric and large peaks as previously discussed (Part 1) (Figure 8.a). The very large peaks associated with the nanometric behavior of the raw powders do not allow their fitting for accurate structural characterization without using PDF analysis. Thus, to determine the impact of the copper content introduction inside the WO_3 crystalline framework, especially on the crystallite size and the unit-cell lattice parameters, pattern-matching refinements of air-annealed at 600°C powders were performed. Figure 8.b shows the diffraction patterns of the powders obtained after the post-annealing under air [22]. The pattern matching of the air-annealed samples can be achieved using the P21/n space group. The matching quality is good, and the reliability factors are far below 10%: for illustration, $R_{\text{exp}} = 2.16\%$; $R_f = 6.55\%$; $R_p = 8.47\%$ for the WOT compound. As in the previous part, from the diffraction pattern peak profiles, it is possible to determine the average crystal size of the particles with the help of the Debye-Scherrer formula.

Chapter III: Results and Discussion



Chpt.III-Figure 8: XRD patterns of undoped and Cu-doped WO₃ raw powders (a). XRD with pattern matching refinement for undoped and Cu-doped WO₃ annealed powders under air at 600°C (b). Evolution of undoped and Cu-doped WO₃ annealed powders lattice parameters as a function of Cu dopant percentage (c). Calculation of the Cu doping effect on the Cu-doped WO₃ pseudo-cubic lattice parameter considering W⁶⁺ for Cu²⁺ substitution without electronic compensation versus length of the coordination spheres number around copper taken for calculation (d). W⁶⁺ for Cu²⁺ substitution with double oxygen vacancies creation for electronic compensation (e). Calculated and experimental lattice parameter values (f).

The calculated nanometric sizes were obtained equal to (i) 5.5, 3.2, 3.5, 2.6 nm for raw WO, WCu05, WCu1, and WCu2 respectively, (ii) 25.6, 22.34, 19.8, 21.8 nm for the same series of samples after post-annealing: WOT, WCuT05, WCuT1, and WCuT2, respectively. The copper doping leads so, especially for the post-annealed samples, to a decrease in the average particle size, which argues for an efficient introduction of the copper ions inside the WO₃ crystalline framework. As shown in Figure 8.b, the decrease of the crystallite size is associated with the decrease of the intensity of major diffraction peaks such as (020), (002) and (200) with increasing Cu concentration. This trend can be a result of the formation of the copper ion clusters and crystal defects which can limit the growth of the Cu-coped WO₃ NPs. Furthermore, the incorporation of Cu ions into the WO₃ crystal affected the lattice parameters of Cu-doped WO₃ as the Cu²⁺ ions and W⁶⁺ ions have different ionic radii, which are 7.3 and 6.0 Å in 6-coordinated spheres, respectively, as well as different oxidation states (aliovalent doping). One can notice that Rietveld refinement performed on Cu-doped samples did not reveal any electronic residues in the interstitial position (for illustration in the icosahedral sites, which are known to be preferential locations for alkaline dopants in WO₃-type framework [23], [24]). Hence, in the following, the copper ions are considered in substitution for the tungsten ones. Additionally, the copper oxidation states are supposed to be +II, which will be supported by further EPR experiments.

As illustrated in Figure 8.c, further analysis of the monoclinic lattice parameters (*a*, *c* and *β* angle) of Cu-doped samples shows a clear and monotonic decreasing trend as the Cu doping concentration increases. This observation could constitute an interesting paradox as the Cu²⁺ ionic radius is over the

Chapter III: Results and Discussion

W⁶⁺ radius. The evolution of the unit-cell lattice parameters has been interpreted with respect to the bond valence model. However, two different approaches have been applied to better understand the evolution of the Cu-doped WO₃ lattice parameters upon doping with Cu. First, for simplification, the evolution of the unit-cell parameters was resumed to the pseudo-cubic unit-cell parameter (considering the equivalent cubic cell with Z, the number of WO₃ units per cell, equal to unity). In a rough model, in a first approximation, a pseudo-cubic lattice parameter was calculated taking into consideration a W⁶⁺ for Cu²⁺ substitution without electronic compensation. In a more accurate model, the creation of a double oxygen vacancy creation for electronic compensation is considered. In this latter case, for the calculation, the two oxygen vacancies are created along the z-axis, in the first neighboring of the introduced copper ions, i.e., considering that copper II ions are so located in regular square plane sites (in good agreement with the 3d⁹ Cu²⁺ electronic configuration). In both approaches, the same used bond-valence model in part 1 (Brown model) was used to predict from geometrical modeling the drastic modifications of the W-O interatomic distances around the Cu²⁺ defect points. Indeed, the bond valence law expresses that the bond length (r_i), the coordination number (n), the electronic flux on each bond (v_i) and the ion oxidation state (or total ion valence: V) are both linked by the Equation 1, here V is equal to the oxidation degree modulus (6 for W⁺⁶, 2 for Cu²⁺), r_0 is tabulated equal to 1.917 Å W⁺⁶-O⁻²-bond, and 1.679 Å for Cu²⁺-O⁻²-bond. This model is very adequate to explain that an aliovalent doping by a low valence, but bigger radius ion could paradoxically lead to a decrease of the unit-cell parameters, exactly as observed for Cu-doped WO₃ samples. Indeed, even if the Cu-O bonds are longer than the standard W-O bonds, the increase of the electronic flux of the W-O bonds at the proximity of the copper defect leads to a contraction of these W-O bond lengths. Indeed, it is mandatory for the surrounding crystalline network around the copper defect to compensate for the low electronic flux between oxygen and copper, because the total valence equal to 2 of the Cu-bonded oxygen anions must still be constant.

In addition, we use the Vegard law (i.e., a mixing law) to evaluate the lattice parameter considering the valence bond modification from neighbor to near-close bond fluxes up to the tenth coordination sphere from copper ions. For the first model, the lattice parameter remains the same for all three axes, whereas in the second model, for which a double oxygen vacancy (V_O) was introduced along the z-axis, the lattice parameter on z axis a_z differs from the x and y axes ($a_x = a_y \neq a_z$). Then the average calculated pseudo-cubic unit-cell parameter a is taken as $a = (a_x \cdot a_y \cdot a_z)^{1/3}$. Thus, for both the first and the second models, a pseudo cubic parameter for x copper concentration (n being the number of coordination spheres around copper taken in the model) can be calculated from Equation 5. The two models are diverging in the way to calculate near-close bond fluxes.

$$a_n = 2 \cdot d_{(W-O)} (1-2x) + 2 \cdot x \cdot d_{(Cu-O)} + \sum_{i=0}^{i=n} 2 \cdot x \cdot d_i \quad \text{Chpt.III-Equation 5}$$

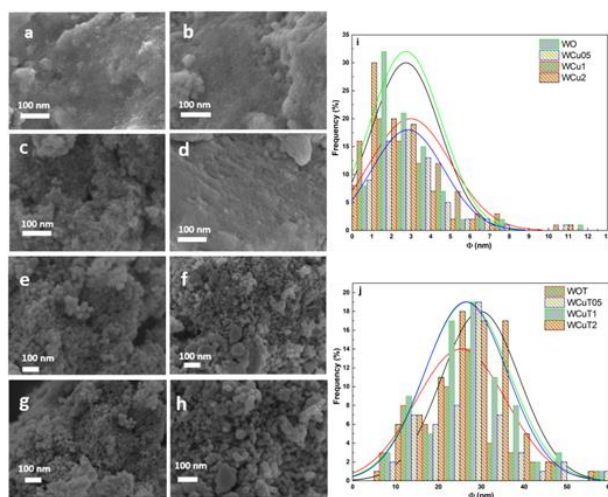
$$\text{with } d_i = r_{0(W/Cu-O)} - 0.37 \cdot \ln(v_i) \quad \text{Chpt.III-Equation 6}$$

The final calculation for both models is represented in Figure 8.d and Figure 8.e, respectively for non-vacancy approximation, and double oxygen vacancy approximation. The second applied model is in

Chapter III: Results and Discussion

good accord with the experimental values, which confirms that substituting W^{6+} with Cu^{2+} causes a decrease in the lattice parameters and leads to shrinkage of the unit cell. The fact that the second model leads to calculation so close to the experimental values tends to validate that compensation of copper doping with a double oxygen vacancy is the convenient way to relax the constraints brought by the aliovalent substitution.

The sample morphologies are reported in the SEM images in Figure 9. As shown in Figure 9.a,d, the raw sample particles are very small with a size around 3 nm. The crystallite size distribution extracted from SEM image treatment is reported in Figure 9.i. All the doped and un-doped NPs have almost a superimposed particle size distribution. This very small size is in good agreement with the previous discussion extracted from the X-ray diffraction patterns. The air-annealed powders show significantly larger isotropic particles of about 50 nm average diameters (Figure 9.e,h). However, the doped NPs did not exhibit a change in their morphology and size distribution in comparison with the un-doped NPs. The coherent domain decrease with the copper concentration shown from X-ray patterns is not confirmed. May, the slight enlargement of the peak width versus copper content observed in X-ray diffraction comes more from constraints created by copper introduction than from a decrease in the average crystallite size. While the monoclinic samples were deeply analyzed in terms of X-ray diffraction technique to confirm the substitution of tungsten cation for copper due to their well-defined X-ray diffraction patterns, in the following of the study, we will focus on raw powders, these latter samples being the only one exhibiting the target photochromic properties.

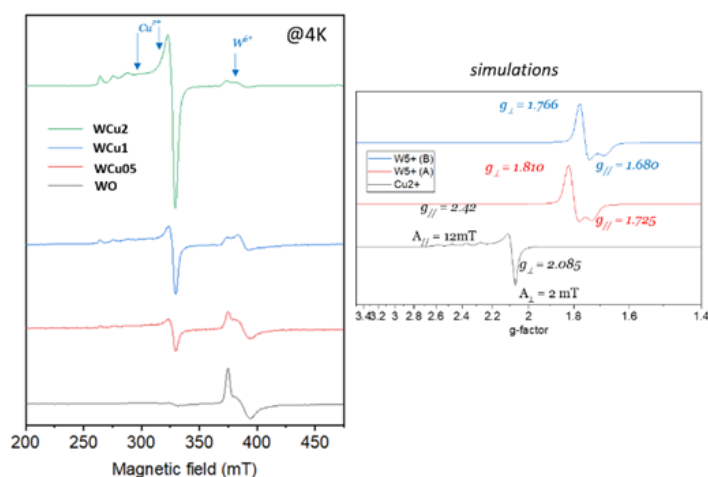


Chpt.III-Figure 9: SEM images of the various raw and post-annealed samples: WO (a), WCu05 (b), WCu1 (c), WCu2 (d), WOT (e), WCuT05 (f), WCuT1 (g), WCuT2 (h) and their associated particle size distribution (i & j).

EPR was performed to evaluate the appearance of free electrons and to track the evolution of Cu^{2+} and W^{5+} content in the studied products. First, the copper II ions are well detected in all Cu-doped samples. The evolution of the signal intensity evolves linearly with the copper concentration as shown in Figure 10. Clearly, the experiment shows that copper is well introduced in the WO_3 -type crystalline structure and with mainly the +II oxidation number. Nevertheless, the lack of detection of the Cu^+ ion, for which the EPR is very low sensitive and only in special cases [25], does not prove the total

Chapter III: Results and Discussion

absence of Cu^+ ions as a minor copper fraction. Secondly, one can focus on the W^{5+} EPR signal. For the WO sample, the axial EPR signal with $g_{\perp} = 1.76$ and $g_{\parallel} = 1.71$ is observed at low temperature (5 K) and is associated with W^{5+} ions in a quite 6-coordinated regular site (probably with C_{4v} symmetry) in good agreement within the WO_3 structure [26]. Versus copper concentration, two observations can be made on W^{5+} signals: (i) the intensity of the signal is progressively decreasing, showing that copper insertion plays an oxidative role besides neighboring tungsten ions; (ii) the W^{5+} signal becomes more and more clearly a multicomponent signal, showing the perturbation of the W^{5+} local environments. Indeed, for the highest copper concentrations, at least two different environments with clearly diverging g_{\perp} and g_{\parallel} values must be used to well simulate the W^{5+} signal.

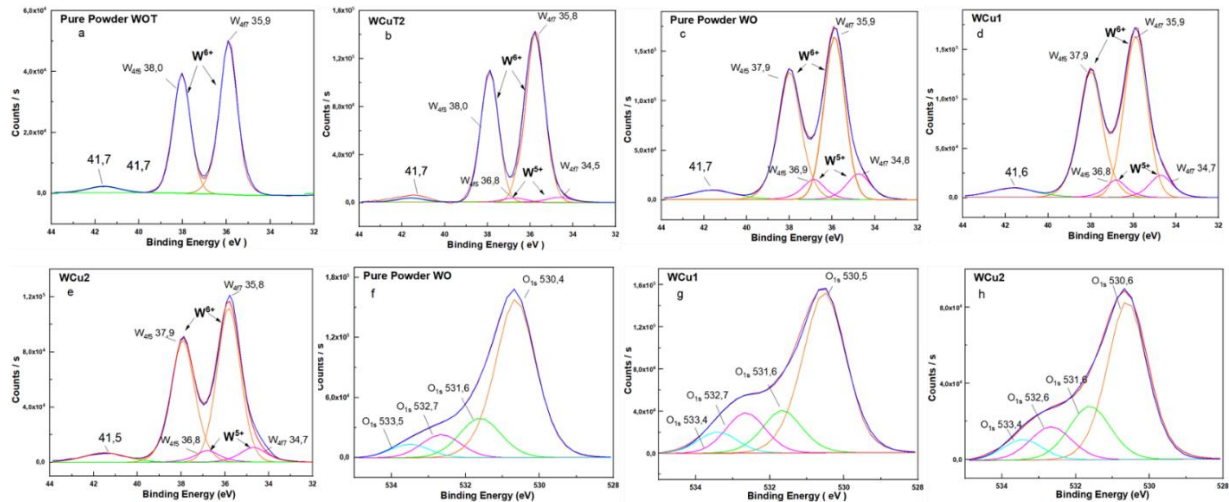


Chpt.III-Figure 10: Low temperature (4K) X-band EPR spectra of undoped and doped Cu-WO₃ raw powders (a). Simulation of the Cu^{2+} and W^{5+} ions EPR signals, showing the two different environments exerted on W^{5+} ions (b).

XPS was used to analyze the surface composition as a coupling and complementary analysis technique to EPR. Indeed, a clear picture of the tungsten oxidation states can be achieved whereas EPR was obviously non-sensitive to the W^{6+} diamagnetic cations. Furthermore, the environment of the oxygen anions in the powders, especially the ability to distinguish oxygen anions in a bulk environment from the ones perturbed by oxygen vacancies is very useful for materials understanding. Firstly, the XPS spectra of two air-annealed compounds, the un-doped (WO) and the 2 mol% Cu-doped sample (WCuT2) are compared. Figure 11. shows that the air annealing post-treatment produces the full oxidation of the tungsten ions up to the +VI oxidation state in the WOT samples. Indeed, the WOT spectrum is constituted only by two peaks which were assigned without any doubt to the W^{6+} state ($4f^{7/2}$ peak at 36.02 eV and $4f^{5/2}$ at 38.35 eV) [17]. However, the W_{4f} fitting of the air-annealed WCuT2 shows a residual signal of W^{5+} . The W^{5+} signal corresponds to the two relatively low-intensity peaks located at 33.95 and 36.10 eV, which confirms the substitution of W^{6+} by the dopant Cu^{2+} . Indeed, W^{5+} may be created from a redox reaction proceeded from intervalence electronic transfer between W^{6+} and Cu^{2+} cations to lead to W^{5+} and Cu^+ cations. Also, the occurrence of W^{5+} inside the WCuT2 compound is in coherence with the pale green color of the annealed powder compared to the yellow color of the un-doped WOT powder.

Chapter III: Results and Discussion

Figure 11.c shows the high-resolution fitting of W_{4f} spectra in the pure WO sample where the two major peaks were assigned to W^{6+} while the two minor peaks were assigned to W^{5+} cation. The W^{5+} state occurrence indicates the creation of oxygen vacancies as a result of a partial reduction of W^{6+} due to the reducing medium used during the polyol synthesis, as reported in our last work [1]. Therefore, the un-doped tungsten oxide NPs have an oxygen sub-stoichiometry with the formula: WO_{3-x} .



Chpt.III-Figure 11: High-resolution XPS spectra of W_{4f} (an up to e) and O_{1s} (f, g, h) in WOT (a), WCuT2 (b), WO (c and f), WCu05 (d and g), WCu2 (e and h).

Similarly, the fitting of W_{4f} spectra of each of the raw Cu-doped WO_{3-x} samples revealed two doublets each for W^{6+} and W^{5+} states [29]. Nevertheless, the ratio between the tungsten V and tungsten VI peaks is clearly decreasing versus the copper concentration. Hence, W^{5+} content in the WO sample is calculated to be equal to 0.19 and was found to be decreased to 0.14 and 0.10 in WCu05 and WCu2, respectively.

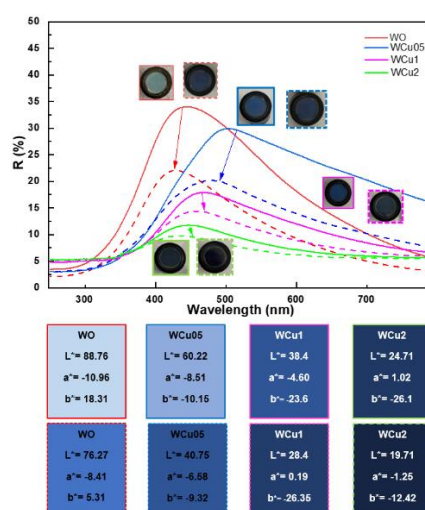
For all the powders, the high-resolution oxygen spectra (O_{1s} spectra) were fitted with three components to bring supplementary interpretation elements. As shown in Figure 11.f, g, h, the strongest signal at 530.66 eV corresponds to the oxygen atoms contained in the stoichiometric structure of WO_3 , i.e., introduced in a well-defined 6-coordinated oxygen site [27]. The second signal (531.8 eV) is related to the existence of oxygen defects in the sub-surface planes of the powders. The signal at 533.81 eV corresponds to oxygens bound to carbon atoms, which could come from the synthesis route (polyol-mediated precipitation). Interestingly, the peak intensity of the O_{1s} state relative to oxygen defects (located at 531.8 eV) shows a significant increase upon Cu doping increase. This leads to an estimation of the oxygen vacancy (V_O) content equal to 0.12 in the un-doped sample, and to 0.24, and 0.36 in WCu05, and WCu2, respectively. This last observation so indicates a drastic increase in the oxygen vacancies in WO_{3-x} after Cu doping, due to the aliovalent character of the chemical doping. Indeed, the drastic difference in the valence state of dopant Cu ion in regard to the host W ions of the matrix should be electronically compensated from oxygen vacancies. This

Chapter III: Results and Discussion

observation is in good agreement with the variation of the unit-cell parameters versus copper concentration, which was discussed previously.

2.2.2 Powder photochromic properties

The optical photochromic response of the as-prepared powders under UV irradiation was studied on the whole UV-visible-NIR range by measuring the diffuse reflectance spectra of un-doped and doped raw powders. All samples were characterized before UV irradiation and after 5 min irradiation as shown in Figure 12. Briefly, as previously already discusses in Part 1, the doped and un-doped powders possess a fully total absorption in the UV, i.e., typically characteristic of a wide-gap semiconductor, with the gap being located at 420 nm for the un-doped and shifted to 485 nm for doped powder. Furthermore, a quite important absorption in the visible and the near-infrared part of the spectrum is due to the inter-valence charge transfers between W^{5+} and W^{6+} or even can be described from the creation of the free charge carriers in the conduction band associated with the reduction of tungsten ions as explained by the Drude electronic cloud theory [28]. For the non-irradiated compounds, the infrared absorption increases with the copper concentration. Because the W^{5+} ion concentrations were shown to decrease with the copper concentration, the increase of the intervalence transfer probability with copper supports the participation of the copper to electronic mobility: the occurrence of multi-site charge transfers as in the short chains: $W^{5+} - Cu^{2+} - W^{6+} \rightarrow W^{6+} - Cu^+ - W^{6+} \rightarrow W^{6+} - Cu^{2+} - W^{5+}$, can explain the phenomenon. Nonetheless, the oxygen substoichiometry linked to the copper defects, as was confirmed by the XPS results, can also be at the origin of the absorption of more photons of the visible energy range, enhancing the charge depletion mechanism. The maximum reflectivity percentage located at 480 nm decreases from 35% for the raw sample, to 30% for the WCu05, to 17% for the WCu1, and 10% for the WCu2. Hence, as shown from the sample photographs as well as the reconstructed sample colorations from their L^* , a^* and b^* colorimetric coordinates, the color of samples become darker upon increasing copper concentration.



Chpt.III-Figure 12: Diffuse reflectance spectra of the undoped and Cu-doped WO_3 raw powders and their associated L^* , a^* , b^* parameters before irradiation (solid line) and after 10 min UV irradiation (dashed line).

Chapter III: Results and Discussion

Even if the studied samples exhibit less photochromic amplitude (color contrast between bleached and colored states) than the pre-oxidized samples (WOX) studied in the previous part, irrespective of their copper doping attribute, all the samples exhibit a huge photochromism in comparison with previous investigations reported on WO_3 photochromism [20]. Once again (see the conclusion of the 1st Part: § 1.4), we attribute this behavior to the nanometric aspect of the crystallite sizes. Indeed, thermodynamically, the relaxation of the steric constraints linked to the photoreduction promoting the creation of new W^{5+} color centers, would preferentially take place on oxide surfaces from oxygen anions desorption/absorption facilities. Highly divided materials definitively show improved photochromic properties.

The associated chromatic coordinates in L^* , a^* , b^* space presented in Figure 12 allow the comparison of the photochromic efficiency of the various samples from the optical contrast calculated between the non-irradiated and 10 min. irradiated samples. Indeed, even if our samples exhibit a photochromic effect mainly concentrated in the near-infrared part of the spectrum, the impact of the intervalence transfers in the visible range allows the observation of visible ΔC contrast (as previously defined in section 1.2.3). Photochromic contrasts are about 55.5, 50.6, 25.6 and 20.1 for WO, WCu05, WCu1 and WCu2, respectively. From the darkening of the non-irradiated compounds versus copper concentration, the copper introduction tends so to decrease the powder photochromic efficiency in terms of optical contrast between bleached and colored states.

2.2.3 Thin film photochromic properties

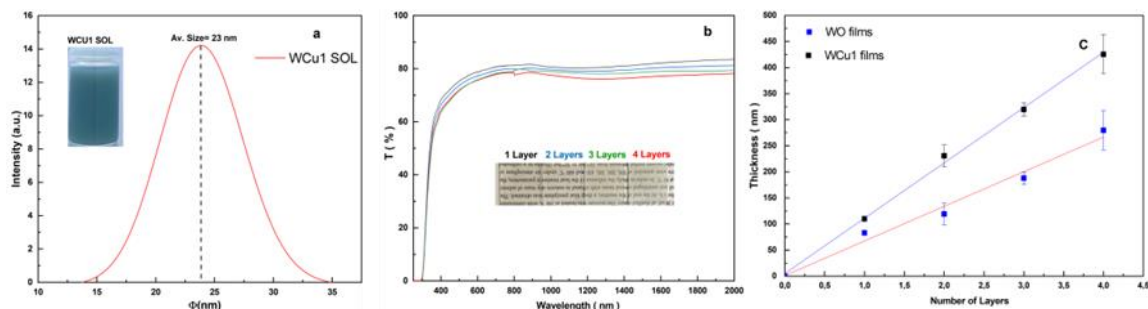
The next part devoted to the elaboration from powder to thin films and the characterization of its photochromic properties is focused on the comparison between the un-doped tungsten oxide (WO) thin film and the 1 mol% Cu-doped WO_3 (WCu1) thin film.

The elaboration of thin films of good quality requires the elaboration of well-dispersed colloidal suspensions. DLS measurements were used to track the size variation of the 90 g.L^{-1} dispersed NPs in suspension. Figure 13.a shows that powder in ethanol suspension with a Gaussian particle size distribution from the WOCu1 powder (similar curve is obtained for the WO powder) centered on an average size equal to 23 nm is obtained from the adequate protocol already experimented in the previous Ph.D. manuscript of Marie Bourdin [17]. The suspension remained stable with no sedimentation observed over time.

Different films issued from successive dip-coating steps (with 1, 2, 3 or 4 successive coated layers) have been studied. The transmission spectra of as-prepared thin films show a good visible transmission with a very low scattering coefficient (Figure 13.b). The films show a maximum transmission equal to 80 % at 600 nm, irrespective of the film thickness. However, a distinct low-intensity absorption band appearing at wavelengths around 1200 nm is observed on the 3- and 4-layer films. This absorption band can be without any doubt attributed to the presence of W^{5+} ions due to the intervalence charge transfer (IVCT) between W^{5+} and W^{6+} ions in the crystal network of the WO_{3-x} . The film thickness is plotted versus the number of deposited layers in Figure 13.c. The variation of the

Chapter III: Results and Discussion

film thickness versus the number of coating layers is almost linear: about 100 nm thickness is achieved for each coating.



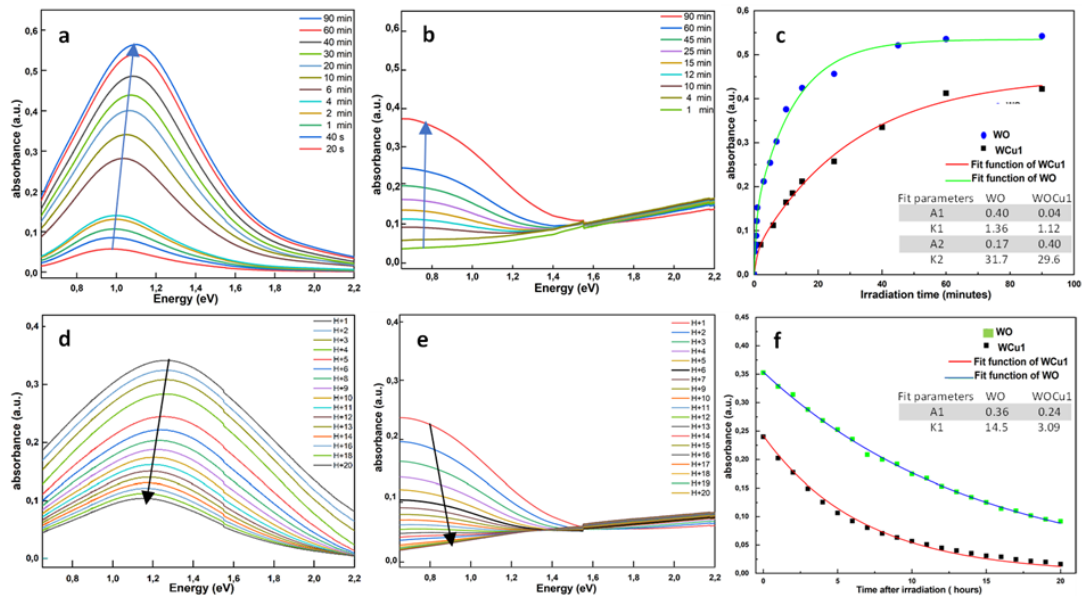
Chpt.III- Figure 13: Particle size distribution of WCu1 NPs in ethanol suspension (a), Transmission spectra and photographs of WCu1 films issued from 1 up to 4 successive dip-coated layers (b), Evolution of raw and doped film thickness as a function of number of dip-coated layers (c).

A preliminary photochromic test with fixed irradiation conditions (UV lamp, 8 W, 30 min.) has been conducted on all studied films. A focus is made on the 3-layer film since significant IVCT transfer in the NIR-region is observed; these preliminary tests have shown that UV-irradiation well generates the photochromism effect. Therefore, the evolution of the spectrum of both WO and WCu1 films versus irradiation time was collected (Figure 14.a,b) and the evolution of the absorbance at 1.1 eV for WO films and 0.75 eV for WCu1 film is extracted to investigate further the photo-redox kinetic (Figure 14.c). As shown in Figure 14.a,b, the initial absorbance of the films (before UV-irradiation) was considered as the reference absorbance (without any absorbance).

As seen from Figure 14.c, the absorbance at 1.1 eV (corresponding to the energy at which the IVTC band is the greater) of WO film seems to change rapidly in the first minutes of irradiation, then seems to slow down beyond 15 min of irradiation until almost no longer evolving after 90 min. In turn, the absorbance of WCu1 seems to change slower than the WO in the first minutes of irradiation, then stabilizes after 90 min. Also, the absorbance band maximum is shifted at 0.75 eV. This change of position of the absorbance phenomenon is coherent with the participation of the Cu^{2+} to the IVCT (W^{6+} to W^{5+} via Cu^{2+} ions in intermediate positions) as a proposed mechanism to explain the darkening of the pristine oxide coloration before irradiation. In comparison with coloring kinetic performed on powder samples (WOX) in Part 1, the thin films transmission allows more accurate characterizations and it appeared that to better express the differences between both films, a double exponential function (a combination of two first-order kinetic laws) must be used to fit the experimental data (absorbance evolution at its maximum), according to the:

$$Y = A1. [1-\exp(-t/K1)] + A2.[1-\exp(-t/K2)] \quad \text{Chpt.III-Equation 7}$$

Chapter III: Results and Discussion



Chtp.III- Figure 14: Evolution of absorbance during irradiation (coloring) of WO film (a), WCu1 film (b). For both films, absorbance at 1 eV (WO) or 0.75 eV (WCu1) evolution versus irradiation time and the associated kinetic parameters (coloring kinetic) (c). Evolution of absorbance in dark conditions (bleaching) of WO film (d), WCu1 film (e). For both films, absorbance evolution at 1 eV (WO) film or 0.75 eV (WCu1) in dark conditions (bleaching kinetic) (f).

With t in min, and so two characteristic times (K_1 and K_2) in min, and two characteristic amplitudes (A_1 and A_2). The values of the four parameters are shown in Figure 14.c. For both films, the coloring kinetic consists of two convoluted kinetic phenomena: a fast-kinetic component (K_1 is about 1 minute), and a slow-kinetic component (K_2 is about half an hour). Hence, in both cases (doped or undoped thin films): (i) the fast kinetic (during the very first minutes) could correspond to a quick photoreduction of the surface cations from W^{+6} to W^{+5} then, the surface after a short time will be saturated with W^{+5} ions and this fast mechanism stop; the slow kinetic could correspond to the ionic diffusion of the W^{5+} from the surface to the material bulk, allowing W^{5+} surface desaturation and so new surface photoreduction. Nonetheless, a significant difference is observed comparing the doped and un-doped film: while on the un-doped WO film, the coloring under UV irradiation is mainly governed by the fast kinetic phenomenon ($A_1 = 0.4$ whereas $A_2 = 0.17$), the WCu1 film coloring is mainly governed by the diffusive slow kinetic ($A_1 = 0.04$ whereas $A_2 = 0.4$). The quasi-quenching of the fast kinetic takes its origin in the defects associated with the Cu-doping. Basically, when Cu atom takes the W site in WO_3 , it produces three possible effects: (a) the narrowing of the fundamental band gap of the system due to the strong d-p coupling between Cu and O, which in turn leads O 2p level up, (b) the creation of an acceptor impurity narrow band above the valence band of WO_3 which is formed by the empty Cu 3d (e_g) orbital, (c) the creation of electronic compensating oxygen vacancies as bulk/surface defect [29], [30]. Thus, upon irradiation, after the appearance of electron/hole pairs which are generated at conduction band minimum (CBM) and valence band maximum (VB), respectively, then non-radiative recombination can be amplified from these defects. For illustration, Cu^{2+} can easily capture the electron to become Cu^+ with a full-filled electronic structure, resulting in a by-pass of the W^{6+} to W^{5+} photoredox mechanism. In another illustration, a segregation of the compensating oxygen vacancies at

Chapter III: Results and Discussion

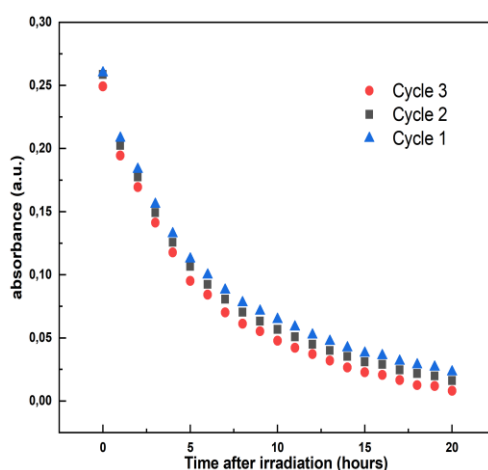
the surface avoids the valence band's holes/oxygen recombination required to close the photo-redox process.

For the bleaching properties, one can first notice that many research groups reported that the bleaching kinetic is very slow for tungsten oxide-based materials. Self-bleaching (when the product is only left in a dark environment to relax) is even most of the time not observed at all, i.e., it is often necessary to heat the film at 80°C-100°C in the air or under ozone (oxidative conditions) to obtain a complete relaxation [31][33]. In our case, the 3-layers WO and WCu1 films which were previously irradiated for 45 min (to nearly gain the coloring saturation) and let in the dark at room temperature for self-bleaching, show photochromic reversibility. The bleaching study was performed in the spectrometer chamber (dark condition) to record the evolution of the transmission spectra: a spectrum analysis is automatically performed every hour for 20 hours, stopping the sample illumination at 500 nm to produce any electron/hole pair creation. The absorbance spectra are shown in Figure 14.d,e for WO and WCu1, respectively.

Bleaching evolution was followed recording the absorbance at 1eV for the WO film and at 0.75 eV for the WCu1 film, in agreement with previous studies. First, for the WO films, the residual absorbance at 1 eV obtained after 20 hours of darkening is still important: equal to about 0.3, whereas the bleaching is total for the WCu1 film, with absorbance equal to 0.02 (Figure 14.f). The absorbance evolution for both films can be fitted from a single exponential decay trend overall 20 first hour's range. The single exponential decay function to fit the experimental data, according to the equation:

$$Y = A1.exp(-t/K1) \quad \text{Chpt.III- Equation 8}$$

Comparing both films (, the speed of the bleaching mechanism in WCu1 is almost five times faster than for the WO film: K1 = 3.09 and 14.05 hours, respectively. Thus, copper greatly improved photochromic reversibility.



Chpt.III- Figure 15: WCu1 film absorbance evolution at 0.75 eV versus darkening time through three successive coloring/bleaching cycles.

Chapter III: Results and Discussion

Finally, the great bleaching properties observed on copper-doped WO_3 film have allowed cycling tests to be performed. Cycling tests (3 cycles) were carried out on the WCu1 film as depicted in Figure 15. Irradiation steps were applied for 45 min irradiation, with sufficient darkening duration (15 hours, i.e., very near night & day real cycling conditions) in between each of the irradiation steps to let the compound fully self-bleached. The results show that the three cycles are almost identical which confirms the strong stability of the films under successive cycling and this augurs to be able to apply such thin films as smart windows for environmental buildings.

Briefly, in WO film, the phenomenon of re-oxidation of W^{5+} to W^{6+} by the oxygen in the air is very slow resulting in a long bleaching time. This represents a severe restriction for the large-scale application of such thin films as smart window photochromic films. In WCu1 film, the enhancement in photochromic reversibility, i.e., with a drastic increase of the bleaching kinetic, was ascribed to several factors, based on the characterization results. Notably, the increase in oxygen vacancies in WO_3 after Cu doping could extend the light-harvesting ability to the visible and near-infrared region. Also, the double injection mechanism added to the improved electron interactions thanks to the existence of W^{6+} , W^{5+} , Cu^+ and Cu^{2+} ions, surely plays a significant role in the bleaching improvement. The “de-trapping” of color center electrons created on 5d tungsten orbitals during UV irradiation thanks to an additional, new $\text{W}^{5+} - \text{Cu}^{2+} \rightarrow \text{W}^{6+} - \text{Cu}^+$ intervalence electronic transfer is proposed. Furthermore, the energetic proximity of the copper 3d (e_g) level and oxygen 2p levels, favoring p-d coupling, can further lead to close the photo redox loop through the recombination of the defect electron trapped as Cu^+ defect above the valence band and the hole created in the maximum of the VB band during irradiation.

2.3 Conclusion for Part 2

In conclusion, doping of WO_3 with Cu prepared by the polyol method has been proved to be an effective strategy to improve the bleaching mechanism and so kinetic of the smart photochromic films. The photochromism (coloring/bleaching) kinetic of these composites was thoroughly studied with a deep accuracy allowed by the obtaining of non-scattering thin films. These last experiments have supported the conclusion already given in Part 1' conclusion: (i) the coloring mechanism of undoped films is governed mainly by fast components consisting of quick photo-reduction of the surface cations from W^{+6} to W^{+5} ; (ii) then the surface after a short time becomes saturated with W^{+5} ions and this fast mechanism stop to let place to a slower diffusive mechanism (W^{6+} ions have probably to move from bulk to surface in order to regenerate the possibility of surface photo-reduction). The WCu1 film coloring kinetic is governed by the slow component only. But the WCu1 film records faster bleaching with an order of 3.09 hours compared to 14.05 hours for the WO film. The bleaching kinetic was enormously enhanced due to the increase in oxygen vacancies in WO_3 after Cu doping, which could, in turn, extend the light-harvesting ability of this compound to the visible and near-infrared region. In addition, the cycling study on WCu1 film confirms the efficiency of the product in optical applications. This study provides compelling evidence for the versatile usability of our films across various optical applications, including smart textiles, windows, and optical filters.

Chapter III: Results and Discussion

Chapter III: Results and Discussion

3 Part 3: Thin and thick plastic thin film based on WO_{3-x} active NPs

In this part, we introduce a new type of photochromic smart windows consisting of window glass coated with a thin film of tungsten trioxide/polyvinyl alcohol (WO_{3-x}/PVA) composites that can modify their transparency properties autonomously with incident light intensity. In comparison with the results shown on thin films obtained from dip-coating of WO₃-EtOH suspensions (Part 1&2), the WO_{3-x}/PVA composite films that will be herein obtained are thick and with a large and tuneable quantity of WO₃ active particles that the light will intercept through the films, increasing thus the photochromic effect amplitudes. A focus will be made on the “smart thermal insulating properties” of such composite films, with the target of their usability as smart (photochromic energy-saving materials) building windows.

3.1 Elaboration and characterization of NPs and plastic films

Preparation of WO_{3-x}/PVA films from WO_{3-x}/PVA coating suspension

Firstly, a 10 wt% transparent PVA solution was prepared by dissolving PVA (80% hydrolyzed) in DI water at 25 °C under stirring for 5 h. Then, the as-synthesized WO_{3-x} nanopowders (equivalent to the WOR powder previously described in the two previous parts) were added to the prepared PVA. The mixtures were stirred at 500 rpm for 30 min and then agitated strongly using a stirring bar at 1000 rpm for 1 h to gain the homogeneous WO_{3-x}/PVA suspension.

The plastic films were prepared using solvent casting (SC) and dip coating (DC) methods. For the DC method, the WO_{3-x}/PVA suspensions were dip-coated on a standard glass substrate to obtain WO_{3-x}/PVA composite thin films. The dip-coating parameters are (i) the dip-coating speed: 133 mm.min⁻¹ and (ii) the number of successive coating steps to produce multilayers. In this case, a 30 min drying is operated between each step in an oven (75 °C). In the case of the SC method, different quantities of the suspension were dried in the dissolved PVA plastic substrates for 1 day at room temperature then the films were peeled off and kept for post-characterization.

3.2 Suspension study: Results and discussions

To tune the PVA matrix uptake percentage in the 30 mL aqueous suspension of the as-prepared blue WO_{3-x} nano-powders (NPs) from the polyol process, a fixed concentration of WO_{3-x} 65 g.L⁻¹ was mixed with different weight percentages of the PVA dispersant (0, 1, 2, 3, 4, 5, 10 wt%), as shown in the photograph reported in Figure 16.a (inset). It shows a progressive change of color from highly turbid blue suspension to light transparent blue with the increase of the PVA content. Indeed, the higher the dosage of the PVA, the more transparent the film is until the colloidal suspension color stabilizes in 5-10% of PVA. DLS measurements were used to track the size variation of the 65 g.L⁻¹ dispersed NPs as a function of the PVA dose. A remarkable decrease in the average size was observed once using the PVA dispersant as revealed in Figure 16.a. The average size drops from 442 nm in 0% PVA to 62 nm in 1% PVA until it reaches the size of almost 10 nm in the 5 or 10% PVA sample. The PVA plays a dual role in the polymeric suspension as a polymer matrix (in the way, after the suspension drying, WO₃ – PVA polymeric-matrix composites could be obtained) and dispersant for the

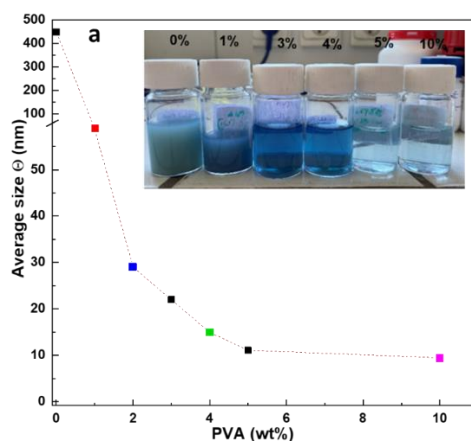
Chapter III: Results and Discussion

WO_{3-x} NPs aqueous suspensions. Table 4 summarizes the values of mean size and the polydispersity index (PDI) (defined as the standard deviation (σ) of the NPs diameter distribution divided by the mean NPs diameter) for all samples.

Chpt.III-Table 4: Summary of the mean size and PDI of the studied series.

PVA (wt%)	Mean size (Intensity)	PDI
0	442 ± 15 nm	0.65
1	62 ± 12 nm	0.35
2	29 ± 3.5 nm	0.32
3	22 ± 1.5 nm	0.22
4	16 ± 1.9 nm	0.21
5	10 ± 2.2 nm	0.25
10	9 ± 1.4 nm	0.13

Furthermore, the light transmission of the suspension series was measured into a quadrat optical cuvette with a 1 cm path length. Due to the O²⁻→W⁶⁺ transfer (wide band gap semiconducting properties) and the Gaussian absorption band due to the W⁵⁺→W⁶⁺ intervalence charge transfer (IVCT) in the near-infrared region (band centered at about 1,2 μm), a transparency window can so be reached in the visible part of the spectrum. The photochromic activity of the particles is well maintained: the IVCT band still can be modulated in intensity from UV irradiation.



Chpt.III-Figure 16: a) Evolution of the average NPs size as a function of the PVA weight percentage. Inset: photograph of the as-prepared PVA/WO_{3-x} suspensions.

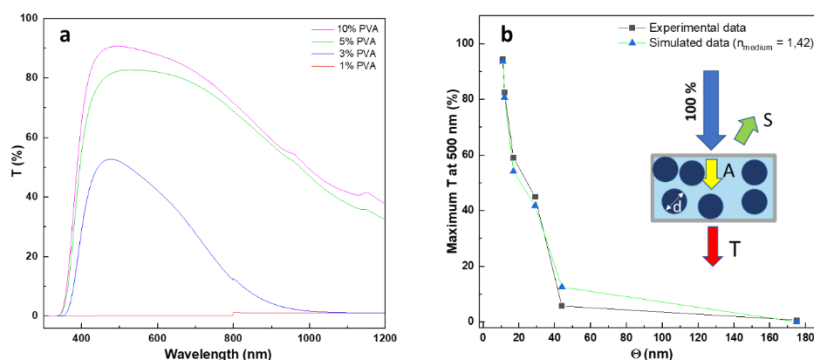
In the visible range, the suspension transparency improved as the average particle size decreases (with the PVA charging dose increases), Figure 17.a. In addition, the suspension with lower than 3% PVA almost loses NIR transmittance modulation ability. The 1 or 3% PVA suspensions exhibit a very low transmittance in the near-infrared range, i.e., for wavelengths for which the photochromism takes place due to a large scattering phenomenon taking place on each particle. On the contrary, the 5 or 10% PVA suspension shows the largest optical modulation potentiality in the infrared region thanks to

Chapter III: Results and Discussion

their very low turbidity. Thus, it appears that suspension turbidity due to the particle scattering phenomenon has to be limited to optimize the suspension photochromism.

To evaluate the impact of the PVA dispersion efficiency on the particle size in the studied series, a simulation of the optical transmittance using the Mie calculator software was carried out as illustrated in Figure 17.b in parallel to the experimental data. When a beam of light propagates into a medium, the beam will be attenuated and the transmittance can be calculated following the equation: $T = e^{-(TAC * l)}$, where TAC is the total attenuation coefficient, and l is the thickness of the scattering medium (l is so fixed to 1 cm, the path length of the quadrate optical cuvette, for direct comparison of the simulated and the experimental measurements). The TAC value can be obtained through the Mie scattering calculator program. Various important parameters have to be integrated into the modeling: sphere diameter (d), wavelength (calculation has proceeded for monochromatic irradiation), index of refraction of the dispersive medium, real and complex refractive indexes of the WO_3 colloidal spheres, and particles concentration (number of spheres per cubic micron, $C = N_{part}/V_{medium}$) [34]. Rigorously simulating the colloidal suspension turbidity faces a complex issue since the suspension offers different scattering interfaces: WO_3 -water, WO_3 -PVA, and PVA-water, and potential multi-scattering phenomena. As PVA macromolecules get an efficient dispersing effect, it was considered that the particles are well embedded in PVA shells and so that the active scattering interface, in first approximation, is mainly the WO_3 NPs – PVA shells interface. In addition, the used simulation software with a 2-flux approximation does not consider multi-scattering eventualities. The real index of refraction (n) of the WO_3 spheres at different wavelengths, was extracted from literature references ($n-WO_3 = 2.3$) [35]. As an additional difficulty, the exotic blue color for the as-prepared oxygen-sub stoichiometric tungsten oxide NPs is associated with the exotic k index which cannot be extracted from literature results. Furthermore, the k complex refractive index evolves versus wavelength. That is why, the suspension turbidity simulation was performed for an irradiation wavelength of 500 nm, *i.e.*, in the middle of the transparency window (far from the occurrence of both the electronic band transfer and the IVCT), where the k index can be considered nearly null. The simulated results are summarized in Figure 17.b where the particle size d varies from 500 nm to 10 nm. Comparing the experimental data (transmission through the cuvette at this fixed 500 nm wavelength) and the simulated data, which are almost superimposed, one can conclude that the transparency of the suspension in the visible band is well directly correlated to the particle size diameter and that the average diameter of the tungsten oxide particles dispersed in solution is well efficiently decreased thanks to PVA addition.

Chapter III: Results and Discussion



Chpt.III-Figure 17: a) Optical transmission of different PVA/WO_{3-x} suspensions depending on the PVA wt.%, b) Comparison of the experimental transmission at 500 nm through the 1cm length cuvette and the simulated transmission at the same wavelength through the same medium thickness as a function of average particle diameter. Inset: additional schematic illustration of the simulated parameters and method.

3.3 From suspension to film: elaboration and optical properties

This section is devoted to the elaboration from suspension to composite films and the characterization of their optical properties, focusing on the comparison between the films prepared from two adopted coating processes: dip-coating (DC) and solvent casting (SC).

All samples were prepared from suspensions using the NPs concentration equal to 65 g.L⁻¹, and 5 wt.% of PVA plastic matrix, i.e., the suspensions for which the best transparency was observed (previous section). The first PVA-WO₃ composite film series (“thin” films) was issued from successive dip-coating steps (with 1, 2, 4, 8, or 10 successive coated layers) on glass substrates, where the number of successive coatings allows the control of the final film thickness. The second batch of films (“thick” films) was prepared by solvent casting, producing a well-controlled thickness mainly tuning the amount of the casted suspension (20, 40, 80, 100, or 130 g of the 5% PVA) on a 2 cm² glass substrate surface. The film labels and associated thickness are listed in the table below (Table 5). Dip-coating and solvent casting processes lead to two well-separated series on the point of view of the film thickness as “sub-micrometric thin films” from 0.1 up to 1.35 μm for the DC films, and “sub-millimetric thick films” from 100 up to 550 μm about. In their pristine state (before UV-irradiation), the transmission spectra of as-prepared thin films show a well-visible and NIR transmission with a quite low scattering coefficient (Figure 18.a). Film transmission at 600 nm, where the absorption of the WO₃ particles is nearly null (in the middle of their transparency window), well allow the particle scattering effect. Besides, as shown in previous parts 1 & 2, at 1200 nm, the transmission is, above all, affected by the intervalence charge transfer (IVCT) between W⁵⁺ and W⁶⁺ ions (absorption) of the WO₃ particles. The DC films show a maximum transmission equal to 87 % at 600 nm (D1 sample), then the decrease of this value is observed versus the film thickness increment down to 45% for the D5 sample. The D6 sample exhibits low transmittance, due to the degradation of film homogeneity and quality, with the successive coating number. In addition, in the near-infrared region, the transmission at 1200 nm varies from 80% for the 98 nm-thick film (D1) down to 37% for the 838 nm-thick one (D5). Whereas, as shown in Figure 18.c, the SC films show a slightly lower transmission

Chapter III: Results and Discussion

around 75% in the middle of the visible range with also slight degrading transparency with the increasing of the film thickness. In the NIR range, transmission value varies from 65% for the 112 μm -thick film (S1) down to 31% only for the 225 μm -thick film (S3).

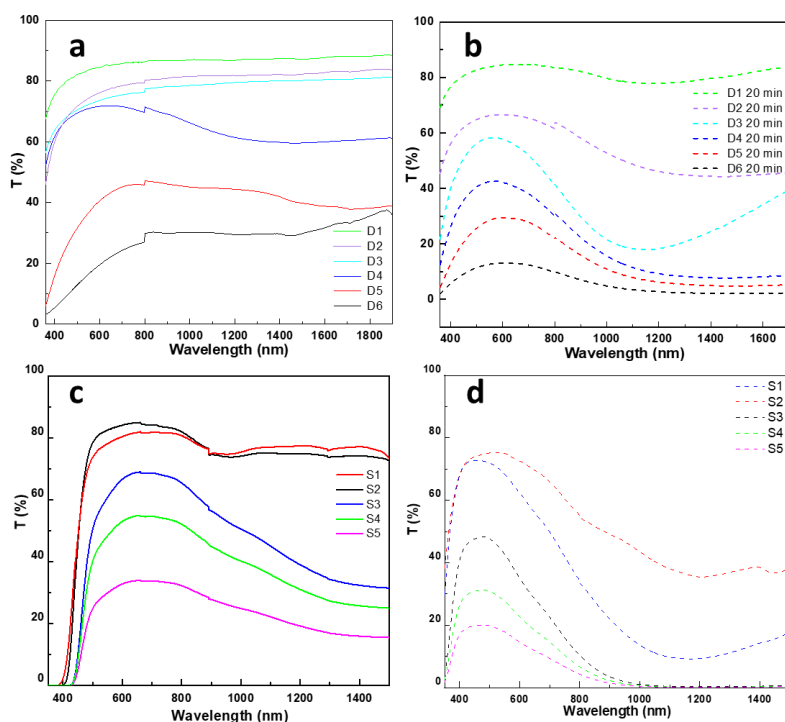
t for the SC ones.

Chpt.III-Table 5: Dip-coated and solvent-casted films and their measured associated thickness from profilometric analyses.

Coating process	Film ID	Thickness (μm)
	D1	0.098
Dip Coating	D2	0.215
	D3	0.422
	D4	0.622
	D5	0.838
	D6	1.355
Solvent Casting	S1	112
	S2	180
	S3	225
	S4	356
	S5	552

A preliminary photochromic test with fixed irradiation conditions (UV lamp with 8 W, 20 min associated with irradiation surface power of 5.6 W.cm^{-2}) has been conducted on all studied films as shown in Figures 18.b and d. The irradiation affects all film optical properties, especially at the frontier between the visible and near-infrared regions, with higher activity in the near-infrared region. Indeed, due to the photochromic activity of the NPs embedded into the composite films, direct exposure to UV irradiation produces a pale blue coloration of the films suggesting a significant increase in W^{5+} content. In all elaborated films, an important loss of transmission was observed at 1200 nm while this decrease is not that obvious at 600 nm, showing the governing mainly from absorption or scattering respectively at high or low wavelengths. The contrasts between colored and bleached states (contrasts between irradiated and non-irradiated states) will be independently investigated in the visible range and the NIR range and discussed in the next part.

Chapter III: Results and Discussion



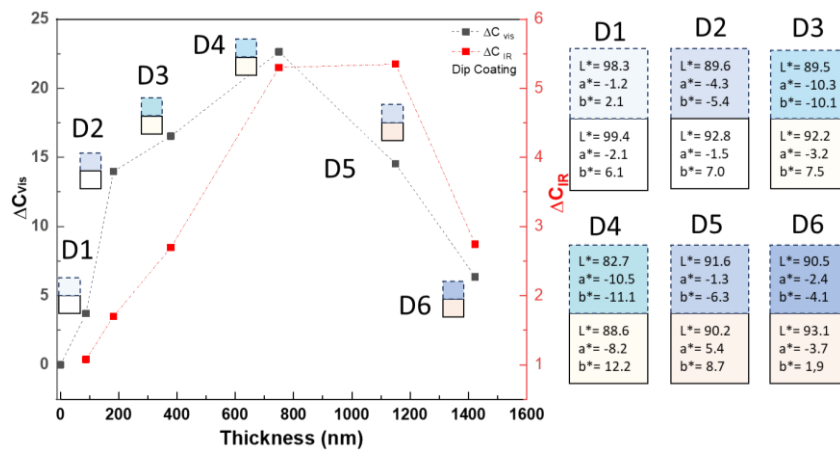
Chpt.III-Figure 18: Transmission spectra before irradiation (in solid line) and after irradiation (in dashed line) of a, c) dip-coated films, b, d) solvent-cast films.

In the visible range, the transmission spectra allow the calculation of the associated chromatic coordinates in L^* , a^* , and b^* space and so the ΔC_{vis} visible contrast (as previously defined) (reported in Figure 19 and Figure 20 for respectively the DC and SC samples). The visible contrasts allow the comparison of the photochromic efficiency of the samples issued from both coating processes. In the near-infrared, where the photochromic efficiency is the highest in terms of transmittance modulation, such an “optical contrast” cannot obviously be extracted. Thus, we proposed an infra-red optical contrast (ΔC_{IR}), calculated as the average transmission difference in the range 800 nm up to 2500 nm, between the two states (non-irradiated and irradiated states) of each film (what can be seen as the area difference between the two transmission curves corresponding to the pristine and irradiated state in the whole NIR region).

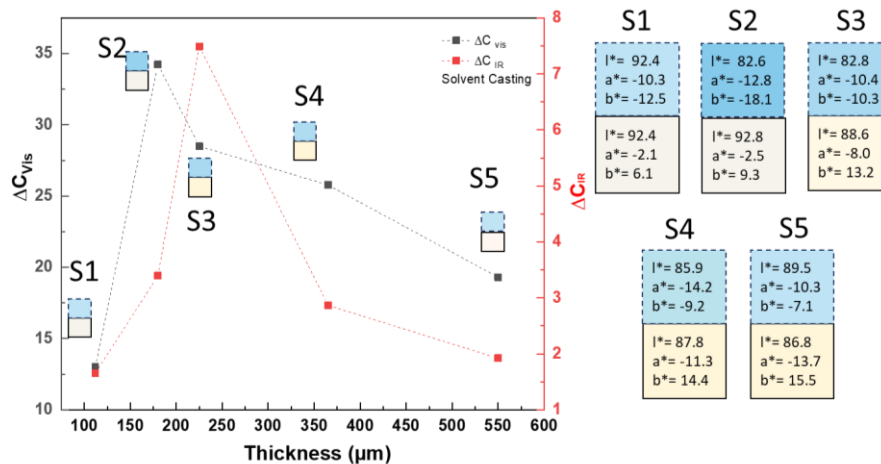
The evolution of both ΔC_{vis} and ΔC_{IR} are reported in Figure 19 and Figure 20, respectively for the DC samples and the SC samples. For both film series, bell shape curves are obtained for the visible contrast as well as for the NIR contrast, meaning an optimal film thickness is reached in both cases. This result can appear as surprising since the two series differ greatly in terms of thickness. At this stage, only hypotheses can be proposed. The degradation of the contrasts with increasing the film thickness can be produced: (i) either by scattering phenomena (which can be linked to film homogeneity degradation as the inclusion of pores in between the successive coated layers of the DC series, for illustration); (ii) or by too large light absorption through films (while an equivalent thickness of WO_3 powder becomes too high for the thicker films as for the last samples of the SC series, for illustration). The maximal values of the ΔC_{vis} and ΔC_{IR} are 34.37 and 7.9, which were

Chapter III: Results and Discussion

recorded for the S2 and S3 films, respectively; whereas ΔC_{vis} and ΔC_{IR} reached less than 20.2 and 5.4 for the best films issued from the DC process (D4 and D5). Hence, the casted films, exhibit the best photochromic amplitude despite a large thickness thanks to the conservation of a highly visible and still moderate NIR transparency. SC films are also the most promising for their use as solar filters, *i.e.*, with the best contrast between visible and near-infrared transmission, especially in their irradiated state. At this stage, it can be supposed that the SC process, which is a “one step” coating process, preserves composite films homogeneity regarding the DC process, which leads to the degradation of films homogeneity from the inclusion of pores, inhomogeneity, or other defects in between layers during the successive coating operations.



Chpt.III-Figure 19: Calculated optical and infrared contrasts of DC films as a function of their thickness and their associated L^* , a^* , b^* parameters before irradiation (solid line) and after 20 min UV irradiation (dashed line).



Chpt.III-Figure 20: Calculated optical and infrared contrasts of SC films as a function of their thickness and their associated L^* , a^* , b^* parameters before irradiation (solid line) and after 20 min UV irradiation (dashed line).

3.4 Photochromic properties of the films: kinetic aspects

In these measurement series, a focus was made on the 665 nm (DC) (D4 sample) and 220 μm (SC) (S2 sample) films since for both samples, a significant high photochromic efficiency associated with a drastic increase of IVCT transfer versus irradiation time are observed, especially in the NIR-region.

Chapter III: Results and Discussion

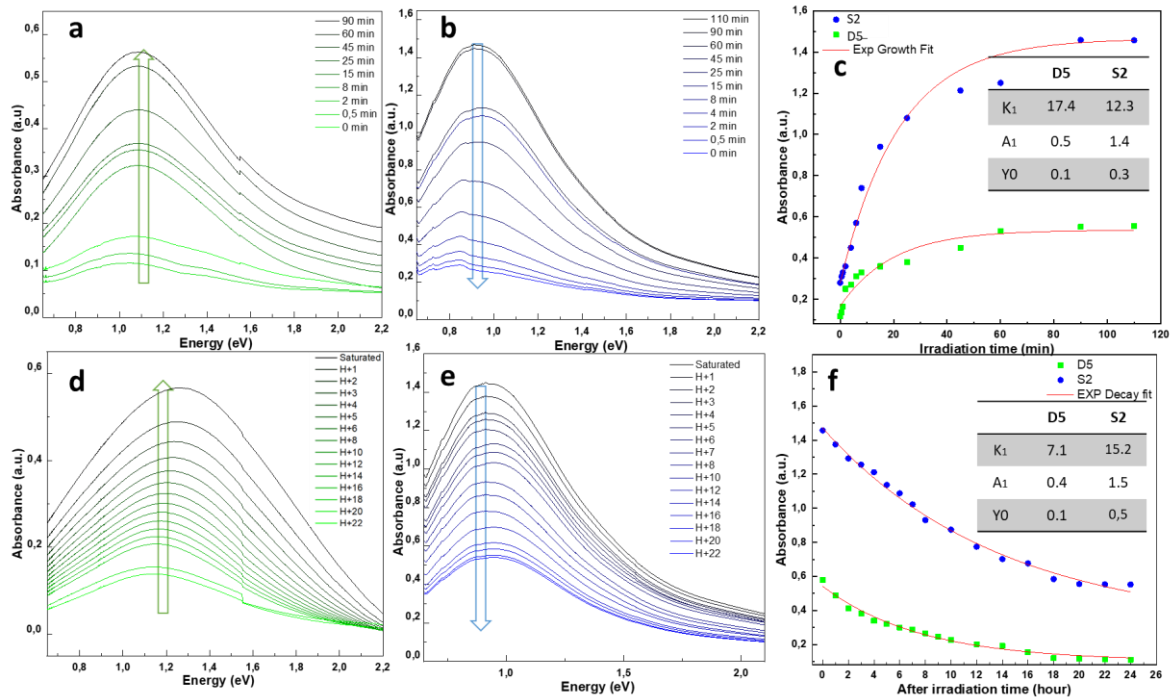
These two samples were the ones in their respective series, which possess the best visible contrast and the second-best infrared contrast. The two films were irradiated with previously fixed irradiation conditions. Therefore, the evolution of the absorbance ($A = -\log(T)$) spectrum of both films versus irradiation time was collected (Figure 21.a,b). The absorbance evolution at 1.1 eV is extracted to investigate further the photo-redox kinetics (Figure 21.c). As for the diffuse reflectance of the included powders (see Parts 1 & 2), the films' absorbance at 1.1 eV (corresponding to the energy at which the IVTC band is the maximum) seems to change rapidly in the first minutes of irradiation, then it slows down beyond 20 min of irradiation until almost no longer evolving after 90 min. To better express the differences between both films, an exponential growth function (first-order kinetic law) was used to fit the experimental data (absorbance evolution at its maximum), according to:

$$Y (\text{"total absorbance"}) = Y_0 + A_1 \cdot [1 - \exp(-t/K_1)] \quad \text{Chpt.III- Equation 9}$$

with t in min, K_1 is the characteristic coloring time in min, A_1 is the characteristic growth (coloring from IVCT absorbance band) amplitude and Y_0 is the y-offset due to scattering phenomena mostly. The values of the three parameters are shown in the inset of Figure 21.c,f. The SC film recorded slightly faster coloring kinetics compared to DC one (12.3 to 17.4 min). Moreover, significantly higher absorbance amplitude (A_1) is observed for the latter, which can be attributed to the higher thickness containing multiple numbers of absorption centers as was proven by the two-flux model discussion. As a reminder, for both films, the coloring kinetic consists of photo-reduction of the surface cations from W^{+6} to W^{+5} until the surface becomes saturated with W^{+5} ions. Compared with the coloring kinetic of powders (part 1), the polymer matrix slows down a bit the coloring times. Coherently, the thick films (SC films) get so a coloring kinetic more significantly decreased than the thin films (DC films). For the bleaching properties, the studied films that were previously irradiated for 120 min (to nearly gain the coloring saturation) and let in dark at room temperature for self-bleaching, show photochromic reversibility. The spectra during the self-bleaching process are recorded while avoiding re-exciting the sample from UV irradiation (spectra recorded only on visible – NIR ranges). The absorbance spectra for the bleaching half cycle are shown in Figure 21.c,d for SC and DC films, respectively.

Similarly, to the methodology conducted to study the coloring kinetic, the bleaching evolution was followed by recording the absorbance at 1.1 eV. First, for the SC film, the residual absorbance at 1.1 eV obtained after 20 hours of darkening is still important: equal to about 0.38, whereas it is almost 0.08 in the DC film (Figure 21.e). It seems that while near-full reversibility is well maintained for the DC films, a partially non-reversible photochromism is reached for the SC films. The absorbance evolution for both films can be fitted from a single exponential decay trend on the complete 20 first-hour range. The single exponential decay function to fit the experimental data, according to Equation 3, with t and K_1 in hours,

Chapter III: Results and Discussion



Cpt.III-Figure 21: Evolution of absorbance during irradiation (coloring) of the D5 DC film (a), and the S2 SC film (b). For both films, absorbance at 1 eV evolution versus irradiation time and the associated kinetic parameters (coloring kinetic) (c). Evolution of absorbance in dark conditions (bleaching) of the same D5 (d) and S2 (e) films. For both films, absorbance evolution at 1 eV in dark conditions (bleaching kinetic) (f).

where A_1 is the characteristic bleaching amplitude and Y_0 is the y-offset reached after 120 min irradiation. Comparing both films, the speed of the bleaching mechanism in DC is almost two times faster than for the SC film: $K_1 = 7.1$ and 14.2 hours, respectively. As for coloring mode, these bleaching tests confirm the fact that the PVA acts as a non-neutral function in terms of kinetic, especially in bleaching mode because the polymer matrix should soften the reoxidation possibilities. From this point of view, thin films (obtained from the dip-coating process: DC films) are more efficient than thick ones (obtained from slip casting process: SC films).

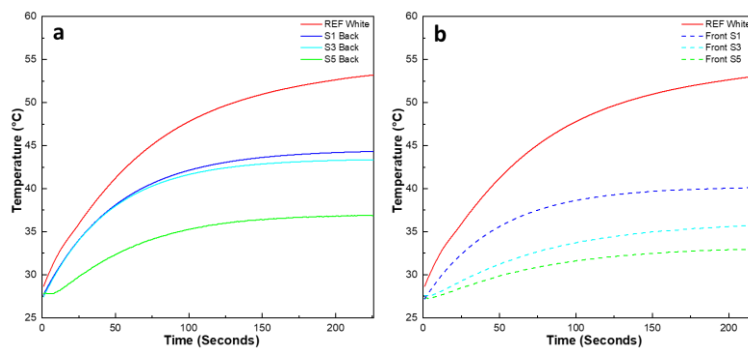
3.5 Thermal insulation properties

First, we conducted a preliminary test on various films (S1, S3, and S5) to evaluate the effect of thickness on the efficiency of thermal insulation. Our designed prototype room was used as a model equipped with a $WO_{3-x}/PVA/Silica$ photochromic window and painted white inside (see Figure 22.a). Thermal insulation performance was measured by introducing a thermocouple in the inner room and then recording the changes in temperature after irradiation under an artificial solar source lamp in real-time (Figure 23). As a reference, a virgin boro-silica window was also tested. The measurement was conducted in a special room designed for sensing applications in the I2M laboratory. This means that the temperature of the room was controlled to be always at 20°C with no opened external windows or airflow.

Chapter III: Results and Discussion

Furthermore, the measurements were recorded one time with the film facing (front model) the solar source and another time with the film opposite (back model) to the solar source. Under the powerful solar irradiation used the film changes its color from transparent to blue within less than a few 10 s, i.e., very quickly regarding the recording time of the temperature evolution and that is the key (the maximum of optical modulation) to efficient thermal insulation. Indeed, it can be considered that films have reached their colored state with all the absorbance centers that will act as a thermal barrier.

In both designs (front and back), all photochromic windows successfully act as a thermal barrier and block the temperature from raising inside the room with higher efficiency compared to a virgin window without coating as shown in Figure 22.a,b. In all tested films, the front design exceeds the back one in terms of temperature difference (defined as thermal difference at the maximal temperature $\Delta T_i = T_{back/front} - T_{REF}$) as shown in Table 6. To better decide which film is more suitable for the post-insulation application, we calculated the difference between $\Delta T_{front} - \Delta T_{back}$ as resumed in Table 6, the S3 film has a maximum contrast equal to 6.9 (between the back and front designs) among all films which make it the best choice for post thermal application. This film can serve as a thermal barrier and regulator depending on the deposition side (front or back) with the least required materials to be fabricated.



Chpt.III-Figure 22: Temperature-time dependent change of the inner room: b) Back design, c) Front design.

Chpt.III-Table 6: Thermal difference parameters extracted from Figure 22 a, b.

Film ID	ΔT_{back}	ΔT_{front}	$\Delta T_{front} - \Delta T_{back}$
S1	11.5	13.3	1.8
S3	12.6	19.5	6.9
S5	19	23	4

As the thermal efficiency was tested under coloring mode, the S3 film was chosen to characterize more deeply the thermal insulation behavior in two differently painted rooms. Two wooden room designs were adopted: one using a white-painted inner room and the second one with a black one. Six measurement series are so executed (white ref and black ref are for the measurements that were made on a white and black-painted box with the standard window series, and white-front, black-front, white-back, and black-back addressed the four experimental combinations) to find the best design for

Chapter III: Results and Discussion

this application. To better quantify the photo-thermal behavior of the film, the temperature-time curves were modeled using a bi-exponential model for each segment alone (i.e., during solar irradiance exposure for the first segment, and natural cooling down after stopping solar exposure for the second segment):

$$Y(t) = \begin{cases} T_0 + Ag \cdot (1 - e^{-t/\tau_g}) & t \leq tc \\ T_0 + Ag \cdot (1 - e^{-(t-tc)/\tau_d}) \cdot e^{-tc/\tau_g} & t > tc \end{cases} \quad \text{Chpt.III-Equation 10}$$

$Y(t)$ is the temperature at a given time, and T_0 is the starting temperature at which the experiment starts. Ag is the growth amplitude of the first exponential segment (we have supposed that the growth and decay amplitude are the same since the reversibility will be total because of that the inner box will be well equilibrated after a long time, with the exterior ambient temperature, which did not undergo any variation). tc is the offset time between exponential growth and decay. τ_g is the exponential growth term (irradiation is ON) and τ_d is the exponential decay term (irradiation is OFF). From the bi-exponential curve fits shown in Figure 23.b,c, we obtained the fitting parameters listed in Table 7.

Chpt.III-Table 7: Summary of the fitting parameter results using the bi-exponential function.

ID	T ₀	Ag	τ _g (s)	τ _d (s)	ΔT _{back}	ΔT _{front}
REF White	28.7	24.7	80.3	85.6	-	-
REF Black	32.6	23.2	107.6	96.5	-	-
White Front	27.5	7.1	58.6	89.6	-	19.5
White Back	28.1	12.5	62.3	74.7	12.6	-
Black Front	31.2	6.8	53.8	106	-	20.2
Black Back	31.9	10.2	71.0	115	15.5	-

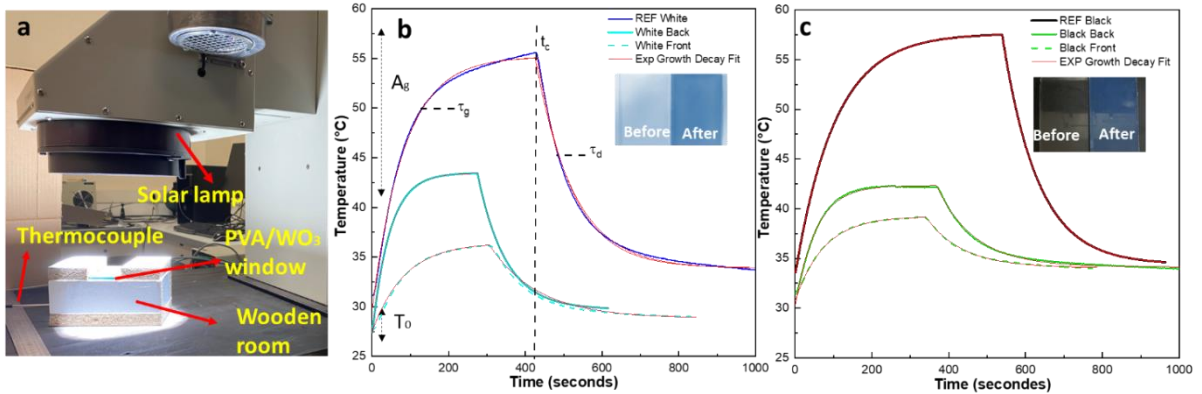


Figure 23: a) Photograph of our room design equipped with the smart window coated PVA/WO₃, Temperature-time dependent change of the inner room: b) white model, c) black model (with photographs of each smart window before and after irradiation).

Chapter III: Results and Discussion

With the standard (virgin) glass window, the heating amplitude is about 24°C for both black and white boxes. Surprisingly, the equilibrium temperature is not significantly impacted by the inner color of the wooden room. The white and black room designs and both models (front and back) provide very good thermal insulation properties compared to the reference, which was also recorded in the same conditions. The front model in both designs (black and white) gives a superior thermal difference at the maximal temperature: in the case of the white room the $\Delta T_{\text{front}} = 19.5$, compared to $\Delta T_{\text{back}} = 12.6$ for the back model. In the black-painted room, the thermal insulation properties were almost the same as the white room design with a $\Delta T_{\text{front}} = 20.2$ and $\Delta T_{\text{back}} = 15.5$. The findings of this study have solidified the notion that the inner paint color has no impact on the thermal equilibrium of the system comprising the room and window. This crucially implies that our films deliver consistent performance, regardless of whether the inner wall color is black or white. As revealed from the fitting parameter, the growth time is lower than the decay time in both designs (black and white) which was expected since the decay phase takes more time to reestablish the thermodynamic balance with the exterior atmosphere. The black model requires more time to come back to its initial state due to its color that can absorb part of the heat adding more time to reach the balance again. Table 8 summarizes the performance of various based photochromic films reported in the literature. The obtained photochromic windows exhibit a comparable performance when compared to many of the previous reports on such properties on other systems. Also, considering the simplicity of film fabrication and materials consumption one can conclude that our films offer supplementary superior economic/performance properties. The smart window design proved to be an efficient future solution for energy-saving applications.

Chpt.III-Table 8: The performance of the current films and those reported.

Materials	Fabrication method	X-chromic effect	Photoresponse time/wavelength	ΔT (°C) $T_{\text{REF}} - T_{\text{Room}}$	Ref.
VO₂/Graphene/Cu/PET	CVD+sputtering +Etching	Thermochromic	30 min, artificial sunlight	64-38=26	[36]
WO₃/Quantum dots/PVA	Casting+molding	Photochromic	1 min, 365 nm	47-32=15	[37]
V_{0.8}W_{0.2}O₂@SiO₂+ (PNIPAm) microgel	Sol-gel	Thermochromic	8 min, 0.1 W.cm ² infrared lamp	49-34=15	[38]
WO_{3-x}/PVA	Solvent casting	Photochromic	53 seconds artificial sunlight	56-36=20	Our work

3.6 Conclusion for Part 3

Effective thermal insulation has been achieved using the as-prepared composite smart windows by solvent casting method. In these films, WO_{3-x} nanoparticles ensure the role of the photochromic

Chapter III: Results and Discussion

centers, and the PVA matrix is used as transparent polymer matrix as well as an efficient dispersing agent of the tungsten oxide colloids. A simple two-flux model (Kubelka Munk theory) was applied to track the correlation of the absorption and scattering coefficients in both adopted methods to fabricate composite films: solvent casting and dip coating processes. The calculations revealed the increase of the K absorption coefficient versus the thickness of the films while the S scattering coefficient was higher in the case of the DC method, even if DC films are thinner than SC films. Thus, simulated and experimental data proved that the SC method has superior advantages over DC including less scattering and higher absorption so higher photochromic efficiency (i.e., higher photochromic contrast between colored and bleached states). The photochromism (coloring/bleaching) kinetics of both these composite series (SC and DC) were thoroughly studied. On this aspect, thin DC films exhibit a bit superior photochromic speed than SC films, surely due to a photo-redox reaction blocking effect from the PVA matrix. In addition, the thermal insulation measurements, performed on the SC film series, indicated a very good thermal regulation performance of our smart windows, especially when the smart films are deposited on the front side of the window glasses beside the irradiation source. With this front size design, white or black-painted model rooms are well thermally insulated, with a gain of temperature moderation compared to a virgin glass window of almost $\Delta T = 20.2$ and 19.5°C respectively, with white or black room design. This study is proof of the promising usability of our smart windows in the field of energy-saving materials and thermal insulating smart windows for the next generation of buildings.

Chapter III: Results and Discussion

Chapter III: Results and Discussion

4 Part 4: Developing plastic photochromic fibers for sensing application: the combination of 0D WO_{3-x} structure in a 1D polymeric matrix.

As we have mentioned in Chapter 1, the combination of organic and inorganic compounds can offer multiple novel properties coming from the contribution of both. In this part, we investigate for the first time, the integration of the nanostructured WO_{3-x} inside plastic optical fibers (POFs) using innovative methods. In this section, we introduce a new type of polyethersulfone (PES) POFs functionalized by photochromic cladding and its detailed properties. In addition, we investigate the different properties of the as-fabricated POFs.

4.1 Functionalization of polysulfone plastic optical fibers by WO_{3-x} :

4.1.1 Core-fiber drawing (signal quality control of the non-modified PES POFs)

Commercial PES (provided by Goodfellow, rod-like preform with a diameter of 20 mm) was chosen as the polymeric matrix to fabricate transparent plastic fibers. The plastic optical fibers were drawn using a 3-m-high optical fiber drawing tower with an electrical furnace with a sharp temperature profile. First, the plastic preform is heated up above its glass transition temperature T_g at $20\text{ }^\circ\text{C}/\text{min}$ to initiate the elongation process. Once the drop is formed and tied up on the drum the preform is slowly fed into the furnace while the drawing parameters (temperature, drum speed, feed rate) are continuously monitored. Performs were successfully drawn into hundreds of meters-long fibers with diameters ranging from $100\text{ }\mu\text{m}$ to $660\text{ }\mu\text{m}$. The process was performed under an oxygen gas flow ($2\text{ L}/\text{min}$) to avoid any external pollution of the preform surface.

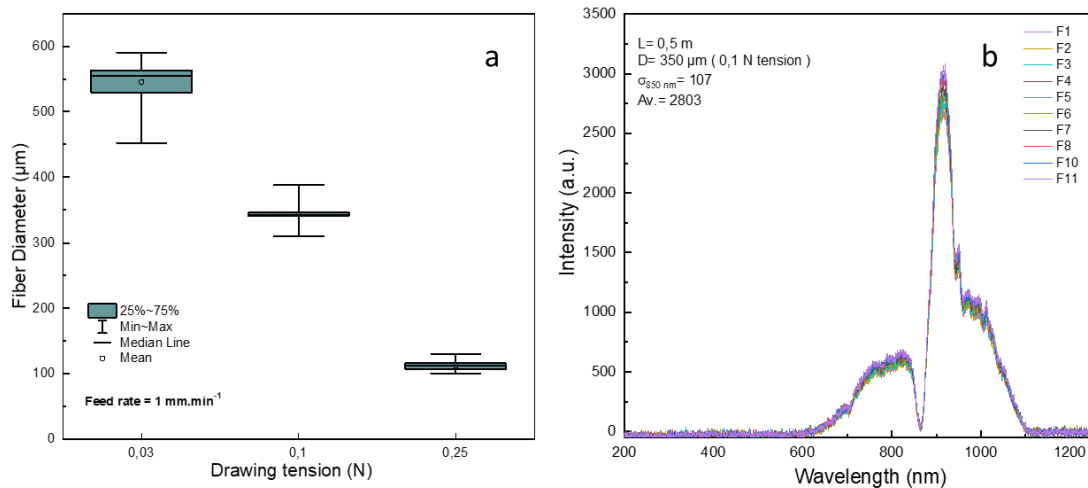
Different diameters of fibers (D_f) can be issued from the preform drawing process by changing the preform speed feed (V_f) or/and the fiber drawing speed (V_d). The commercial non-modified PES preform was used in this experiment and drawn into fibers. The diameter of the resulting PES fibers was experimentally controlled as a function of the drawing tension (T) values, linked to the drawing speed. The values of fiber diameters were accurately recorded in situ, with the tension values adjusted at regular intervals during the fibering process. This automated recording ensured precise control of the fiber diameter. (Commercial-PES)-fibers with three distinct groups with three different average diameters were elaborated: noted cF1, cF2 and cF3, respectively from the largest down to smallest average diameter. Each group of fiber diameters is associated with a corresponding tension with different standard deviations as shown in Figure 25.a and resumed in Table 9. The group of fibers produced under a tension value of 0.1 N (cF2) proofed to be effectively stable, as evidenced by the lowest standard deviation among all the groups. This low standard deviation indicated a high level of consistency and repeatability in the fibering process for this set of drawing parameters.

Chapter III: Results and Discussion

Chpt.III-Table 9: The 3 sets of drawing process parameters and associated fiber diameters

Fiber ID	T _{draw} (°C)	V _f (mm/min)	V _d (m/min)	T (N)	D _p (mm)	D _f (μm)-measured
cF1	225	1	0.5	0.03	20	549±29.4
cF2	225	1	1.5	0.1	20	344±5.3
cF3	225	1	2.5	0.25	20	112±15.8

In the following sections, we mainly focus on the cF2 fibers, since it has proven to be the most stable group during the drawing process. The quality of the cF2 fibers have been determined by registering the transmission signal of 11 different 50 cm-long cuts with the same diameters (344±5.3 μm) from the same conditions of fibering (V_f= 1 mm/min, V_d= 1.5 m/min, T=0.1 N). Also, the entrance and end faces of each piece of fiber were polished in the same manner prior to each measurement. The fixed drawing and pre-measurement conditions help to eliminate any external effects of drawing process differences on the quality of measurement. Hence, the goal of this study is to give an approximated idea about the homogeneity and quality of lab-made plastic optical fibers. As can be seen from Figure 24.b, the transmitted signal through the 11 different cuts of the identical cF2 fibers (same diameter and length) is almost superimposed with an average maximum transmission intensity of 2803 and a standard deviation of 107. A stable transmitted signal through the 11 different cuts is well achieved.



Chpt.III-Figure 24: a) Dispersion study of the fiber diameters for the 3 fiber groups associated with the 3 drawing tension levels, b) Dispersion of the signal intensities of 11 fiber segments cut with the same length, for the cF2 optical fibers.

4.1.2 The different routes used for the WO₃-PES composite fibers

In the next sections, various processes of fabricating modified PES/WO₃ optical fibers will be explored; associated characteristics will be characterized. The specific methods developed in the fabrication process involve three main routes to modify the PES- preform/fiber (Figure 25):

Chapter III: Results and Discussion

Route (1): surface modification of the preform via dip-coating in different suspensions.

Route (2): bulk modification of the preform by embedding NPs.

Route (3): post-coating of PES-optical fibers.



Chpt.III-Figure 25: the three main routes to obtain the modified photochromic fibers.

For all of these methods, we made use of commercial PES tubes (from Goodfellow) with a diameter $D_p = 20$ mm. Tubes were left at 75 °C under vacuum prior to drawing to exhaust inner moisture.

Following the fiber fabrication, an extensive characterization is performed on each model of the modified PES optical fiber. These analyses provide valuable insights into the performance and potential applications of the modified PES optical fibers.

Route (1): pre-drawing route: surface modification of the preform via dip-coating.

In this method, a suspension of PES/ WO_{3-x} was prepared by dissolving the granulate of PES in chloroform and then mixing it with the raw NPs (weight content in NPs: 85 g.L^{-1}). Then the preforms were dipped in the modified suspension prior to the drawing step. The dip-coating parameters are (i) the dip-coating speed (here 133 mm.min^{-1}) and (ii) the number of successive dip-coating steps (here 3 layers), which were separated by 30 min drying at 90 °C in an oven in between each step. The fiber was labeled as F01.

Route (2): pre-drawing route: bulk modification of the preform by embedding NPs.

Here the PES preforms were drilled and cut to obtain a hollow cylindrical preform with a ratio of inner/outer diameter equals to $0.4 \text{ cm}/1.5 \text{ cm}$. The preform surface was protected with a resistive tape, then the central hole of the preform was immersed in the prepared PES/ WO_{3-x} suspension (as-prepared in Route 1) three times to ensure a complete cover of the inner surface with the photochromic suspension. Then the modified preform was drawn into fibers and the studied segment was labeled as F02.

Route (3): post-drawing route: Post-coating of the final drawn plastic fibers (cladding addition)

After the PES fibers were drawn, an additional and immediate coating step was taken to achieve the modification goal. The PES fibers were post-coated with a suspension of the prepared Ethanol/ WO_{3-x} solution (prepared accordingly to the specifications mentioned in part 1). To facilitate the post-coating

Chapter III: Results and Discussion

step, an efficient house-made coating system consisting of a coating chamber filled with the desired coating suspension was deployed. The coating speed was fixed using the drum rotation of 1.5 m/min.

Following the coating process, the coated fibers were dried in a dark environment at 60°C in a drying oven for 2 hours. This step is crucial to ensure: (i) an adequate solidification of the post-coating layer, (ii) the removal of excess liquid, and (iii) the proper adhesion of the coating onto the fiber surface. The final fiber was labeled as F03.

4.1.3 SEM photographs of the different issued fibers

The surface morphology from the SEM cross-sectional and surface images for the 3 different segments of each prepared fiber: F01, F02, and F03 fibers are depicted in Figure 26. In Figure 26.c,e the fibers were embedded in an opaque epoxy resin then the surface was polished to improve the visualization of the cross-section. The rest of the fibers were cut by a diamond cleaver and fixed vertically facing the SEM detector. First, the different segments of F01 fibers obtained from the surface-modified PES perform exhibit a smooth surface without any imperfections (Figure 26.a-c). However, due to the estimated nanometric of the cladding ($D_p/D_F = 20/0.5 = 40$), it was complicated to measure or observe the thickness of the cladding layer. Second, for the F02 hallow fiber obtained from the physically modified drilled preform, the surface photos also revealed a continuous and defects-free appearance (Figure 26.d,f). Furthermore, to get more details about the nature of the inner core of the fiber, the F02 fiber was cleaved longitudinally as shown in Figure 26.e. The analysis of the hallow core confirmed the presence of a continuous layer within the hallow core, with no signs of contamination or aggregation of the NPs. Lastly, the F03 fiber, derived from the post-coating of the virgin fibers shows residual WO_{3-x} aggregates on the surface of the fibers (Figure 26.g). This observation suggests the presence of localized areas where the coating material did not uniformly adhere, likely due to two main factors: the random distribution of the NPs inside the coating ethanol suspension and the non-uniform drying of ethanol. As a reminder, the average size of the WO_3 NPs in ethanol suspension (Figure 16) is equal to 435 nm. This micro size can lead to uneven dispersion during the coating step. This non-uniform distribution may result in various aggregate areas with different concentrations (higher or lower), leading to the creation of gaps or aggregates on the fiber surface. Also, the drying mechanism of the ethanol may not occur uniformly across the fiber surface. Overall, the F01 and F02 fibers exhibit an acceptable surface quality and a continuous core, indicating the successful application of the proposed techniques. Nevertheless, the post-coating technique quality suggests a need for further optimization to achieve a more uniform coating.

Chapter III: Results and Discussion

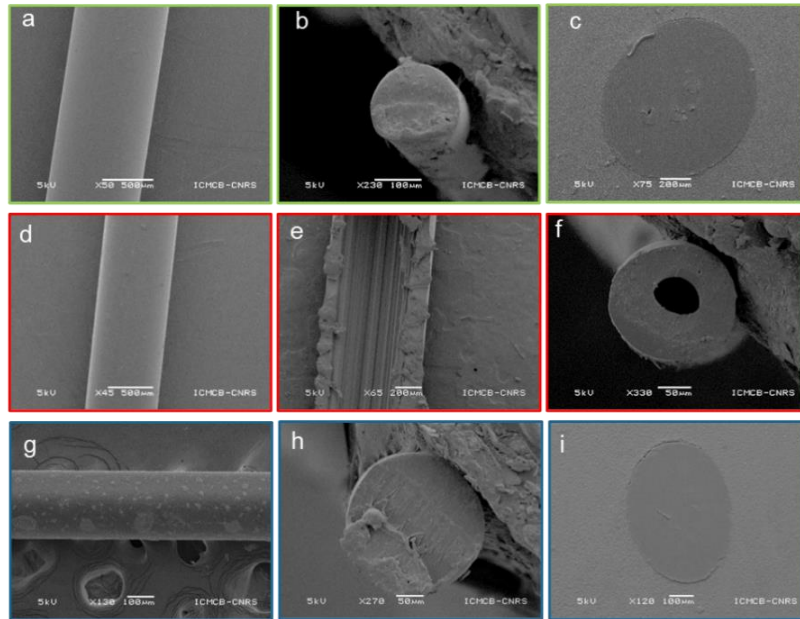


Figure 26: The morphologies photos of different segments of F01, a) Top (surface) view, b,c) cross-sectional view; F02: d) Surface view, e) the core cleaved longitudinally (surface view), f) hollow core (cross-sectional view), F03: g) Surface view, h, i) cross-sectional view.

4.1.4 Photochromic properties of the prepared fibers

In this measurement, three segments of the F01, F02, and F03, with a length of 12 cm and $350 \pm 12 \mu\text{m}$ diameter, were selected to evaluate their photochromic properties. The longitudinal transmission signal through the fibers was collected using the same set up of the signal quality measurement.

All the fibers were irradiated with the same irradiation conditions (same UV-dose). The evolution of the transmission spectrum of the F01,02,03 fibers versus irradiation time was collected in Figure 27.a,b,d. The maximum intensity evolution at 650 nm is extracted to investigate further the photo-redox kinetic Figure 27.c. An intriguing observation was made in both the modified cladding fibers (F01 and F03), where the transmitted signal is amplified (increased) upon the UV excitation (Figure 27.c). This observation is novel and has not been reported yet and we can refer to it as “negative” photochromism. In contrast, the signal in F02 (core-modified fiber) is quickly degraded upon irradiation as the result of the absorption increase by the photochromism (coloring mode) of the embedded WO_{3-x} NPs (Figure 27.d) into the fiber core. Indeed, reasonably, in the case of F02 fiber, the WO_3 acts as an absorption center leading to an increased transmission loss and though a degradation of the signal over time. The inset in Figure 27.a shows the intense blue color of the F03 fiber after irradiation. Thus, the increase of the transmission through the fiber core seems well linked to the coloring under UV of the WO_3 NPS inside the cladding. In contrast, for the other fibers, the effect of coloring was weak and not notable due to the low concentration of NPs in the case of F01 and F02.

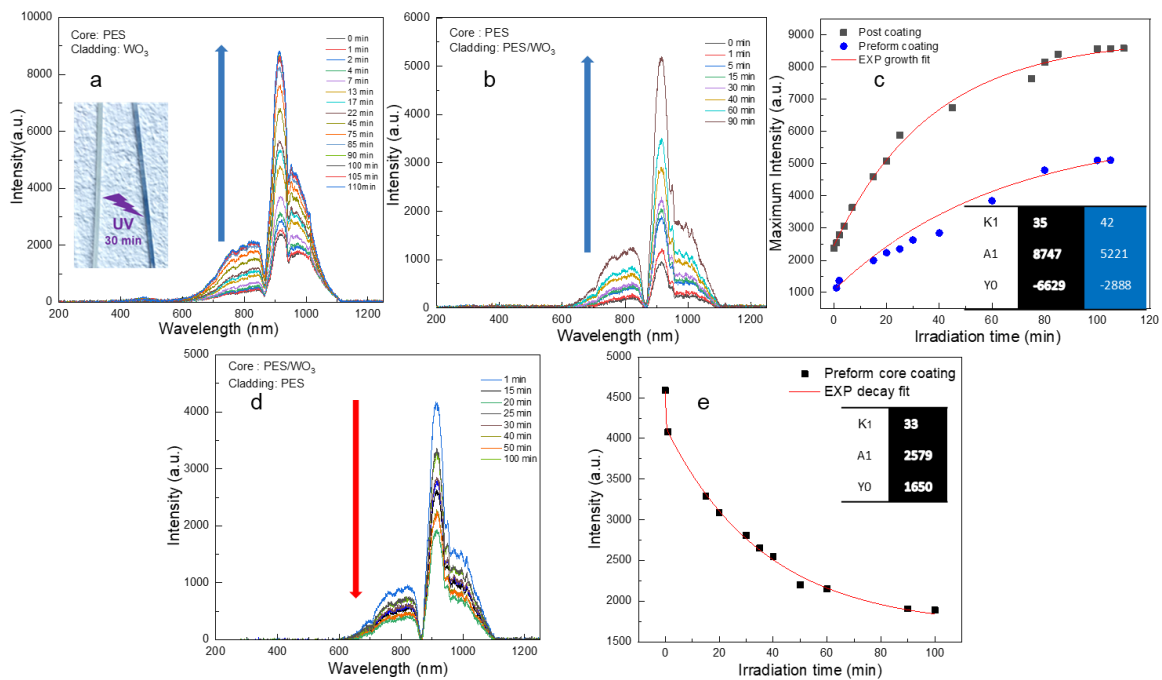
To quantify the negative photochromism, an exponential growth function was according to Equation 9. The values of the three parameters are shown in the inset of Figure 27.c. Notably, the F03 recorded faster coloring kinetics compared to F01 (35 to 42 min). The characteristic kinetic times are in good

Chapter III: Results and Discussion

agreement with the photochromic kinetics already performed on WO_3 -powders or WO_3 -doped films. Moreover, a significantly higher absorbance amplitude (A_I) is observed for the latter, which can be attributed to the higher concentration of the NPs in the case of the post-coating fibers. In contrast, in the case of F01, where the coating is applied directly to the preform, the coating layer is elongated to nanometric size. The obtaining, in this case, of very thin cladding results in a lower percentage of WO_{3-x} NPs incorporated within the PES matrix of the cladding. Consequently, the concentration of NPs within the cladding of F01 fibers is comparatively low. One can assume that the higher concentration of NPs in F03 cladding, leads to a greater extent of light transmission modification, resulting in a higher “negative photochromic contrast” (higher absorbance amplitude (A_g) in the exponential fit of the kinetic plots) compared to F01.

On the other hand, in the F02 fiber, the kinetic was fitted using the same function but within the decaying sense. As shown in the inset of Figure 27.e, the specific time is $\tau d=33$ min, indicating a close kinetic to the latter one (so well also linked to WO_3 NPs photochromism). In the case of F02 fiber, the photochromism well controls the degradation of the transmission signal: upon UV-irradiation the WO_{3-x} NPs in the core act as increasingly efficient absorption centers.

In all fibers, the coloring kinetic as well as the fiber longitudinal transmission seem associated with the photo-reduction (photochromism source) of the surface cations from W^{+6} to W^{+5} of the WO_3 NPs inserted into the fiber cladding (F01 and F03 fibers) or the fiber core (F02 fiber). However, depending on the localization of the particles into the cladding or the core, opposite transmission evolutions are observed.



Chpt.III-Figure 27: The evolution of the longitudinal transmitted signals versus UV-irradiation: a) F03 fiber with an inset of a real photo of the fiber before and after irradiation, b) F01 fiber, d) F02 fiber. The study of the coloring kinetic (maximum intensity versus irradiation time) of c) F01 and F03 fibers, e) the F02 fiber.

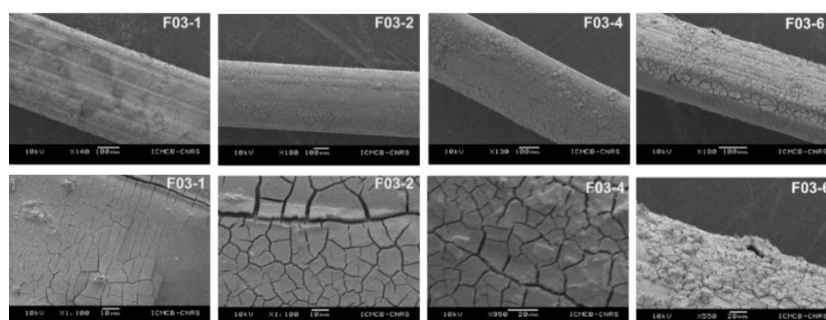
Chapter III: Results and Discussion

4.1.5 Revitalizing the post-coating method: Unleashing its potential as a powerful fiber modification technique

As revealed by the coloring kinetic, the F03 fiber demonstrated an original and unexpected negative photochromism with a remarkably clear amplification of the transmission signal from the WO_3 -cladding coloration under UV irradiation. Furthermore, the post-coating method is widely used in industrial applications making it an optimal route to modify pour optical fibers. In previous experiments, the SEM analysis has shown the inhomogeneous distribution of the NPs along the cladding. Thus, the post-coating method needs to be optimized in terms of cladding coverage and homogenous distribution of the NPs along the fiber. To enhance cladding coverage, we must investigate the optimal thickness of the coating by making successive dipping into the WO_3 -EtOH suspension. By carefully applying different coating thicknesses, we aim to find the optimal number of layers that ensures maximum coverage. This optimization process allows us a more uniform and consistent distribution of NPs throughout the cladding to be achieved. Furthermore, a second time, we have explored the dispersion of the NPs inside a polymeric matrix which should be compatible with the used solvent (ethanol). By adopting this second approach, we aim to enhance the overall performance of the modified fiber by achieving better cladding coverage and improving the stability and durability of the coating, thereby extending the lifespan of the modified fiber. Obviously, to amplify again the discovered negative photochromic effect.

4.1.5.1 The study of the optimal thickness of post-coated WO_3 claddings

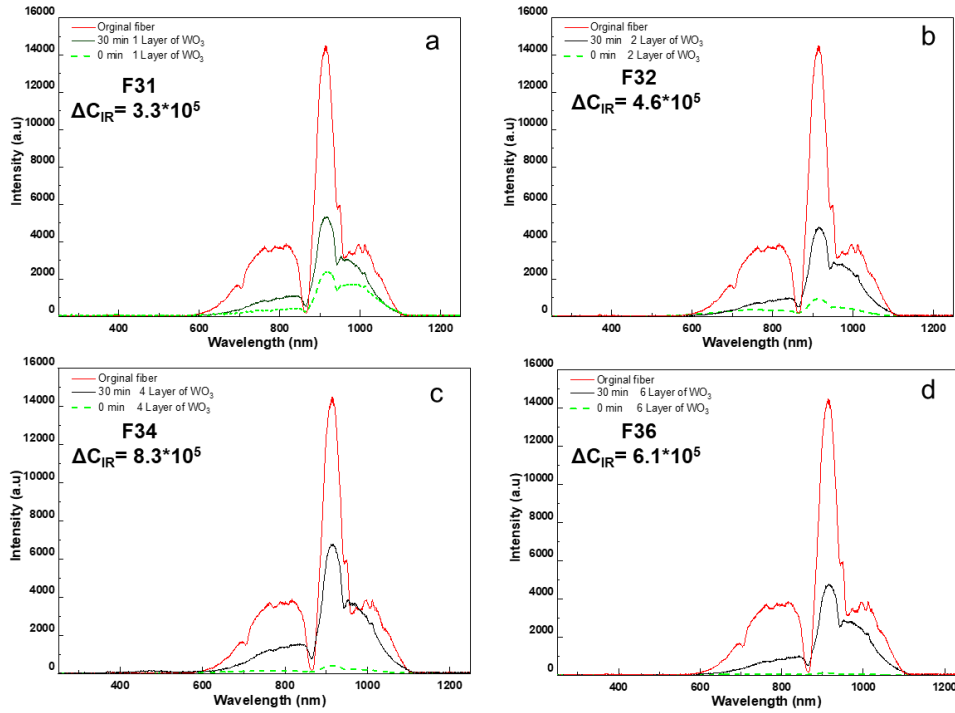
In this approach, different fibers have been modified by depositing different numbers of layers of the WO_{3-x} /ethanol layer. By varying the number of coating layers, the resulting fibers were labeled uniquely to indicate the number of layers present as F03-1, F03-2, F03-4, and F03-6, representing 1, 2, 4, and 6 layers of the coating suspension, respectively. As shown in Figure 28, the SEM photos show a progressive coverage increase with WO_{3-x} particles as the successive coating number is increased from 1 to 6 layers. The dried layer on the cladding surface exhibits the WO_{3-x} NPs as a porous but continuous structure in all the prepared fibers. Despite its porosity, the layer maintains its integrity, forming a continuous coating along the cladding surface. This continuity ensures optimal coverage and adhesion, providing a reliable platform for the incorporation of WO_{3-x} NPs. However, cracks occurring probably during drying are more visible than the coated WO_3 claddings are thick.



Chpt.III-Figure 28: The SEM photos of the different prepared fibers (labeled by the name of each fiber).

Chapter III: Results and Discussion

To evaluate the thickness effect, the prepared fibers were irradiated for 30 min to extract the fiber optical NIR contrast (difference of longitudinal transmission before and after irradiation). The ΔC_{IR} was calculated as mentioned in part 3. In addition, the original fiber signal without the coating was recorded for each fiber before the coating step. As shown in Figure 29, the non-irradiated state signal is highly degraded as the number of layers is increased which may be attributed to the complete coverage of the cladding surface. An in-depth understanding of the physics governing this behavior will be fully presented in a later section. The maximal value of the ΔC_{IR} is 8.3×10^5 , which was recorded for the F03-4 fiber making it the best candidate for diverse optical and sensing applications.



Chpt.III-Figure 29: Transmitted signal variation between non-irradiated and irradiated states.

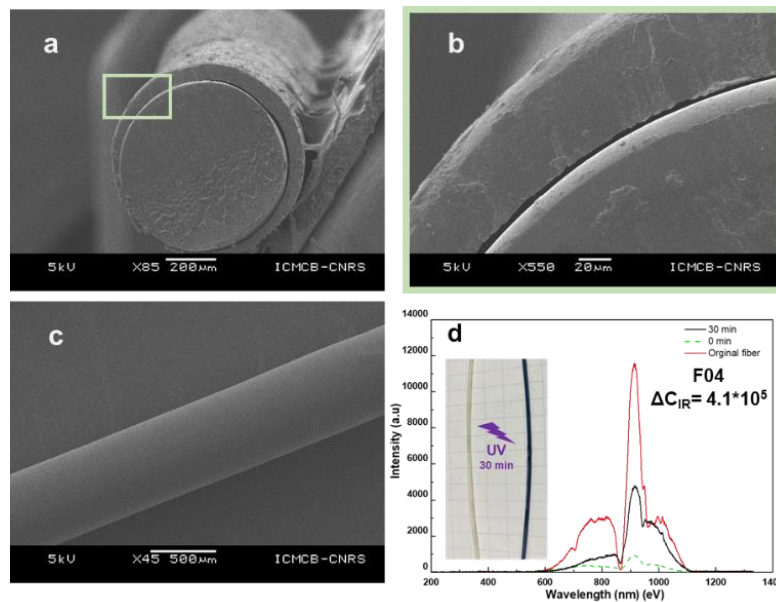
4.1.6 WO₃-PVP composite claddings

4.1.6.1 The PVP/WO_{3-x} coating as an effective replacement for the WO_{3-x} powder-based coating

As we have presented in Figure 28, the coating layer suffers from several constrains: 1) the powder-based coating is subjected to a direct degrading by different factors such as humidity, 2) the low adhesion to the surface limits the flexibility of the fiber in terms of bending and mechanical strength, 3) additionally, the existing coating does not offer complete protection of the NPs since it is directly in contact with the surrounding conditions. By addressing the constrained, we explored a new type of suspension where the NPs are well-protected and dispersed homogeneously. With this aim, the NPs were dispersed in a suspension of polyvinyl pyridine (PVP, $M_w = 60,000$) in ethanol with a weight ration of (1/10 wt%) respectively. The suspension was stirred magnetically at room temperature for 2 hours with the addition of 0.1%wt of Titron X was added to improve the homogeneity of the suspension. The total mix was used for post coating step. The produced fibers are labeled F04.

Chapter III: Results and Discussion

The DLS results indicated a 113 nm average size of the NPs inside the PVP medium with a PDI=0.52. Comparing these results to the suspension without any PVP (0%wt), which had an average size of 442 nm, it is evident that the average NPs average size has significantly improved. The NPs were able to achieve a more uniform and reduced size distribution by adding PVP to the medium, which led to improved characteristics and dispersity. The SEM photos in Figure 30.a,b of the F04 shows that the 550 μm core PES fiber is homogeneously coated with a 45 μm layer of a well-dispersed WO_{3-x} inside the PVP matrix. The surface morphology of the fiber shows a continuous surface without any imperfections or contaminations (Figure 30.d). Compared with the SEM photos of the powder-based coating, the proposed developed coating shows a superior property in terms of flexibility and protection of the NPs.



Chpt.III-Figure 30: SEM images of the F04 fiber: a) cross-section with b) magnification of the contact area between the core and the cladding, c) top view of the cladding surface, d) the photochromic behavior of the F04 fiber with a real photo of the fiber before and after irradiation.

A preliminary photochromic test was performed to evaluate the F04 fiber. Figure 30.d shows that the F04 fiber has a good photochromic property between (0 and 30 min) with a $\Delta C_{IR} = 4.1 * 10^5$. Indeed, the photo in the inset of Figure 30.d, proves that the cladding of F04 was colored more homogeneously in a dark blue shade than the F03 fiber (inset Figure 27.a) after 30 minutes of irradiation.

4.1.6.2 The effect of NPs concentration on the photochromic behavior

To get more insights into the effect of the photochromic active compound's concentration on the coloring/bleaching kinetics of the new designs, a series of post-coated fibers were prepared with different concentrations of WO_3 in the WO_3/PVP composite cladding. The used parameters for the three fibers sample series are detailed in Table 10 :

Chapter III: Results and Discussion

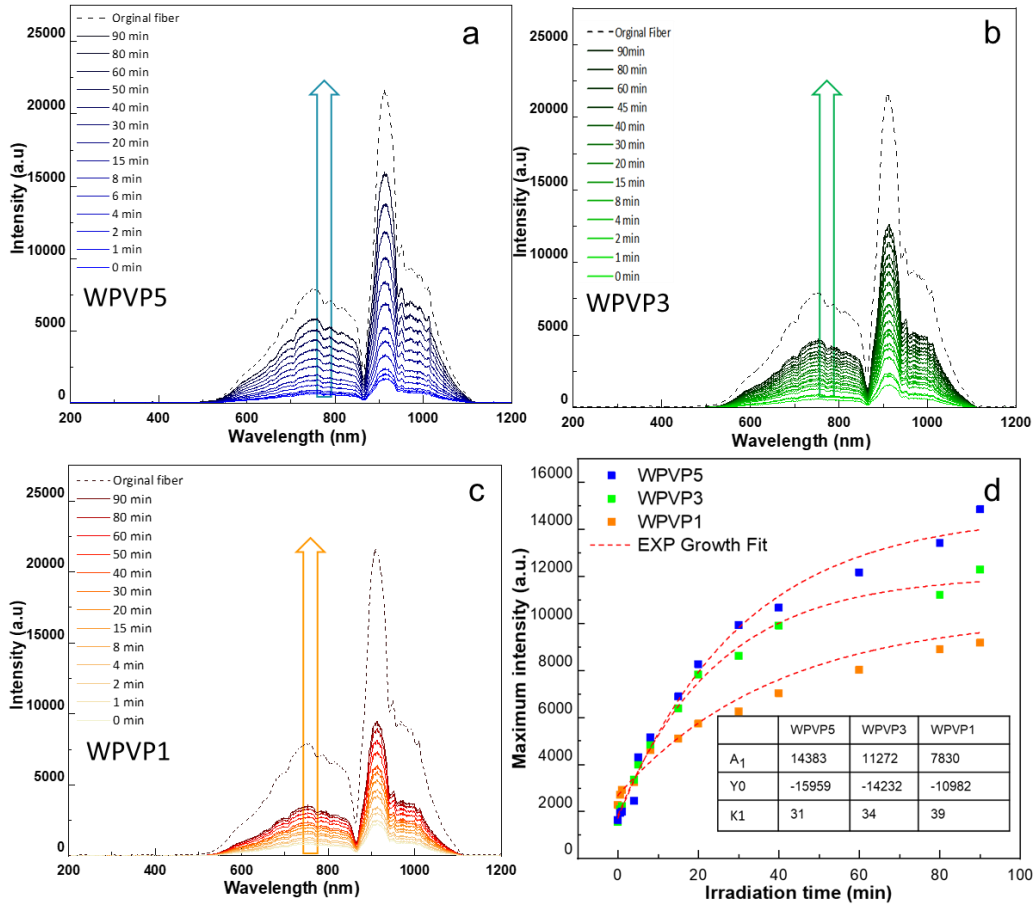
Chpt.III-Table 10: Post-coated fibers samples details.

Fiber	PVP (wt%)	WO_{3-x}(wt%)	Layers	Drying step (min)	speed (m/min)
WPVP1	10	1	2	30	1.5
WPVP3	10	3	2	30	1.5
WPVP5	10	5	2	30	1.5

The three as-elaborated fibers: WPVP1, WPVP2 and WPVP3, are all with a length of 40 cm and 350 μm diameter. As previously, to evaluate the photochromic properties, the axial transmission versus irradiation time was followed. The longitudinal transmission signal through the fibers was collected using the same set up of the signal quality measurement. Each fiber was irradiated with irradiation conditions: UV lamp 8 W, the power per surface unit received by the sample is equal to 5.6 W/m^2 . The use of such low fluence is to mimic the real condition in a smart device (window or textiles) that is exposed to daily light. Bleaching mode was also recorded following the evolution of the fiber transmission in dark conditions after 2 hours long irradiation.

The evolution of the transmission spectrum of each fiber versus irradiation time was collected in Figure 31.a-c. The maximum intensity evolution at 900 nm is extracted to investigate further the photo-redox kinetic Figure 31.d. Upon irradiation, the transmitted signal is quickly amplified as a response to the UV excitation. The coloring kinetic was obtained by fitting the experimental data according to Equation 9. As revealed from the kinetic parameters the concentration of NPs plays a significant role in increasing the transmission contrast and as well the speed of the coloring mechanism (but in a very slight way). With a characteristic kinetic time of about 30 min, for the series of fibers, the transmission modulation is well issued from the photo-reduction of the surface cations from W^{+6} to W^{+5} ions. The slight increase of the photochromic characteristic time observed with the WO_3 concentration (31, 34 and 39 min for WPVP1, WPVP-2 and WPVP-3, respectively) may occur from a saturation effect on the photochromic powder efficiency.

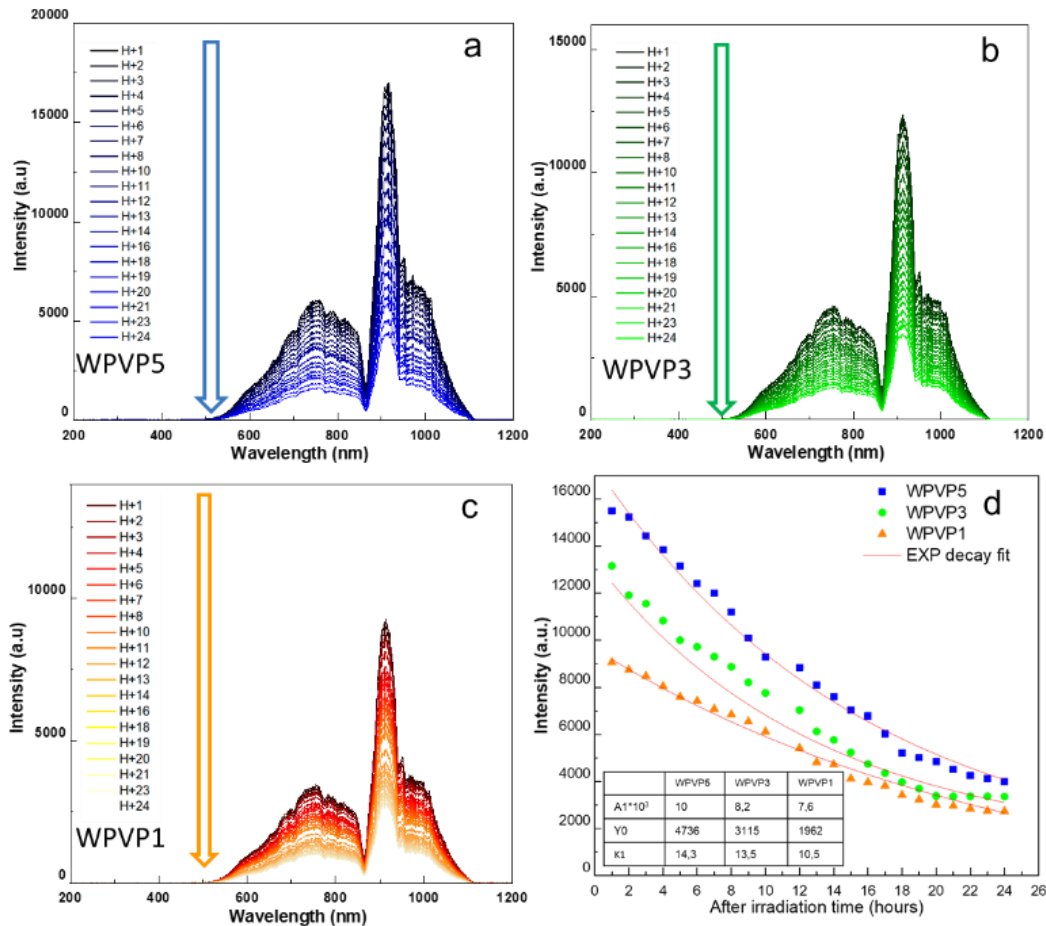
Chapter III: Results and Discussion



Chpt.III-Figure 31: Evolution of transmission signal during irradiation (coloring) of a) WPVP5, b) WPVP3, c) WPVP1 fibers, d) evolution of maximum intensity at 900 nm versus irradiation time and the associated kinetic parameters (coloring kinetic).

For the bleaching properties, the studied fibers were previously irradiated for 120 min (to nearly gain the coloring saturation) and let in the dark at room temperature for self-bleaching. The signal was recorded using the spectrum analysis automatically for 24 hours as shown in Figure 32.a-c. The maximum transmission intensity evolution can be fitted from a single exponential growth trend on the complete 20-first-hour range. The single exponential growth function to fit the experimental data, according was used. The bleaching mechanism is mainly governed by the phenomenon of reoxidation of W^{5+} to W^{6+} by the oxygen diffusing inside the PVP cladding, with characteristic times very similar to the ones observed on the WO_3 -PVA thin and thick films. From the fitting parameters in Figure 32.d, in accordance with the observations just made on coloring kinetics, surely from a saturation effect, the bleaching mechanism speed is slightly slowed down as the concentration of the WO_3 NPs increased.

Chapter III: Results and Discussion



Cpt.III-Figure 32: Evolution of transmission signal in the dark conditions (bleaching) of a) WPVP5 fiber, b) WPVP3 fiber, c) WPVP1 fiber, d) maximum intensity at 900 nm evolution versus after irradiation time with the associated bleaching parameters (bleaching kinetic).

As proofed by the coloring/bleaching mechanism, the cladding with rich NPs shows faster coloring with a bit slower bleaching. Nevertheless, the modified PVP cladding could maintain the higher concentration with the same function and phenomena without the formation of cracks or imperfections. The physics behind the (negative) photochromism phenomena will be discussed in the next section to propose a full interpretation of this new phenomenon.

Chapter III: Results and Discussion

4.1.7 Interpretation of the “negative photochromism”

Virgin fibers transmit much better than fibers coated with our claddings, whether they are WO₃ powders from WO₃-EtOH suspensions or WO₃-PVP composite claddings. Clearly, the higher the refractive index contrast between core and cladding, the better the transmission as predicted from theory whatever step-index multimode fibers or single-mode fibers are obtained (see chapter II, section 1.12.2). In this sense, the absence of cladding leads to the highest possible core-air contrast and the best transmissions. We therefore clearly interpret, intuitively and from the outset, the observed transmission modulation (negative photochromism: re-increase in transmitted signal with cladding coloration) by the decay of the effective refractive index of the cladding with the coloration of WO₃ powders. In more detail, we have modeled the behavior of our fibers as far ahead as possible.

First, the fibers are injected with a focused laser and have a Gaussian geometric radiation dispersion. The geometric parameters of Gaussian focused radiation are described in Figure 33.a,b, where $w(z)$ is the characteristic beam width at a distance z from its focusing plane (in w_0). The w_0 , $w(z)$, z distance and the laser wavelength (λ) are linked by the following equations:

$$w(z) = w_0 \times (1 + (z \lambda / \pi w_0^2))^2 \quad \text{Chpt.III- Equation 11}$$

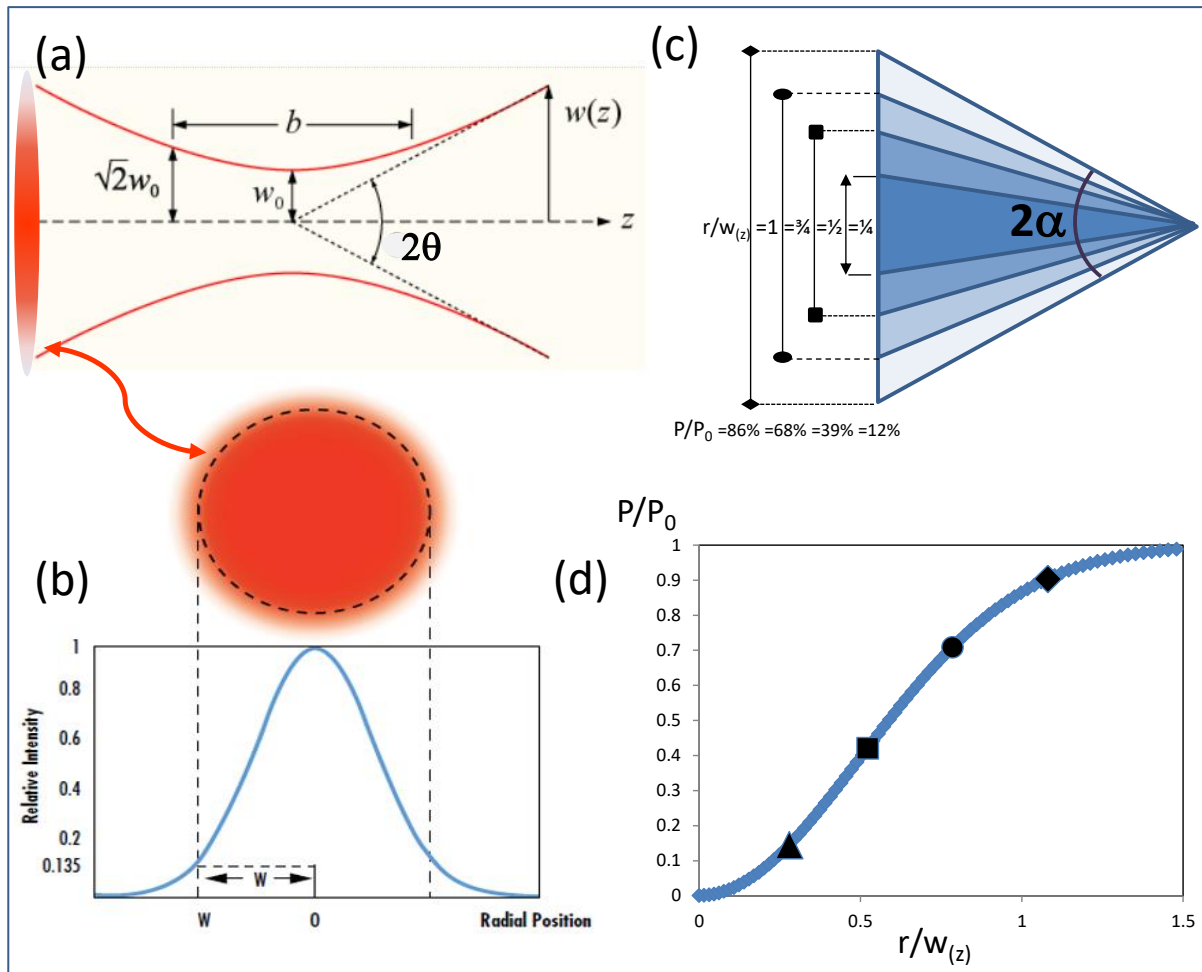
Furthermore, the percentage of beam power passing through a disk of radius r , at a distance z from the focusing plane, is given by law already well known (*Equation 12*), thus relating the ratio P/P_0 as a function of the ratio $r/w(z)$ (Figure 33.c,d)[39].

$$P(r,z)/P_0 = 1 - \exp(-2r^2/w(z)^2) \quad \text{Chpt.III- Equation 12}$$

To use such a law to interpret the evolution of our longitudinal transmissions, it is useful to relate this ratio $r/w(z)$ as a function of the angle 2α of the associated cone (Figure 33.c).

On the other hand, it is important to note that the decrease in the effective cladding index is well predicted by the Kramers-Kronig laws [40]. Indeed, around an absorbing resonance (associated with a Gaussian absorption band linked to the absorption index k of a material), the n real index of the material evolves according to the pattern shown in Figure 34.a. In more detail, the n index is submitted to a sudden modulation around the absorption frequency, with an increase in the index at low frequencies and a decrease at high frequencies of the resonance phenomenon. The WO_{3-x} NPs have tungsten V → tungsten VI interval bands centered between 1 and 2 microns in wavelength. The NIR transmissions tracked are therefore in the zone where the index is indeed lowered by the increase in IVTC absorption (Figure 34.a).

Chapter III: Results and Discussion



Chpt.III-Figure 33: a) & b) Schemes with the associated parameters of a Gaussian laser; c) & d) relationship in between the ratio between transmitted and injected power (P/P_0), the $r/w(z)$ ratio and the 2α cone angles.

Considering that the fibers, here of large diameter, are such that they present a multimodal transmission (step-index multimode transport), due to a focusing diameter beam (w_0) much smaller than the diameter of our fibers (or $w(z)$ by analogy with the previous laws). In other words, most of the transmission comes from signals that undergo multiple reflections at the core/sheath interfaces. The observed modulations can then be interpreted by considering that the signal is transmitted only if the angles at the core/cladding interface are greater than the angle of total reflection. If this is not the case, we can certainly consider that the non-reflected rays penetrating the cladding are absorbed or scattered by the WO_3 particles in the cladding and do not "return" to the core to continue their transport: they are lost.

Thanks to:

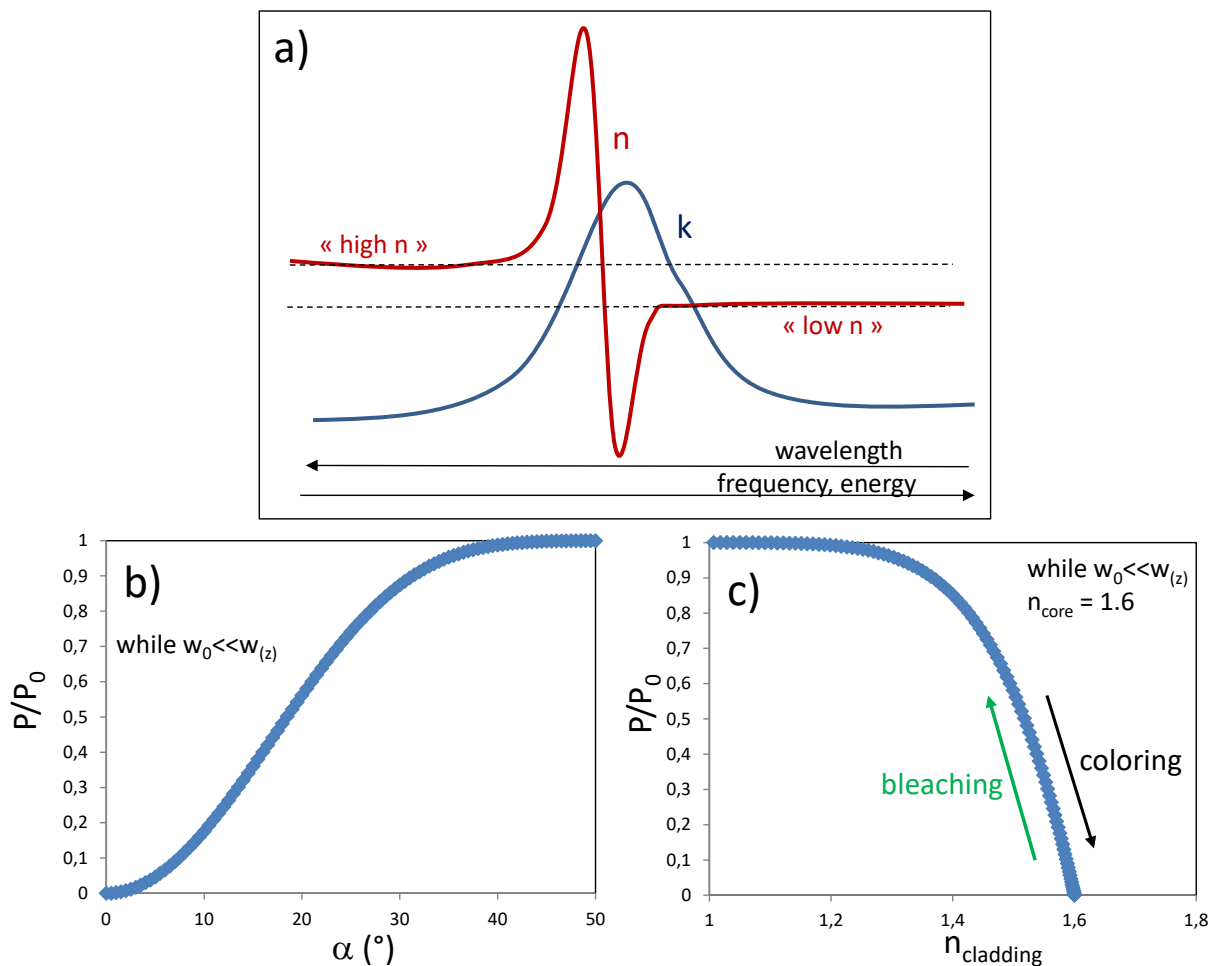
- (i) the direct mathematical link between the ratio $r/w(z)$ and the angle of the associated cones (2α) (Equation 11) (Figure 33.c);
- (ii) the use of the direct relationship we've just established between this angle (2α) and the critical angle for total core/gain reflection combined with Equation 12 (which allow us to establish the P/P_0 ratio vs α angle, Figure 34.b);

Chapter III: Results and Discussion

(iii) finally, the use of Snell's relationship (see equation 4, in chapter II) links the angle of total reflection and the pair of indices of an interface (here core and cladding).

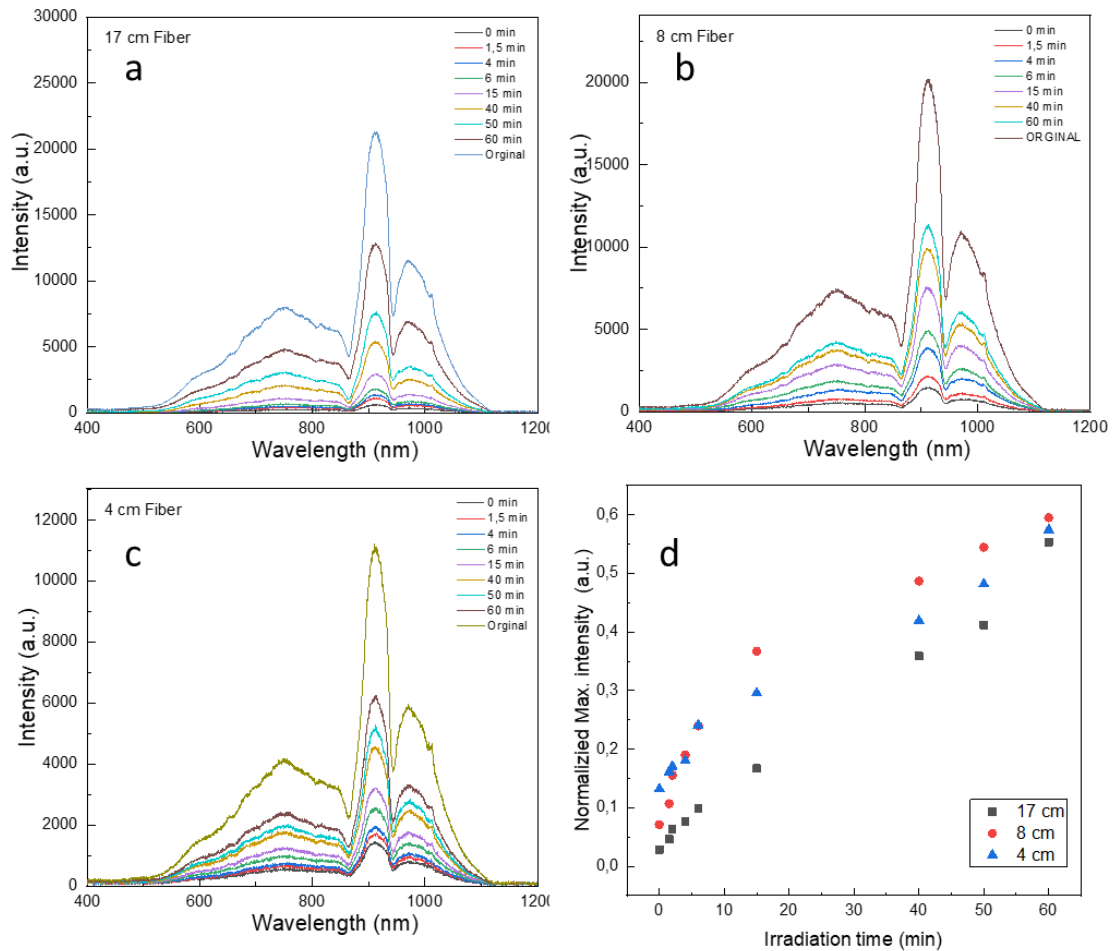
it can be proposed the evolution of transmitted power as a function of the cladding's effective index (Figure 34.c). Here, we have taken the effective index of the core to be the index of the PES (1.6), while the index of the PVP is 1.55 [41] [42]. At first glimpse, it is easy to see that a modulation of the refractive index of powder dispersed within the PVP would lead to a wide modulation of the axial transmission through the fiber core.

Note that photochromism measurements on fiber segments of very different lengths, while the transmitted powers vary by several decades, show no significant variation in the phenomenon of negative photochromism as shown in Figure 35.d where the coloring kinetics of the three different fibers (17,8,4 cm) are following the same trend. This tends to support our hypothesis that the fibers constructed have largely multimode transmissions and that our proposed interpretation based solely on the transmission of beams responding to the angle of total reflection is valid.



Chpt.III-Figure 34: a) A simplified representation of n and k dependencies governed by Kramers-Kronig laws, b) evolution of the P/P_0 ratio versus the critical angle, c) evolution of the P/P_0 ratio versus the effective refractive index of the cladding for a core refractive index taken to 1.6 (PES value).

Chapter III: Results and Discussion



Chpt.III-Figure 35: The coloring mechanism for different fibers (core: PES, cladding: PVP/WO₃): a) 17 cm, b) 8 cm, c) 4 cm, d) the coloring kinetic of the three studied fibers.

4.2 Conclusion of Part 4

In this part, we have shown a detailed roadmap of the fabrication of different POFs using three main techniques: Preform modification by coating in suspensions, preform core modification and post-coating of the POFs. In general, the three produced fibers showed good photochromic (coloring) behavior with superior kinetics for the post-coated fibers. Then, the post-coating method was thoroughly investigated by changing the number of coating layers on the virgin fibers. The maximal value of the ΔC_{IR} is 8.3×10^5 was recorded for the 4 layers of fiber. In addition, this suspension coating was developed using a polymeric dispersant (PVP) to enhance the performance of the final fiber. The proposed developed coating showed better properties in terms of flexibility and protection of the NPs. Another series of post-coated fibers were prepared with different concentrations of WO₃ in the WO₃/PVP composite cladding to understand the role of the NPs. As proofed by the coloring/bleaching mechanism, the cladding with rich NPs showed faster coloring with a bit slower bleaching and could maintain the same function even at higher concentrations. In the final part, we have modeled the mechanism of the fibers to get more insights into the “negative photochromism” phenomena.

Chapter III: Results and Discussion

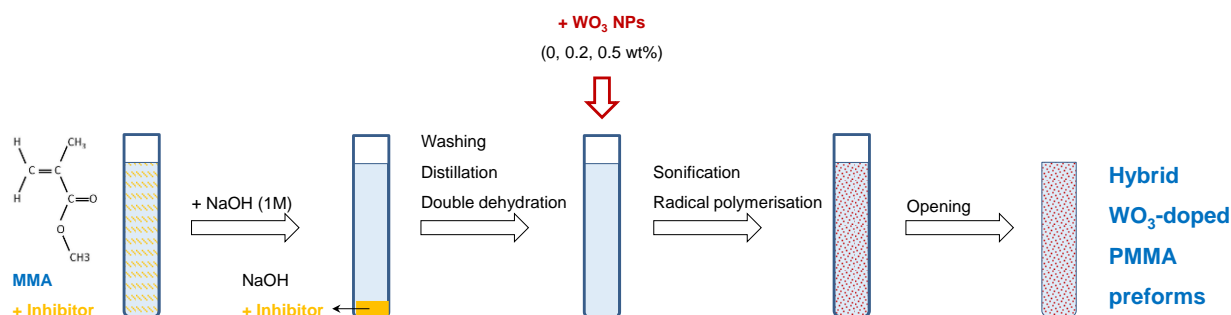
Chapter III: Results and Discussion

5 Part 5: Hybrid organic-inorganic PMMA optical fibers functionalized with photochromic active WO₃ nanoparticles: from materials design to photochromic fabrics

In this part, we present a new class of transparent PMMA fibers doped with tungsten oxide compounds (WO₃), for X-chromic applications. As discussed previously in part 4, the use of commercially available fibers has proven its efficiency as a new class of photochromic fibers using different models (core or cladding modification). Nevertheless, the need to develop a better polymer with higher transparency is crucial for various applications. Hence, we develop a new class of lab-made fibers with internal function with WO₃ to offer a new model where we do not use a suspension for changing the surface properties or using additional equipment to reach our functionalizing purposes.

5.1 Elaboration of the lab-made PMMA doped with WO₃

Composites preform preparation. The co-doped PMMA preforms were fabricated using methyl methacrylate (MMA, 99%) monomers, benzoyl peroxide (BP, 70%), sodium hydroxide (NaOH, 98%) and WO₃ as the doping agent. First, the monomer stabilizer (inhibitor) was removed by washing with a 1M NaOH solution several times. Following, the MMA was distilled and double-dried using column chromatography to remove any traces of water or moisture. Different amounts of surface-modified WO₃ nanoparticles (0, 0.2 and 0.5%wt) and MMA were placed into sealed pyrex tubes (12 mm in diameter). The dispersions were sonicated for 30 min and kept for 10 hours in the dispersed state to achieve complete wetting of the particle surface. For each solution, 0.5%wt of BP was added to initiate the radical polymerization in the tube. The polymerization was performed at 70 °C for 24 hours under argon atmosphere. The rod-like preforms were obtained after breaking the glass tube. Finally, the preforms were kept for 10 days in a vacuum oven to ensure the complete drying of the preforms prior to the drawing step. Three different preforms with WO₃ doping of 0, 0.2 and 0.5%wt, labeled as PM00, PM02 and PM05 respectively, were prepared following this process, illustrated in Figure 36.



Chpt.III-Figure 36: Road map of the used techniques to elaborate the lab-made preform.

Composite 1D fiber drawing. The plastic optical fibers were drawn using a 3-meter-high optical fiber drawing tower as reported in part 4 (section 4.1.1) with the same conditions. The fibers prepared

Chapter III: Results and Discussion

from the preforms PM00, PM02 and PM05 were labeled as FPM00, FPM02, and FPM05, respectively.

Composite 2D textile preparation. Photochromic pieces of FPM02 fibers were woven manually into a fabric with dimension $2 \times 2 \text{ cm}^2$ to produce as prototypic textile object.

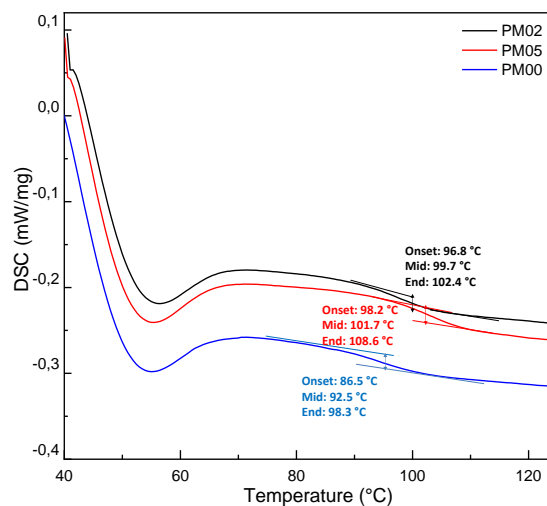
5.2 Main results and discussions

5.2.1 WO_3 particle size distribution into monomer suspensions

The particles are hydrophobized by surface modification with (tBuPO₃H₂), which is required to block the formation of aggregates and to increase the wettability of the monomer and polymer [43]. DLS measurements were used to track the size variation of the NPs as a result of the surface modification of WO_3 by phosphonic acid groups in the monomer solution before the polymerization. Three samples were investigated: 0%wt WO_3 , 0.2%wt WO_3 and 0.5%wt WO_3 . The DLS indicates a clear decrease in the average size as a result of surface modification. The average size drops from 632 nm with polydispersity index (PDI = 0.72) in the 0.2%wt WO_3 (un-modified) in MMA to 38 nm (PDI = 0.35) in 0.2%wt WO_3 (modified). Comparing the two functionalized-particle samples, increasing the particle content to 0.5%wt (average size of 42 nm, PDI = 0.16) does not cause aggregation in the monomer recording almost the same distribution as the 0.2%wt sample.

5.2.2 Composites preform characterizations

Thermal behavior. The thermal behavior of the prepared PMMA preforms doped with different concentrations of WO_3 (0%wt, 0.2%wt and 0.5%wt) was studied with the means of differential scanning calorimetry (DSC) (Figure 37). The DSC thermograms of undoped and doped PMMA preforms exhibit a similar thermal behavior with a clear transition centered at 90 °C, which is attributed to the glass transition temperature typical of PMMA polymer [44], [45].



Chtp.III-Figure 37: DSC curves of the hybrid WO_3 -doped PMMA preforms.

The values of T_g are resumed in Table 11. For comparison purposes, we also included the T_g of a commercially available PMMA, labeled as PMCom. PM00 shows a T_g (86.5 °C) close to the one of

Chapter III: Results and Discussion

the commercial PMCom (90.4 °C). In comparison, both doped PMMA preforms (PM02, PM05) show a higher T_g , by about +10 °C, than the undoped PM00. This could indicate that the mobility of the PM00 chain segments decreases upon charging with WO_3 during radical polymerization, i.e., PMMA/ WO_3 composite preforms become more rigid than the pure PMMA preform.

Chpt.III-Table 11: Glass transition temperature and melt flow index for the WO_3 -doped PMMA preforms.

Sample ID	T_g (°C)	MFI (g/10 min)
PM00	86.5	15.5±0.22
PM02	96.8	13.25±0.12
PM05	98.2	13.88±0.42
PMCom	90.4	17.5

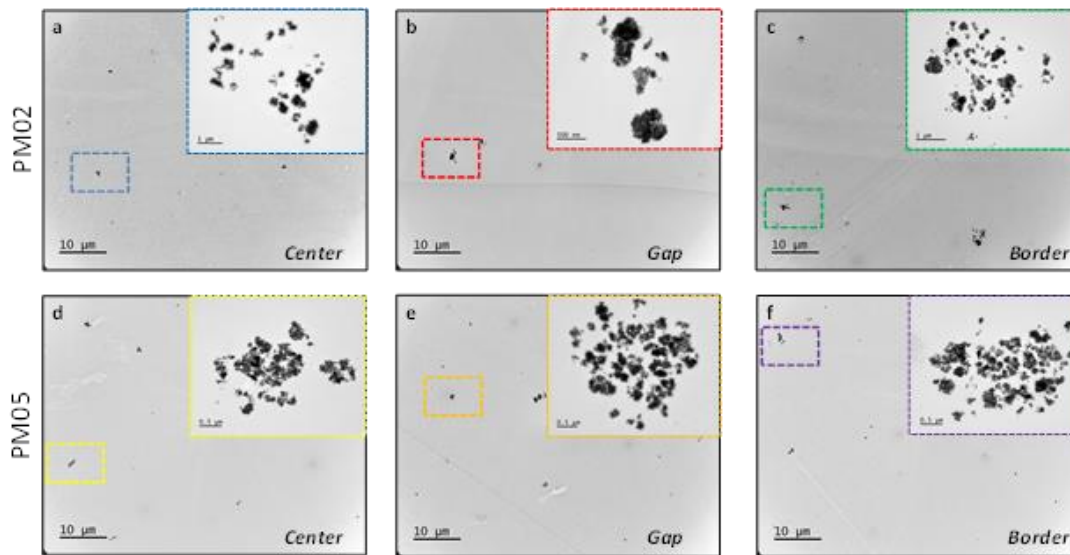
Some organic/inorganic composites have also been known to show trends like the ones reported here in the glass transition increment upon doping with various nanoparticles [46]. Hammani *et al.* [44] showed an enhancement in T_g by up to 60 °C with increasing ZnO NPs loading in the PMMA matrix from 0 to 40%wt. They found that the dispersion of ZnO NPs in the PMMA matrix hinders the movement of macromolecules and increases the T_g of the sample. In another study, Nikolaidis *et al.* [47] attributed the increase of T_g of nanocomposites (PMMA/Cloisite) to their higher molecular weight distribution than the pure PMMA.

Melt flow index. MFI of polymers was measured to provide more details on the flow behavior of the preforms, which is valuable information for their usability in fiber drawing. MFI gives insight into the molecular weight distribution (MWD) of polymer chains and the weight ratio of the flow rate of polymers over a specific time and temperature range [48]. Hence, the polymer composite with lower MFI (low flow) has longer chains and higher MWD. Table 1 indicates the flow properties of PMMA/ WO_3 preforms. PM00 exhibits a melt flow index value of 15.5 g /10 min which is close to the commercial values of the PMCom (17.5 g/10 min). With that respect, this is important to highlight that the PMCom preform could be shaped into fiber. Hence, we consider its MFI value as a reference for the fiber drawing ability of the lab-made preforms. It is observed that the MFI decreases with the insertion of WO_3 in the PMMA, from 15.5 (0%wt WO_3) to 13.88 g/10 min (0.5%wt WO_3), which may be linked to the reduced fluidity of the polymer chains as a result of the addition of NPs. A similar trend was observed by El Hady *et al.* [49], as they reported that the addition of fillers (0.5%wt of organoclay) in cross-linked polyethylene decreased the MFI from 6.46 to 1.21 g/10 min. They explained that the MFI decrease may be traced to flow hindrance by the organoclay particles. Based on the MFI conclusion, to maintain a good drawing ability, we selected the PM02 preform (0.2%wt WO_3) for further study into fiber and fabric shapes.

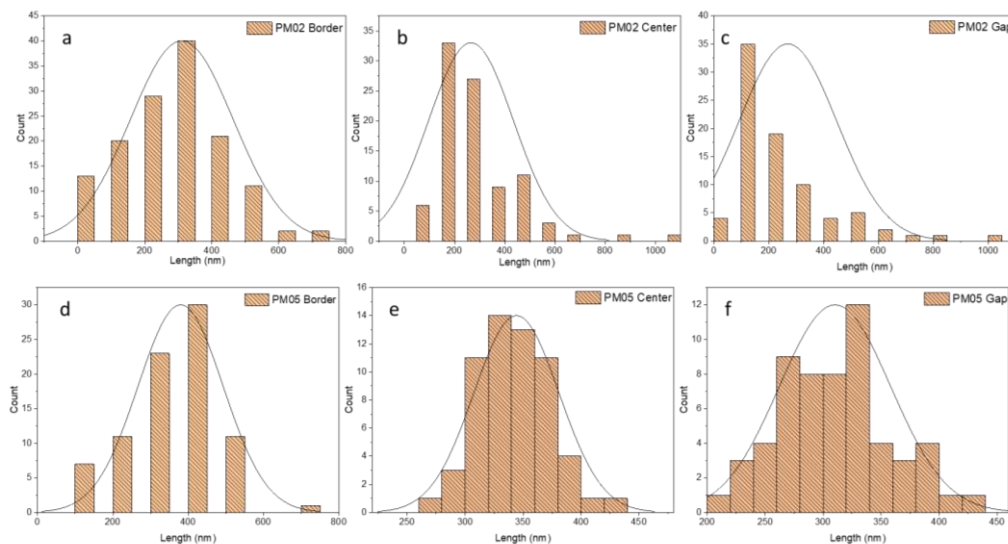
WO_3 particle size distribution inside preforms. High-resolution transmission electron microscopy (HR-TEM) was performed to provide more insights into the dispersion quality of the NPs inside the

Chapter III: Results and Discussion

polymerized transparent preform. To ensure a complete scan of the preforms slices, all measurements were observed in three different areas, from center, to gap (in between border and center) to border (Figure 38). The slices observed by HR-TEM had a thickness of 70 nm for a surface of $300 \times 300 \text{ nm}^2$. All of them exhibit phase-separated WO_3 NPs agglomerates embedded in the PMMA matrix, both for the PM02 and PM05 compounds (Figure 38: upper and lower panels respectively). Despite slight phase separation, the PM02 keeps a good transparency with no visual defects or macro bubbles, while the PM05 exhibits a homogeneous opaque blue coloration with no visual defects.



Chpt.III-Figure 38: TEM micrographs in a) center b) gap and c) border section of the PM02 sample, and in d) center; e) gap and f) border section of the PM05 sample (inset marge magnification on aggregates)



Chpt.III-Figure 39: Histograms obtained from TEM micrographs analysis in a) center b) gap and c) border section of the PM02 sample, and in d) center; e) gap and f) border section of the PM05 sample.

Particles are grouped in large agglomerates consisting of separated groups of lower-size aggregates, following a fractal organization, as depicted in the inset of Figure 38. The strongly inhomogeneous

Chapter III: Results and Discussion

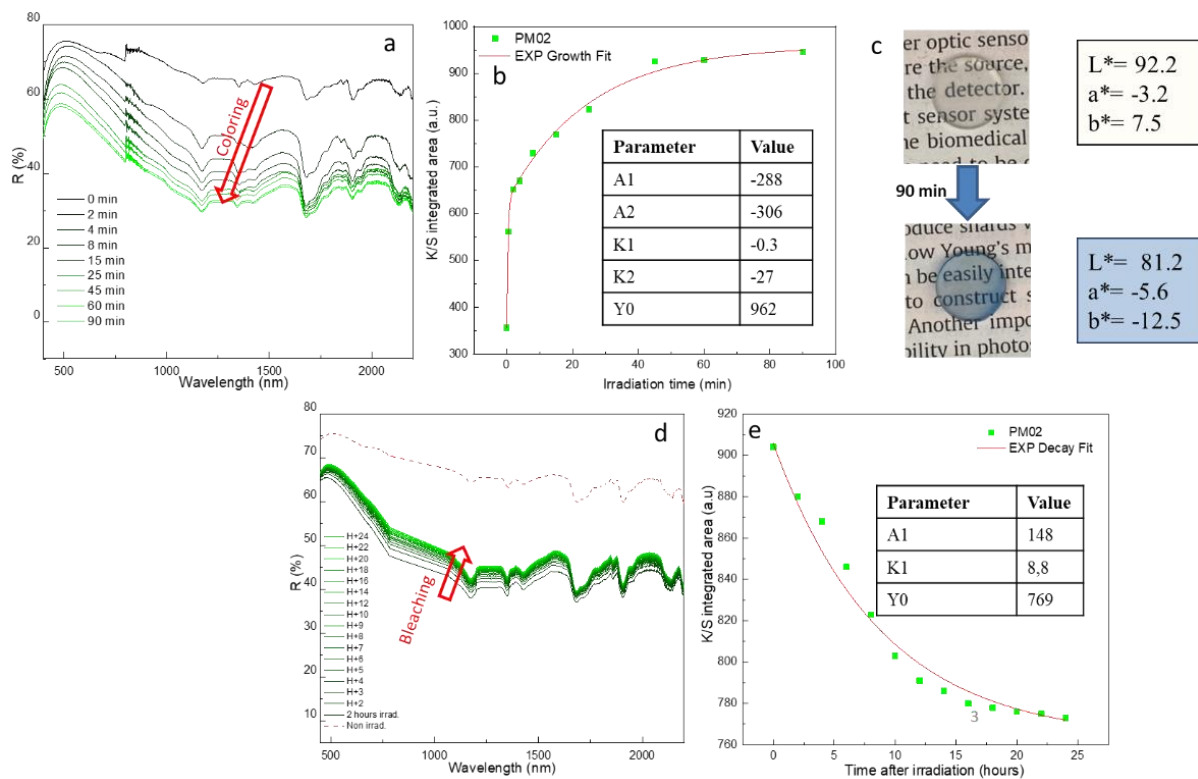
distribution of the NPs domains makes such statistical study very challenging. With this limitation said an attempt for a detailed statistical study of the average size of the aggregates using Image-J software is proposed as shown in Figure 39. The histograms present the length distribution of the aggregation of WO₃ NPs inside each preform in three main sections: center, border, and gap. The measurement was averaged after scanning 6 segments (6 photos) in each section (center, border, and gap) of the PM02 and PM05 modified preforms using J-Image software. The number of measurements was 120 per section. The length of the lower-size individual aggregates in each section for PM02 and PM05 is averaged on three different aggregate regions. This approximation gives a clear vision of the length/size of aggregation in each domain. From the histograms, the average length of the aggregates in PM02 in the border section (374±47 nm) is higher than the center (262±52 nm) and again higher than in the gap sections (181±38 nm). As shown in Figure 38 (d-f), the aggregations in PM05 record a larger overall size: borders (408±32 nm), center (312±28 nm), and gap (358±44 nm). The formation of aggregations was previously observed by Wegener *et al.* [43] in PMMA doped with ZnO NPs by bulk radical polymerization, where they reported on the polymerization-induced segregation of the primary particles to form domains within the bulk polymer. In another study, Xu *et al.* [50] prepared PMMA-based nanocomposite films with ultra-high-loading ZnS quantum dots via the bulk thermo-curing copolymerization method. Here also, they noticed the formation of aggregates and irregular phase domains in the PMMA/ZnS nanocomposites.

Photochromic study of the doped preforms. The PM02 preform was selected to study photochromic properties as it maintains good transmission properties close to the PM00 associated with proper thermal drawing ability. A 1 mm slice was cut from the PM02 preform and employed for a photochromic study using Halon as a white reference. Ex-situ diffuse reflectance (R%) measurements were performed after 2, 4, 8, 15, 25, 45, 60 and 90 min of irradiation (Figure 40.a) on the preform slice deposited on a 100% reflective white background. Hence, its reflectance can be in first approximation (*i.e.*, considering that scattering phenomena from the WO₃ particles have a negligible effect on the signal) complementary to the WO₃ absorbance. The reflectance of the PM02 vs. UV-light irradiation time on the 450-2200 nm wavelength range was recorded and transformed in Kubelka-Munk absorbance spectra ($K/S = (1-R)^2/(2 \times R)$) [51]. As shown in Figure 40.a, the PM02 exhibits a photochromic effect mainly observed in the near-infrared part of the spectrum (due to the W⁵⁺ → W⁶⁺ inter-valence charge transfer responsible for the visible-NIR absorption band centered at about 1 μm wavelength). The associated chromatic coordinates in L*, a*, b* space are presented in Figure 40.c, which quantifies the photochromic efficiency of the PM02 from the optical contrast calculated between the non-irradiated and 90 min irradiated states. It allows the calculation of visible $\Delta C = 22.9$ in between the initial and the 90 min irradiated states (a contrast above 5 becomes clearly visible by human eyes). To better express the photochromic coloring kinetic, a double exponential function (a combination of two first-order kinetic laws) was used to fit the experimental data, according to Equation 7.

Chapter III: Results and Discussion

The values of the parameters are shown in Figure 40.b. Compared with our previous study on the mechanism of photochromism in WO_3 -based films and powders [17], [52], we observe quite a similar coloring kinetic. It consists of two kinetic phenomena with almost the same amplitude ($A1$ almost equal to $A2$): a fast-kinetic component ($K1 = 0.3$ min) affecting the coloring mainly during the very first minutes, and a slow-kinetic component ($K2 = 27$ min). We proposed in previous works [17] that the fast kinetic corresponds to a quick photo-reduction of the surface cations from W^{6+} to W^{5+} , then the surface becomes saturated with W^{5+} ions and this fast mechanism stops. The slow kinetic presents the ionic diffusion of the W^{5+} from the surface to the material bulk, allowing W^{5+} surface desaturation and so new surface photoreduction.

For the bleaching study, the 90 min irradiated PM02 slice was left in the dark for self-bleaching, directly in the spectrometer chamber, automatically recording the evolution of the reflection spectra for 24 hours. In a similar manner to the coloring study, the reflection spectra in Figure 40.d were transferred to K/S and shown in Figure 40.e. The gap between the spectrum obtained after 24 hours of darkening and the spectrum of the initial state remains important. The reflectance contrast (ΔR), taken as equal to the reflectance difference in the IR range at 1200 nm between the 24-hour bleached sample (H+24) and the initial state (90 min just irradiated) shows that the reversibility rate is only about 21% (percentage calculated from the ratio between the H+24 and the initial states). For the bleaching kinetic, the fitting of the experimental data was achieved using a single decay component following Equation 8.



Cpt.III-Figure 40: Photochromic reflectance spectra of the 0.2% WO_3 -doped PMMA preform (PM02) vs time for a) coloring versus irradiation and d) bleaching under dark. Kinetic study based on the evolution of the average K/S absorbance

Chapter III: Results and Discussion

(400-2500 nm): b) during coloring and e) during bleaching. c) PM02 slice before and after 90 min irradiation with the corresponding colorimetric coordinates.

In this case, the A1 and Y0 fitting parameters have poor physical signification since the bleaching is not complete. Nonetheless, the A1/Y0 ratio, equal to 20%, is directly associated with the fitted reversibility rate. The phenomenon of re-oxidation of W^{5+} to W^{6+} by the oxygen in the air is predicted to be very slow compared to the photoreduction of W^{6+} to W^{5+} under UV irradiation [53]. K_I is 8.8 hours. Hence, we can conclude that the PM02 preform shows poor bleaching behavior at room temperature, with very slow kinetic and uncompleted reversibility.

Much research in photochromic composite compounds confirms that oxygen molecules improve the bleaching of the WO_3 -based composite, which can be accomplished by the oxidation of the W^{5+} metal centers (at the origin of the blue coloration) from electron transfer from the +V metal ions to the oxygen molecules [54]. Oxygen can be mainly provided from polymers with enough OH groups such as vinyl polymers [55], nano cellulose [56] and hydrogel [57]. However, since the proposed hybrid PMMA/ WO_3 contains many structural C=O groups and insufficient OH groups, such a polymeric matrix can block rapid spontaneous reoxidation and stabilize the blue coloration [58]. Noteworthy, the bleaching behavior of WO_3 -based materials can be improved by heating the material to 80-100 °C in air or under ozone (oxidative conditions) to obtain a complete relaxation [52]. This route was not investigated as it is outside of the scope of this study. Hereafter, we will show that the blocking effect of the polymeric matrix besides the bleaching behavior is drastically limited for shaped fibers.

5.2.3 Single fiber characterization

The aspect ratio of the fibers. Following, the preforms were thermally stretched down into optical fibers (labeled as FPM00, FPM02 and FPM05 with respect to the WO_3 particle content). Different diameters of fibers (D_{fib}) were issued from the preform drawing process by changing the preform feed velocity (V_{feed}) or/and the fiber drawing velocity (V_{draw}). The diameter of the lab-made PMMA fibers can be theoretically calculated with respect to the preform diameter (D_{pref}) using the equation of mass conservation [49]:

$$\frac{D_{pref}^2}{D_{fib}^2} = \frac{V_{draw}}{V_{feed}} \quad \text{Chpt.III-Equation 14}$$

Thin and large diameter fibers were stretched down from each of the three preforms. The drawing parameters (T_{draw} , V_{feed} , V_{draw} , D_{pref}), along with the calculated and measured diameters are listed in Table 2 with varying drawing velocities. For each change in V_{draw} , measurement of D_{fib} was performed (afterward using the optical microscope) on fully stabilized sections of fibers, as an average of 3 meters of fiber is needed to reach again a uniform section.

The increase of the recorded drawing temperature with the increase of the tungsten oxide content is in good agreement with the variation of the T_g , which increases upon doping with WO_3 due to the blocking of the chain segments of PMMA. Furthermore, the calculated diameters are found relatively

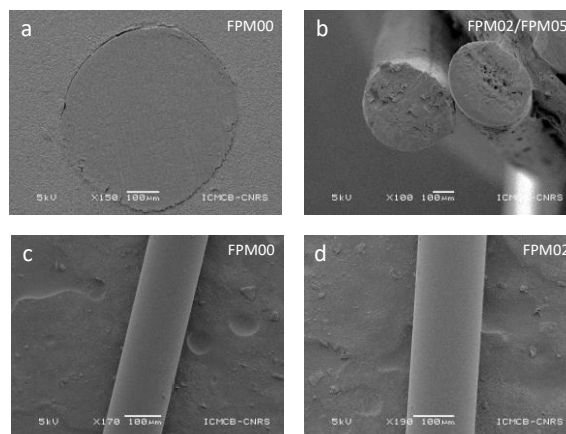
Chapter III: Results and Discussion

close to the measured ones (accuracy estimated at about 10%), which confirms the feasibility of fiber diameter control by drawing parameters.

Chpt.III-Table 12: Calculated and measured diameters of the issued WO₃-doped PMMA fibers

Fibre		T_{draw} (°C)	V_{feed} (mm/min)	V_{draw} (m/min)	D_{pref} (mm)	$D_f(\mu\text{m})$ calculated	$D_f(\mu\text{m})$ measured
FPM00	Large	124	1	0.5	12	537	550±50
	Thin	124	1	4	12	190	145±15
FPM02	Large	138	1	0.5	12	537	420±40
	Thin	138	1	6	12	154	135±15
FPM05	Large	142	1	0.5	12	537	620±60
	Thin	142	1	1	12	379	385±40

The SEM analysis in cross-sectional and longitudinal views of the lab-made PMMA/WO₃ hybrid FPM00, FPM02, and FPM05 fibers are shown in Figure 41. The fiber sample FPM00 (Large) was embedded in an epoxy resin, the surface was then polished to improve the visualization of the cross-section (Figure 41.a). The samples FPM02 and FPM05 were cut by a diamond cleaver and fixed vertically facing the SEM detector (Figure 41.b). For all samples observed in longitudinal view, the SEM images indicate a good surface quality (Figure 41.c-d). No surface imperfection (micro cracks, pores, defects) could be detected on the cross-section or surface of the fibers. The six studied fibers cannot be differentiated either by visual inspection or by SEM images due to the nanometric doping which cannot be tracked using the SEM device resolution.



Chpt.III-Figure 41: SEM micrographs of lab-made WO₃-doped PMMA hybrid fibers. Cross-sectional views of a) FPM00, b) FPM02 and FPM05 fibers. Longitudinal views of c) FPM00 and d) FPM02 fiber.

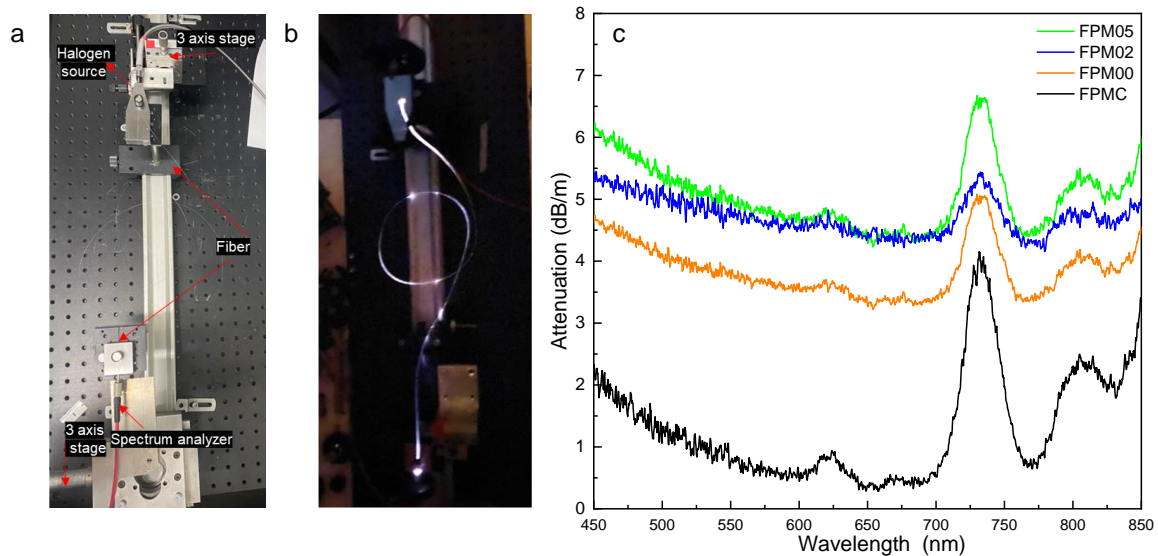
Optical signal quality: attenuation of the fibers. Attenuation measurement in optical fibers was recorded using the well-established cut-back method. The attenuation coefficient is defined as the

Chapter III: Results and Discussion

logarithm relationship between the transmitted input power $P(0)$ and the output power $P(x)$ observed after propagation of a distance x in an optical fiber system [59]:

$$\alpha_{\text{total}} \text{ (dB/km)} = (10/x) \cdot \text{Log}[P(0)/P(x)] \quad \text{Chpt.III-Equation 15}$$

This equation is known as Beer's Law and clearly shows that the power of the transmitted signal decreases exponentially with the propagated distance. The attenuation of the FPM00, FPM02 and FPM05 fibers (thin diameters) has been measured in the range of 450-850 nm (Figure 42). A commercial PMMA fiber (labeled as FPMC) provided by *XLY Fiber company* ($D_f = 350 \mu\text{m}$) was used as a reference.



Chpt.III-Figure 42: Loss measurements on the WO_3 -doped PMMA hybrid fibers a) Photograph of the cut-back measurement set up, b) A 2.5-meters-long FPM02 fiber excited by the Halogen lamp under dark conditions, c) Loss spectrum (attenuation factor) of the lab-made PMMA/ WO_3 thin fibers with various WO_3 content along and comparison with a commercial PMMA fiber (FPMC).

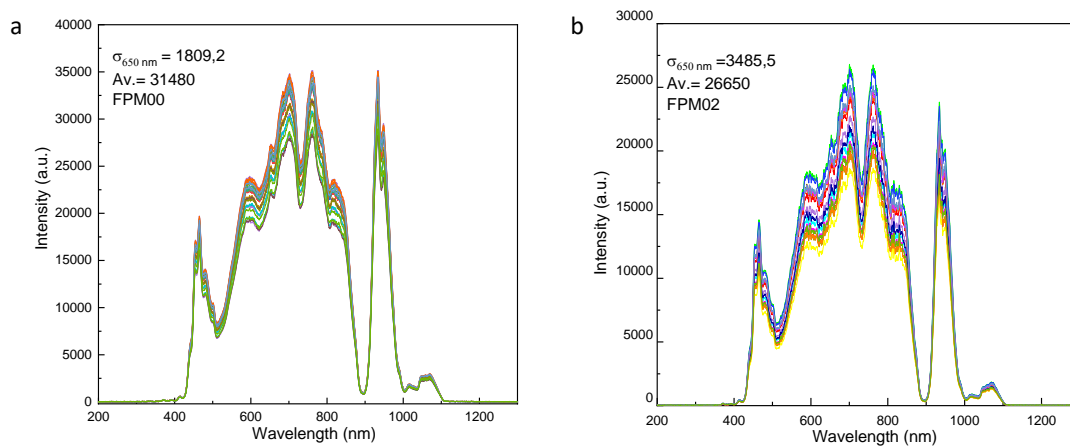
As shown in Figure 42.c, the attenuation curves of the lab-made fibers exhibit a similar shape to the commercial fiber, yet with a higher loss level. Attenuation in PMMA can be caused by intrinsic or extrinsic loss. Intrinsic loss mechanisms result from the chemical and physical structure of the PMMA fiber. The first types are the absorption losses, which mainly consist of the molecular vibrational absorption of the C-H bonds and the absorption due to electronic transitions between different energy levels within the molecular bonds [60]. The C-H vibrational absorption can be observed at higher wavelengths as shown at the local maximum (732 nm) which increases from 4.2 dB/m in FPMC to 6.7 dB/m in FPM05. Also, the extrinsic loss mechanism can originate from absorption by contaminants, water or extrinsic doping materials (herein WO_3) incorporated in the fiber [60], [61].

The second type are caused by Raleigh/Mie scattering occurring from the WO_3 nanoparticles, dust inclusions, microporosity or even density and composition fluctuations in the PMMA polymer. Rayleigh scattering happens when the scattering source diameter is at least 10 times smaller than the

Chapter III: Results and Discussion

wavelength of the light [62]. Meanwhile, Mie scattering occurs when the particle diameter is equal or higher to the wavelength of light [63]. Rayleigh scattering occurs at all the wavelengths, but with a clear decrease of its intensity versus wavelength increase whereas Mie scattering efficiency is negligibly depending on wavelength. Since the size of the incorporated WO_3 particles varies between 200 and 5000 nm, as predicted from the size of aggregation inside the preforms, both Rayleigh scattering and Mie scattering can occur inside the fibers. This confirms the fact that WO_3 particles are expected to play a dual role as scattering and absorption centers leading to increased optical loss in comparison with undoped PMMA fibers. Here the amplified attenuation with the WO_3 doping originates from both the scattering and the absorption properties of WO_3 particles.

Optical signal quality: reproducibility of the transmission measurements. In the following section, we mainly focus on the FPM02 hybrid fiber since it exhibits a lower attenuation than the FPM05 fiber, which makes it a better candidate for the desired optical application. Two new samples: a 0.2 wt% doped and an undoped sample were prepared; in order to eliminate any external effects on the consistency of the measurements the fibers were produced in the same drawing conditions ($V_f = 1$ mm/min, $V_d = 2$ m/min, with 275 ± 25 μm diameter) and the entrance and end faces of each piece were polished in the same manner. First, in order to assess the longitudinal homogeneity of the lab-made FPM00 and FPM02 fibers, we recorded the transmission signal of 15 different 5-cm-long cuts. As can be seen in Figure 43.a, the transmitted signal through the 15 different cuts of a FPM00 fiber superimposed relatively well, with an average maximum transmission intensity of 31480 and a standard deviation of 1809. In comparison, the transmitted signal through the 15 cuts of the FPM02 fiber exhibits a lower maximum of 26650 and a higher standard deviation of 3485 (Figure 43.b).



Chpt.III-Figure 43: Optical transmission signal intensity variations for 15 cuts of the lab-made PMMA optical fibers a) FPM00 fiber and b) FPM02 fiber.

It appears that the incorporation of the WO_3 NPs within the PMMA fiber leads both to a decrease in the total transmitted optical signal and a deterioration of the signal homogeneity along the fiber. This result could be predicted since the WO_3 NPs are acting as extrinsic scattering and absorption centers. Bulk scattering using metal oxide such as zinc oxide (ZnO), titanium dioxide (TiO_2) or magnesium oxide (MgO) in POFs has already been reported, with the purpose to realize radial light emission by

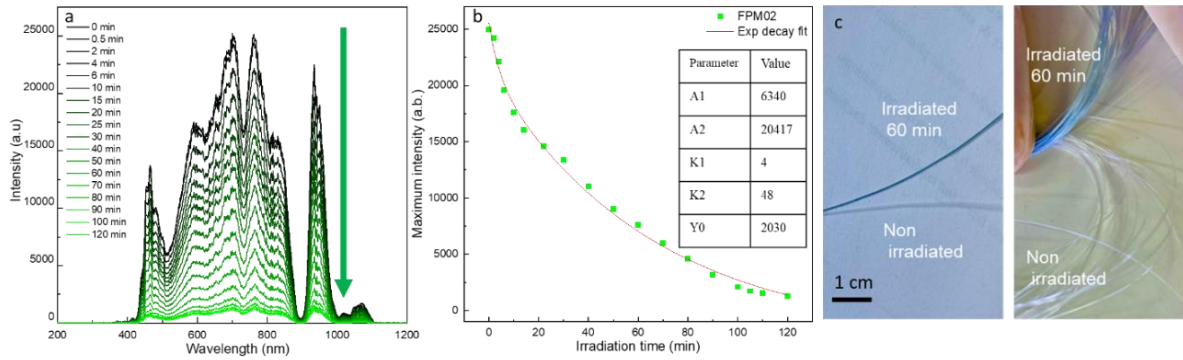
Chapter III: Results and Discussion

increasing the scattering leading to a higher attenuation and direct activation of side emission [41]. Nevertheless, within these limitations, the quality of the transmitted signal remains steady and significantly high for both fibers, assessing our protocol for the elaboration of hybrid WO_3/PMMA fibers.

Photochromic properties of single plastic fibers (axial transmission). Samples with a length of 5 cm (diameter of 275 μm) were used to evaluate the photochromic properties of the FPM02 fiber. The fiber was irradiated with the same conditions of irradiation in the thin film setup. The evolution of the transmission spectrum of the FPM02 versus irradiation time is depicted in Figure 44.a. The maximum intensity evolution at 650 nm was extracted to investigate further the photo-redox kinetic (Figure 44.b). Upon irradiation, the transmitted signal quickly degrades because of the increased absorption of WO_3 NPs under UV excitation (as also reported in part 4, section: 4.1.4) where the mass doping of the PES preforms led to the same phenomenon “positive photochromism”. The tungsten oxide acts as an absorption center, leading to an increased transmission loss. As shown in Figure 44.c, the color of the FPM02 fibers (single fiber and bundle) turned from transparent to blue after 1 hour of irradiation. Consistently with the previous study on the WO_3 -doped preform slices, the coloring kinetic is expressed by the same double exponential function with a reverse signal. The fitting of the experimental data is depicted in Figure 44.b. The maximum intensity of FPM02 drops rapidly in the first 15 minutes of irradiation, then slows down beyond 15 min of irradiation, until almost no longer evolving after 120 min. The coloring kinetic consists of two kinetic phenomena: a fast-kinetic component ($A_1 = 6340$, $K_1 = 4$ min) and a slow kinetic component ($A_2 = 20417$, $K_2 = 48$ min). In fibers, as was already the case for the preforms, the coloring kinetic seems mainly governed by the kinetic of WO_3 , as reported in our last paper [53], which confirms the weak effect of the PMMA matrix on photochromism (for the coloring mechanism). It can however be noticed that, because of different shapes and especially a different surface/volume aspect-ratio, the two characteristic times describing the coloring kinetic are both a bit lower for fibers than preforms. Indeed, instead of an intrinsic modification of the composite response under the UV-irradiation, our hypothesis to explain the slower coloring of fibers compared to preform is a lesser efficiency of the irradiation in the former case, since the penetration of the UV irradiation source inside the fibers are lowered by the cylindrical aspect of the fibers.

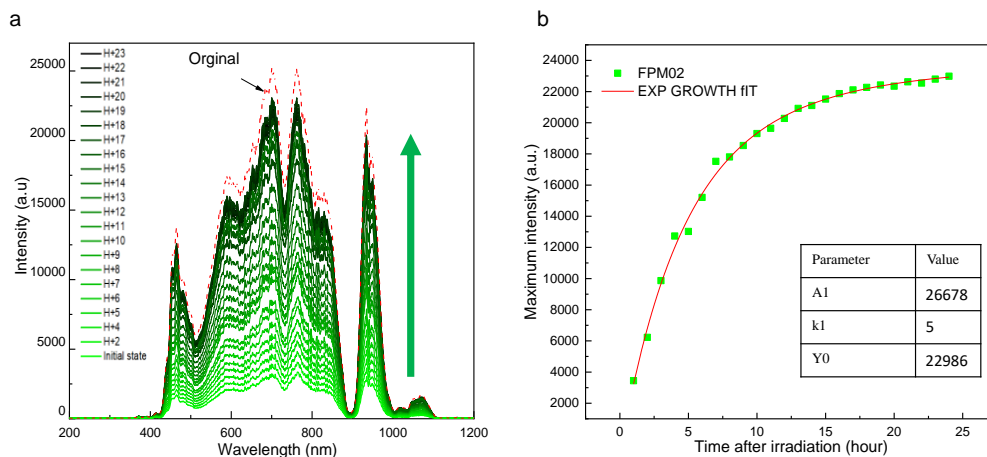
The same pre-irradiated FPM02 fiber was used for the bleaching study (Figure 45). The fiber was left in the dark at room temperature for self-bleaching using the same set-up while automatically recording the evolution of the transmission signal. Unlike observations made on the PM02 preform, the FPM02 shows a reversible and almost complete bleaching mechanism, returning to its transparent appearance after 24 hours in the dark (Figure 45. a)

Chapter III: Results and Discussion



Chtp.III-Figure 44: Photochromic coloring of the 0.2% WO_3 -doped PMMA fiber (FPM02). a) Axial transmission spectra vs irradiation times, b) Kinetic study based on the transmission intensity (at 650 nm) vs irradiation time, c) Photographs of a single fiber and a bundle of FPM02 fibers before and after irradiation.

The maximum transmission intensity evolution can be fitted from a single exponential growth trend on the complete 20 first-hour range, according to the Equation 3 already used on preform slices with a reverse signal (growth). Beforehand, the bleaching mechanism is governed by the phenomenon of reoxidation of W^{5+} to W^{6+} by the oxygen from the atmosphere. We assume that the principal changes from preform to fiber are again their aspect-ratio. Considering aspect-ratio, the evolution of diameter from preform to fiber is given by: $D_p/D_f = 12000/265 \mu m = 45.3$, which we believe leads to higher proximity of the WO_3 nanoparticles to the fiber surface and so the oxidizing atmosphere. The bleaching kinetic of the fibers is nearly close to the one of WO_3 powder beds, reported in previous works [1]. This confirms that the slower and partially non-reversible bleaching only observed for the preforms was due to the « optical passivation » of the dispersed particles in the PMMA matrix, which is poorly oxygen diffusive, i.e., the PMMA matrix in preform (thick) geometry tends to prevent the redox reaction at the origin of the WO_3 particle photochromism.



Chtp.III-Figure 45: Photochromic bleaching under the dark of the 0.2% WO_3 -doped PMMA fiber (FPM02). a) Evolution of axial transmission signal in dark conditions, b) kinetic study based on the transmission intensity (at 650 nm) vs time after irradiation.

Chapter III: Results and Discussion

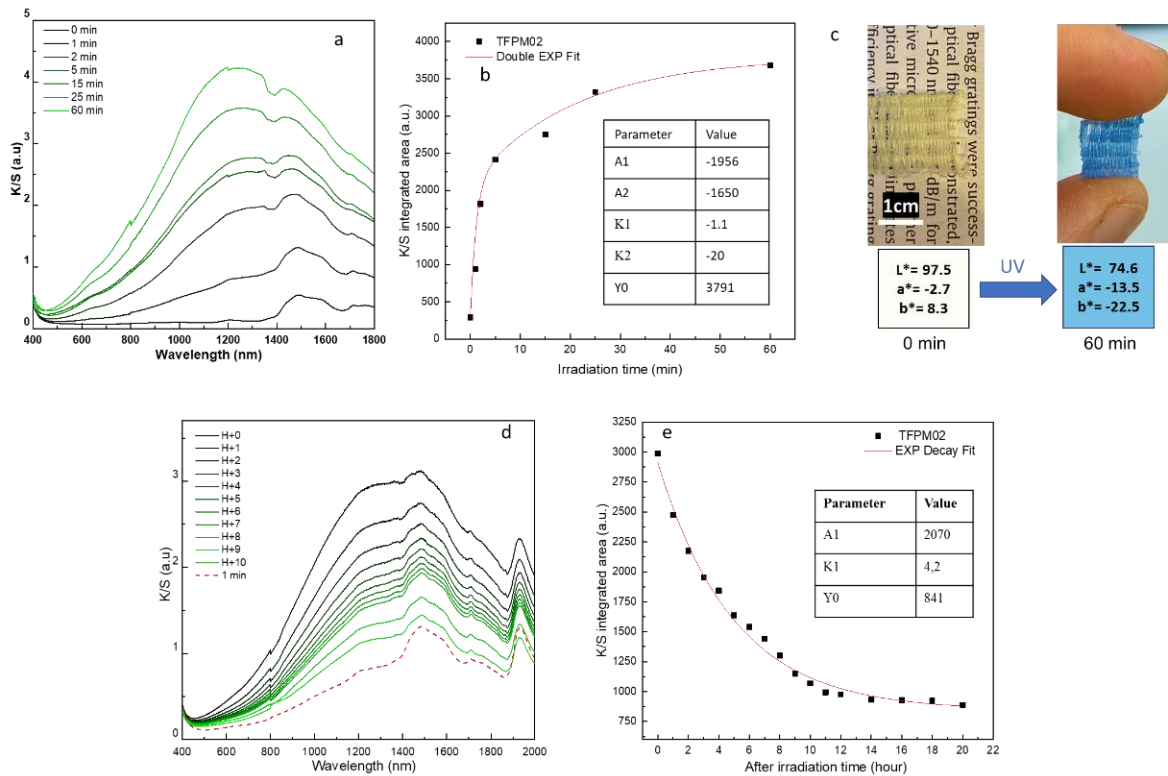
5.2.4 Photochromic properties of 2D textile

In this section, we discuss the optical properties of a 2D system consisting of photochromic pieces of FPM02 fibers woven manually into a fabric with dimension $2 \times 2 \text{ cm}^2$ (Figure 46). The fibers were selected from the same fiber drawing section with similar diameters. Ex-situ diffuse reflectance (%R) of the fabric after exposure of 1, 2, 5, 15, 25 and 60 min under a UV lamp (8 W) were recorded and the results are presented in Figure 46.a.

Compared to other research in the field, Bao *et al.*[64] produced photochromic cotton fabric via thiolene click chemistry using the spiropyrane derivatives as the photochromic active part and a commercial cotton substrate. The synthesized photochromic materials show a good color-changing rate and fading rate with visible contrast of around 50 between non-irradiated and irradiated states. Notably, our 2D fabric exhibits a quick response after 1 min of irradiation, as proofed by the quick degradation of the reflectance curve between 0 and 1 min. The coloring kinetic was evaluated by fitting the experimental (Figure 46.b) (based on the K/S absorption spectra which is a most adequate representation of the color evolution for the 2D fabric). In the case of the fabric, the two kinetic phenomena show almost the same amplitude (A_1 almost equal to A_2) with $K_1 = 1.1 \text{ min}$ and $K_2 = 20 \text{ min}$. The associated chromatic coordinates in L^* , a^* , b^* space are calculated for the 0- and 60-min irradiated states (Figure 46.c). The visible $\Delta C = 43.6$. Indeed, the textile gives a very good color contrast, which is important for application as smart textile. Hence, in terms of kinetic and contrast, 2D textiles exhibit the quickest and deepest coloring properties. The slight improvement in comparison with the coloring of a single fiber from its axial transmission is surely due to the capacity of the textile to intercept efficiently the UV irradiation from the UV lamp. Hence, the shaping step to applicative manufactured 2D products, with a large surface/thickness ratio is associated with improved photochromic coloring.

For the bleaching study, the irradiated fabric investigated above was left in the dark in the spectrometer chamber for self-bleaching. As for the coloring study, the reflection spectra were transferred to K/S (Figure 46.d). As expected, the fabric shows a reversible behavior like single FPM02 fibers. Bleaching kinetic was followed by recording the evolution of average K/S vs. after-irradiation time (Figure 46.e). The K/S evolution can be fitted from the same used single exponential decay. The kinetic of the bleaching mechanism of the fabric appears to be almost the same as that of the fiber FPM02: the characteristic decay time K_1 is equal to 4.2 hrs, to be compared to the one calculated for the fiber (5.0 hrs). Thus, the fabric exhibits a reversible photochromism, returning to almost its initial state for 20 hrs (with more than 90% recovery after 8 hrs), i.e., one night is sufficient for reinitializing and re-using the as-prepared smart textile.

Chapter III: Results and Discussion



Chpt.III-Figure 46: Photochromic K/S spectra of a 2D fabric made of 0.2% WO₃-doped PMMA fibers (PM02) vs time for a) coloring versus irradiation and d) bleaching under dark. Kinetic study based on the evolution of the average K/S absorbance (400-2500 nm): b) during coloring and e) during bleaching c) Photographs of the fabric before and after irradiation with the corresponding colorimetric coordinates.

5.3 Conclusion for Part 5

We explored the fabrication and photochromic features of hybrid inorganic/organic WO₃-doped PMMA/PES optical fibers in this part of the study. In the first section, we investigated various models of elaborated core/cladding PES-modified fibers. We discovered that cladding modification resulted in negative photochromism (signal enhanced by irradiation) and core modification resulted in positive photochromism (signal decreased by irradiation). Using various suspensions, we also explored the post-coating procedure as a favored modification approach. The use of PVP as a dispersant increased the suspension and cladding structure's stability. In the second section, we fabricated lab-made WO₃-doped PMMA optical fibers. The macroscopic preforms have been successfully synthesized by the radical polymerization of MMA doped with modified photochromic WO₃ nanoparticles, followed by their thermal stretching into tens-of-meters-long optical fibers with diameters ranging from 200-600 μm . The 0.2% WO₃-doped preform shows a slow coloring mechanism and an irreversible photochromic behavior while single fibers exhibit more intense and more rapid coloring and bleaching phenomena, comparable to the photochromic parameters of WO₃ powder beds. This shows that, even if the PMMA matrix contributes to blocking the oxygen diffusion as the source of the WO₃ redox activity and color changes, the design of thin composite fibers enables recovering the redox photochromic activity of the embedded WO₃ nanoparticles. Moreover, we have presented a hand-

Chapter III: Results and Discussion

made 2D photochromic fabric made with 0.2%-WO₃ doped fibers. It shows a fast-bleaching response, with a decay time of 4.2 hours, along with a very large visible contrast ($\Delta C = 43.6$).

5.4 References

- [1] M. Bourdin et al., “Nanoparticles (NPs) of WO₃-type compounds by polyol route with enhanced electrochromic properties,” *J Alloys Compd*, vol. 823, p. 153690, 2020, doi: <https://doi.org/10.1016/j.jallcom.2020.153690>.
- [2] R. Gross, A. Marx, D. Einzel, and S. Geprägs, “Festkörperphysik,” De Gruyter, 2018. doi: 10.1515/9783110566130.
- [3] I. Trenque, S. Mornet, E. Duguet, and M. Gaudon, “New insights into crystallite size and cell parameters correlation for ZnO nanoparticles obtained from polyol-mediated synthesis,” *Inorg Chem*, vol. 52, no. 21, pp. 12811–12817, Nov. 2013, doi: 10.1021/ic402152f.
- [4] I. D. Brown, “The chemical bond in inorganic chemistry,” *J Mater Sci*, vol. 52, pp. 9959–9962 Nov. 2017, <https://doi.org/10.1007/s10853-017-1215-2>.
- [5] A. A. Coelho, P. A. Chater, and A. Kern, “Fast synthesis and refinement of the atomic pair distribution function,” *J Appl Crystallogr*, vol. 48, no. 3, pp. 869–875, Jun. 2015, doi: 10.1107/S1600576715007487.
- [6] T. H. Fleisch, G. W. Zajac, J. O. Schreiner, and G. J. Mains, “An XPS study of the UV photoreduction of transition and noble metal oxides,” *Appl Surf Sci*, vol. 26, pp. 488–497, 1986.
- [7] J. Díaz-Reyes, R. Castillo-Ojeda, M. Galván-Arellano, and O. Zaca-Moran, “Characterization of WO₃ thin films grown on silicon by HFMOD,” *Adv Condens Matter Phys*, vol. 2013, pp. 1–9, 2013, doi: 10.1155/2013/591787.
- [8] M. Naftaly et al., “Sheet resistance measurements of conductive thin films: a comparison of techniques,” *Electronics (Basel)*, vol. 10, no. 8, p. 960, Apr. 2021, doi: 10.3390/electronics10080960.
- [9] I. Miccoli, F. Edler, H. Pfnür, and C. Tegenkamp, “The 100th anniversary of the four-point probe technique: the role of probe geometries in isotropic and anisotropic systems,” *J Phys Condens Matter*, vol. 27, no. 22, p. 223201, Jun. 2015, doi: 10.1088/0953-8984/27/22/223201.
- [10] K. Huang and Q. Zhang, “Giant persistent photoconductivity of the WO₃ nanowires in vacuum condition,” *Nanoscale Res Lett*, vol. 6, no. 1, p. 52, Sep. 2010, doi: 10.1007/s11671-010-9.
- [11] S. Lany and A. Zunger, “Anion vacancies as a source of persistent photoconductivity in II-VI and chalcopyrite semiconductors,” *Phys Rev B*, vol. 72, no. 3, p. 035215, Jul. 2005, doi: 10.1103/PhysRevB.72.035215.

Chapter III: Results and Discussion

- [12] M. Kumar, C. Y. Lee, H. Sekiguchi, H. Okada, and A. Wakahara, "Demonstration of a large-area AlGaIn/GaN Schottky barrier photodetector on Si with high detection limit," *Semicond Sci Technol*, vol. 28, no. 9, p. 094005, Sep. 2013, doi: 10.1088/0268-1242/28/9/094005.
- [13] P. V. Karthik Yadav, B. Ajitha, Y. A. K. Reddy, V. R. Minnam Reddy, M. Reddeppa, and M.-D. Kim, "Effect of sputter pressure on UV photodetector performance of WO₃ thin films," *Appl Surf Sci*, vol. 536, p. 147947, Jan. 2021, doi: 10.1016/j.apsusc.2020.147947.
- [14] J. M. Wu and W. E. Chang, "Ultrahigh responsivity and external quantum efficiency of an ultraviolet-light photodetector based on a single VO₂ microwire," *ACS Appl Mater Interfaces*, vol. 6, no. 16, pp. 14286–14292, Aug. 2014, doi: 10.1021/am503598g.
- [15] B. Cook et al., "Heat-assisted inkjet printing of tungsten oxide for high-performance ultraviolet photodetectors," *ACS Appl Mater Interfaces*, vol. 10, no. 1, pp. 873–879, Jan. 2018, doi: 10.1021/acsami.7b15391.
- [16] G. Liu et al., "Effects of growth substrates on the morphologies of TiO₂ nanowire arrays and the performance of assembled UV detectors," *Appl Surf Sci*, vol. 315, pp. 55–58, Oct. 2014, doi: 10.1016/j.apsusc.2014.07.115.
- [17] M. Bourdin et al., "Investigation on the coloring and bleaching processes of WO_{3-x} photochromic thin films," *J Mater Chem C Mater*, vol. 8, no. 27, pp. 9410–9421, 2020, doi: 10.1039/D0TC02170A.
- [18] C.-C. Lin, W.-H. Lin, and Y.-Y. Li, "Synthesis of ZnO nanowires and their applications as an ultraviolet photodetector," *J Nanosci Nanotechnol*, vol. 9, no. 5, pp. 2813–2819, May 2009, doi: 10.1166/jnn.2009.008.
- [19] S. M.-L. Pfaendler and A. J. Flewitt, "High-resistivity metal-oxide films through an interlayer of graphene grown directly on copper electrodes," *Graphene Technol*, vol. 3, no. 1, pp. 11–18, Mar. 2018, doi: 10.1007/s41127-017-0016-3.
- [20] X. Dong et al., "Efficient charge transfer over Cu-doped hexagonal WO₃ nanocomposites for rapid photochromic response," *J Photochem Photobiol a Chem*, vol. 425, p. 113716, Mar. 2022, doi: 10.1016/j.jphotochem.2021.113716.
- [21] Y. Nukui, N. Srinivasan, S. Shoji, D. Atarashi, E. Sakai, and M. Miyauchi, "Vertically aligned hexagonal WO₃ nanotree electrode for photoelectrochemical water oxidation," *Chem Phys Lett*, vol. 635, pp. 306–311, Aug. 2015, doi: 10.1016/j.cplett.2015.07.006.
- [22] S. Zhang, S. Cao, T. Zhang, Q. Yao, A. Fisher, and J. Y. Lee, "Monoclinic oxygen-deficient tungsten oxide nanowires for dynamic and independent control of near-infrared and visible light transmittance," *Mater Horiz*, vol. 5, no. 2, pp. 291–297, 2018, doi: 10.1039/C7MH01128H.

Chapter III: Results and Discussion

- [23] C. Avellaneda, "Photochromic properties of WO_3 and WO_{3-x} ($X=\text{Ti}$, Nb , Ta and Zr) thin films," *Solid State Ion*, vol. 165, no. 1–4, pp. 117–121, Dec. 2003, doi: 10.1016/j.ssi.2003.08.023.
- [24] X. Dong et al., "Rational modification in the photochromic and self-bleaching performance of hierarchical microsphere $\text{Cu}@h\text{-WO}_3/\text{WO}_3 \cdot n\text{H}_2\text{O}$ composites," *Solar Energy Mater Solar Cells*, vol. 219, p. 110784, Jan. 2021, doi: 10.1016/j.solmat.2020.110784.
- [25] A. Goldstein, V. Chiriac, and D. Becherescu, "On some d_1 ions spectra in oxide glasses," *J Non Cryst Solids*, vol. 92, no. 2–3, pp. 271–277, Jul. 1987, doi: 10.1016/S0022-3093(87)80044-3.
- [26] H. F. Mollet and B. C. Gerstein, "An EPR study of W^{5+} in a recently discovered triclinic tungsten bronze, $\text{Na}_{0.33}\text{WO}_3$," *J Chem Phys*, vol. 60, no. 4, pp. 1440–1446, Feb. 1974, doi: 10.1063/1.1681217.
- [27] J. Díaz-Reyes, R. Castillo-Ojeda, M. Galván-Arellano, and O. Zaca-Moran, "Characterization of WO_3 thin films grown on silicon by HFMOD," *Adv Condens Matter Phys*, vol. 2013, pp. 1–9, 2013, doi: 10.1155/2013/591787.
- [28] S. K. Deb, "Opportunities and challenges in science and technology of WO_3 for electrochromic and related applications," *Solar Energy Mater Solar Cells*, vol. 92, no. 2, pp. 245–258, Feb. 2008, doi: 10.1016/j.solmat.2007.01.026.
- [29] X. Bai, H. Ji, P. Gao, Y. Zhang, and X. Sun, "Morphology, phase structure and acetone sensitive properties of copper-doped tungsten oxide sensors," *Sens Actuators B Chem*, vol. 193, pp. 100–106, Mar. 2014, doi: 10.1016/j.snb.2013.11.059.
- [30] B. M. Alshabander, "Copper (II)-doped WO_3 nanoparticles with visible light photocatalytic antibacterial activity against gram-positive and gram-negative bacteria," *Inorg Nano-Met Chem*, vol. 50, no. 12, pp. 1329–1333, Dec. 2020, doi: 10.1080/24701556.2020.1749075.
- [31] R. Pardo, M. Zayat, and D. Levy, "Photochromic organic–inorganic hybrid materials," *Chem Soc Rev*, vol. 40, no. 2, p. 672, 2011, doi: 10.1039/c0cs00065e.
- [32] T. J. DeJournett and J. B. Spicer, "The influence of oxygen on the microstructural, optical and photochromic properties of polymer-matrix, tungsten-oxide nanocomposite films," *Solar Energy Mater Solar Cells*, vol. 120, pp. 102–108, Jan. 2014, doi: 10.1016/j.solmat.2013.08.023.
- [33] T. He and J. Yao, "Photochromic materials based on tungsten oxide," *J Mater Chem*, vol. 17, no. 43, p. 4547, 2007, doi: 10.1039/b709380b.
- [34] S. Guan et al., " VO_2 films obtained by V_2O_5 nanoparticle suspension reduction," *Opt Mater (Amst)*, vol. 127, p. 112117, May 2022, doi: 10.1016/j.optmat.2022.112117.
- [35] L. U. Krüger et al., "Photochromism of doped and undoped WO_3 sol-gel films: Determination and analysis of optical constants," *Opt Mater (Amst)*, vol. 128, p. 112357, Jun. 2022, doi: 10.1016/j.optmat.2022.112357.

Chapter III: Results and Discussion

- [36] H. Kim et al., “Flexible thermochromic window based on hybridized VO₂/Graphene,” *ACS Nano*, vol. 7, no. 7, pp. 5769–5776, Jul. 2013, doi: 10.1021/nn400358x.
- [37] Y. Zhu et al., “WO₃ quantum dot photochromical film,” *Solar Energy Mater Solar Cells*, vol. 239, p. 111664, Jun. 2022, doi: 10.1016/j.solmat.2022.111664.
- [38] R. Zhang et al., “Energy-efficient smart window based on a thermochromic microgel with ultrahigh visible transparency and infrared transmittance modulation,” *J Mater Chem A Mater*, vol. 9, no. 32, pp. 17481–17491, 2021, doi: 10.1039/D1TA03917B.
- [39] H. Kogelnik, “On the propagation of gaussian beams of light through lens like media including those with a loss or gain variation,” *Applied Optics*, Vol. 4, Issue 12, pp. 1562-1569, vol. 4, no. 12, pp. 1562–1569, Dec. 1965, doi: 10.1364/AO.4.001562.
- [40] J. Gulgowski and T. P. Stefański, “Generalization of Kramers-Krönig relations for evaluation of causality in power-law media,” *Commun Nonlinear Sci Numer Simul*, vol. 95, p. 105664, Apr. 2021, doi: 10.1016/J.CNSNS.2020.105664.
- [41] S. Shabahang, S. Forward, and S.-H. Yun, “Polyethersulfone optical fibers with thermally induced microbubbles for custom side-scattering profiles,” *Opt Express*, vol. 27, no. 5, p. 7560, Mar. 2019, doi: 10.1364/OE.27.007560.
- [42] N. Huo and W. E. Tenhaeff, “High refractive index polymer thin films by charge-transfer complexation,” *Macromolecules*, Mar. 2022, doi: 10.1021/ACS.MACROMOL.2C02532.
- [43] M. M. Demir, M. Memesa, P. Castignolles, and G. Wegner, “PMMA/Zinc oxide nanocomposites prepared by in-situ bulk polymerization,” *Macromol Rapid Commun*, vol. 27, no. 10, pp. 763–770, May 2006, doi: 10.1002/marc.200500870.
- [44] S. Hammani, A. Barhoum, and M. Bechelany, “Fabrication of PMMA/ZnO nanocomposite: effect of high nanoparticles loading on the optical and thermal properties,” *J Mater Sci*, vol. 53, no. 3, pp. 1911–1921, Feb. 2018, doi: 10.1007/s10853-017-1654-9.
- [45] S. Abrate, R. Gaudino, and G. Perro, “Step-index PMMA fibers and their applications,” in *Current Developments in Optical Fiber Technology*, InTech, 2013. doi: 10.5772/52746.
- [46] M. Jachak, R. Bhise, A. Chaturvedi, V. Kamble, and G. Shankarling, “Pyrroloquinoline based styryl dyes doped PMMA, PS, and PS/TiO₂ polymer for fluorescent applications,” *J Inorg Organomet Polym Mater*, vol. 32, no. 7, pp. 2441–2454, Jul. 2022, doi: 10.1007/s10904-022-02285-1.
- [47] A. K. Nikolaidis, D. S. Achilias, and G. P. Karayannidis, “Synthesis and characterization of PMMA/Organomodified montmorillonite nanocomposites prepared by in situ bulk polymerization,” *Ind Eng Chem Res*, vol. 50, no. 2, pp. 571–579, Jan. 2011, doi: 10.1021/ie100186a.
- [48] K. Pal, “Effect of different nanofillers on mechanical and dynamic behavior of PMMA based nanocomposites,” *Compos Commun*, vol. 1, pp. 25–28, Oct. 2016, doi: 10.1016/j.coco.2016.08.001.

Chapter III: Results and Discussion

- [49] S. ElHady, O. Amin, and I. S. Fahim, "Fabrication of bio-plastic composite pellets from agricultural waste and food waste," *Int J Eng Trends Technol*, vol. 69, no. 3, pp. 133–137, Mar. 2021, doi: 10.14445/22315381/IJETT-V69I3P221.
- [50] J. Xu and D. Li, "Preparation and photoluminescence of transparent poly (methyl methacrylate)-based nanocomposite films with ultra-high-loading pendant ZnS quantum dots," *Polymers (Basel)*, vol. 10, no. 11, p. 1217, Nov. 2018, doi: 10.3390/polym10111217.
- [51] A. Roy, R. Ramasubramaniam, and H. A. Gaonkar, "Empirical relationship between Kubelka–Munk and radiative transfer coefficients for extracting optical parameters of tissues in diffusive and nondiffusive regimes," *J Biomed Opt*, vol. 17, no. 11, p. 115006, Nov. 2012, doi: 10.1117/1.JBO.17.11.115006.
- [52] Y. Badour, S. Danto, C. Labrugère, M. Duttine, and M. Gaudon, "Cu-doped and un-doped WO₃ photochromic thin films," *J Electron Mater*, vol. 51, no. 4, pp. 1555–1567, Apr. 2022, doi: 10.1007/s11664-021-09389-3.
- [53] Y. Badour et al., "Low-cost WO₃ nanoparticles / PVA smart photochromic glass windows for sustainable building energy savings," *Solar Energy Mater Solar Cells*, vol. 255, p. 112291, Jun. 2023, doi: 10.1016/j.solmat.2023.112291.
- [54] L.-M. Ai, W. Feng, J. Chen, Y. Liu, and W. Cai, "Evaluation of microstructure and photochromic behavior of polyvinyl alcohol nanocomposite films containing polyoxometalates," *Mater Chem Phys*, vol. 109, no. 1, pp. 131–136, May 2008, doi: 10.1016/j.matchemphys.2007.11.002.
- [55] A. L. Popov et al., "PVP-stabilized tungsten oxide nanoparticles: pH sensitive anti-cancer platform with high cytotoxicity," *Mater Sci Engineering: C*, vol. 108, p. 110494, Mar. 2020, doi: 10.1016/j.msec.2019.110494.
- [56] B. Zhang, R. Liu, Y. Pan, Q. Wang, and B. Liu, "Cellulose-based WO₃ nanocomposites prepared by a sol–gel method at low temperature," *IOP Conf Ser Mater Sci Eng*, vol. 301, p. 012075, Jan. 2018, doi: 10.1088/1757-899X/301/1/012075.
- [57] O. Oderinde, O. Ejeromedoghene, and G. Fu, "Synthesis and properties of low-cost, photochromic transparent hydrogel based on ethaline-assisted binary tungsten oxide-molybdenum oxide nanocomposite for optical memory applications," *Polym Adv Technol*, vol. 33, no. 3, pp. 687–699, Mar. 2022, doi: 10.1002/pat.5400.
- [58] D. K. Hwang, H. J. Kim, H. S. Han, and Y. G. Shul, "Development of photochromic coatings on polycarbonate," *J Solgel Sci Technol*, vol. 32, no. 1–3, pp. 137–141, Dec. 2004, doi: 10.1007/s10971-004-5778-4.
- [59] N. Ioannides et al., "Approaches to mitigate polymer-core loss in plastic optical fibers: a review," *Mater Res Express*, vol. 1, no. 3, p. 032002, Sep. 2014, doi: 10.1088/2053-1591/1/3/032002.

Chapter III: Results and Discussion

- [60] A. Charas et al., “Gain and ultrafast optical switching in PMMA optical fibers and films doped with luminescent conjugated polymers and oligomers,” *Frontiers of Optoelectronics in China*, vol. 3, no. 1, pp. 45–53, Mar. 2010, doi: 10.1007/s12200-009-0092-y.
- [61] C. Whittaker, C. A. G. Kalnins, D. Ottaway, N. A. Spooner, and H. Ebendorff-Heidepriem, “Transmission loss measurements of plastic scintillating optical fibres,” *Opt Mater Express*, vol. 9, no. 1, p. 1, Jan. 2019, doi: 10.1364/OME.9.000001.
- [62] P. Kubelka, “New contributions to the optics of intensely light-scattering materials part I,” *J Opt Soc Am*, vol. 38, no. 5, p. 448, May 1948, doi: 10.1364/JOSA.38.000448.
- [63] G. Latour, M. Elias, and J.-M. Frigerio, “Determination of the absorption and scattering coefficients of pigments: application to the identification of the components of pigment mixtures,” *Appl Spectrosc*, vol. 63, no. 6, pp. 604–610, Jun. 2009, doi: 10.1366/000370209788559719.
- [64] B. Bao, S. Bai, J. Fan, J. Su, W. Wang, and D. Yu, “A novel and durable photochromic cotton-based fabric prepared via thiol-ene click chemistry,” *Dyes and Pigments*, vol. 171, p. 107778, Mar. 2019, doi: 10.1016/j.dyepig.2019.107778

Supplementary chapter

Supplementary chapter

Prospective life cycle assessment of photochromic textiles made in labs for commercial application

In this part, we discuss the valorization of lab-scale photochromic textiles as future commercialized products. The main goal of this chapter is to focus on the environmental impact of photochromic textiles using the life cycle assessment method and to raise awareness about the possible environmental impact of “fast fashion” in the field of smart textiles. In the first part, we start by defining the goal and scope of this study, then we construct the life cycle inventory in detail where we emphasize on the different used materials and adapted processes from the database. In the second part, we present the assessment of the product design and its environmental impact through the interpretation of our results.

1 Life cycle assessment: a powerful technique to evaluate the environmental impacts of products

Life Cycle Assessment (LCA) is a standardized method for assessing the potential environmental impacts of a specific product or service throughout its life cycle, from raw material extraction (cradle) to waste management (grave) [1]. An LCA is performed in four stages, according to ISO 14040 and 14044 standards (ISO, 2006a, 2006b) as illustrated in Figure 1:

- 1) Goal and scope definition, which includes establishing the study's system boundaries and the functional unit. This is a quantifiable assessment of the product's function allowing the product comparisons.
- 2) Life cycle inventory analysis (LCI), in which a comprehensive list of relevant inflows and outflows, including emissions to air, water, and soil, as well as resource use in the form of energy, water, material, and land area, is gathered for each process included in the product's life cycle.
- 3) Life cycle impact assessment (LCIA), which uses characterization parameters to link inflows and outflows from the LCI to probable environmental impacts. Common impact categories include climate change, acidification, human toxicity, ecotoxicity, eutrophication, and resource depletion. Finally, data interpretation, which includes deriving inferences from the LCI and LCIA data and establishing the level of confidence in the results. The stages described by ISO standards create a systematic approach for performing LCIA. Some stages are required, while others are optional:

Classification (mandatory): The inventory flows are classified based on the method used and the sort of environmental impact they cause. CH₄ emissions, for example, are linked to climate change.

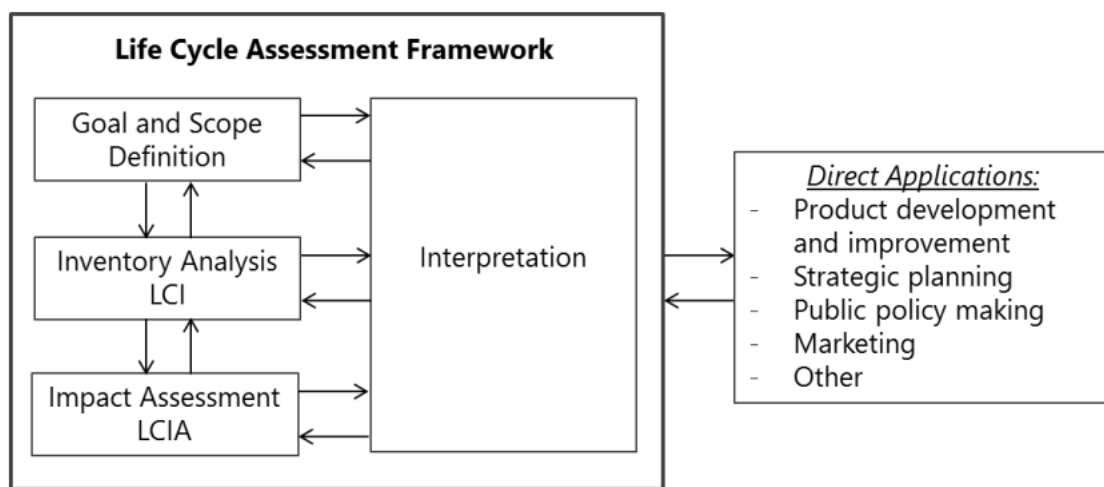
Characterization (mandatory): The substance fluxes must be characterized after they have been categorized. This entails combining all flows that have the same environmental impact into a single representative unit. For example, CH₄ can be transformed into CO₂-equivalent.

Normalization (optional): This stage establishes the strain on the environment by providing a reference context (e.g., country, region, or global) for each evaluated environmental effect category.

Supplementary chapter

Grouping (optional): In this phase, the impact categories are sorted and ranked, if applicable.

There are two techniques for performing an environmental life cycle assessment (E-LCA): consequential and attributional. The attributional LCA approach defines the environmental performance of a specific system at a specific time in the past, present, or future, whereas the consequential LCA considers the potential changes in the entire system resulting from the adoption or modification of a product or system [2,3]. For example, an attributional LCA is appropriate when addressing the question of which product has the best environmental performance, whereas the consequential systemic method is appropriate when addressing the question of what are the implications of selecting this product.



Chpt.V-Figure 1: The four phases of an LCA and their interrelations in the LCA framework, from the International Standard ISO 14040 (ISO, 2006a).

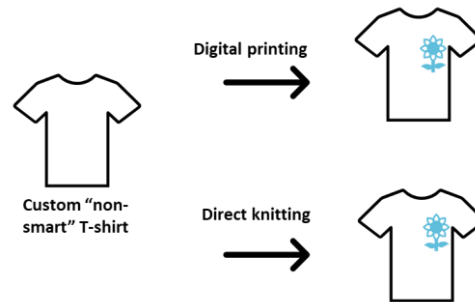
2 Goal and scope of research

Textile production has a wide range of environmental impacts, including global warming, water scarcity, and land-use changes [4]. These effects are likely to worsen due to rising textile consumption, which is being driven by increasing global per capita income levels and shorter apparel utilization cycles known as "fast fashion" [5]. According to a study conducted by the European Commission's Joint Research Centre (JRC) the textile industry contributes significantly and mainly to the depletion of material resources and water, as well as having a significant impact on land usage and climate change [6].

The purpose of this LCA study is to analyze the impact of different configurations of a photochromic T-shirt to select the most environmentally friendly model at the production level. We present an analysis of the life cycle stage from cradle to gate of a casual T-shirt made of commercialized well-known polymer" polyester". The main comparison is focusing on the utilization of tungsten oxide in the production process either by digital printing or direct-to-garment knitting methods. To our

Supplementary chapter

knowledge, this study is novel and has never been reported in the field of smart textiles and we aim to raise awareness regarding the impact of the production of these functionalized textiles.



Chpt.V-Figure 2: The proposed methods to produce a smart t-shirt.

3 Function and functional unit

The function of a T-shirt is to wear and show coloration changes under sunlight so that it can protect the human body and give multiple appearances for a lifetime of 200 days (equal to the lifetime of a regular digital printed t-shirt [20-22]). It can be for sport or casual wear. The incorporation of photochromic chemicals into textiles opens new possibilities, such as color-changing or light-responsive qualities that can improve functionality and user experience. The functional unit of the study is fabricating a 5*5 cm² photochromic spot on two medium size T-shirts using the proposed methods namely digital printing or direct knitting.

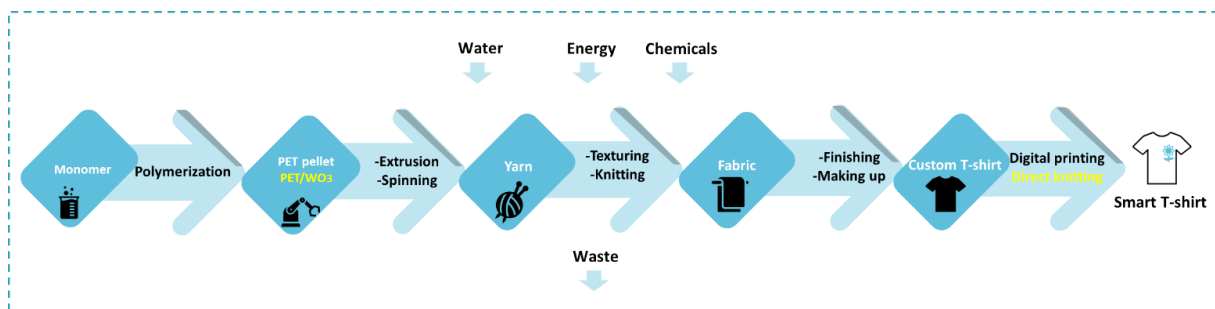
4 System boundaries

This study evaluates the cradle-to-gate impacts of the studied product systems meaning that the end-of-life and use phases are excluded from the study (It will be included in the future publication, this part is under developing). The proposed system boundary and value chain of production of a casual T-shirt (1.56 m² textile, 270 g) is shown in Figure 3. The system boundary consists of processes and materials flow. In this schematic, we address the conventional production of a custom/smart T-shirt made from polyester. All processes will be discussed in the following section. For the modeling of the two systems, the LCA software tool OpenLCA (version 3.8) together with version 2.6 of the database Ecoinvent were used in this study. The ReCiPe 2016 Midpoint (H) is used as the life cycle impact assessment (LCIA). With the ReCiPe method, the product systems are evaluated in several midpoint impact categories in order to identify if the burden-shifting of the environmental impact is taking place [19]. The following 12 impact categories (Table 1) are included and will be explained separately in the results and discussion part.

Supplementary chapter

Chpt.s-Table 1: Midpoints categories included in this study.

Impact category	Unit
Global warming potential	kg CO ₂ -eq
Stratospheric ozone depletion	kg CFC-11-eq
Ozone formation damage to humans	kg PM _{2.5}
Particulate matter formation	kg PM _{2.5}
Ionizing radiation	kB _q ²³⁵ U-eq
Terrestrial acidification	kg SO ₂ eq
Eutrophication of freshwater	kg Peq
Ecotoxicity of freshwater	CTUe
Land use	P _t
Water scarcity	m ³
Fossil resource scarcity	kg oil eq
Mineral resource scarcity	kg Cu eq



Chpt.V-Figure 3: System boundaries of the production process of the smart and custom photochromic T-shirt.

5 Life cycle inventory analysis (LCI)

The steps for the LCI phase include data collection, modeling of the various process, and The LCI began with identifying which data sets were relevant to include in the study, and then data collection began. The database for the (LCI) was obtained from Ecoinvent (v3.8). The LCI was built using data from technical handbooks, and literature sources describing the best available process and chemical production method. The final stage in the LCI phase was to use the obtained data to develop supply chain models.

- **LCI of the production phase**

The value chain starts with the extraction and refining of the required chemicals to produce the PET pellets via the polymerization step. Then the chemical industry sells the pellets to the textile industry, which spin and knits the pellets into fabrics. This process also includes the addition of photochromic additives namely tungsten oxide to impart specific properties to the produced fibers. Finally, the clothing industry makes the final garments using the provided fabrics.

Supplementary chapter

Polymer synthesis: Condensation of ethylene glycol with TPA results in the formation of ethylene terephthalate units, which are then connected via ester linkages (CO-O) to create the long chains of PET [7]. The large aromatic ring gives PET notable stiffness and strength, especially when the polymer chains are arranged in an orderly manner, as in the case of textile fibers, making PET highly resistant to biodegradation at its end-of-life phase [7]. Finally, PET is compressed into pellets for sale. The LCI database of the production of PET pellets (granulates) is available in the Ecoinvent database.

Fiber production: Melted PET pellets are extruded and spun into filaments. Thermal drawing is then used on these filaments to increase mechanical qualities like toughness. PET molecules are reoriented in the fiber direction and solidified during the drawing process. As a result, the crystallinity of the fiber is affected by the draw ratio used. In this step, we can add the photochromic fillers to functionalize the fibers with the active compounds (WO_3) to obtain the photochromic fibers as the building blocks for the modified yarn and fabric. This step was proofed by our work with Rescoll company (as mentioned in our Future Outlooks section) and recent academic references on using tungsten oxide as a photochromic filler in different polymer matrixes [8,9]. It is commonly to introduce additives in the spinning step of polyester to improve its quality or add novel properties [10]. Depending on our work and last paper [11], the additive weight percentage was fixed to 0.2 wt% of each 1 kg of pellets. This percentage is the lowest requirement to have an efficient photochromic fiber with the highest contrast between the two states before and after irradiation. The energy requirement for spinning is used from different previous LCA studied on garments production and summarized in Table 2.

Yarn production: The produced (non-modified or photochromic) filaments can be mixed and processed and combined to form yarns. Yarns can be prepared from either small staple fibers or long infinite filaments using spinning or extrusion processes. Similarly, yarns can be texturized at various levels to soften or make them more flexible, which can be accomplished through thermal or mechanical deformation of individual filaments [12,13]. To avoid misinterpretation, the textile industry uses a variety of ways to accurately express yarn thickness. Two significant units are often used in these systems: "tex" (sometimes designated as dtex or decitex, equivalent to 0.1 tex) and "denier." It is worth noting that 1 dtex equals 1 gram per 10 kilometers, whereas 1 denier equals 1 gram per 9 kilometers. We consider a drawn textured yarn (DTY) with a count of (47 den) and (52 dtex) [14]. The LCI database for yarn production is combined with the production of the fiber in Table 2.

Fabric production: The yarns finally are knitted to produce the fabric. The fabrics are then cut and sewed to make up the final T-shirt [15]. The energy requirements for knitting and making up the T-shirt are listed in Table 2. Several steps of making up, sewing and finishing are required to be applied on the fabric to get the final t-shirt. The energy required per t-shirt was averaged from several industrial and literature reviews and summed up in Table 2.

Supplementary chapter

Tungsten oxide production: The polyol synthesis method of the photochromic WO₃ was reported in the results chapter and it was scaled up to the industrial level. The LCI of the primary materials such as tungsten salt (tungsten hexachloride) and the polyol solvent and the scaled processes was built up and listed in Table 8. The scaling up of the different post process of drying and centrifuging were developed using the well know reference [16].

Digital printing (DP): Digital printing is a common industrial process to produce textiles with the additional design using reactive ink and connected software to design the desired shape. DP clothes need an additional finishing step mainly consists of steaming after washing and centrifuging [17]. Unlike screen printing, DP eliminates the requirement for water during the photochromic active spot printing process [18]. Water is still necessary for post-treatment before the digital printing stage operations like washing. The LCI database for DP is presented in Table 4.

Direct knitting (DK): This method is simply knitting the desired photochromic spot using the modified photochromic filaments. The LCI of this process is resumed in Table 5.

Chpt.V-Table 2 : LCI database for production chain of 1 kg of custom polyester fabric [20–25].

Inputs/outputs	Ecoinvent dataset	amount	unit
Inputs			
Deionized water	market for water, deionized- Eu w/o Switzerland	24.8	kg
PET pellet	polyethylene terephthalate production, granulate, amorphous - RER	1.05	kg
PET extrusion	electricity, medium voltage - Eu w/o Switzerland	0.89	kWh
PET spinning	electricity, medium voltage - Eu w/o Switzerland	0.3	kWh
Yarn knitting	electricity, medium voltage - Eu w/o Switzerland	1.22	kWh
Yarn knitting	heat, natural gas, at boiler condensing modulating < 100 kW/RER U	1.05	kg
Yarn texturing	electricity, medium voltage - Eu w/o Switzerland	0.5	kWh
Yarn transportation	transport, freight, rail/RER U	0.2	tkm
Fabric transportation	transport, lorry >32 t, EURO5/RER U	0.1	tkm
Output			
Wastewater	market for wastewater-Eu w/o Switzerland	0.0248	m ³
PET waste	disposal, polyethylene terephthalate, 0.2% water, to municipal incineration/CH U	0.05	kg

Chpt.V-Table 3: Production of one piece of custom t-shirt [26,27].

Inputs/outputs	Ecoinvent dataset	amount	unit
----------------	-------------------	--------	------

Supplementary chapter

Inputs			
PET fabric	-	0.27	kg
Finishing	electricity, medium voltage - Eu w/o Switzerland	0.15	kWh
Making up	electricity, medium voltage - Eu w/o Switzerland	0.33	kWh

Chpt.V-Table 4: LCI database for the digital printing process for one t-shirt [28,29]

Inputs/outputs	Ecoinvent dataset	amount	unit
Inputs			
Digital printing	electricity, medium voltage - Eu w/o Switzerland	0.3	kWh
Finishing	electricity, medium voltage - Eu w/o Switzerland	0.13	kWh
Inkjet	custom process	0.0056	kg
Water for washing	market for water, deionized- Eu w/o Switzerland	1.2	kg

Chpt.V-Table 5: LCI database for the direct knitting process for one t-shirt.

Inputs/outputs	Ecoinvent dataset	amount	unit
Inputs			
PET/WO₃ filament	custom process	0.002	kg
Filament knitting	electricity, medium voltage - Eu w/o Switzerland	0.01	kWh
Finishing	electricity, medium voltage - Eu w/o Switzerland	0.013	kWh
Output			
PET waste	disposal, polyethylene terephthalate, 0.2% water, CH U	0.0005	kg

Chpt.V-Table 6: LCI database to produce 1 kg of inkjet for DP method.

Inputs/outputs	Ecoinvent dataset	amount	unit
Inputs			
Tungsten oxide	custom process	0.02	kg
Isopropanol	isopropanol production, S-RER	0.73	kg
Ethylene glycol	ethylene glycol production, S-RER	0.25	kg
Energy	electricity, medium voltage - Eu w/o Switzerland	1.06	kWh

Chpt.V-Table 7: LCI database to produce 1kg of PET/WO₃ by extrusion.

Inputs/outputs	Ecoinvent dataset	amount	unit
Inputs			
Deionized water	market for water, deionized- Eu w/o Switzerland	24.8	kg
Tungsten oxide	custom process	0.021	kg
PET pellet	polyethylene terephthalate production, granulate, amorphous - RER	1.05	kg
PET extrusion	electricity, medium voltage - Eu w/o Switzerland	0.85	kWh
Output			

Supplementary chapter

PET waste	disposal, polyethylene terephthalate, 0.2% water, to municipal incineration/CH U	0.05	kg
------------------	--	------	----

Chpt.V-Table 8: LCI to produce 1 kg of tungsten hexachloride by chlorination of tungsten and the production of 1 kg of Tungsten oxide (WO₃) by polyol method [30].

Inputs/outputs	Ecoinvent dataset	amount	unit
Inputs			
Nitrogen for cleaning	air separation, cryogenic, nitrogen, liquid - RER	4	kg
Tungsten metal	market for tungsten concentrate-GLO	1.01	kg
Chlorine gas	chlor-alkali electrolysis, diaphragm cell, chlorine, gaseous, - RER	4.8	kg
Energy	electricity, medium voltage - Eu w/o Switzerland	1.5	kWh
Output			
Waste	Chlorine - Emission to water	4.5	kg

Chpt.V-Table 9: LCI of the production of 1 kg tungsten hexachloride.

Inputs/outputs	Ecoinvent dataset	amount	unit
Inputs			
Solvent	ethylene glycol production, diethylene glycol- RER	22.3	kg
Energy	electricity, medium voltage - Eu w/o Switzerland	4.0	kwh
Deionized water	market for water, deionized- Eu w/o Switzerland	3.9	kg
Tungsten hexachloride	custom process	1.45	kg
Output			
Recovered solvent	Diethylene glycol- (recovered)	10.5	kg
Waste	Chemical waste, unspecified - Waste	16.2	kg

6 Results and discussions:

LCA analysis results of the three different T-shirts namely (custom (normal), smart DP, and smart DK) were reported for the chosen environment impact categories. These results were evaluated for each stage starting from PET pellet production to the T-shirt production. First, we present the results of the production of a custom T-shirt followed by a detailed explanation of each contribution.

Figure 4 shows the contribution analysis for each step to produce a custom non-smart T-shirt. For all categories, the energy consumption (pellets extrusion, yarn knitting, yarn texturing, and T-shirt production) are the main responsible for the highest contribution. In the following discussion, we will focus mainly on the main midpoints that are important for our study:

Global warming potential (GWP)

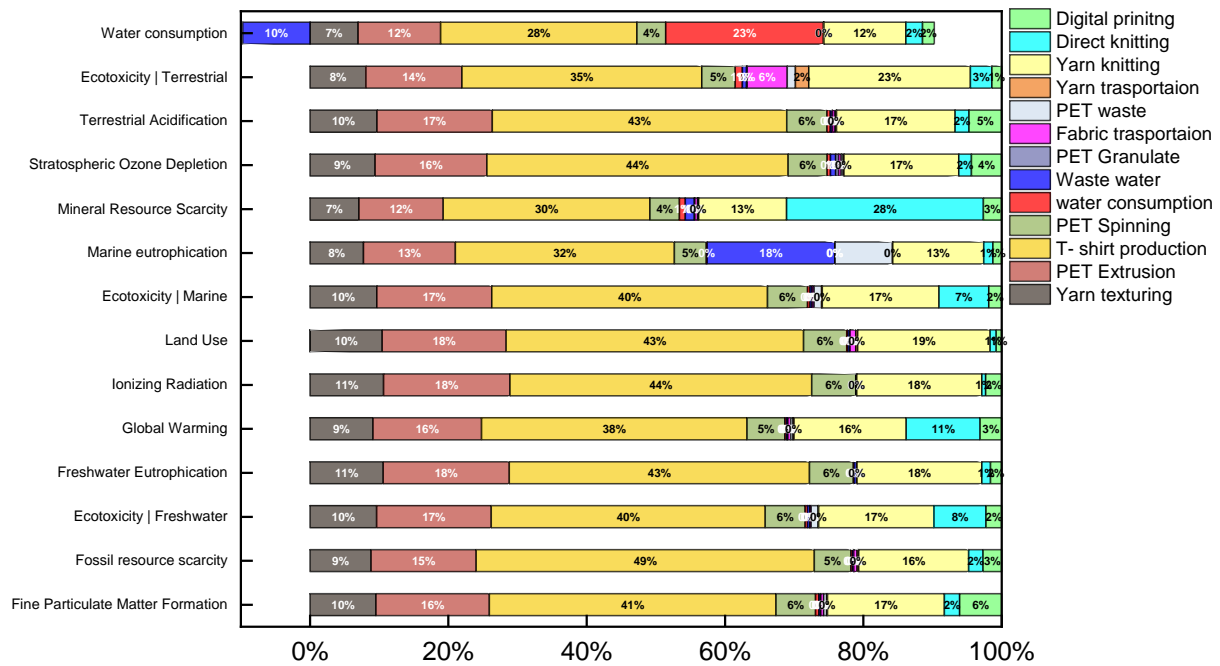
GWP is a measure of greenhouse gases such as carbon dioxide, nitrous oxide, and methane. GWP is expressed in kilos of carbon dioxide equivalent [2]. The CO₂ equivalent of GHGs is also known as the carbon footprint. Among the examined production steps, the highest GWP values were determined to

Supplementary chapter

be related to (16% yarn knitting, 16% pellets extrusion, and 38% T-shirt production) as illustrated in Figure 3. In addition to these processes, (9% yarn texturing and 5% fibers spinning) have minor impacts on GWP. In the yarn processing into the fabric using the knitting process, the highest GWP impact is caused by electricity use (64%) and consumption of heat (36%) which was supplied by natural gas [24,25]. During the yarn processing, the highest GWP impact is caused mainly by the knitting phase which uses most of the energy to convert yarn into fabric [21]. T-shirt production has the highest GWP values, and the GWP mostly originated from fossil fuel-based electricity utilized in making up, sewing machines, and ironing processes [20]. Lastly, Texturing involves numerous simultaneous processes on the filament yarn, such as drawing, heating, and twisting. In our estimates, we assumed a texturing energy usage of 1 kWh/kg. This figure is an average based on information from different studies [20, 31]. It is important to note that the energy used in these devices is mostly used to heat the material to the desired temperature. As a result, the GWP in this process is mainly governed by the energy consumption which is mostly determined by the weight of the material being processed. From Figure 5, using the photochromic inkjet in the DP process has a low GWP contribution (3%) which is attributed mainly to the energy consumption (heating, stirring, centrifuging, and drying) during the polyol synthesis of WO_3 and the inkjet preparation. In the case of direct knitting, the dominant factor contributing to the GWP value is the extrusion and the spinning of the PET/ WO_3 composites, accounting for a significant 11% of the total GWP. This GWP value can be linked directly to the higher required energy to produce the composite photochromic filament compared to ink synthesis.

Stratospheric ozone depletion: The ozone layer is critical in protecting the Earth from damaging UV rays emitted by the sun via absorption. According to the results, t-shirt production is the leading contributor to ozone depletion potential (ODP), accounting for 44% of the total followed by pellet extrusion (16%) and fabric production (yarn knitting) (17%). Additionally, other manufacturing stages, such as yarn texturing (9%) and fiber spinning (6%), contributes to the total increase in ODP. Indeed, wet processes in fabric manufacture need the use of high-quality process water [32]. These operations may emit halogenated organic chemicals into the air, depending on the treatment technology used [33]. Furthermore, the treatment operations necessitate the use of power generated from fossil fuels, which increases the release of volatile organic compounds (VOCs) into the atmosphere, contributing to ODP [34]. As proofed by Figure 4, the DK has contributed with a value (of 2%). While the DP has a bit higher impact (4%) because of using deionized water for post treatment process. Also, the use of organic compounds (isopropanol, ethylene glycol...) can release a significant number of VOCs into the atmosphere.

Supplementary chapter



Chpt.V-Figure 4: Contribution analysis results for all production stages of one piece of custom, smart DK, and smart DP shirts.

Abiotic depletion potential (ADP): As shown in Figure 4, the same dominant processes are still responsible for most of the impact due to the consumption of energy in the form of heating and electricity. The major mineral scarcity impact is developed once we use the WO_3 as the photochromic active compound reaching 28% in the DK method. This impact originates from using tungsten concentrate as a raw material which is known as critical metal in Europe [35]. On the other hand, using the DP has a lower impact (3%) due to the small quantity of WO_3 to produce the inkjet. The fabric production process, on the other hand, has a significant fossil scarcity of about 39% due to the use of fossil fuels in the knitting process.

Marine eco-toxicity (ME): Pollutant discharge into clean water sources and inorganic emissions emitted into the air have an impact on the ME. According to this study, the fabric and t-shirt production stages have the greatest ME value (57%). The use of high-quality process water and the necessity for natural gas during fabric manufacture increases the eco-toxicity potential [36]. Furthermore, reliance on electricity generation from fossil fuel power plants results in high inorganic emissions, particularly hydrogen fluoride (HF), which contributes significantly to the overall impact. This result also can be linked to the water consumption indicator which recorded a high contribution for the fabric production phase which requires the use of a considerable amount of water.

7 Comparison of the final products

This section provides an overview and comparison of the environmental impact of smart textile manufacturing utilizing the DP or DK techniques. By analyzing the environmental implications of these manufacturing processes, we can gain significant insights into their respective sustainability

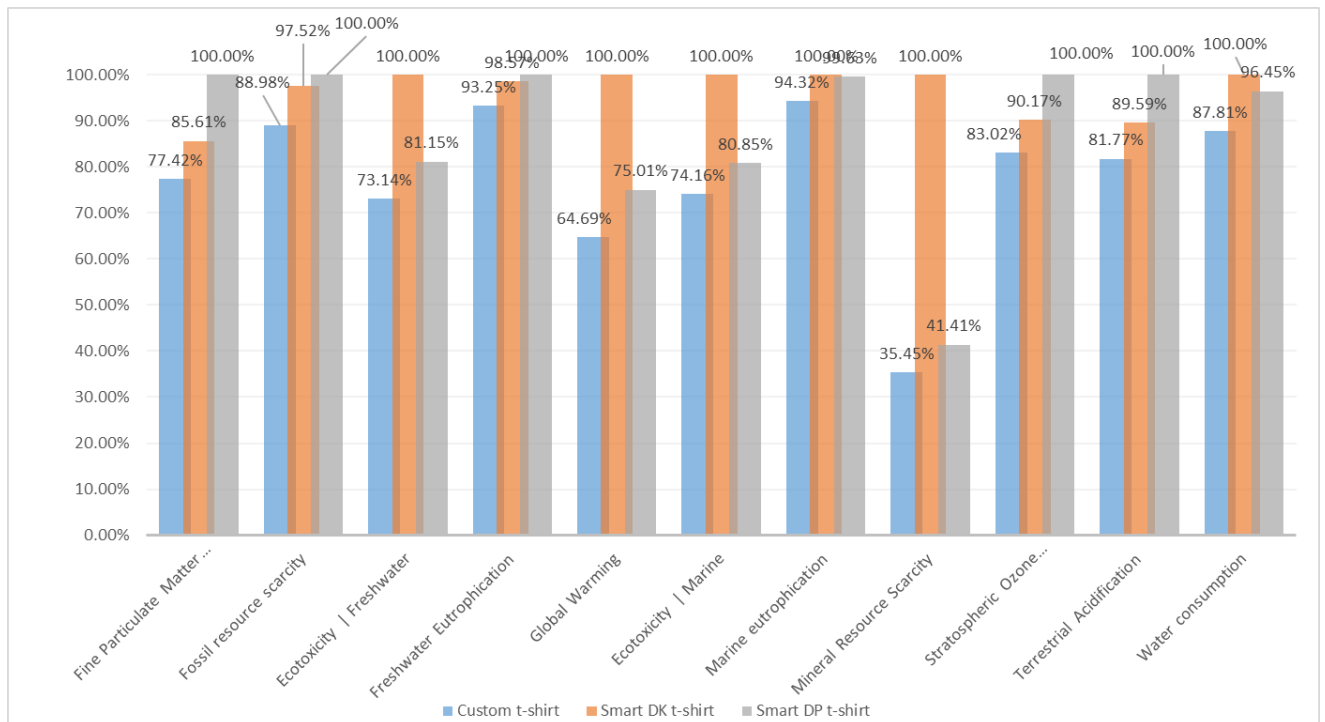
Supplementary chapter

profiles and make informed decisions about the best manufacturing process. In general, the DK and DP methods record a comparable close value for most of the indicators (Figure 5). As discussed in the previous section, most of the processes consume energy in the form of electricity and heat affecting most of the indicators. The use of WO_3 as a filler in DK has a significant effect on mineral scarcity. Whereas, in DP, the amount of inkjet needs it to cover the active spot is less than the weight of the functionalized filaments for the DK technique, but the ink contains a significant amount of organic solvents increasing the impact for some midpoints (for example freshwater eutrophication and stratospheric ozone depletion). To summarize, converting a custom t-shirt into a smart textile utilizing the DP or DK procedures can result in an overall increase in environmental consequences when compared to normal t-shirts. However, it is critical to go deeper into this debate and consider other factors.

Several criteria should be addressed in order to make an accurate estimate of the environmental impact and will be addressed soon in the future:

- **Material Selection:** The materials used for the t-shirt, as well as the dyes and chemicals used in the DP or DK techniques, can have a considerable impact on the environmental impact. Using low-impact dyes and sustainable and eco-friendly materials, such as organic cotton or recycled fibers, can help to minimize some of the negative environmental effects. Our suggestion is to use recycled PET as a source of the polymer.
- **Manufacturing Efficiency:** The DP or DK processes' efficiency in terms of energy and water usage, waste generation, and chemical management can all have an impact on their total environmental impact. Resource-efficient strategies, such as adopting energy-saving equipment, improving industrial processes, and utilizing closed-loop systems for chemical and water management, can all assist to lessen the environmental footprint.
- **Product Lifecycle:** It is critical to evaluate the smart textile's whole lifecycle. This includes thinking about product lifetime, recyclability, and end-of-life management. Smart textiles can have a longer lifespan and generate less waste if they are designed with durability in mind and promote ethical disposal or recycling choices. The analysis of the use and disposal phases will be addressed in the future planning of this project.
- **Comparison:** It is useful to compare the environmental impact of smart textiles produced using DP or DK technologies to that of other methods or ordinary textiles. This research can assist find areas for improvement and provide insights into the relative sustainability of certain production approaches. The comparison should include all the product life cycles to test which method is the best for both the production and use phases.

Supplementary chapter



Chpt.V-Figure 5: Comparison of the three final products for the main midpoint indicators.

8 Conclusion:

This study gives a summary of the preliminary results of the ongoing project with the CYVI group in Bordeaux. The study needs further optimization by completing the use and end-of-life phases to better evaluate the life cycle of the custom/smart t-shirt. Nevertheless, the results of the cradle-to-gate study promote digital printing as a promising method to prepare photochromic textiles. The DP method showed lower environmental impact in most of the main midpoint indicators. In general, the final decision to choose whether DP or DK should be taken after assessing all the production use, and disposal stages (from cradle to grave) which is under development.

9 References

- [1] C. K. Schoff, "An introduction to life cycle assessment," *Coatings Tech*, vol. 12, no. 1, p. 52, 2015, doi: 10.1016/B978-0-323-85451-1.00001-9.
- [2] I. V. Muralikrishna and V. Manickam, "Life cycle assessment," *Environ Manage*, pp. 57–75, 2017, doi: 10.1016/B978-0-12-811989-1.00005-1.
- [3] J. B. Guinée et al., "Life cycle assessment: past, present, and future," *Environ Sci Technol*, vol. 45, no. 1, pp. 90–96, Jan. 2011, doi: 10.1021/es101316v.
- [4] B. Resta, P. Gaiardelli, R. Pinto, and S. Dotti, "Enhancing environmental management in the textile sector: An organisational-life cycle assessment approach," *J Clean Prod*, vol. 135, pp. 620–632, Nov. 2016, doi: 10.1016/J.JCLEPRO.2016.06.135.

Supplementary chapter

- [5] S. S. Muthu, “Life cycle assessment and product carbon footprint modelling of textile products,” in *Assessing the environmental impact of textiles and the clothing supply chain*, pp. 131–141, Jan. 2020, doi: 10.1016/B978-0-12-819783-7.00007-7.
- [6] F. Bárcia de Mattos, V. Esquivel, D. Kucera, and S. Tejani, “The state of the apparel and footwear industry 1”. Jan, 2021.
- [7] M. A. J. Huijbregts et al., “ReCiPe2016: a harmonised life cycle impact assessment method at midpoint and endpoint level,” *Int J Life Cycle Assess*, vol. 22, no. 2, pp. 138–147, Feb. 2017, doi: 10.1007/s11367-016-1246-y.
- [8] K. Pang, R. Kotek, and A. Tonelli, “Review of conventional and novel polymerization processes for polyesters,” *Progress in Polymer Science (Oxford)*, vol. 31, no. 11, pp. 1009–1037, Nov. 2006, doi: 10.1016/j.progpolymsci.2006.08.008.
- [9] Q. Ma, B. Yang, H. H. Li, J. J. Guo, S. Q. Zhao, and G. H. Wu, “Preparation and properties of photochromic regenerated silk fibroin/tungsten trioxide nanoparticles hybrid fibers,” *Compo Commun*, vol. 27, Oct. 2021, doi: 10.1016/j.coco.2021.100810.
- [10] X. Dong, Y. Lu, X. Liu, L. Zhang, and Y. Tong, “Nanostructured tungsten oxide as photochromic material for smart devices, energy conversion, and environmental remediation,” *J Photochem C Photochem Rev*, vol. 53, Dec. 2022, doi: 10.1016/j.jphotochemrev.2022.100555.
- [11] T. V. Pinto et al., “Photochromic polypropylene fibers based on UV-responsive silica@phosphomolybdate nanoparticles through melt spinning technology,” *Chem Eng J*, vol. 350, pp. 856–866, Oct. 2018, doi: 10.1016/j.cej.2018.05.155.
- [12] Y. Badour et al., “Low-cost WO₃ nanoparticles / PVA smart photochromic glass windows for sustainable building energy savings,” *Solar Energy Mater Solar Cells*, vol. 255, p. 112291, Jun. 2023, doi: 10.1016/j.solmat.2023.112291.
- [13] C. Lawrence, “Fibre to yarn,” in *Textiles and fashion*, Elsevier, 2015, pp. 213–253. doi: 10.1016/B978-1-84569-931-4.00010-6.
- [14] D. (Xuedong) Li, “Fundamental of fibers,” in *Cut protective textiles*, Elsevier, 2020, pp. 59–110. doi: 10.1016/B978-0-12-820039-1.00003-1.
- [15] I. G. Crouch, L. Arnold, A. Pierlot, and H. Billon, “Fibres, textiles and protective apparel,” *Sci Armour Mater*, pp. 269–330, Jan. 2017, doi: 10.1016/B978-0-08-100704-4.00006-2.
- [16] D. (Xuedong) Li, “Convert fiber to textile,” in *cut protective textiles*, Elsevier, 2020, pp. 111–127. doi: 10.1016/B978-0-12-820039-1.00004-3.
- [17] F. Piccinno, R. Hischer, S. Seeger, and C. Som, “From laboratory to industrial scale: a scale-up framework for chemical processes in life cycle assessment studies,” *J Clean Prod*, vol. 135, pp. 1085–1097, Nov. 2016, doi: 10.1016/j.jclepro.2016.06.164.

Supplementary chapter

- [18] M. I. Tobler-Rohr, “Handbook of sustainable textile production,” Elsevier, pp. 1–488, Jun. 2011, doi: 10.1533/9780857092861.
- [19] D. Kuscer, “Screen printing,” *Encyclopedia of materials: technical ceramics and glasses*, vol. 1–3, pp. 227–232, May 2021, doi: 10.1016/B978-0-12-803581-8.12082-X.
- [20] S. Horn, K. M. Mölsä, J. Sorvari, H. Tuovila, and P. Heikkilä, “Environmental sustainability assessment of a polyester T-shirt: Comparison of circularity strategies,” *Science of The Total Environment*, vol. 884, p. 163821, Aug. 2023, doi: 10.1016/J.SCITOTENV.2023.163821.
- [21] E. K. E Kaplan, “Investigation of energy consumption in yarn production with special reference to open-end rotor spinning,” *Fibres Text East Eur*, vol. 18, no. 79, pp. 7–13, 2010.
- [22] E. Ç. E Koç, “Analysis of energy consumption in woven fabric production,” *Fibres Text in East Eur*, vol. 18, no. 79, pp. 14–20, 2010.
- [23] T. Walser, E. Demou, D. J. Lang, and S. Hellweg, “Prospective environmental life cycle assessment of nanosilver T-shirts,” *Environ Sci Technol*, vol. 45, no. 10, pp. 4570–4578, May 2011, doi: 10.1021/es2001248.
- [24] G. G. Smith and R. H. Barker, “Life cycle analysis of a polyester garment,” *Resour Conserv Recycl*, vol. 14, no. 3–4, pp. 233–249, 1995, doi: 10.1016/0921-3449(95)00019-f.
- [25] N. M. Van Der Velden, M. K. Patel, and J. G. Vogtländer, “LCA benchmarking study on textiles made of cotton, polyester, nylon, acryl, or elastane,” *Int J Life Cycle Assess*, vol. 19, no. 2, pp. 331–356, Feb. 2014, doi: 10.1007/S11367-013-0626-9/TABLES/10.
- [26] B. M. K. Manda, E. Worrell, and M. K. Patel, “Prospective life cycle assessment of an antibacterial T-shirt and supporting business decisions to create value,” *Resour Conserv Recycl*, vol. 103, pp. 47–57, Aug. 2015, doi: 10.1016/j.resconrec.2015.07.010.
- [27] S. Moazzem, E. Crossin, F. Daver, and L. Wang, “Assessing environmental impact reduction opportunities through life cycle assessment of apparel products,” *Sustain Prod Consum*, vol. 28, pp. 663–674, Oct. 2021, doi: 10.1016/j.spc.2021.06.015.
- [28] M. Kariniemi, M. Nors, M. Kujanpää, T. Pajula, and H. Pihkola, “Evaluating environmental sustainability of digital printing,” *NIP Digital Fabrication Conf*, vol. 26, no. 1, pp. 92–96, Jan. 2010, doi: 10.2352/ISSN.2169-4451.2010.26.1.ART00025_1.
- [29] H. Ujiie, “Digital printing of textiles,” Elsevier, pp. 1–368, 2006, doi: 10.1533/9781845691585.
- [30] M. Bourdin et al., “Nanoparticles (NPs) of WO_{3-x} compounds by polyol route with enhanced photochromic properties,” *Nanomater*, vol. 9, no. 11, p. 1555, Nov. 2019, doi: 10.3390/nano9111555.

Supplementary chapter

- [31] A. Demir and H. M. Behery, “Synthetic filament yarn: texturing technology,” *Synthetic Filament Yarn: Texturing Technology*, p. 1, 1997.
- [32] S. Moazzem, F. Daver, E. Crossin, and L. Wang, “Assessing environmental impact of textile supply chain using life cycle assessment methodology,” vol. 109, no. 12, pp. 1574–1585, Dec. 2018, doi: 10.1080/00405000.2018.1434113.
- [33] F. M. Piontek and M. Müller, “Literature reviews: life cycle assessment in the context of product-service systems and the textile industry,” *Procedia CIRP*, vol. 69, pp. 758–763, Jan. 2018, doi: 10.1016/J.PROCIR.2017.11.131.
- [34] Y. Zhang et al., “Improved design for textile production process based on life cycle assessment,” *Clean Technol Environ Policy*, vol. 20, no. 6, pp. 1355–1365, Aug. 2018, doi: 10.1007/S10098-018-1572-9/METRICS.
- [35] P. O. of the E. Union, “Study on the review of the list of critical raw materials : final report.,” Sep. 2017, doi: 10.2873/876644.
- [36] A. K. Roy Choudhury, “Environmental impacts of the textile industry and its assessment through life cycle assessment,” pp. 1–39, 2014, doi: 10.1007/978-981-287-110-7_1.

General conclusion

General conclusion and prospective

This doctoral thesis work was dedicated to the study of tungsten oxide (WO_{3-x}) based materials and the feasibility to develop different devices for X-chromic applications.

In the first part, we investigated the possibilities to improve the photochromism mechanism of WO_{3-x} by structural modification. In the first step, we successfully tuned the sub-stoichiometry of the as-prepared WO_{3-x} nanoparticles via reductive polyol precipitation followed by a partial chemical re-oxidation thanks to peptization into chromate aqueous solutions. W/O stoichiometric ratio has been analyzed by multiple technics. The most re-oxidized samples exhibited the best selectivity (high visible transparency but with high NIR absorptivity) for the use of these compounds as solar filters, i.e., with the best contrast between the visible and near-infrared transmission. The coloring mechanism under UV irradiation of the studied samples was governed mainly by fast photo-reduction of the surface cations from W^{+6} to W^{+5} associated with facile surface oxygen absorption-desorption. The detailed structural analysis of the WO_{3-x} nanocrystallites was performed by coupling XRD pattern analysis, PDF analysis and TEM graphs. The crystal structure of all studied samples can be described in terms of exhibiting a monoclinic framework with P21/n space-group but with monoclinic distortion maintained despite the obtaining of the very low crystallite size. Moreover, thin films were prepared by dip-coating starting from $\text{WO}_{3-x}/\text{EtOH}$ suspensions. From an applicative point of view, the UV photo-detection measurements yielded a good responsivity of 0.37 A/W and external quantum efficiency of 123.5% even at a very low power density (9.2 W/m^2) of the UV illumination. The as-prepared thin films can so be used as UV micro-dose sensors.

Following the first route for improving the photochromism, we tried doping by copper as an alternative method. Indeed, it was already reported in the literature that doping of WO_{3-x} with Cu ions constituted an effective strategy to improve the bleaching mechanism of our studied films. The photochromism (coloring/bleaching contrasts and kinetics) of these Cu-doped nanoparticles obtained from the polyol method was thoroughly studied. The coloring mechanism of un-doped films governed mainly by fast components consists of a quick photo-reduction of the surface cations from W^{+6} to W^{+5} . Then the surface becomes saturated after a short time with W^{+5} ions, and this fast mechanism stops. On the contrary, the WCu1 film kinetic, which is governed by the slow component, corresponds to the ionic diffusion of the W^{5+} from the surface to the material bulk. The WCu1 film records faster bleaching with an order of 3 hours compared to 14 hours for the WO film. The bleaching kinetic was enormously enhanced due to the increase in oxygen vacancies in WO_3 after Cu doping, which could in turn extend the light-harvesting ability of this compound to the visible and near-infrared region. In addition, the cycling study on WCu1 film confirms the efficiency of the product in optical applications.

By taking advantage of the photochromic NPs, we introduced a new study to disperse the WO_{3-x} in the polymeric matrix to combine the flexibility/transparency of the matrix and the photochromism of the NPs. Different thin/thick films were prepared using dip-coating and solvent-casting methods. In these films, WO_{3-x} nanoparticles ensured the role of the photochromic canters, and the PVA matrix was used as transparent polymer matrix as well as an efficient dispersing agent of the tungsten oxide colloids.

General conclusion and prospective

The photochromism behavior of both composite series (SC and DC) was again thoroughly studied. On this aspect, thin DC films exhibit a superior photochromic speed than SC films, surely due to a photo-redox reaction blocking effect from the PVA matrix. In addition, the thermal insulation measurements, performed on the SC film series, indicated a very good thermal regulation performance of our smart windows, especially when the smart films are deposited on the front side of the window glasses beside the irradiation source. With this front size design, white or black-painted model rooms are well thermally insulated, with a gain of temperature moderation compared to a virgin glass window of almost $\Delta T = 20.2$ and 19.5°C respectively, with white or black room design.

In a separate part, we moved from the study of 0D (nanoparticles: NPs) and 2D (thin and thick photochromic films) to 1D system (fibers) and 2D (textile). For the 1D system, we investigated the preparation of functionalized PES commercial fibers by WO_{3-x} by three main methods: surface modification of the preform via dip-coating in different suspensions, bulk modification of the preform by embedding NPs, and post-coating of PES-optical fibers (named as “F03 series” in Chapter III – Part 4). As one main discovery revealed by the coloring kinetic, the F03 fibers (modified by post coating method) demonstrated higher coloring intensity upon UV irradiation with a remarkably clear amplification of the axial transmission signal through the fiber: negative photochromism. Moreover, the post-coating method was thoroughly developed by using the PVP as a dispersant agent. As revealed from the coloring and bleaching kinetic parameters, the concentration of NPs played a significant role in the negative photochromism amplitude as well as in the speed of the coloring mechanism. Furthermore, the modified PVP cladding could maintain the higher active NPs concentration with the same function and phenomena without the formation of cracks or imperfections.

Also, we studied another 1D system consisting of hybrid inorganic/organic WO_3 -doped PMMA optical fibers. Macroscopic preforms have been successfully synthesized by the radical polymerization of MMA doped with modified photochromic WO_3 nanoparticles, followed by their thermal stretching into tens-of-meters-long optical fibers with diameters ranging from 200-600 μm . The 0.2% WO_3 -doped preform showed a slow coloring mechanism and an irreversible photochromic behavior while single fibers exhibited more intense and more rapid coloring and bleaching phenomena, comparable to the photochromic parameters of WO_3 powder beds. This showed that the PMMA matrix contributed to blocking the oxygen diffusion as the source of the WO_3 redox activity at the origin of the color changes. Thus, the effect, intense for the thick preforms, became negligible for fiber shapes, opening their potential application as photochromic textile fibers. Moreover, we have presented a 2D photochromic fabric made of hand-made woven 0.2%- WO_3 doped fibers. It showed a fast-bleaching response, with a decay time of 4.2 hours, along with a very large visible contrast ($\Delta C = 43.6$). The proposed hybrid WO_3 /PMMA composites were thermally stable and amenable for shaping, without compromising the sensitivity of their photochromic phenomena. The successful coloring/bleaching mechanism of the proposed 1D single fibers and 2D fabric systems, conjugated to

General conclusion and prospective

a fast response to UV excitation, demonstrates their potential as flexible fiber-based UV-sensor devices and smart textiles.

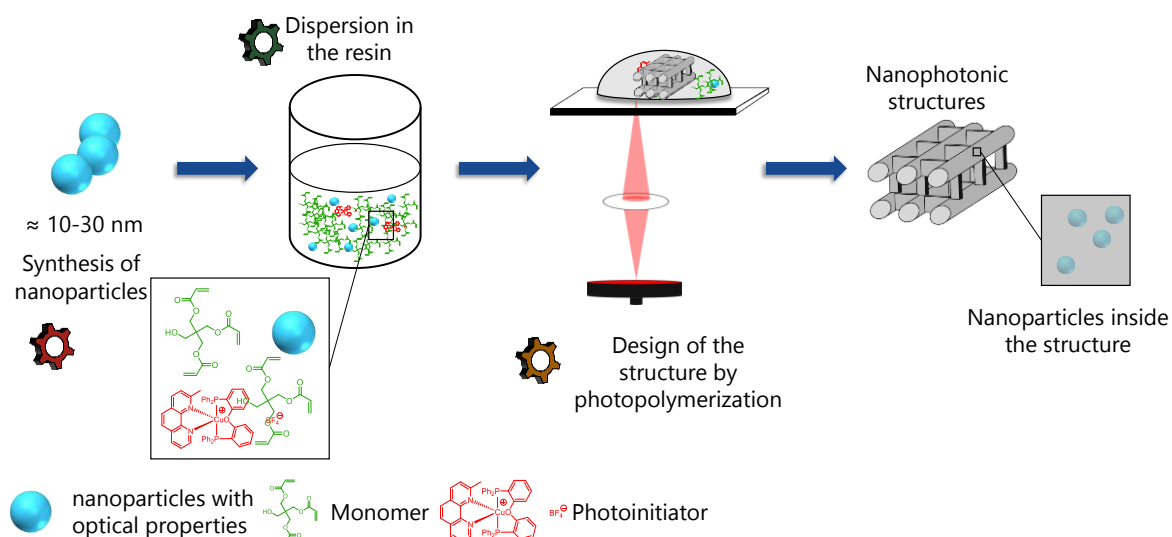
Ongoing work and Future outlooks:

This Ph.D. work constitutes the first brick of three different ongoing or soon-expected projects in the research team:

- (i) Smart photonic crystals made from 2D photo-polymerization of composite WO₃ NPs / photopolymer composite resins.
- (ii) Design of negative photochromic envelopes based on WO₃ photochromic NPs for IR camouflage.
- (iii) FDM-based 3D additive manufacturing of various photochromic devices

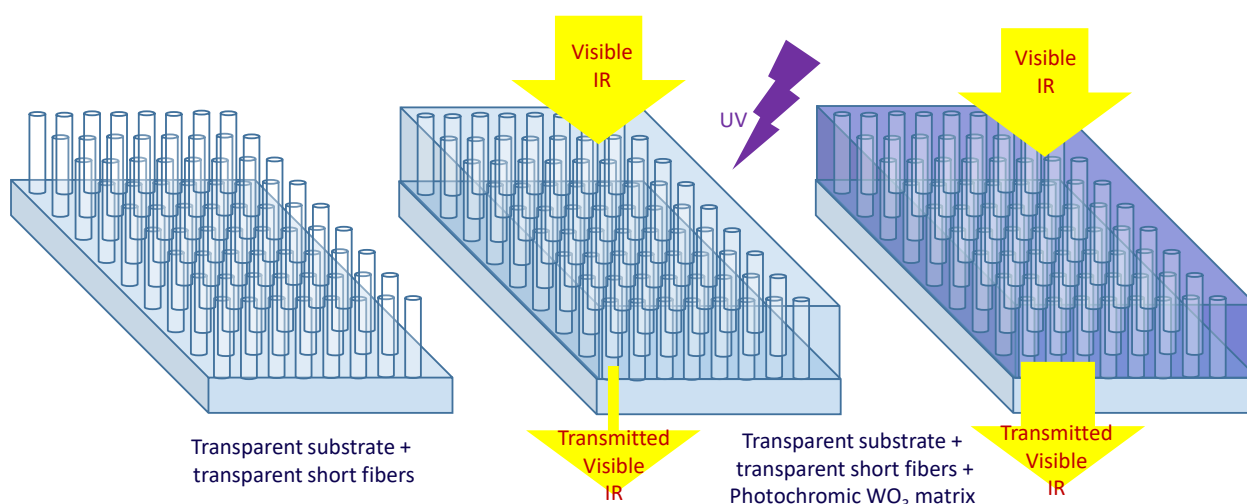
(i) In a context where new technologies require the development of a growing number of multifunctional devices, the fabrication of nano- and micro-structured materials structures is of major interest. Nanoscale structured materials offer unique physical, chemical and biological properties that differ from their larger counterparts and can be used for a wide range of applications in the fields of optics, catalysis, etc. However, their architecture needs to be finely controlled, which is possible with the printing techniques developed over the past decade. This is the background to the Ph.D. of Ludovic Belhomme (started: October 2022), during which he aims to fabricate 2D and 3D multifunctional materials using two-photon lithography. This technique enables the creation of polymer microstructures with complex geometries and very high resolution, by focusing a femtosecond laser to promote localized (point) polymerization in the laser's focal region (vortex). His approach is based initially on the synthesis of photochromic WO₃ nanoparticles (NPs) and then the incorporation of these NPs into a polymer resin to obtain a functional photopolymerizable ink. The final stage involves the two-photon polymerization of this ink to fabricate functional photopolymerizable structures (photonic crystals) containing photochromic NPs, with synergistic properties (Figure 1).

General conclusion and prospective



C-Figure 1: The main steps' scheme of Ludovic Belhomme's program.

(ii) Our discovery of the potential for negative photochromism based on tungsten oxide, by architecting photochromic tungsten oxides and transparent polymer fibers, will be one of the central points of the COSTUME project (de Clair-Opaque à Sombre-Transparent: Un Masque Efficace, ANR Astrid 2023). As shown in Figure 2, it is ambitious by the deposition of thin layers around transparent PES fibers (even of relatively poor morphological quality, with thickness variability, cracks and uncontrolled porosities) combined with UV excitation of the photochromic "cladding" to produce a strong increase in axial transmission in the transparent range of the polymer fiber. The best is to be able to transfer what was observed in this Ph.D. on single 1D long-fibers to "short-fiber carpets" (of the order of an mm) (Figure 2). It is therefore entirely conceivable to obtain films whose transparency could undergo a negative photochromic phenomenon. Applications as camouflage envelopes for both civil and military applications are expected to be opened.



C-Figure 2: The negative-photochromic carpets allow manipulating the visible/IR transmission through UV irradiation.

General conclusion and prospective

(iii) finally, in a first attempt to fabricate 3D filaments made of commercial PMMA granulates with different loadings of WO_{3-x} nanopowders, we have successfully proofed the feasibility of this project thanks to a collaboration with the RESCOLL company in Pessac. Myself, I spend the few last days of my Ph.D. experimentally initiating the project.

Methods: Prior to extrusion, the PMMA polymer was subjected to a drying process in a vacuum oven at 80°C for up to 4 hours to eliminate any moisture content. In a second step, the WO_{3-x} nanopowders were mixed with the PMMA pellets by manually mixing and shaking to insure the electrostatic adsorption of the NPs on the surface of the pellets. The PMMA/ WO_{3-x} was extruded at 195°C . A spinning system was equipped to collect the produced filaments/fibers. The process uses the following equipment:

- A single-screw extruder, Thermofisher model Haake Rheomex OS.
- The screw used was a 19 mm diameter screw with a compression ratio of 3 and an L/D ratio of 25.
- A capillary die is equipped with a pressure sensor, a temperature sensor, and a nozzle. Different filament diameters can be obtained using a monofilament nozzle with various diameters (0.5, 1, 2 mm).
- A conveyor belt for filament stretching and a winder to collect the filaments.

The conditions of fabrication of the filaments and the fibers are resumed in Table 1.

C-Table 1: Extrusion conditions for filament and fiber production.

Sample	Extrusion speed (rpm)	Temperature ($^\circ\text{C}$)	Collecting speed (rpm)
Filament (1.75 mm)	20	200	7
Fiber (200 μm)	5	200	57

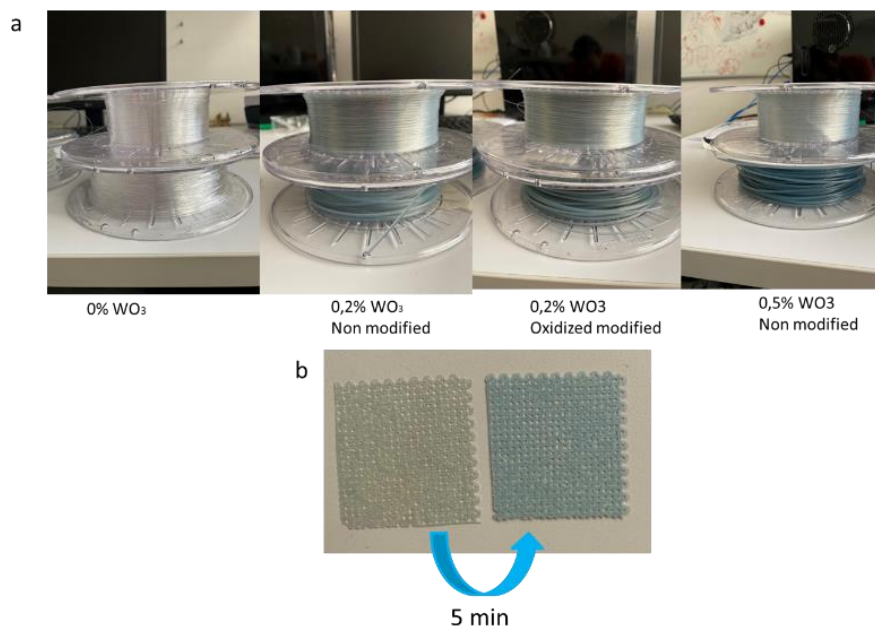
The list of extruded filaments and fibers (8 in total) are listed in Table 2 and shown in Figure 3.a.

C-Table 2: List of the extruded filaments and fibers.

Powder (wt%)	0% WO_3	0,2% WO_3 Non modified	0,2% WO_3 Modified (oxidized)	0,5% WO_3 Non modified
Fiber	✓	✓	✓	✓
Filaments	✓	✓	✓	✓

General conclusion and prospective

To test the performance of the photochromic filaments, they were printed into a carpet of (10x10 cm²) using fused deposition modeling (FDM), also known as fused filament fabrication. The FDM is a process for additive manufacturing that includes passing a material filament through a heated extrusion nozzle. The 0.2% unmodified filament with a diameter of 1.75 ± 0.07 mm was extruded using the FDM process for the purpose of 3D-printing carpet structure. Before each 3D-printing cycle, the temperatures of the extrusion nozzle were meticulously verified and set at 120 °C which correspond to the T_g of the PMMA polymer. A primary photochromic test was made to verify the feasibility of the filament as a new class of photochromic materials. As shown in Figure 3.b, the carpet changes its color within 5 minutes from pale white to pale blue confirming the photochromic properties of the filaments. Further quantitative and qualitative measurements are required to develop and verify all the filament properties, including mechanical and morphological properties.



C-Figure 3: The different issued filaments (bottom) and fibers (top) from the extrusion process.

Finally, the supplementary chapter revealed preliminary findings from an ongoing initiative with the CYVI group in Bordeaux, concentrating on the life cycle of a custom/smart t-shirt. While more work is needed to complete the assessment of the usage and end-of-life phases, the cradle-to-gate study has already shown that digital printing offers significant promise for creating photochromic fabrics. To make a well-informed decision between DP and DK procedures, all stages of manufacture, use, and disposal must be considered, encompassing the complete life cycle of the t-shirt. This complete study will provide vital insights into the environmental impacts and overall sustainability of each practice, from cradle to grave. This project will be fully completed during the last two months of my Ph.D.

Titre : Étude des matériaux à base d'oxyde de tungstène photochromique (WO_{3-x}) : Synthèse, caractérisations et élaboration de systèmes organiques-inorganiques hybrides (0D, 1D, 2D) pour des applications optiques.

Résumé : L'incorporation d'oxyde de tungstène X-chromiques WO_{3-x} dans une matrice polymère est le sujet principal de cette thèse. Cela représente une contribution significative à la recherche en cours sur les matériaux "X-chrome" à l'ICMCB. Dans la première partie de cette thèse, nous étudions la mise en œuvre de différentes techniques pour développer le photochromisme de l'oxyde de tungstène WO_{3-x} nanostructuré. La première méthode consiste à ajuster la sous-stœchiométrie en oxygène des nanoparticules préparées à partir d'un processus de peptisation des nanoparticules dans des solutions aqueuses de différentes concentrations de $Cr_2O_7^{2-}$. Le rapport stœchiométrique W/O a été analysé par plusieurs techniques. Les échantillons les plus réoxydés présentent la meilleure sélectivité (une grande transparence visible mais une grande absorptivité proche infrarouge) pour l'utilisation de ces composés en tant que filtres solaires, c'est-à-dire avec le meilleur contraste entre la transmission visible et proche infrarouge. Les films minces préparés par trempage se révèlent efficaces pour la photo-détection UV même à une densité de puissance très faible ($9,2 \text{ W/m}^2$) d'illumination UV. La deuxième méthode est le dopage structural par le cuivre (Cu). La cinétique de décoloration est considérablement améliorée en raison de l'augmentation des lacunes d'oxygène dans le WO_{3-x} après le dopage au cuivre, ce qui pourrait à son tour étendre la capacité de captage de lumière de ce composé à la région visible et proche infrarouge. Dans la deuxième partie, nous présentons la fabrication de films composites WO_{3-x} /PVA en tant que revêtements photochromiques intelligents sur un substrat en verre selon deux méthodes : le moulage par solvant (SC) et le trempage (DC). Après avoir analysé attentivement la relation entre les caractéristiques des films SC et DC et les performances optiques, nous avons conclu que la méthode SC offre des films de meilleurs candidats pour une application post-optique en termes de réduction de la diffusion, d'amélioration du contraste visible/infrarouge et d'efficacité photochromique accrue. Les fenêtres photochromiques intelligentes SC proposées ici sont tout aussi efficaces tout en étant plus abordables que les panneaux électrochromiques ou les films minces thermochromiques à base de VO_2 pour réduire la température intérieure de la maison (près de 20°C) lors d'une irradiation solaire, démontrant ainsi leur grand potentiel en tant que matériaux intelligents et économiques en énergie. Dans la dernière partie, nous étudions pour la première fois l'intégration du WO_{3-x} nanostructuré à l'intérieur de fibres polymères. Nous discutons l'incorporation directe de nanoparticules de WO_{3-x} dans une matrice de fibres optiques plastiques (POF) en polyméthacrylate de méthyle par polymérisation radicalaire en masse. La préforme dopée fabriquée présente un comportement photochromique irréversible. De manière surprenante, la fibre unique se révèle efficacement photochromique grâce à une dégradation du signal de transmission lors de l'irradiation UV. Il a été prouvé que le WO_{3-x} joue un double rôle en tant que centres d'absorption intrinsèques et extrinsèques, entraînant ainsi des pertes de transmission plus élevées. Néanmoins, l'étude de coloration de la fibre unique dopée a révélé une réponse rapide à la dose d'UV en fonction du temps d'irradiation. Les systèmes proposés (fibres plastiques dopées) ont démontré leur grand potentiel en tant que matériaux inorganiques/organiques novateurs dans le domaine des capteurs photochromiques fibrés. De plus, nous proposons la conception d'une fibre optique plastique cœur/gaine. La gaine est composée du WO_{3-x} nanostructuré avec une coeur commerciale en polyéther sulfone (PES). Pour finir, nous avons étudié l'impact environnemental de nos produits d'une échelle du laboratoire à une échelle industrielle en utilisant la méthode d'évaluation du cycle de vie.

Mots clés : Polymer ; Photochromique ; Fibres ; Inorganique ; Optique ; Oxyde de tungstène.

Title :Unlocking the Potential of Photochromic Tungsten Oxide (WO_{3-x}) Materials : Synthesis, Characterization, and Shaping of Hybrid organic-inorganic WO₃-doped Systems (0D, 1D, 2D) for Optical Applications.

Abstract : The incorporation of X-chromic tungsten oxides WO_{3-x} in a polymer matrix is the core subject of the thesis. It represents a significant contribution to the ongoing research on "X-chrome" materials at ICMCB. In the first part of this thesis, we investigate the implementation of different techniques to develop the photochromism of nanostructured tungsten oxide WO_{3-x}. The first method is the tuning of the oxygen sub-stoichiometry of as-prepared NPs from a polyol process via peptization of the NPs in an aqueous solution of different Cr₂O₇²⁻ concentrations. The W/O stoichiometric ratio has been analyzed by multiple technics. The most re-oxidized samples exhibit the best selectivity (high visible transparency but with high NIR absorptivity) for the use of these compounds as solar filters, i.e., with the best contrast between the visible and near-infrared transmission. The prepared thin films by dip coating proved to be efficient for UV photo-detection even at a very low power density (9.2 W/m²) for UV illumination. The second method is structural doping by copper (Cu). The bleaching kinetic is enhanced due to shallow states created in the band gap of the WO₃ semiconductor associated with copper cation doping, which could in turn extend the light-harvesting ability of this compound to the visible and near-infrared region. In the second part, we present the fabrication of WO_{3-x}/PVA composite films as smart photochromic coatings on glass substrate by two methods: solvent casting (SC) and dip-coating (DC). After carefully analyzing the relationship between the SC and DC film characterizations and their optical performance, we conclude that the SC method leads to films that are better candidates for post-optical application in terms of scattering reduction, improved visible/infrared contrast, and better photochromic efficiency. The photochromic SC smart windows proposed here are equally efficient while being more affordable than electrochromic panels or VO₂ thermochromic thin films to reduce the inner house temperature (almost 20°C) upon solar irradiation, demonstrating their great potential as smart cost-effective energy-saving materials. In the last part, we investigate for the first time, the integration of the nanostructured WO_{3-x} inside microfibers. We discuss the direct incorporation of NPs in a matrix of plastic optical fibers (POFs) of polymethyl methacrylate by bulk radical polymerization. The fabricated doped preforms show an irreversible photochromic behavior. But surprisingly, the single fiber proves to be an efficient photochromism through a large degradation of transmission signal upon UV irradiation and nearly full reversibility (regain of the transmission under dark conditions through WO₃ bleaching). Furthermore, the coloring study of the single-doped fiber reveals a fast response to the UV dose upon irradiation time. The WO₃-polymer composite fibers demonstrate their great potential as novel inorganic/organic materials in the domain of photochromic sensors and textiles. Additionally, we propose the design of polymer core / composite cladding fibers. Here the cladding consists of the nanostructured WO_{3-x} dispersed in a PVP matrix coated on a commercial core of polyether sulfone (PES). The photochromic plastic fibers show a phenomenon of "negative" photochromism where the transmitted signal is amplified under UV irradiation. Finally, in the last part, we investigate the environmental impact of our lab-scale products on an industrial scale using the life cycle assessment method.

Keywords : Polymer ; Photochromic ; Fibers ; Inorganic ; Optical ; Tungsten oxide.

Unité de recherche

Institut de Chimie de la Matière Condensée de Bordeaux, UMR 5026, 87, Avenue du Dr. Albert Schweitzer, 33608 Pessac cedex.